Dynamics, Topology and Quantum Geometry in Non-Hermitian Exciton-Polariton Systems

Yow-Ming Robin Hu

A thesis submitted for the degree of
Doctor of Philosophy at
The Australian National University

March 2026

Declaration

This thesis is an account of research undertaken between March 2022 and October 2025 at The Department of Quantum Science and Technology, Research School of Physics, The Australian National University, Canberra, Australia.

Except where acknowledged in the customary manner, the material presented in this thesis is, to the best of my knowledge, original and has not been submitted in whole or part for a degree at any other university.

Yow-Ming Robin Hu
March 2026

Acknowledgements

The past four years of my life at the Australian National University have been one of the most unforgettable and exciting periods of my entire life. I had the opportunities to learn many new skills, travel to many new places for conference and research visits, and meeting many wonderful people. I was very fortunate to be able to conduct my research in ANU and to be able to finish my program. I am especially fortunate to have such great colleagues and supervisors who supported me in the past four years.

First, I owe my deepest gratitude to my supervisors, Prof. Elena Ostrovskaya and Dr Eliezer Estrecho, for their guidance and wisdom in the past four years. This thesis would not be possible without their constant support. I am also very grateful that they have always encouraged me to apply for grants, to attend various conferences, and to publish my work, and to help me finish this very Thesis. I also want to thank other past and present members of my research group, ANU Polariton BEC Group, Prof. Andrew Truscott, Dr Mateusz Król, Bianca Rae Fabricante, Sheil Sequiera, Sarka Vavreckova, Robert Pellegrino, Dr Matthias Wurdack and many more, for their various feedback, and being such wonderful colleagues in the past four years.

I also want to acknowledge the support from the Australian Research Council Centre of Excellence in Future Low-Energy Electronic Technologies (FLEET) through the Center of Excellence Grant CE170100039. I want to thank FLEET, especially to Dr Tich-Lam Nguyen and Dr Jason Major, for always organising the best workshops and networking events which allow me to meet many amazing young physicists all across Australia, and learn about their works, and to develop various skills that helped my writing, interview and my day-to-day life.

I also want to thank the Robert and Helen Crompton Awards for supporting my visit to Aalto University in Finland and Nanyang Technological University in Singapore in 2024. I would like to thank Prof. Päivi Törmä and her research group for hosting me at Aalto University, especially Kristian Arjas for valuable discussion in his research and showing me around during my stay at Aalto. I also thank Dr Javier Cuerda for insightful discussion in his research in non-Hermitian quantum geometric tensor. I also want to thank Prof. Tim C. H. Liew and his research group at Nanyang Technological University. They were kind enough to host me in Singapore and share their expertise and help me with my work on non-Hermitian skin effects and nonlinear physics.

I also want to thank my collaborators throughout the last four years. First, I have to thank Dr Olivier Bleu from Monash University for valuable discussion on wavepacket dynamics and quantum geometric tensor in exciton polaritons. I also want to thank Dr Daria Smirnova from ANU for their help and valuable discussion on the non-Hermitian skin effects and nonlinear physics, as well as Prof. Alex Yakimenko from Taras Shevchenko National University of Kyiv for his expertise and help on pseudospin defects dynamics.

I also want to thank everyone from the KOALA 2023 Organizing Committee: Neuton Li, Sarah Dean, Fedor Kovalev, Joshua Jordaan, Marcus Cai, Jack Lang and Shridhar Manjunath. Thank you all guys for doing most of the works to make the student conference possible.

I also want to thank the great community of the Ursula Hall Laurus Wing, especially my residential mentors: Baek and Rizka. All the wonderful people and great events at the Ursie's certainly made my life much more enjoyable in the past two years. I certainly also owe my gratitude to the great community at Fenner Hall North Forth Floor 2023 as well, and to the wonderful senior residents, Jack and Marianne, for holding the events and the weekly pod meeting, which made my life significantly less lonely.

Finally, I want to express my gratitude to my family, who always supported me unconditionally. Especially my mother, who raised my brother and me alone after my father passed away; my little brother, who always kept me company and would love to chat to me about history (a hobby of mine that is sadly not shared with anyone else in my social circle); and my grandparents, who generously and unconditionally supported me and my career choice.

Abstract

Hermiticity of observable operators is one of the fundamental axioms in quantum mechanics, which then ensures that the observables are real-valued. However, an open dissipative system can be described by an effective non-Hermitian Hamiltonian operator, which gives rise to complex-valued eigenenergies, with the imaginary part of the energy describing gain or loss. With non-Hermitian Hamiltonians, we expect novel behaviour that does not exist in their Hermitian counterparts, such as new topological invariants [1], breakdown of conventional bulk-boundary correspondence [2], new topological edge states [3] and more [4, 5].

One important consequence of the non-Hermiticity of the Hamiltonian is that the eigenenergy becomes complex-valued. This gives rise to new degeneracies such as the bulk Fermi arcs, where the real parts of the eigenenergies cross while the imaginary parts anti-cross, the imaginary Fermi arcs, where the imaginary parts of the eigenenergies cross while the real parts anti-cross, and the exceptional points, where both the real and imaginary parts of the eigenenergies cross. The latter also gives rise to a new topological invariants, known as the spectral winding that measures the change in the phase of the eigenenergies in the complex plane along a closed loop [6]. Another important novel topological effects in non-Hermitian systems is the breakdown of bulk-boundary correspondence and emergence of new topological edge states. Unlike the Hermitian system where both bulk states and topological edge states exist in the presence of non-zero topological invariants, in the presence of point-gap topology in non-Hermitian systems, where the eigenspectrum under periodic boundary condition forms a loop on the complex plane, all eigenstates localise to the edge of the systems under open boundary condition, which is known as the non-Hermitian skin effect [2].

Another emerging issue with non-Hermitian systems is the generalisation of the quantum geometric tensor, which is a Hermitian tensor. Its real part is the quantum metric tensor, which measures the distance between quantum states in the Hilbert space. Its imaginary part is the Berry curvature, which is an effective magnetic field in momentum space [7]. However, since right and left eigenstates are not equal due to the non-Hermiticty of the Hamiltonian operators, there have been different ways to define the components of the quantum geometric tensor: one defined using only the right eigenstates [8, 9], and the other defined in terms of both the right and left eigenstates [10, 11].One of the goals in this Thesis is to resolve the ambiguity arising from these two different definitions by analysing the wavepacket dynamics.

In this Thesis, I investigate non-Hermitian physics using an experimentally relevant model describing a hybrid light-matter system known as the exciton polaritons. The exciton polaritons are composite particles arising from strong coupling between excitons and cavity photons [12, 13], which are inherently dissipative mainly due to their photonic components [14]. Furthermore, the polaritons decay by emitting photons that escape

the microcavity, and by detecting these photons, one can directly measure the physical observables of the polaritons. The exciton-polariton spectrum can also exhibit exceptional points [15] and Fermi arcs [16] in momentum space instead of parameter space. Therefore, I can investigate the consequence of these spectral degeneracies for the dynamics of the system. This includes the investigation of the exciton-polariton wavepacket dynamics in Chapters 2–4, the pseudospin dynamics in Chapter 5 and the topological edge states in Chapter 6.

In Chapter 1, I give an introduction to the background literature. I briefly review the topological materials in solid state physics and the bulk-boundary correspondence, the connection between the topological invariants and topological edge states. I then review the literature on non-Hermitian physics and discuss the concept of spectral winding and non-Hermitian skin effect. I also review the quantum geometric tensor in both Hermitian and non-Hermitian systems. Finally, I briefly discuss the exciton polaritons and introduce the models that are used in the later Chapters.

In Chapter 2, I describe the self-acceleration of wavepackets in a non-Hermitian exciton-polariton system. I show how the non-Hermiticity of the Hamitonian operators modifies the Ehrenfest's theorem [17] and allows for change of centre-of-mass momentum without an external force. I also derive the asymptotic group velocities of the wavepackets under self-acceleration in different phases.

Then in Chapter 3, I discuss the roles that the two non-Hermitian generalisations of quantum geometric tensor play in the wavepacket dynamics in non-Hermitian systems. I explicitly derive a semi-classical equation of motion showing that both definitions of the non-Hermitian quantum geometric tensor play a significant role in the dynamics. I also show how the two generalised quantum geometric tensors can be experimentally measured in an exciton-polariton system.

In Chapter 4, I investigate the non-Hermitian generalisation of the Zitterbewegung effect. The Zitterbewegung effect was originally proposed to describe the motion of relativistic electrons, but later used to describe the trembling motion of non-relativistic wavepackets due to spin precession. In this Chapter, I generalise this effect to non-Hermitian systems, where the pseudospin dynamics is qualitatively different to that in the Hermitian systems.

In Chapter 5, I present my analysis on emergent pseudospin defects. My simulation suggests that there are emergent pseudospin defects on the imaginary Fermi arcs in momentum space. I investigate the dynamics of these defects using different non-Hermitian models and suggest how their signatures can be experimentally measured in an exciton-polariton system.

In Chapter 6, I present my analysis on non-Hermitian skin effects. Although it is difficult to experimentally realise the non-Hermitian skin effect in a continuous (i.e. non-periodic, non-discrete) system, I theoretically show that the localisation of the eigenstates can be induced in momentum space in an exciton-polariton system via a complex-valued potential in real space, which is experimentally achievable. I show how the localisation is tied to the imaginary potential and also investigate the interplay between the momentum-space skin effects and nonlinear interaction.

Finally, in Chapter 7, I summarise the results presented in this Thesis and discuss future directions.

List of Publication

Published Works

- Y.-M. Robin Hu; Elena A. Ostrovskaya; Eliezer Estrecho, Wave-packet dynamics in a non-Hermitian exciton-polariton system, *Phys. Rev. B* **108**, 115404 (2023).
- Y.-M. Robin Hu; Elena A. Ostrovskaya; Eliezer Estrecho, Generalized quantum geometric tensor in a non-Hermitian exciton-polariton system [Invited], *Optical Materials Express* **14**, 3, 664-686 (2024)
- Y.-M. Robin Hu; Elena A. Ostrovskaya; Eliezer Estrecho, Quantum geometric tensor and wavepacket dynamics in two-dimensional non-Hermitian systems, *Phys. Rev. Research* **7**, L012067 (2025)
- Y.-M. Robin Hu; Elena A. Ostrovskaya; Eliezer Estrecho, Zitterbewegung effect and quantum geometry in non-Hermitian exciton-polariton systems, *Appl. Phys. Lett.* **127**, 253101 (2025)
- Yow-Ming Robin Hu, Elena A Ostrovskaya, Alexander Yakimenko, Eliezer Estrecho, Emergent momentum-space topological pseudospin defects in non-Hermitian systems, arXiv preprint arXiv:2509.14605 (2025)
- Y.-M. Robin Hu, M. Król, D. Smirnova, B. R. Fabricante, K. Winkler, M. Kamp, C. Schneider, S. Höfling, T. C.H. Liew, A. G. Truscott, E. A. Ostrovskaya, and E. Estrecho, Momentum-space non-Hermitian skin effect in an exciton-polariton system, arXiv preprint arXiv:2512.10146 (2025)

Contents

Chapter 1

Introduction

The Hermiticity of the Hamiltonian operator, which guarantees the real-valued eigenspectrum, is one of the basic axioms in quantum mechanics. This property also results in the orthonormality of the eigenvectors as well as the completeness relations. However, this is only true for a conservative system. There have been several attempts to include the effects from gain or/and loss in a closed quantum system such as the Feynman-Vernon theory [18], the Lindblad master equation [19] and the Landau-Lifschitz-Gilbert equation [20, 21]. The formalism which I will use in this Thesis is to describe the gain or/and loss in the system using an effective non-Hermitian Hamiltonian [4, 5, 22, 23], which I will explain in this Section.

1.1 Non-Hermitian Physics

Let us first consider a simple two-by-two Hamiltonian in the form of

$$H = \begin{pmatrix} a & b \\ c & d \end{pmatrix}. \tag{1.1}$$

In conventional quantum mechanics where the Hamiltonians are assumed to be Hermitian, the diagonal terms $a, d \in \mathbb{R}$ describe onsite energy, while the off-diagonal terms can be complex-valued, but need to satisfy the condition $c = b^*$. The off-diagonal terms describe the symmetric coupling between the two levels, and the complex angle $\arg(c) = -\arg(b)$ corresponds to a phase. Here, the Hermiticity also guarantees the eigenenergy to be real-valued. However, if the system is not conservative, this does not always have to be the case. If there is an onsite gain or loss in the system, it can be described by adding an imaginary part to a or d. While if there is an asymmetric coupling between the two levels, it can be described by setting $\mathrm{Re}[b] \neq \mathrm{Re}[c]$. Moreover, if there is a dissipative coupling, it can be described by setting $\mathrm{Im}[b] \neq -\mathrm{Im}[\mathrm{c}]$. Furthermore, the non-Hermiticity also makes it possible for the eigenenergies to be complex-valued, where the imaginary parts now describe the inverse lifetime of the corresponding eigenstates. This opens up possibility for new physics forbidden in the Hermitian quantum mechanics. In the following, I will briefly review the history of non-Hermitian physics and its exciting development.

One early work in non-Hermitian quantum mechanics was by George Gamow in 1928 [24]. In this work, Gamow explained the alpha decay using quantum tunneling, and he also described the effective decay rate by adding an imaginary term to the eigenenergy

[24]. Another significant early work was by Feshbach, Porter and Weisskopf in 1954 [25], where they added an imaginary term to the potential to describe the absorption of an incident nucleon into the nucleus in the formation of a compound nucleus.

Despite these early developments, the non-Hermitian quantum mechanics never attracted much attention until the pioneering works by Bender and his co-authors in 1998 [26, 27]. They showed that even when the system is non-Hermitian, the eigenspectra will be guaranteed to be real-valued if the Hamiltonian is invariant under the parity-time (PT) symmetry, which maps x to $-x$, i to $-i$ and t to $-t$ [26, 27, 28, 22, 23]. This was further generalised by Mostafazadeh in Ref. [29], where he proposed an even stronger condition for the real-valued eigenspectrum in a non-Hermitian system, called pseudo-Hermiticity, where the Hamiltonian operator can be transformed to its Hermitian conjugate $H = \eta^{-1}H^{\dagger}\eta$ via some Hermitian invertible operator η. Furthermore, the PT-symmetry was experimentally realised and observed using optical systems which attracted further interests in non-Hermitian quantum mechanics [30, 31, 32].

More recently, there has been a new direction in the research of non-Hermitian systems. Instead of looking for the real-valued spectrum, more works have started to focus on novel physics made possible by the complex values of the eigenspectrum. This new physics includes the new spectral degeneracy known as the exceptional points [1, 33], new topological invariants [1, 33, 6] as well as new topological edge states [1, 3, 34, 35].

Another consequence of the non-Hermitian Hamiltonian is the left and right eigenstates, $|\psi_n^R\rangle$ and $|\psi_n^L\rangle$

$$\begin{aligned} H|\psi_n^R\rangle &= E_n|\psi_n^R\rangle \\ \langle\psi_n^L|H &= \langle\psi_n^L|E_n. \end{aligned} \tag{1.2}$$

Unlike their Hermitian counterparts, the sets of left and right eigenstates are non-orthogonal themselves, that is $\langle\psi_n^{L(R)}|\psi_m^{L(R)}\rangle \neq 0$ for $n \neq m$, but are instead bi-orthogonal

$$\langle\psi_n^L|\psi_m^R\rangle = \langle\psi_n^R|\psi_m^L\rangle = \delta_{nm} \tag{1.3}$$

where the left and right eigenstates corresponding to different energy levels are orthogonal to each other. Similarly, the completeness of the eigenstates is modified as

$$\sum_n |\psi_n^L\rangle\langle\psi_n^R| = \sum_n |\psi_n^R\rangle\langle\psi_n^L| = \mathbb{I} \tag{1.4}$$

for non-Hermitian systems.

In this Section, I will review on the concept of the novel topological invariant and topological edge states in non-Hermitian systems. Topological invariants refer to quantities that are unchanged under continuous deformation, specifically, topological invariants are quantities preserved under homeomorphism, continuous bijection with continuous inverse function [36, 37, 38]. In the conventional systems, there exists the bulk-boundary correspondence where the presence of non-zero topological invariants in the bulk energy band structure corresponds to the existence of robust edge states protected against back-scattering with defects or impurities [39]. In Section 1.2, I will discuss topological invariants and edge states in more detail. For review on non-Hermitian physics in general,

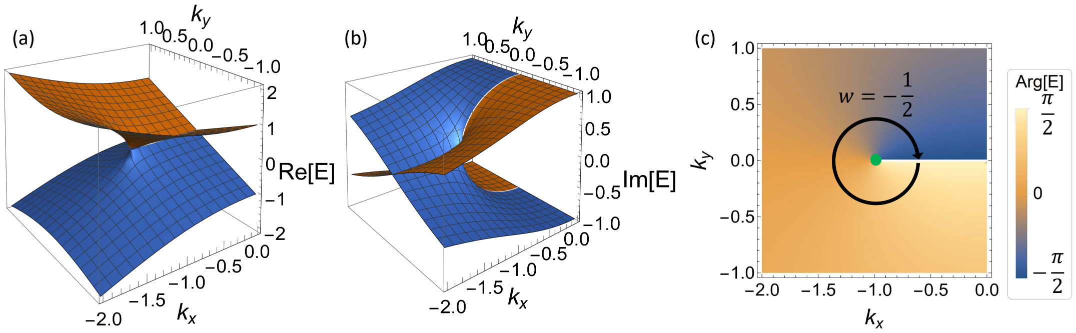

Figure 1.1: A schematic plot of the (a) real and (b) imaginary parts of eigenenergy of the Hamiltonian defined by Eq. (1.5) near an EP. (c) showing the complex angle around the EP (highlighted by the green dot) and the non-zero spectral winding defined by Eq. (1.6).

please refer to Refs. [4, 5, 22, 23, 28].

1.1.1 Exceptional Points and Spectral Winding

One consequence of non-Hermiticity is the emergence of new spectral degeneracy and the new topological invariants that accompany it. To illustrate this, let us consider a simple non-Hermitian model with the Hamiltonian (which we will come back to in more detail in later Sections)

$$H = \begin{pmatrix} 0 & k_x - i(k_y - i) \\ k_x + i(k_y - i) & 0 \end{pmatrix}. \tag{1.5}$$

As we can see in Figs. 1.1(a,b), whenever the real parts of eigenenergies cross, the imaginary parts would anti-cross and vice versa. However, there are two non-Hermitian degenerate points at $\mathbf{k} = (\pm 1, 0)$ where both the real and imaginary parts of the eigenenergies become degenerate. These are called the exceptional points, which are defective, meaning that at these points, the Hamiltonian is not diagonalisable and the eigenstates become linearly dependent on each other [6]. Interestingly, at these exceptional points, the eigenstates coalesce and become proportional to each another [40]. The exceptional points are not just a mathematical curiosity. They have potential application in sensing [11, 41, 42], and have also been shown to enhance superconductivity [43].

One interesting consequence of the complex-valued eigenenergy is a new topological invariant known as the spectral windings, which measures the change in the complex phase of the eigenenergy along a closed loop [see Fig. 1.1(c)] [5, 6, 33, 40]

$$w_{mn} = \frac{1}{2\pi} \oint_C \nabla_{\mathbf{k}} \arg[E_m - E_n] \cdot d\mathbf{k}. \tag{1.6}$$

Interestingly, Zhang et al. have shown in Ref. [44] that in a one-dimensional system, the non-zero spectral winding is connected to the presence of a novel non-Hermitian topological edge states known as the non-Hermitian skin effects, which will be explored in details in the next section.

1.1.2 Non-Hermitian Skin Effect and the Breakdown of Bulk-Boundary Correspondence

Another surprising consequence of non-Hermiticity is the breakdown of bulk-boundary correspondence [2] and the accumulation of wavefunction on the edge of the system, known as the non-Hermitian skin effect (NHSE) [4, 5, 22, 45]. The localisation and delocalisation arising from the non-Hermiticity of the Hamiltonian was first discussed by Hatano and Nelson in their pioneering works in Refs. [46, 47, 48] using a simple model of a single-particle Hamiltonian under an imaginary gauge transformation $p \rightarrow p + ig$

$$H = \frac{p + ig}{2m} + V(x). \tag{1.7}$$

Recently, the connection between the NHSE, the winding topology and the gap in complex energy has been further established [6, 40, 44, 49]. Due to the complex-valued energy, there are two different types of gaps in non-Hermitian system; the line gap, where there is a line on the complex plane separating the eigenenergies [see Fig. 1.2(a)], and the point gap, there there is a point on the complex plane circled by the eigenenergies [see Fig. 1.2(b)] [6, 40, 49]. Unlike the line gap, which is similar to the energy gap in Hermitian systems, the point gap is a fundamentally non-Hermitian phenomenon, and is accompanied by the existence of non-Hermitian skin modes and the sensitivity to boundary conditions. For if a system exhibits point-gap topology, its eigenstates remain delocalised under the periodic boundary condition (PBC), while under the open boundary condition (OBC), all eigenstates localise at the edge and the energy spectrum collapses to a line on the complex plane [see Fig. 1.3(b)] [3, 49].

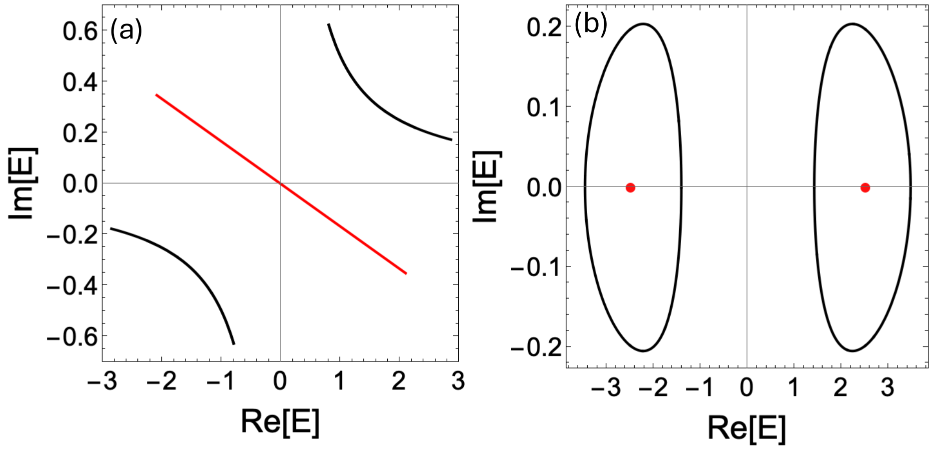

Figure 1.2: Schematic plot of (a) line gap and (b) point gap on the complex plane. Here, the black lines denote the eigenspectrum, while in panel (a), the region forbidden for the eigenspectrum to cross is topologically equivalent to a line (shown schematically as the red line), therefore known as the line gap. While in panel (b), the regions forbidden for the eigenspectrum to cross are topologically equivalent to points (shown schematically as the two red dots), therefore known as the point gap.

The most well-known example is the discretised version of the Hamiltonian in Eq. (1.7) proposed by Hatano and Nelson, which is called the Hatano-Nelson model. This simple model describes a single-band, one-dimensional chain with non-reciprocal nearest-neighbor hopping [47, 48]

$$H_{HN} = \sum_{j}^{N} t_L c_j^\dagger c_{j+1} + t_R c_{j+1}^\dagger c_j, \tag{1.8}$$

where c_j ($c_j^\dagger$) denotes the annihilation (creation) operator and t_R (t_L) denotes the hopping to the right (left) [see Fig. 1.3(a)]. Here, the hoppings t_L, t_R are assumed to be real-valued in this simple case. Under PBC, we can apply Fourier transform to the operators, c_j and $c_j^\dagger$, which provide the eigenenergy of the Hamiltonian in terms of the wavenumber k as

$$E_{PBC}(k) = (t_L + t_R)\cos k + i(t_L - t_R)\sin k. \tag{1.9}$$

For $t_L \neq t_R$, the PBC spectrum forms a loop on the complex plane, and has a winding number of $w = 1$ if $t_L > t_R$, and $w = -1$ if $t_L < t_R$ [see Fig. 1.3(b)], and all the eigenstates are delocalised [see Fig. 1.3(c)]. Under OBC, the spectrum collapses into a line enclosed by $E_{PBC}(k)$ on the complex plane [see Fig. 1.3(b)], and all the eigenstates accumulate on the left-hand side (right-hand side) of the open chain if $t_L > t_R$ ($t_L < t_R$) [see Fig. 1.3(d)].

In one-dimensional systems, the existence of NHSE usually require either non-reciprocal coupling, which has been studied extensively in Refs. [1, 3, 35, 44] using non-Hermitian generalisation of the SSH model, or the combination of on-site dissipation and a flux generated using an Aharonov-Bohm chain [50, 51, 52, 53]. The topological nature of NHSE was demonstrated using index theorem in Ref. [54], and the correspondence between non-zero spectral winding and the existence of NHSE was also shown in Ref. [44]. In the absence of the point-gap topology and therefore $w = 0$, the NHSE disappears, namely, the eigensgtates become delocalised.

While in the usual topologically non-trivial materials in Hermitian systems the bulk states co-exist with the topological edge states, in non-Hermitian systems that exhibit NHSE, all bulk states localise at the edge under OBC, and therefore the conventional bulk-boundary correspondence is no longer valid [2]. There are two ways to tackle this problem and to predict the presence or absence of non-Hermitian skin modes. One is to reconstruct bulk-boundary correspondence using bi-orthogonal observables, known as the bi-orthogonal bulk-boundary correspondence [34]. The other is to define a non-Bloch band theory and a generalised Brillouine zone (GBZ) to re-establish bulk-boundary correspondence [55]. The non-Bloch band theory approach also has been generalised beyond tight-binding models to continuous periodic [56] and non-periodic systems [57].

The NHSE has also been generalised from tight-binding models to continuous periodic systems [56, 58]. Surprisingly, the NHSE is robust and can also occur without periodicity [51, 59, 60, 61]. In this case, the eigenstates are localised towards the edge of the trapping potential [51, 60, 59, 61]. This localisation can be induced by, for example, an imaginary vector potential [48, 60, 57], a combination of onsite loss and Rashba-Dresselhaus spin-orbit coupling [59] or by controlling the boundary conditions, such as restricting the higher order derivatives of the wavefunction to vanish at the boundary [57]. There are

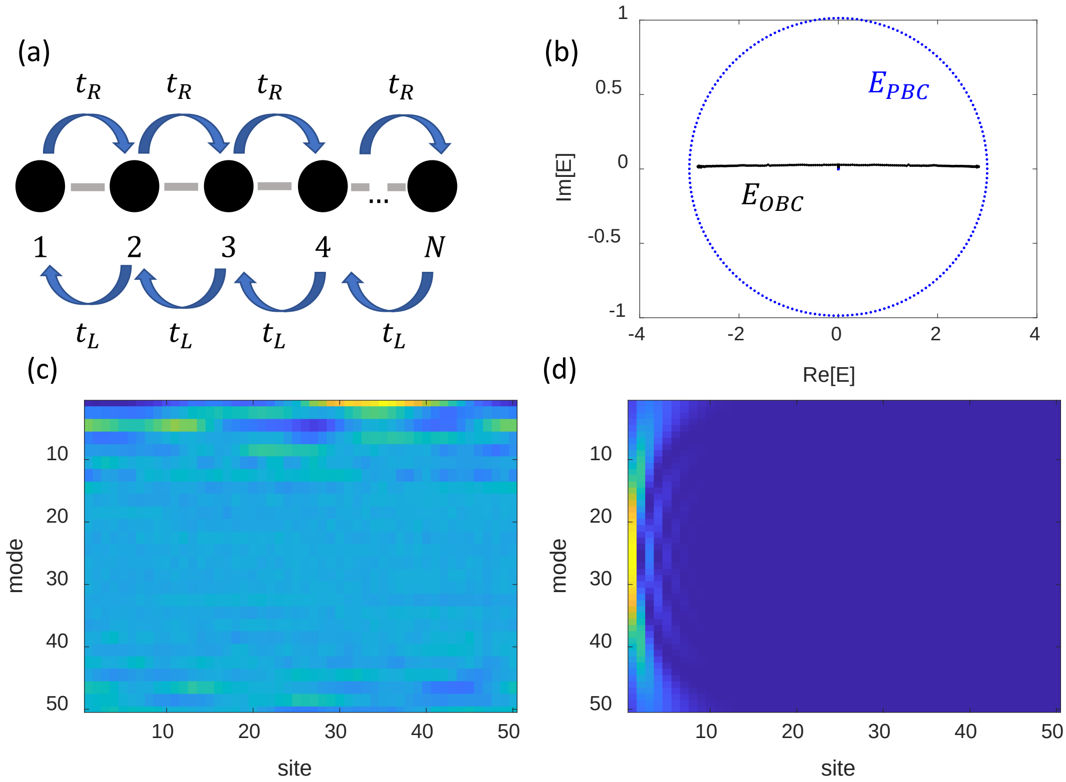

Figure 1.3: (a) A schematic plot of the Hatano-Nelson model (1.8) with non-reciprocal hopping. (b) PBC and OBC spectrum of an exemplar Hatano-Nelson model, showing sensitivity to boundary conditions, which is a signature of NHSE. Also showing the wavefunction distribution under (c) periodic and (d) open boundary conditions. Here, $t_L = 2$, $t_R = 1$ and the number of sites is $N = 50$. The wiggles in the OBC spectrum in panel (b) arises from the finite size of the grid in the numerical simulation.

already numerous proposals on how this can be done in different platforms, including [62, 63], magnonic systems [64], exciton-polariton systems [65, 66, 67, 59], cold atoms [50, 51], reflected waves in Hermitian topological insulators [68], elastic medium [69, 70] and more. There are experimental realisations of the NHSE in discrete systems based on electric circuits [71], photonics [72, 73, 74], cold atoms [53] and mechanical systems [75], but to date, there is no experimental demonstration of NHSE in continuous systems.

The NHSE is interesting from the perspective of fundamental research as a topological phase associated with novel topological invariants. It also has various potential applications, for instance, its anomalous scaling with system size [76] has been shown to enhance quantum sensing [77, 42], and the edge bursts [78] can potentially be used to improve energy efficiency [79]. These effects demonstrate the applied potential of the NHSE.

In Chapter 6, I will present my results, which predict that the non-Hermitian skin effects can be realised in non-Hermitian exciton-polariton systems.

1.2 Topological Systems

Topology is the mathematical field that studies the quantity that is preserved under continuous deformation. Recently, the idea of topology has been applied to a class of physical systems, where one can define non-zero topological invariants using its band structure [39, 80, 37]. In this section, I will give a brief overview of these topological materials, starting from the discovery of the quantum Hall effects in the 1980s [81, 82]. Please refer to Refs. [39, 83, 84, 36, 85] for a general overview on topological materials and quantum Hall effects.

In 1879, Edwin H. Hall discovered that when an external magnetic field is applied to a conducting material, the Laurence force pushes the electrons toward one edge, resulting in an electric potential across the conducting materials, called the Hall voltage, and this effect became known as the Hall effect [86, 87]. After this, in 1980, von Klitzing, Dorda, and Pepper made a curious discovery while investigating a two-dimensional electron gas at low temperature under a strong magnetic field. They observed the Hall resistance forming plateaus in units of h/e^2, where h is the Planck constant and e is the electric charge. Consequently, the Hall conductance is quantized in units of e^2/h. This later became known as the integer quantum Hall effect [81].

Two years later, Tsui, Stormer, and Gossard observed similar quantized Hall conductance in a system with fractional filling number of Landau levels, later known as the fractional quantum Hall effect [82]. In 1981, Laughlin explained quantized charge transport using a model of a flux passing though a loop formed by a ribbon of metal, where the gauge invariance results in the current being quantized in units of e^2/h [88, 89]. Later, the topological nature of the quantum Hall effects was fully unveiled by the pioneering work of Thouless, Kohmoto, Nightingale and den Nijs in Ref. [90], where they identified the quantized Hall conductance with a topological invariant, which was then called the TKNN integer, later identified as the Chern number [91]. The topological nature of the quantum Hall effects was then shown to be connected to the presence of an energy gap [92]. Later, the theory was generalised to fractional quantum Hall effects by including many-body effects [93].

In this Section, I will give a brief overview on the importance of topology in condensed matter physics. I will first explain the Berry connection and its connection to topology. Then, I will explain the topological invariants in the band structure and bulk-boundary correspondence. Finally, I will also introduce another type of topology in condensed matter systems, which manifests itself in the spin textures.

1.2.1 Berry Connection, Berry Curvature and Chern Number

In 1984, Michael Viktor Berry discovered that a quantum state acquires a quantized phase factor when it is adiabatically transported along a closed loop [94]. In his pioneering work, Berry showed that when a state $|u_n(\mathbf{k})\rangle$, where n, $\mathbf{k}$ denote the energy level and the momentum, evolves adiabatically along a closed loop C, the state acquires a geometric phase factor

$$\gamma_n = \oint_C \langle u_n | i \nabla_{\mathbf{k}} u_n \rangle \cdot d\mathbf{k}, \tag{1.10}$$

this phase factor γ_n later becomes known as the Berry phase, and the integrand $\mathbf{A}_n = \langle u_n | i\nabla_{\mathbf{k}} u_n \rangle$ becomes known as the Berry connection [85, 94, 95]. Using the Stokes' theorem, the Berry phase can also be rewritten as

$$\gamma_n = \iint_S \Big(\nabla_{\mathbf{k}} \times \mathbf{A}_n(\mathbf{k}) \Big) \cdot d^2\mathbf{k} \tag{1.11}$$

where S denotes the area enclosed by the closed loop C. Here, the quantity $\nabla_{\mathbf{k}} \times \mathbf{A}_n(\mathbf{k})$ is known as the Berry curvature $\mathbf{\Omega}_n(\mathbf{k})$ defeined as

$$\Omega_{n,ij} = i \Bigg(\langle \partial_i \psi_n | \partial_j \psi_n \rangle - \langle \partial_j \psi_n | \partial_i \psi_n \rangle \Bigg), \tag{1.12}$$

where $\mathbf{\Omega}_n(\mathbf{k}) = (\Omega_{n,yz}(\mathbf{k}), \Omega_{n,zx}(\mathbf{k}), \Omega_{n,xy}(\mathbf{k})) = \nabla_{\mathbf{k}} \times \mathbf{A}_n(\mathbf{k})$. The Berry curvature plays a significant role in the anomalous Hall effect. The anomalous Hall effect was discovered by Edwin H. Hall in 1881 when he uncovered that the Hall effects in ferromagnetic materials are much stronger than in the non-magnetic conductors [96]. This effect was first explained by Karplus and Luttinger as arising from an "anomalous velocity" in the transverse direction to the applied electric field experienced by the electrons [97]. Later, the topological roots of the anomalous Hall effect were discovered when Chang et al. linked the anomalous velocity with the Berry curvature of Bloch electrons [98] in the crystal momentum space [95, 99, 87]. This motion can be described by a pair of semi-classical equations of motion of for the centre-of-mass position nd momentum of the Bloch electron wavepacket [95, 99]

$$\begin{aligned} \hbar\dot{\mathbf{r}} &= \nabla_{\mathbf{k}} E_n - \hbar\dot{\mathbf{k}} \times \mathbf{\Omega}_n|_{\mathbf{k}=\mathbf{k}_c} \\ \hbar\dot{\mathbf{k}} &= -e\mathbf{E} \end{aligned} \tag{1.13}$$

,where E_n denotes the energy level, e denotes the electron charge, $\mathbf{E}$ denotes a constant electric field. In a two-dimensional system (which is the focus of my Thesis), the only non-vanishing component of $\mathbf{\Omega}_n$ is the z-component, which contributes to the group velocity transverse to the electric field $\mathbf{E}$, resulting in the anomalous velocity Karplus and Luttiner proposed. This was later generalised to include the time dependence of external field in Ref. [100] and to include the multi-band effect in Ref. [101]. Consequently, the Berry curvature acts as an effective magnetic field in momentum space arising from the band structure [85, 102]. More importantly, when integrating the Berry connection along the Brillouine zone in Eq. (1.10), the Berry phase now becomes quantized, and is known as an important topological invariant called the TKNN invariant, also identified as the Chern number

$$C_n = \frac{1}{2\pi} \iint_{BZ} \mathbf{\Omega}_n(\mathbf{k}) \cdot d^2\mathbf{k}, \tag{1.14}$$

which can be interpreted as the flux of the Berry curvature through the Brillouine zone [90, 91].

1.2.2 Topological Invariants and Edge States: Bulk-Boundary Correspondence

The existence of edge states has long been known, with one famous example being the Su-Schriffer-Heeger (SSH) model describing polyacetylene [103, 104]. The quantized Hall conductance and the non-zero topological invariant in the bulk bands was later linked with robust edge states, this is known as the bulk-boundary correspondence [39, 37]. This was first discussed by Halperin to describe an integer quantum Hall system in 1982 [105]. The connection between the edge current and the quantized Hall conductance was further discussed by McDonald and Středa in 1984 [106] and the connection between the edge current and the topological invariant was established by Hatsugai in 1993 [107]. Today, the discussion of bulk-boundary correspondence has been extended to other systems such as the quantum anomalous Hall systems, where the quantum Hall effect and edge current exist without an external magnetic field [108, 109], and the quantum spin Hall systems, where the system exhibits helical transport (where the spin-up and spin-down electrons propagate in different directions) [110, 111]. In this section, I present a short review on the Haldane model of graphene and the quantum anomalous Hall effect, as well as a brief discussion on its generalisation in Kane and Mele's work and $\mathbb{Z}_2$ quantum spin Hall effect.

The realisation of integer quantum Hall effect usually required an external magnetic field. However, in 1988, Haldane proposed a model of graphene, and demonstrated an integer quantum Hall effect arising from breaking time-reversal symmetry via magnetisation even in the absence of total magnetic flux [108]. In Haldane's model, the effective Hamiltonian described spinless electrons on the hexagonal lattice partitioned into two sublattices, A-sites and B-sites. Haldane then defined two sets of vectors, $(\mathbf{a}_1, \mathbf{a}_2, \mathbf{a}_3)$ defined as the displacement from an A site to its nearest neighboring B site (and vice versa), and $(\mathbf{b}_1, \mathbf{b}_2, \mathbf{b}_3)$ defined as the displacement between an A site and nearest A site (and vice versa for nearest neighboring B sites). For the spinor wavefunction $(\psi_A(\mathbf{k}), \psi_B(\mathbf{k}))^T$, the Bloch Hamiltonian of the Haldane model takes the forms

$$\begin{aligned}
\hat{H}(\mathbf{k}) &= h_0(\mathbf{k})\mathbf{I} + h_x(\mathbf{k})\sigma_x + h_y(\mathbf{k})\sigma_y + h_z(\mathbf{k})\sigma_z \\
h_0(\mathbf{k}) &= 2t_2 \cos\phi \Big(\sum_i \cos(\mathbf{k}\cdot\mathbf{b}_i) \Big) \\
h_x(\mathbf{k}) &= t_1 \sum_i \cos(\mathbf{k}\cdot\mathbf{a}_i) \\
h_y(\mathbf{k}) &= t_1 \sum_i \sin(\mathbf{k}\cdot\mathbf{a}_i) \\
h_z(\mathbf{k}) &= M - 2t_2 \sin\phi \Big(\sum_i \sin(\mathbf{k}\cdot\mathbf{b}_i) \Big)
\end{aligned} \tag{1.15}$$

where σ_i denotes the i-th 2-by-2 Pauli matrix, t_1 is the nearest-neighbor hopping (inter-sublattice hopping), t_2 is the second nearest-neighbor hopping (intra-sublattice hopping), M denotes the onsite energy where the A (B) sites have on-site energy of $+M$ ($-M$), and t_2 acquires a phase ϕ from the flux through the unit cell [see Fig. 1.4(a)]. The

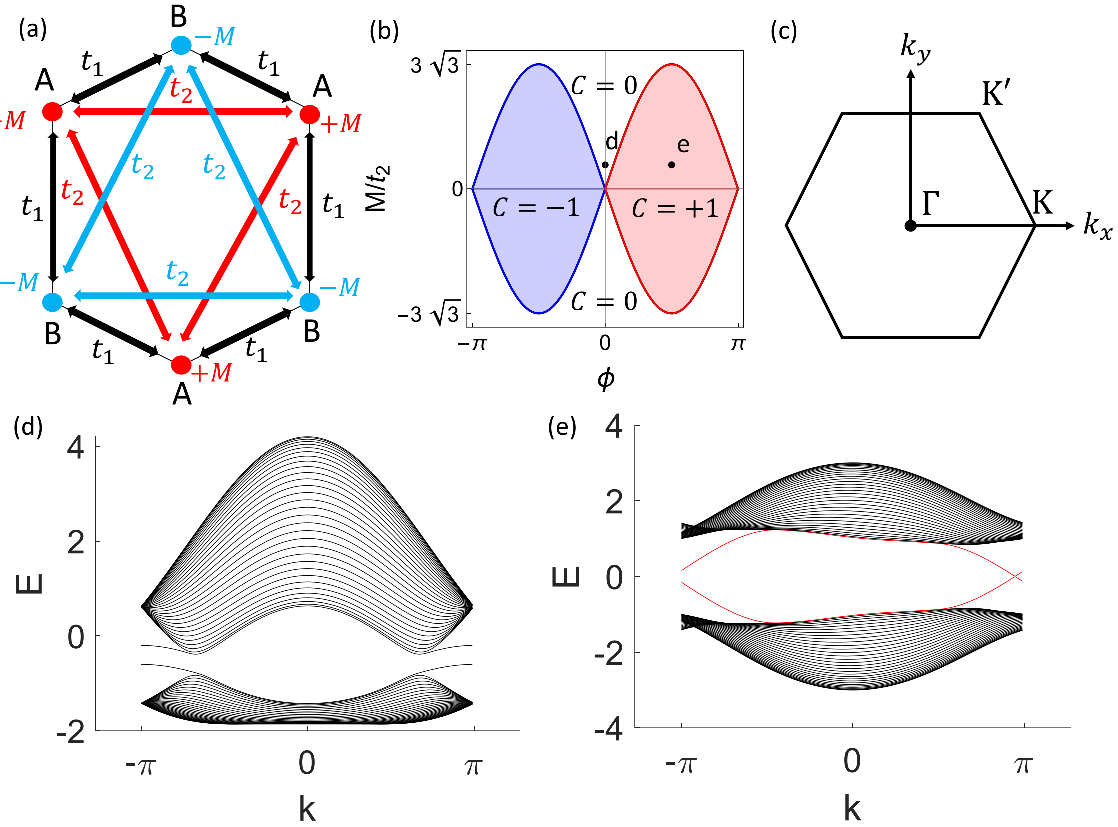

Figure 1.4: (a) Schematic plot of the Haldane model (1.15) showing the nearest-neighbour hopping t_1, the second nearest-neighbour hopping t_2 and the on-site energy $\pm M$ on the honeycomb lattice. (b) Phase diagram of the Haldane model, with the two phases with non-zero Chern numbers distinguished by color. (c) The Brillouine zone of the honeycomb lattice, highlighting the **K** and **K**′ points. Also showing the band structure in the topologically (d) trivial and (e) non-trivial phases with zigzag edges [108, 114], shown as the black dots in (b). The black lines denote the bulk bands and the red lines denote the edge bands. Here, $t_1 = 1$, $t_2 = 0.2$ and $M = 0.2$ with $\phi = 0$ and $\phi = \pi/2$ for (d,e), respectively.

Hamiltonian presented in Eq. (1.15) has the eigenenergies

$$E_{\pm}(\mathbf{k}) = h_0(\mathbf{k}) \pm \sqrt{h_x^2(\mathbf{k}) + h_y^2(\mathbf{k}) + h_z^2(\mathbf{k})}. \tag{1.16}$$

The system has spectral degeneracy at $h_x(\mathbf{k}) = h_y(\mathbf{k}) = h_z(\mathbf{k}) = 0$, which is satisfied at the **K** and **K**′-points at $|M/t_2| = 3\sqrt{3}\sin\phi$, see Fig. 1.4 [112, 113, 108, 37, 84]. When $|M/t_2| > 3\sqrt{3}\sin\phi$, the spectrum is gapped, and the system is a time-reversal symmetric insulator [see Fig. 1.4(d)]. However, at $|M/t_2| < 3\sqrt{3}\sin\phi$, the time-reversal symmetry is broken. In this phase, the system is topologically non-trivial and has the Chern number of ± 1 [see Fig. 1.4(e)], therefore, it behaves as a quantum Hall system even without having an external magnetic field [108].

The Haldane model can be expanded at low momentum near the **K**, **K**′-points, $\mathbf{q} = \mathbf{k} - \mathbf{K}$ (or alternatively $\mathbf{q} = \mathbf{k} - \mathbf{K}$’) [see Fig. 1.4(c)] which leads to an effective low-energy

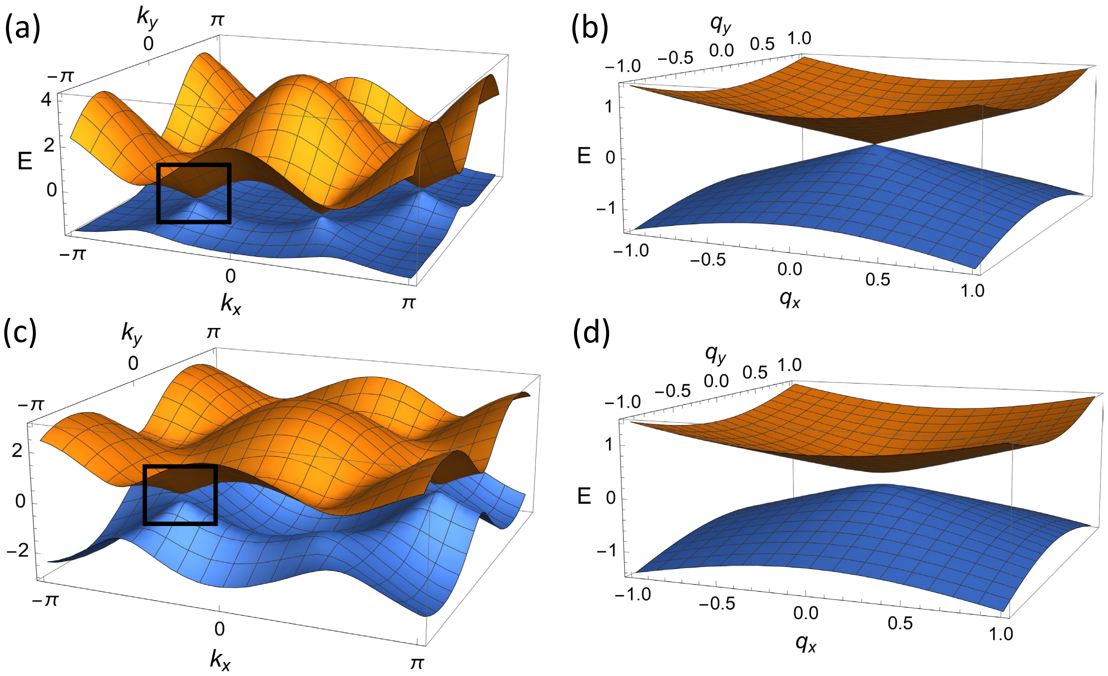

Figure 1.5: The band structure of Haldane model (1.15) in the (a) gapless and (c) gapped phases. Also showing the band structure of the Dirac model (1.17) in the (b) gapless and (d) gapped phases, which are low-energy effective models of the Haldane model near th $\mathbf{K}$-point (highlighted in black square in (a, c)). Here, $t_1 = 1$, t_2, and for (a): $M = \phi = 0$, while for (c): $M = 0.2$, $\phi = \pi/2$.

Hamiltonian:

$$\hat{H}(\mathbf{q}) = \hbar v_F q_x \sigma_x + \hbar v_F q_y \sigma_y + m\sigma_z, \tag{1.17}$$

where v_F is the velocity and m arises from the $h_z(\mathbf{k})$-term at the $\mathbf{K}$ or $\mathbf{K}'$-point. This Hamiltonian coincides with the massive Dirac Hamiltonian [112, 113, 115, 116, 117, 118, 119, 120, 37, 121], where the elementary excitations are described by relativistic electrons proposed by Paul Dirac in 1928 in Ref [122]. At $m = 0$, it exhibits a spectral degeneracy in the form of a conical intersection at $\mathbf{q} = 0$ [see Figs. 1.5(a,b)], which was first described by Hamilton and Lloyd as optical conical diffraction in Refs. [123, 124], but nowadays, better known as the Dirac point. At nonzero m, if the signs of m at the K-point and the K'-point are the same (which is the case $|M/t_2| > 3\sqrt{3}\sin\phi$), the time-reversal symmetry is preserved and the Hamiltonian is a trivial insulator. On the other hand, if the signs of the m-term at the $\mathbf{K}$-point and the $\mathbf{K}'$-point are the opposite, then the time-reversal symmetry is broken and the system becomes a topological insulator [see Figs. 1.5(c,d)], which exhibits gapped bulk band and gapless edge states [see Fig. 1.4(e)][37, 84, 108, 121, 125]. The integer quantum Hall effect arising due to broken time-reversal symmetry without an external magnetic field is coined as the quantum anomalous Hall effect [109].

Another key discovery was the $\mathbb{Z}_2$ quantum spin Hall effect by Kane and Mele in 2005 in Refs. [110, 111]. Kane and Mele generalised Haldane's model of graphene and included Rashba spin-orbit coupling [126]. Using this generalised model, they demonstrated that the graphene can exhibit quantum spin Hall effect, which manifests as dissipationless spin transport at the edge where the electrons with opposite spins propagate at the opposite directions (hence the term "helical transport") [110]. Moreover, Kane and Mele also showed that the quantum spin Hall effect can take place even when the time-reversal symmetry is preserved, that is, when the Chern number vanishes [111]. In this case, the edge spin transport is instead protected by a $\mathbb{Z}_2$ (inegers modulo 2) topological index [111, 127, 128, 129, 130].

So far in this section, I focus on topology arising from the energy band structure. However, there is another type of topological invariant defined by the winding around the centre of a point defect in spinor fields.

1.2.3 Topological Point Defects

Skyrmions are topologically protected field configurations, originally proposed as solutions of a nonlinear mesonic field theory in nuclear physics [131, 132], and often interpreted in lower-dimensional systems as point-like defects. In recent years, they were investigated in the broad context of spinor fields $\mathbf{S}$, such that of photons with distinct polarization states [133, 134, 135] and electronic spins in solid-state systems [136, 137, 138]. These defects are topologically protected, i.e. they preserve the associated integer-valued topological winding (such as vorticity and skyrmion number), and therefore have potential applications in the lossless transmission of quantum information and memory in spintronics devices [136, 137, 138, 139].

The point defects in spinor systems can be classified using a topological invariant known as the skyrmion number, which measures the winding of the spin texture described by the Stokes vector $\mathbf{S} = (S_x, S_y, S_z)$ around the core of the defect [138, 137, 136, 133]:

$$N_{sk} = \frac{1}{4\pi} \int \mathbf{S} \cdot (\partial_x \mathbf{S} \times \partial_y \mathbf{S}) d^2\mathbf{r}. \tag{1.18}$$

Here, the Stokes vectors can be written as the expectation value $S_j = \langle\psi|\sigma_j|\psi\rangle$ where σ_j is the j-th two-dimensional Pauli matrices and the integral is taken over the area from the core to the edge of the defect, which measures the winding of the spin texture around the core of the defect [138, 137, 136, 133]. The skyrmion number can also be re-written in terms of two other topological indices:

$$N_{sk} = \nu \cdot p, \tag{1.19}$$

where ν denotes the vorticity and p denotes the polarity. The vorticity characterises the winding of the in-plane Stokes vectors $[S_x, S_y]$ around the defect core

$$\nu = \frac{1}{2\pi} \oint d\mathbf{r} \cdot \nabla_{\mathbf{r}} \Phi(\mathbf{r}), \tag{1.20}$$

where $\Phi(\mathbf{r}) = \frac{1}{2} \arctan[S_y(\mathbf{r})/S_x(\mathbf{r})]$ [136, 140] is the azimuthal angle of the Stokes vector, and a vortex (anti-vortex) has $\nu = 1$ ($\nu = -1$).

The polarity p measures the rotation of the out-of-plane Stokes vector S_z from the core ($\mathbf{r}_{core}$) to the edge ($\mathbf{r}_{edge}$) of the defects [138, 137, 136, 141] and is defined as:

$$p = \frac{1}{2}\Big[S_z(\mathbf{r}_{core}) - S_z(\mathbf{r}_{edge})\Big]. \tag{1.21}$$

In this Thesis, I consider skyrmion numbers $N_{sk} = \pm 1, \pm 1/2$ corresponding to the common skyrmions and merons. Core-up (core-down) skyrmions have $S_z = 1$ ($S_z = -1$) at the core with polarity of $p = 1$ ($p = -1$) as $S_z(\mathbf{r}_{edge}) \to -1$ ($S_z(\mathbf{r}_{edge}) \to -1$), i.e. the core and edge have opposite spins. For a core-up defect, a skyrmion number of $N_{sk} = 1$ ($N_{sk} = -1$) corresponds to a skyrmion (an anti-skyrmion) [136, 138, 137]. Figures 1.6(a-d) show examples of core-up skyrmions and anti-skyrmions. Conversely, for a core-down defect, I follow the convention in Refs. [138, 134] and flip the sign so that a core-down skyrmion and a core-down anti-skyrmion is characterized by $N_{sk} = -1$ and $N_{sk} = 1$, respectively. In this convention, a skyrmion (an anti-skyrmion) corresponds to a vortex (an anti-vortex) with an integer-valued polarity.

The polarity can also take half-interger values $p = \pm 1/2$ corresponding to $S_z(\mathbf{r}_{edge}) \to 0$, i.e. the defect edge has no S_z-component. These half-skyrmions are called merons and anti-merons. Core-up merons and anti-merons have the skyrmion numbers of $N_{sk} = 1/2$ and $N_{sk} = -1/2$, respectively [136, 138, 137]. Examples of core-up meron and anti-meron in a real space of a two-dimensional spinor field are shown in Figs. 1.6(e, f).

Other than the polarity and vorticity, there is a third observable that plays an important role in defining the textures of the skyrmions, known as the helicity ξ. In a polar coordinate system (r, ϕ) centred at the defect core ($r = 0$ at $\mathbf{r}_{core}$), ξ is defined by the global rotation of the in-plane Stokes vector with respect to the azimuthal coordinate ϕ, $\Phi = \nu\phi + \xi$ [136, 138, 62]. There are two special cases of the helicity ξ that correspond to the two types of common skyrmion textures, namely the Neel-type and the Bloch-type. The Neel-type skyrmion has zero azimuthal component of Stokes vectors, $S_\phi = 0$, and a helicity of $\xi = 0$, while the Bloch-type skyrmion has no radial component of Stokes vector $S_r = 0$ and a helicity of $\pi/2$. Similarly, Fig. 1.6(c,d) show two anti-skyrmions with helicities of $\xi = 0$ and $\xi = \pi/2$, respectively, while Fig. 1.6(e,f) show a meron and an anti-meron, both with helicity of $\xi = \pi/2$.

Although the skyrmion number and the associated quantities are usually defined in position space, they can also be defined in momentum space [134]. For example, it has been shown that the topological winding of polarization vortices in momentum space corresponds to the robustness of optical bound state in continuum [142, 143, 140].

The different types of point defects have attracted a great amount of interest in various physical systems, including but not limited to magnetic systems [144, 145, 146, 147, 148, 149, 150, 151], nematic liquid crystals [152, 153, 154, 155, 156, 157], photonic [133, 134, 135], plasmonic [158, 159, 160, 161, 162, 163, 62], and hybrid photonic (polaritonic) systems [164, 165, 166, 167].

Topological defects can appear in position space due to symmetry breaking in active liquid crystals [153, 168], or the Dzyaloshinsky-Moriya interaction [169, 170, 144, 145, 146, 147, 148, 149, 150, 151] or dipole-dipole interaction [139, 171, 172] in magnetic systems. They can also be generated by artificial gauge field arising from photonic spin-orbit interaction and anisotropy in photonic, plasmonic, and polaritonic systems [135,

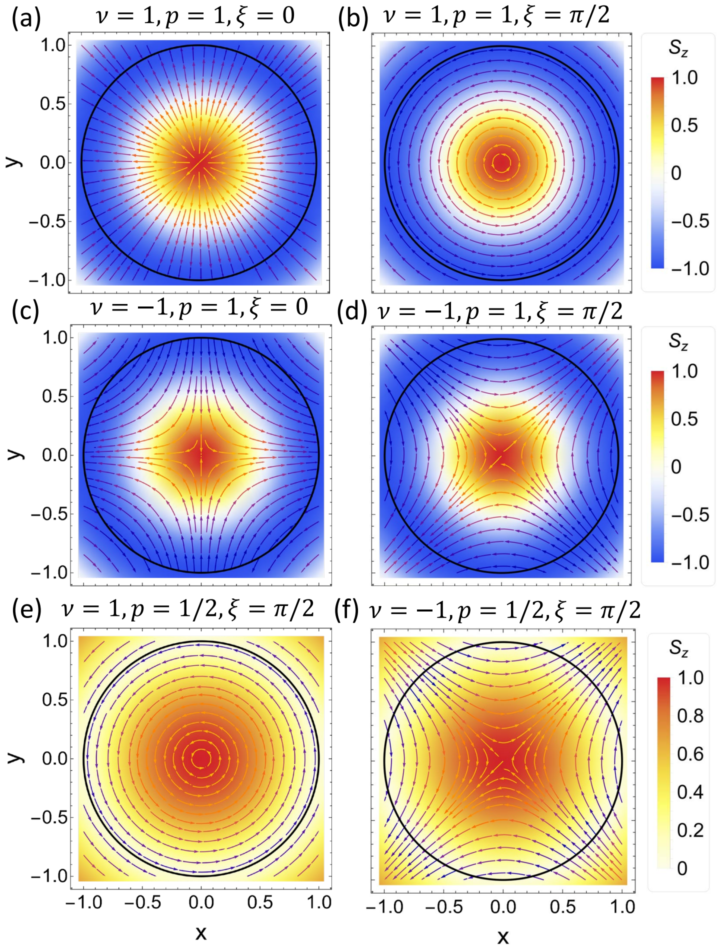

Figure 1.6: Spin textures of core-up defect of (a) a Neel-type (helicity $\xi = 0$) and (b) a Bloch-type ($\xi = \pi/2$) skyrmion, (c,d) anti-skyrmions with helicities of (c) $\xi = 0$ and (d) $\xi = \pi/2$, and (e, f) a meron and an anti-meron with helicity of $\xi = \pi/2$. The arrows represent $[S_x, S_y]$ and the color map represents S_z, the defects are centred at $\mathbf{r}_{core} = (0, 0)$ and the black line outlines the edge of the defects, $\mathbf{r}_{edge}$ where $|\mathbf{r}_{edge}| = 1$. Compared with these configurations, the core-down defects have the same in-plane spin textures but the opposite S_z.

158, 159, 160, 161, 162, 163, 62, 164, 165, 166, 167], and more recently, via the Kelvin-Helmholtz instability in spinor Bose-Einstein condensates [173, 174].

In Chapter 5, I will present my results on the generation of topological defects in two-dimensional non-Hermitian polaritonic systems.

In this Section, I have discussed the topology in both the band structure and the spinor field configuration. However, the topology of the system is closely related to its geometry, which will be discussed in the next Section.

1.3 Quantum Geometric Tensor

The Berry curvature presented in the previous Section is in fact, part of a more complex quantity known as the quantum geometric tensor (QGT). In this Section, I will present the concept of quantum geometric tensor as well as its generalisation to non-Hermitian systems.

Quantum geometry plays an important role in various areas such as nonlinear current [175, 176], second harmonic generation [177], perturbative correction to the anomalous Hall drifts [178, 179, 180], and flat-band superconductivity [181, 182, 183]. The real part of the QGT also corresponds to the fidelity susceptibility and plays an important role in quantum information and identifying ground state degeneracy [184, 185, 186, 187, 188].

1.3.1 Quantum Geometric Tensor in Hermitian Systems

The quantum geometric tensor was first proposed by Provost and Vallee in 1980 to define a Riemannian metric that defines the distance in Hilbert space of quantum states [7]. For a class of quantum states $\{\psi(\xi)\}$ smoothly dependent on an N-dimensional parameter $\xi = (\xi_1, ...\xi_N)$, the distance in the Hilbert space of the quantum states corresponding to an infinitesimal change in the parameter space $\xi \to \xi + d\xi$ can be written as:

$$ds^2 = ||\psi(\xi + d\xi) - \psi(\xi)||^2 \tag{1.22}$$

where $||\cdot||$ denotes the norm. Here, the term $\psi(\xi + d\xi)$ can be expanded up to first order in $d\xi$ using Taylor expansion

$$\psi(\xi + d\xi) = \psi(\xi) + \sum_i^N \partial_{\xi_i}\psi(\xi)d\xi_i + O(d\xi^2) \tag{1.23}$$

where where ξ_i denotes the i-th component of the parameter ξ. Using the usual definition of norm in quantum mechanics in the bra-ket notation, $|||\psi\rangle||^2 = \langle\psi|\psi\rangle$, the distance can be written as

$$\begin{aligned} ds^2 &= (\langle\psi(\xi + d\xi)| - \langle\psi(\xi)|)(|\psi(\xi + d\xi)\rangle - |\psi(\xi)\rangle) \\ &= \sum_{i,j}\langle\partial_i\psi|\partial_j\psi\rangle d\xi_i d\xi_j \end{aligned} \tag{1.24}$$

where all higher order terms are dropped, and I denote $\partial_i = \partial_{\xi_i}$ for simplicity. However, the quantity $\langle \partial_i \psi | \partial_j \psi \rangle$ is not invariant under a gauge transformation $\psi \to e^{i\phi}\psi$

$$\langle \partial_i \psi | \partial_j \psi \rangle \to \langle \partial_i \psi | \partial_j \psi \rangle + i\partial_j \phi \langle \partial_i \psi | \psi \rangle - i\partial_i \phi \langle \psi | \partial_j \psi \rangle + \partial_i \phi \partial_j \phi \tag{1.25}$$

which means that it cannot be a valid physical observable. To restore the gauge-invariance, it requires an extra term $-\langle \partial_i \psi | \psi \rangle \langle \psi | \partial_j \psi \rangle$, which under the gauge transformation becomes

$$-\langle \partial_i \psi | \psi \rangle \langle \psi | \partial_j \psi \rangle \to -\langle \partial_i \psi | \psi \rangle \langle \psi | \partial_j \psi \rangle - i\partial_j \phi \langle \partial_i \psi | \psi \rangle + i\partial_i \phi \langle \psi | \partial_j \psi \rangle - \partial_i \phi \partial_j \phi \tag{1.26}$$

and cancels out the extra terms in Eq. (1.25). This yields what is known as the quantum geometric tensor [7]

$$Q_{n,ij} = \langle \partial_i \psi_n | \partial_j \psi_n \rangle - \langle \partial_i \psi_n | \psi_n \rangle \langle \psi_n | \partial_j \psi_n \rangle, \tag{1.27}$$

where $ds^2 = Q_{n,ij} d\xi_i d\xi_j$.

Here, I consider a multi-band system where ψ_n is the n-th eigenstate. The QGT is a Hermitian tensor with complex components. Its real (symmetric) part is the quantum metric tensor (QMT) $g_{n,ij}$ which, as the name suggests, defines the distance of the quantum states in Hilbert space. On the other hand, its imaginary (anti-symmetric) part corresponds to the Berry curvature $\Omega_{n,ij}$

$$\begin{aligned} g_{n,ij} &= \mathrm{Re}[Q_{n,ij}] \\ \Omega_{n,ij} &= -2\,\mathrm{Im}[Q_{n,ij}]. \end{aligned} \tag{1.28}$$

The quantum metric tensor is also associated with the fidelity, $\mathcal{F}$, which measures the overlap between two states

$$\mathcal{F}(|\psi_1\rangle, |\psi_2\rangle) = |\langle \psi_1 | \psi_2 \rangle|^2. \tag{1.29}$$

To understand the relation, let us consider the fidelity between $|\psi(\xi)\rangle$ and $|\psi(\xi + d\xi)\rangle$

$$\mathcal{F}(|\psi(\xi + d\xi)\rangle, |\psi(\xi)\rangle) = \langle \psi(\xi + d\xi) | \psi(\xi) \rangle \langle \psi(\xi) | \psi(\xi + d\xi) \rangle. \tag{1.30}$$

Similar to previous derivation, we can expand the state $|\psi(\xi + d\xi)\rangle$ to the second order

$$|\psi(\xi + d\xi)\rangle = |\psi(\xi)\rangle + \sum_i |\partial_i \psi(\xi)\rangle d\xi_i + \sum_{j,k} \frac{1}{2} |\partial_j \partial_k \psi(\xi)\rangle d\xi_j d\xi_k + O(d\xi^3) \tag{1.31}$$

which yields

$$\begin{aligned}\mathcal{F}(|\psi(\xi+d\xi)\rangle,|\psi(\xi)\rangle) = \sum_{i,j,k}\Bigg(&1+(\langle\partial_i\psi|\psi\rangle+\langle\psi|\partial_i\psi\rangle)d\xi_i+\langle\partial_j\psi|\psi\rangle\langle\psi|\partial_k\psi\rangle d\xi_j d\xi_k \\ &+\frac{1}{2}(\langle\partial_j\partial_k\psi|\psi\rangle+\langle\psi|\partial_j\partial_k\psi\rangle)d\xi_j d\xi_k\Bigg)+O(d\xi^3)\end{aligned} \tag{1.32}$$

where I denote $|\psi(\xi)\rangle = |\psi\rangle$ for simplicity. Using the normalization $\langle\psi|\psi\rangle = 1$, I have two identities

$$\begin{aligned}&\langle\partial_i\psi|\psi\rangle+\langle\psi|\partial_i\psi\rangle=0\\ &\langle\partial_i\partial_j\psi|\psi\rangle+\langle\partial_j\psi|\partial_i\psi\rangle+\langle\partial_i\psi|\partial_j\psi\rangle+\langle\psi|\partial_i\partial_j\psi\rangle=0.\end{aligned} \tag{1.33}$$

Hence, the fidelity can be rewritten as

$$\begin{aligned}\mathcal{F}(|\psi(\xi+d\xi)\rangle,|\psi(\xi)\rangle) =&1-\sum_{i,j}\left(\frac{1}{2}(\langle\partial_i\psi|\partial_j\psi\rangle+\langle\partial_j\psi|\partial_i\psi\rangle)-\langle\partial_i\psi|\psi\rangle\langle\psi|\partial_j\psi\rangle\right)d\xi_i d\xi_j\\ &+O(d\xi^3)\\ =&1-\sum_{i,j}g_{ij}d\xi_i d\xi_j+O(d\xi^3)\end{aligned} \tag{1.34}$$

where the quantum metric is identified as the fidelity susceptibility [185]. Both the fidelity and fidelity susceptibility play important roles in identifying quantum phase transitions [184, 185, 188, 187, 186].

The QMT and Berry curvature can also be written in terms of the derivatives of the Hamiltonians

$$\begin{aligned}g_{n,ij}&=\mathrm{Re}\left[\sum_{m\neq n}\frac{\langle\psi_m|\partial_i H|\psi_n\rangle\langle\psi_n|\partial_j H|\psi_m\rangle}{(E_m-E_n)^2}\right]\\ \Omega_{n,ij}&=i\sum_{m\neq n}\left[\frac{\langle\psi_m|\partial_i H|\psi_n\rangle\langle\psi_m|\partial_j H|\psi_n\rangle}{(E_m-E_n)^2}-\frac{\langle\psi_m|\partial_j H|\psi_n\rangle\langle\psi_n|\partial_i H|\psi_m\rangle}{(E_m-E_n)^2}\right]\end{aligned} \tag{1.35}$$

which arise from perturbation theory, where E_n denotes the n-th eigenenergy [189, 190]. As a result, for a two-band system, where $n = \pm$, it is easy to see that the components of the QGT follow the identities [189, 190]

$$\begin{aligned}g_{+,ij}&=g_{-,ij}\\ \Omega_{+,ij}&=-\Omega_{-,ij}.\end{aligned} \tag{1.36}$$

The Berry curvature is associated with the Chern number and the topology of the band structure, as well as the geometry of the underlying Hamiltonian through the Berry phase. On the other hand, the QMT defines the geometry of the Hilbert space of the quantum states. In 2014, Gao et al. showed that the quantum metric tensor describes the perturbative correction to the anomalous Hall drift [178, 179, 180]. In a first-order perturbation theory, the QMT appears as a correction to the wavepacket centre-of-mass position, as derived in the following.

1.3.2 Quantum Geometric Tensor and Wavepacket Dynamics

As we have seen in Eq. (1.13), the Berry curvature results in the anomalous velocity in the transverse direction to the applied force. In Ref. [178], Gao et al. showed that the QMT appears in the perturbative correction to the Berry connection as field-induced positional shifts. Since the Berry curvature is the curl of the Berry connection, it is expected that the QMT will also describe the perturbative corrections to the anomalous velocity. This links the abstract mathematical concept of the geometry of the manifold of quantum states to the experimentally observable physical effects.

To see what roles the QGT plays in the wavepacket (WP) dynamics, in this Section, I will revisit the derivation from Ref. [178]. First, consider a two-by-two Hamiltonian with perturbation arising from an external force

$$\hat{H} = \hat{H}_0 - \mathbf{F} \cdot \mathbf{r}, \tag{1.37}$$

where the unperturbed Hamiltonian $\hat{H}_0$ has two eigenstates $|u_{0,1}\rangle$ with corresponding eigenenergies $E_{0,1}$. The eigenstates of the perturbed Hamiltonian are denoted $|\tilde{u}_{0,1}\rangle$ and can be obtained from the unperturbed eigenstates expanded to the first order in $\mathbf{F}$

$$|\tilde{u}_0\rangle = |u_0\rangle + \frac{\mathbf{F} \cdot \mathbf{A}_{10}}{E_1 - E_0} |u_1\rangle, \tag{1.38}$$

where $\mathbf{A}_{10} = \langle u_1 | i\partial_{\mathbf{k}} u_0\rangle$ denotes the inter-band Berry connection, and $|\tilde{u}_1\rangle$ can be obtained similarly by exchanging the indices $0 \leftrightarrow 1$. Then, consider a wavepacket in the eigenstate $|\tilde{u}_0\rangle$ under the single-band approximation

$$\begin{aligned} |W\rangle &= \int w_{\mathbf{k}} e^{i\mathbf{k}\cdot\mathbf{r}} |\tilde{u}_0\rangle d^2\mathbf{k} \\ &= \int w_{\mathbf{k}} e^{i\mathbf{k}\cdot\mathbf{r}} \left(|u_0\rangle + \frac{\mathbf{F} \cdot \mathbf{A}_{10}}{E_1 - E_0} |u_1\rangle \right) d\mathbf{k} \end{aligned} \tag{1.39}$$

where w_k denotes the WP distribution in momentum space.

The centre-of-mass position of $|W\rangle$ can be calculated up to the first order in $\mathbf{F}$

$$\begin{aligned} \mathbf{r}_c =& \langle W | \hat{\mathbf{r}} | W \rangle \\ =& \int i w_{\mathbf{k}}^* \partial_{\mathbf{k}} w_{\mathbf{k}} d^2\mathbf{k} + \int |w_{\mathbf{k}}|^2 \left(\langle u_0 | i\partial_{\mathbf{k}} u_0 \rangle + \frac{\mathbf{F} \cdot \mathbf{A}_{10}}{E_1 - E_0} \langle u_0 | i\partial_{\mathbf{k}} u_1 \rangle + \frac{\mathbf{F} \cdot \mathbf{A}_{01}}{E_1 - E_0} \langle u_1 | i\partial_{\mathbf{k}} u_0 \rangle \right) d^2\mathbf{k} \\ =& \int i w_{\mathbf{k}}^* \partial_{\mathbf{k}} w_{\mathbf{k}} d^2\mathbf{k} + \int |w_{\mathbf{k}}|^2 \left(\mathbf{A}_0 + \frac{\mathbf{F} \cdot \mathbf{A}_{10}}{E_1 - E_0} \mathbf{A}_{01} + \frac{\mathbf{F} \cdot \mathbf{A}_{01}}{E_1 - E_0} \mathbf{A}_{10} \right) d^2\mathbf{k}. \end{aligned} \tag{1.40}$$

Here, the coefficient $w_{\mathbf{k}}$ can be rewritten in the form $w_{\mathbf{k}} = |w_{\mathbf{k}}| e^{i\varphi(\mathbf{k})}$ and hence the first term in the third line in Eq. (1.40) can be rewritten as

$$\int i w_{\mathbf{k}}^{*} \partial_{\mathbf{k}} w_{\mathbf{k}} d^2\mathbf{k} = \int i |w_{\mathbf{k}}| \partial_{\mathbf{k}} |w_{\mathbf{k}}| d^2\mathbf{k} - \int |w_{\mathbf{k}}|^2 \partial_{\mathbf{k}} \varphi d^2\mathbf{k}. \tag{1.41}$$

Note that using integration by parts

$$\begin{aligned} \int |w_{\mathbf{k}}| \partial_{\mathbf{k}} |w_{\mathbf{k}}| d^2\mathbf{k} =& \frac{1}{2} \int \partial_{\mathbf{k}} |w_{\mathbf{k}}|^2 d^2\mathbf{k} \\ =& 0, \end{aligned} \tag{1.42}$$

and the only terms left are

$$\mathbf{r}_c = - \int |w_{\mathbf{k}}|^2 \partial_{\mathbf{k}} \varphi d^2\mathbf{k} + \int |w_{\mathbf{k}}|^2 \left(\mathbf{A}_0 + \frac{\mathbf{F} \cdot \mathbf{A}_{10}}{E_1 - E_0} \mathbf{A}_{01} + \frac{\mathbf{F} \cdot \mathbf{A}_{01}}{E_1 - E_0} \mathbf{A}_{10} \right) d^2\mathbf{k}. \tag{1.43}$$

Here, using the identity of the quantum metric in Eq. (1.35) and the fact that the quantum metric tensor is symmetric, $\mathbf{r}_c$ can be re-written in terms of the quantum metric g as

$$\mathbf{r}_c = - \int |w_{\mathbf{k}}|^2 \partial_{\mathbf{k}} \varphi d^2\mathbf{k} + \int |w_{\mathbf{k}}|^2 \left(\mathbf{A}_0 + \frac{2g \cdot \mathbf{F}}{E_1 - E_0} \right) d^2\mathbf{k}. \tag{1.44}$$

In the limit that the WP is infinitely narrow in momentum space $|w_{\mathbf{k}}|^2 = \delta(\mathbf{k} - \mathbf{k}_c)$, the centre-of-mass position can be written as

$$\mathbf{r}_c = -\partial_{\mathbf{k}} \varphi + \mathbf{A}_0 + \left. \frac{2g \cdot \mathbf{F}}{E_1 - E_0} \right|_{\mathbf{k}=\mathbf{k}_c}. \tag{1.45}$$

Now, in order to derive the semi-classical equation of motion of the wavepacket, consider the effective Lagrangian

$$\begin{aligned} L =& \langle W | i\hbar \partial_t - \hat{H}_0 - \mathbf{F} \cdot \mathbf{r} | W \rangle \\ =& i\hbar \partial_t \varphi - E_0 - \mathbf{F} \cdot \mathbf{r}_c, \end{aligned} \tag{1.46}$$

similarly to the derivation of the WP centre-of-mass position shown above. Here, the partial time-derivative of the phase can be re-written as

$$\partial_t \varphi = d_t \varphi - \dot{\mathbf{k}}_c \cdot \partial_{\mathbf{k}} \varphi \tag{1.47}$$

where d_t denotes the total time derivative. By re-writing the term $\partial_{\mathbf{k}} \varphi$ in terms of $\mathbf{r}_c$, this yields the effective Lagrangian in the form of

$$L = \hbar d_t \varphi - \hbar \dot{\mathbf{k}}_c \cdot \left(\mathbf{r}_c - \mathbf{A}_0 - \frac{2g \cdot \mathbf{F}}{E_1 - E_0} \right) - E_0 - \mathbf{F} \cdot \mathbf{r}_c, \tag{1.48}$$

where the total time derivative $d_t \varphi$ will vanish. The equation of motion can now be derived using the Euler-Lagrange equation

$$\frac{\partial L}{\partial q} - \frac{d}{dt}\left(\frac{\partial L}{\partial \dot{q}}\right) = 0. \tag{1.49}$$

Each term can be written as

$$\begin{aligned}
\frac{\partial L}{\partial (\mathbf{r}_c)_i} &= -\hbar(\dot{\mathbf{k}}_c)_i + F_i \\
\frac{d}{dt}\left(\frac{\partial L}{\partial (\dot{\mathbf{r}}_c)_i}\right) &= 0 \\
\frac{\partial L}{\partial (\mathbf{k}_c)_i} &= \sum_j \hbar(\dot{\mathbf{k}}_c)_j \partial_{k_i}\left((\mathbf{A}_0)_j + \frac{2(g\cdot\mathbf{F})_j}{E_1 - E_0}\right) - \partial_{k_i} E_0 \\
\frac{d}{dt}\left(\frac{\partial L}{\partial (\dot{\mathbf{k}}_c)_i}\right) &= -\hbar(\dot{\mathbf{r}}_c)_i + \sum_j \hbar(\dot{\mathbf{k}}_c)_j \partial_{k_j}\left((\mathbf{A}_0)_i + \frac{2(g\cdot\mathbf{F})_i}{E_1 - E_0}\right),
\end{aligned} \tag{1.50}$$

where I denote $\partial_{k_j} = \frac{\partial}{\partial(\mathbf{k}_c)_j}$ and separate the components of the vectors $\mathbf{k}_c$ and $\mathbf{r}_c$ to avoid confusion. By collecting each term in Eq. (1.50) and using the identity in Eq. (1.49), this yields the semi-classical equation of motion as

$$\begin{aligned}
&\hbar\dot{\mathbf{r}}_c = \partial_{\mathbf{k}} E_0 - \hbar\dot{\mathbf{k}}_c \times \left(\mathbf{\Omega}_0 + \nabla_{\mathbf{k}} \times \frac{2g\cdot\mathbf{F}}{E_1 - E_0}\right)\Big|_{\mathbf{k}=\mathbf{k}_c} \\
&\hbar\dot{\mathbf{k}}_c = \mathbf{F}.
\end{aligned} \tag{1.51}$$

Here, the Berry curvature acts on the WP centre of mass as an effective magnetic field in momentum space, resulting in anomalous velocity, while the quantum metric tensor arises from the perturbative correction to the WP centre-of-mass position, resulting in the positional shift. In Chapter 3, I will generalise this semi-classical equation of motion to non-Hermitian systems to investigate the effects of non-Hermiticity on the QGT and WP dynamics.

1.3.3 Measurement of Quantum Geometric Tensor

Remarkably, the components of the quantum geometric tensor in a photonic or a two-level polaritonic system can be directly measured, as suggested by Bleu et al. in Ref. [189]. This technique can be applied to any two-level photonic [189], polaritonic [189, 191] and plasmonic [192] system where the Stokes vectors of the states can be directly measured by detecting the photon emission. This is highly relevant to the research presented later in this Thesis, as I investigate the observable signatures of the QGT in a non-Hermitian exciton-polariton system (see Section 3.3). First, let us consider a two-level system, where the Stokes vectors (pseudospin) $\mathbf{S} = (S_x, S_y, S_z)$ can be written as the expectation value $S_j = \langle\psi|\sigma_j|\psi\rangle$ where σ_j is the j-th two-dimensional Pauli matrices. The state $|\psi\rangle$ can conversely be written in terms of the Stokes vectors as

$$|\psi\rangle = \begin{pmatrix} e^{-i\phi}\cos\frac{\theta}{2} \\ \sin\frac{\theta}{2} \end{pmatrix} \tag{1.52}$$

where ϕ, θ denotes the angle of the Stokes vector on the Bloch sphere

$$\begin{aligned} \theta &= \arccos S_z \\ \phi &= \arctan(S_y/S_x). \end{aligned} \tag{1.53}$$

By substituting the wavefunction back to the definition of the QGT in Eq. (1.27), then the QMT and Berry curvature can be expressed in terms of the angles of the Stokes vectors as

$$\begin{aligned} g_{n,ij} =& \frac{1}{4}\Big(\partial_i\theta\partial_j\theta + \sin^2\theta\partial_i\phi\partial_j\phi\Big), \\ \Omega_{n,ij} =& \frac{1}{2}\sin\theta\Big(\partial_i\phi\partial_j\theta - \partial_j\phi\partial_i\theta\Big). \end{aligned} \tag{1.54}$$

Most importantly, since the Stokes vectors in the photonic and polaritonic systems can be directly measured by measuring the polarization of the photonic emission, this provides a way to directly measure the components of the QGT, which has been achieved in Ref. [191].

1.3.4 Generalised Quantum Geometric Tensors in non-Hermitian Systems

As discussed in Section 1.1, in non-Hermitian systems, the left and right eigenstates are not equal. One consequence is that it creates two different ways to define observables of the eigenstates. For some operator $\hat{O}$, the expectation value can either be expressed by using only the right eigenstates as follows [193]:

$$\langle\hat{O}\rangle = \langle\psi_n^R|\hat{O}|\psi_n^R\rangle, \tag{1.55}$$

where here $|\psi_n^R\rangle$ denotes the right eigenstates of the Hamiltonian instead of the right eigenstates of the operator $\hat{O}$. Alternatively, it can also be expressed using both the left and the right eigenstates

$$\langle\hat{O}\rangle = \langle\psi_n^L|\hat{O}|\psi_n^R\rangle \tag{1.56}$$

using either the notion of bi-orthogonal quantum mechanics [194], or through some metric operator [195, 196, 197] (not to be confused with QMT) which maps the right eigenstate to the left eigenstate of the same energy level. Here, we can think of it as two different ways to define the inner product $||\cdot||$ in the Hilbert space of the right eigenstates $\{|\psi_n^R(\xi)\rangle\}$, namely $\langle\psi_n^R|\cdot|\psi_n^R\rangle$ and $\langle\psi_n^L|\cdot|\psi_n^R\rangle$.

Therefore, there are at least two different ways to define the components of the QGT in non-Hermitian systems. One definition arises from defining the inner product as $||\cdot|| = \langle\psi_n^R|\cdot|\psi_n^R\rangle$, which I will refer to as the right-right (RR) QGT [198, 8, 199, 9, 192]

$$Q^{RR}_{n,ij} = \langle\partial_i\psi_n^R|\partial_j\psi_n^R\rangle - \langle\partial_i\psi_n^R|\psi_n^R\rangle\langle\psi_n^R|\partial_j\psi_n^R\rangle \tag{1.57}$$

and similarly, another definition arises from defining the inner product as $||\cdot|| = \langle\psi_n^L|\cdot|\psi_n^R\rangle$, which I will refer to as the left-right (LR) QGT [200, 201, 10, 202, 203]

$$Q^{LR}_{n,ij} = \langle \partial_i \psi^L_n | \partial_j \psi^R_n \rangle - \langle \partial_i \psi^L_n | \psi^R_n \rangle \langle \psi^L_n | \partial_j \psi^R_n \rangle. \tag{1.58}$$

Although I focus on the RR and the LR versions of the QGT in this Thesis, one can also similarly define the left-left (LL) and the right-left (RL) versions. I also emphasize that for the quantity $Q^{\alpha\beta}_{n,ij}$, with $\alpha, \beta = L, R$, the eigenstates need to satisfy $\langle \psi^\alpha_n | \psi^\beta_n \rangle = 1$ to preserve the gauge invariance.

1.3.5 Generalised Berry Curvatures

Like the QGT, there are also multiple ways to define the non-Hermitian Berry connection $\mathbf{A}_n = \langle \psi_n | i \nabla_{\mathbf{k}} \psi_n \rangle$ as

$$\mathbf{A}^{\alpha\beta}_n = \langle \psi^\alpha_n | i \nabla_{\mathbf{k}} \psi^\beta_n \rangle, \tag{1.59}$$

and similarly, the Berry curvature as

$$\begin{aligned} \Omega^{\alpha\beta}_{n,ij} &= \Big(\nabla_{\mathbf{k}} \times \mathbf{A}^{\alpha\beta}_n \Big)_{ij} \\ &= i \Big(\langle \partial_i \psi^\alpha_n | \partial_j \psi^\beta_n \rangle - \langle \partial_j \psi^\alpha_n | \partial_i \psi^\beta_n \rangle \Big), \end{aligned} \tag{1.60}$$

where the eigenstates need to satisfy $\langle \psi^\alpha_n | \psi^\beta_n \rangle = 1$ for $\mathbf{\Omega}^{\alpha\beta}_n$ to be gauge-invariant. Interestingly, while the LL and RR Berry curvatures are real-valued, the LR and the RL Berry curvatures are generally complex-valued. Therefore, although that the RR (LL) Berry curvature corresponds to the imaginary parts of the RR (LL) QGT

$$\Omega^{RR/LL}_{n,ij} = -2\,\mathrm{Im}[Q^{RR/LL}_{n,ij}], \tag{1.61}$$

the LR (RL) Berry curvature corresponds to the anti-symmetric parts of the LR (RL) QGT

$$\Omega^{LR/RL}_{n,ij} = i \Big(Q^{LR/RL}_{n,ij} - Q^{LR/RL}_{n,ji} \Big). \tag{1.62}$$

Notably, when calculating the Chern number using the non-Hermitian Berry curvatures,

$$C^{\alpha\beta}_n = \frac{1}{2\pi} \iint_{BZ} \Omega^{\alpha\beta}_n(\mathbf{k}) \cdot d^2\mathbf{k}, \tag{1.63}$$

all four Berry curvatures produce the same Chern number $C^{LL}_n = C^{RR}_n = C^{RL}_n = C^{LR}_n$ [6]. In other words, the global topology is independent of the choice of the left or the right eigenstates, despite the different forms of the four Berry curvatures [6]. In Ref. [204], Xu et al. show that the RR Berry curvature describes the non-Hermitian version of anomalous Hall drift in WP dynamics

$$\begin{aligned} \hbar \dot{\mathbf{r}} &= \nabla_{\mathbf{k}} \,\mathrm{Re}[E_n + \mathbf{F} \cdot (\mathbf{A}^{RR}_n - \mathbf{A}^{LR}_n)] - \mathbf{F} \times \mathbf{\Omega}^{RR}_n |_{\mathbf{k}=\mathbf{k}_c} \\ \hbar \dot{\mathbf{k}} &= \mathbf{F} \end{aligned} \tag{1.64}$$

where here **F** denotes the external force, and the correction arising from the RR and LR Berry connections is called the non-Hermitian anomalous Berry connection (NH ABC) [204, 205, 206]. In Ref. [9], Cuerda et al. show that the non-Hermiticity can induce a non-zero RR Berry curvature. There has also been investigation on the LR Berry curvature. In Ref. [202], Fan et al. identify the integral of the imaginary part of the LR Berry curvature over the Brillouine zone as "quantum Hall susceptance", where if it is positive (negative), it shows the system to be a capacitor (inductor). This shows the vast interest in generalised Berry curvature in non-Hermitian systems.

1.3.6 Generalised Quantum Metric Tensors

Defining the RR version of the QMT is straightforward, since the RR QGT is also a Hermitian tensor like its Hermitian counterpart, and we can define the RR version of the QMT as

$$g^{RR}_{n,ij} = \mathrm{Re}[Q^{RR}_{n,ij}]. \tag{1.65}$$

In Ref. [198], Matsumoto et al. show that the RR fidelity susceptibility diverges without forming degeneracy and argued this to be the sign of quantum phase transition without gap closing. Furthermore, in Ref. [8], Solnyshokov et al. argued that the RR QMT plays a significant role in WP dynamics. Interestingly, the procedure suggested for measuring the components of the QGT in the Hermitian [189] case also works in the case of the RR QGT. The RR QMT has been measured using an exciton-polariton system in Ref. [199] while both RR Berry curvature and the RR QMT have been measured using a plasmonic system in Ref. [192].

On the other hand, unlike its RR and Hermitian counterparts, the LR QGT is not Hermitian. Therefore, there are several possible ways to define the LR version of the QMT. In Ref. [203], Ye et al. discussed 3 ways to define the LR QMT, namely the symmetric part of the LR QGT

$$g^{LR}_{n,ij} = \frac{1}{2}\Big(Q^{LR}_{n,ij} + Q^{LR}_{n,ji}\Big) \tag{1.66}$$

the real part of the LR QGT

$$g^{LR}_{n,ij} = \mathrm{Re}\left[Q^{LR}_{n,ij}\right] \tag{1.67}$$

and the real and symmetric part of the LR QGT

$$g^{LR}_{n,ij} = \mathrm{Re}\left[\frac{1}{2}\Big(Q^{LR}_{n,ij} + Q^{LR}_{n,ji}\Big)\right]. \tag{1.68}$$

In earlier works, the LR QMT has also been shown to be sensitive to the exceptional points in Ref. [200]. It has also been used to describe the quantum geometry and phase transition in a PT-symmetric system in Ref. [201] and a pseudo-Hermitian system in Ref. [10]. There have also been studies where the LR version of fidelity susceptibility is used to detect the existence of the exceptional points [207] and phase boundaries [208, 209]. Ye et al. also show that only the LR QMT is needed to correctly describe the quantum phase transition in a non-Hermitian Su-Schrieffer-Heeger system while the RR and the LL would fail to do so [203]. Furthermore, in Ref. [210], the LR QMT has also been shown to describe the superfluid weight in a non-Hermitian flat-band superconductor. This shows the lack of consensus on how to generalise the components of the QGT to non-Hermitian systems.

Despite the increasing interests in the QGT in non-Hermitian systems, the relevance of different definitions of this quantity described above to the observable effects remains an open problem. While both the LR and RR quantities have been shown to play important roles in non-Hermitian systems, it is not clear which one should be used to describe different physical effects, such as the field-induced correction to the wavepacket dynamics previously discussed in Eq. (1.51). In this Thesis, I intend to address this problem by investigating the dynamics in non-Hermitian systems. In particular, I will focus on a hybridized light-matter system known as the exciton polaritons, which will be discussed in the following Section.

1.4 Exciton Polaritons

Exciton polaritons are composite bosonic particles arising from the strong coupling between excitons, electron-hole pairs held together by the Coulomb interaction, and photons. The photons need to be confined, e.g., in a high-quality optical cavity, to achieve strong interaction with excitons. The structure hosting exciton polaritons typically consists of a thin layer of semiconducting material that hosts the excitons sandwiched between two Bragg reflectors that are used to confine the cavity photon [see Fig. 1.7(a)]. Exciton polaritons can form in a wide range of semiconductors, such as GaAs [211, 212], CdTe [213, 214], WS2 [215, 216], perovskites [217, 218], ZnO [219] and organic materials [199]. More recently, a liquid crystal based electrically tunable exciton polariton system has also been demonstrated in Ref. [220]. The exciton polaritons present a prominent platform for non-equilibrium bosonic condensate [213, 211, 221, 212, 222, 214, 223] as well as superfluidity [224, 225, 226, 227, 228]. Furthermore, they exhibit spin-orbit coupling, and therefore they cab also exhibit optical spin Hall effects [229, 230] and can be used to realise topological insulators [231, 232, 233, 217, 234, 220] as well as Zitterbewegung effects [235, 236]. More recently, exciton polaritons have also been studied in the context of applications in quantum simulations [5, 237, 238, 239] and neuromorphic quantum computing [240, 241, 242]. All of these studies highlight the rich physics of this hybrid light-matter system. In this Section, I will present a brief review on the exciton polaritons as an experimentally accessible non-Hermitian system.

First, let us consider a minimalistic model of the exciton polaritons described by a simple two-by-two Hamiltonian [13, 12]

$$H = \begin{pmatrix} E_{exc}(\mathbf{k}) & \hbar\Omega_R \\ \hbar\Omega_R & E_{ph}(\mathbf{k}) \end{pmatrix} \tag{1.69}$$

where E_{exc}, E_{ph} are the energies of uncoupled exciton and cavity photon, respectively, and the Rabi splitting Ω_R characterises the strength of exciton-photon coupling [13]. The dispersion (momentum dependence) of the eigenenergies of this Hamiltonian is known as the upper (UP) and lower polariton (LP) branches

$$E_{UP,LP} = \frac{1}{2}\left(E_{exc}(\mathbf{k}) + E_{ph}(\mathbf{k}) \pm \sqrt{\tilde{\delta}^2(\mathbf{k}) + 4\hbar^2\Omega_R^2}\right) \tag{1.70}$$

where the + sign ($-$ sign) corresponds to the upper (lower) polariton branch and k is the exciton-polariton momentum in the plane of the semiconductor material, $\tilde{\delta}$ denotes the energy detuning $\tilde{\delta} = E_{exc} - E_{ph}$. The corresponding eigenstates can be written as [13]:

$$\begin{aligned}|\psi_{LP,UP}\rangle =&\psi^X_{LP,UP}|X\rangle + \psi^C_{LP,UP}|C\rangle \\ =&\frac{\tilde{\delta}(\mathbf{k}) \pm \sqrt{\tilde{\delta}^2(\mathbf{k}) + 4\hbar^2\Omega_R^2}}{\sqrt{2\left(\tilde{\delta}^2(\mathbf{k}) + 4\hbar^2\Omega_R^2 \pm \tilde{\delta}(\mathbf{k})\sqrt{\tilde{\delta}^2(\mathbf{k}) + 4\hbar^2\Omega_R^2}\right)}}|X\rangle \\ &+ \frac{2\hbar\Omega_R}{\sqrt{2\left(\tilde{\delta}^2(\mathbf{k}) + 4\hbar^2\Omega_R^2 \pm \tilde{\delta}(\mathbf{k})\sqrt{\tilde{\delta}^2(\mathbf{k}) + 4\hbar^2\Omega_R^2}\right)}}|C\rangle,\end{aligned} \tag{1.71}$$

where $|X\rangle$ and $|C\rangle$ denote the vectors $(1,0)^T$ and $(0,1)^T$, and the indices LP and UP correspond to $-$ and $+$ in the equation, respectively.

In the weak coupling regime, the eigenenergy spectra in momentum space resemble the uncoupled exictonic and photonic branches, while in the strong coupling regime, the branches exhibit anti-crossing behaviour and the two new (upper and lower) branches signal the emergence of the half-matter, half-light exciton polaritons [see Fig. 1.7(b)] [13, 12].

The excitonic and photonic fractions in the polariton can be described using the Hopfield coefficients [243] X and C. The Hopfield coefficients are determined by the detuning and the Rabi splitting and can be calculated from the eigenstates in Eq. (1.71)

$$\begin{aligned}|X|^2 = |\psi^X_{LP}|^2 = |\psi^C_{UP}|^2 = \frac{1}{2}\left(1 - \frac{\tilde{\delta}}{\sqrt{\tilde{\delta}^2 + \hbar^2\Omega_R^2}}\right) \\ |C|^2 = |\psi^C_{LP}|^2 = |\psi^X_{UP}|^2 = \frac{1}{2}\left(1 + \frac{\tilde{\delta}}{\sqrt{\tilde{\delta}^2 + \hbar^2\Omega_R^2}}\right)\end{aligned} \tag{1.72}$$

where $|X|^2 + |C|^2 = 1$. In the low-momentum regime, the UP and LP branches can be approximated by parabolic dispersion

$$E_{LP,UP}(\mathbf{k}) \approx E_{LP,UP}(0) + \frac{\hbar^2 k^2}{2m_{LP,UP}}. \tag{1.73}$$

Here, the effective masses of the upper and lower polaritons are determined by the Hop-

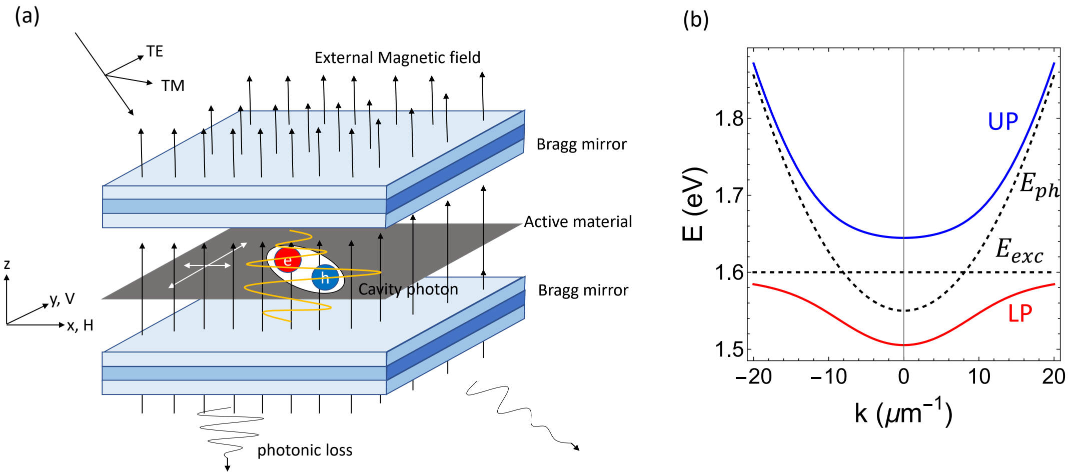

Figure 1.7: (a) A schematic plot of a microcavity exciton-polariton system, consisting of a thin layer of exciton-hosting material sandwiched between Bragg mirrors to confine the photon. Also shown are a constant magnetic field, anisotropy in the active material as well as the TE and TM modes, whose oscillations are perpendicular to the direction of the propagating photon, and photonic losses, all of which will be discussed in later sections. (b) hybridisation of the excitonic (E_{exc}) and photonic (E_{ph}) branches and formation of the upper (UP) and lower polariton (LP) branches in momentum space.

field coefficients

$$\begin{aligned} m_{LP} &= \frac{|X|^2}{m_{exc}} + \frac{|C|^2}{m_{cav}} \\ m_{UP} &= \frac{|X|^2}{m_{cav}} + \frac{|C|^2}{m_{exc}} \end{aligned} \tag{1.74}$$

where m_{exc}, m_{cav} denote the effective masses of excitons and cavity photons.

The above analysis neglects the effects from the photonic or excitonic losses. However, in an actual system, both excitons and cavity photons have finite lifetime, and there are radiative loss of cavity photons γ_{ph} and well as the non-radiative loss of the excitons γ_{exc}. After properly taking the effects of dissipation into account, the upper and lower polariton branches become [13]

$$E_{LP,UP} = \frac{1}{2}\left(E_{exc}(\mathbf{k}) + E_{ph}(\mathbf{k}) - i\hbar(\gamma_{exc} + \gamma_{ph}) \pm \sqrt{\left(\tilde{\delta}(\mathbf{k}) - i\hbar(\gamma_{exc} - \gamma_{ph})\right)^2 + 4\hbar^2\Omega_R^2}\right). \tag{1.75}$$

In this case, in order to have the anti-crossing exciton-polariton branches shown in Fig. 1.7(b), the difference between the excitonic and the photonic dissipation must be smaller than the coupling strength, $|\gamma_{exc} - \gamma_{ph}| < 2\Omega$.

Similar to the effective masses, the effective dissipations of the upper and the lower polaritons are also determined by the Hopfield coefficients as [13]

$$\begin{aligned} \gamma_{LP} &= |X|^2\gamma_{exc} + |C|^2\gamma_{ph} \\ \gamma_{UP} &= |C|^2\gamma_{exc} + |X|^2\gamma_{ph}. \end{aligned} \tag{1.76}$$

In the next Section, I will review a mean-field model that effectively describes the dynamics of (lower) exciton polaritons taking into account the polariton-polariton interactions.

1.4.1 Generalised Gross-Pitaevskii Equation

The polariton-polariton interaction is key to achieving interesting physics in an exciton-polariton system, such as Bose-Einstein condensation [213, 211, 221, 212, 222, 214, 223] and superfluidity [224, 225, 226, 227, 228] of the lower polaritons. Here, I will review a nonlinear theory for interacting polaritons presented in Ref. [244]. This theory is very similar to the Gross-Pitaevskii equation, which I will discuss below.

The Gross-Pitaevskii equation is a nonlinear Schrodinger equation proposed by Gross [245] and Pitaevskii [246] in 1961 to describe the dynamics of the Bose-Einstein condensate. In a condensate, many bosons occupy the same quantum state and, using the mean-field approximation [245, 246], can be described by a single macroscopic wavefunction $\Psi(\mathbf{r}, t)$

$$i\hbar\frac{d}{dt}\Psi = -\frac{\hbar^2\nabla^2}{2m}\Psi(\mathbf{r},t) + V_{ext}(\mathbf{r})\Psi(\mathbf{r},t) + \frac{4\pi\hbar^2 a}{m}|\Psi(\mathbf{r},t)|^2\Psi(\mathbf{r},t) \tag{1.77}$$

where a denotes the atom-atom scattering length and the last term $(4\pi\hbar^2 a)/m = g$ determines the interaction strength of the condensate particles [13].

The Gross-Pitaevskii equation has been generalised to describe an exciton-polariton condensate continuously replenished from an incoherent reservoir of excitons (the so-called incoherent pumping regime) [244]. The model consists of the Gross-Pitaevskii equation for the exciton-polariton wavefunction $\Psi(\mathbf{r}, t)$ and rate equation for the excitonic reservoir density $n_R(\mathbf{r}, t)$

$$\begin{aligned} i\hbar\frac{d}{dt}\Psi &= -\frac{\hbar^2\nabla^2}{2m}\Psi + \frac{i\hbar}{2}\Big(R(n_R) - \gamma\Big)\Psi + \tilde{g}\hbar n_R\Psi + \hbar g|\Psi|^2\Psi \\ \frac{d}{dt}n_R &= P - \gamma_R n_R - R(n_R)|\Psi|^2 + D\nabla^2 n_R \end{aligned} \tag{1.78}$$

where g, $\tilde{g}$ describe polariton-polariton interaction strength and the interaction between polaitons and the reservoir, respectively, $P(\mathbf{r})$ represents a pump rate, $R(n_R)$ describes the stimulated scattering from the reservoir into the condensate and is usually approximated as $R(n_R)$, γ_R is the reservoir loss rate, γ represents the radiative loss of the polaritons, and D is the reservoir diffusion constant [244, 13]. Here, the reservoir scattering is approximated as $R(n_R) \approx Rn_R$, which corresponds to the bottleneck region, and enables the mean-field model to reproduce the threshold-like behaviour of the polariton condensates [247]. The typical lifetime of the reservoir excitons are in the magnitude of τ_R ~1000 ps, while the cavity photons have lifetime of τ_{ph} ~135 ps [248]. As in Eq. (1.76), the lifetime of the polaritons are determined by the Hopfield coefficients, while the lifetime of the excitons are much longer the that of the cavity photons, the lifetime of the lower polaritons can be approximated as $\tau_{LP} = 1/\gamma_{LP}$, where $\gamma_{LP} \approx |C|^2\gamma_{ph}$ [248, 13]. In the exciton-polariton systems available in our research group (ANU Polariton BEC Group), the polaritons are short-living and have lifetime of $\gamma \sim 10$ ps [249].

In this work, I consider the simple case of the linear regime, which corresponds to the polaritons below threshold or polaritons at low density close to the threshold. In this regime, the rate equations in Eq. (1.78) can be approximated as

$$\begin{aligned} i\hbar\frac{d}{dt}\Psi &= -\frac{\hbar^2\nabla^2}{2m}\Psi + \frac{i\hbar}{2}\Big(Rn_R - \gamma\Big)\Psi + \tilde{g}\hbar n_R\Psi \\ \frac{d}{dt}n_R &= P - \gamma_R n_R. \end{aligned} \tag{1.79}$$

Here, I also set $D = 0$ for simplicity, since the typical diffusion rate is in the magnitude of nanometers per picoseconds, which is much smaller than the velocities of the exciton polaritons, which is in the magnitude of micrometers per picoseconds. In this linear case in Eqs. (1.79) where the polariton density is low, the reservoir density has a general steady-state solution

$$\begin{aligned} n_R(\mathbf{r}, t) &= \frac{P(\mathbf{r})}{\gamma_R} + \Big(n_R(\mathbf{r}, 0) - \frac{P(\mathbf{r})}{\gamma_R}\Big)e^{-\gamma_R t} \\ &\xrightarrow{t\to\infty} \frac{P(\mathbf{r})}{\gamma_R}. \end{aligned} \tag{1.80}$$

Assuming the reservoir is in steady state, the equation for Ψ in Eqs. (1.79) can be rewritten as:

$$i\hbar\frac{d}{dt}\Psi = -\frac{\hbar^2\nabla^2}{2m}\Psi + \frac{i\hbar}{2}\Big(\frac{PR}{\gamma_R} - \gamma\Big)\Psi + \frac{\tilde{g}\hbar P}{\gamma_R}\Psi \tag{1.81}$$

where $(i\hbar PR)/(2\gamma_R)$ and $(\tilde{g}\hbar P)/(\gamma_R)$ can be interpreted as the imaginary and real parts of the complex-valued effective potential induced by the pump P. For example, in typical experiments with GaAs-based microcavity polaritons, the depth of the effective optically induced potential is in the magnitude of 1 meV [250]. In Chapter 6, I will use this equation to discuss the non-Hermitian skin effect and show how it can induced by the pump in a realistic exciton-polariton system.

1.4.2 Exciton-Polariton Pseudospins

As mentioned at the start of the Section, exciton polaritons also exhibit interesting physics such as the optical spin Hall effects [229, 230], as well as topological insulating phases [232, 233] arising from photonic spin-orbit coupling. To see how these effects arise, we first need to discuss the concept of the exciton-polariton pseudospin [251].

When projected on the structure-growth axis, electrons have spins $J_z^e = \pm 1/2$, while holes have spins of either $J_z^h = \pm 1/2$, if they are light holes, or $J_z^h = \pm 3/2$, if they are heavy holes. These light and heavy holes arise from the two subspaces of solutions to the Luttinger Hamiltonian proposed in Ref. [252]. Here, light (heavy) holes are formed when the projections of the hole angular momentum and spin are anti-parallel (parallel) to each other [251]. Since holes are not the main focus of this thesis, I have kept it brief, here. For those interested, please refer to Ref. [253] for more details.

The spin of the excitons is determined by the combination of the spins of the electrons and the holes, thus excitons have spins of $J_z = \pm 1$ and $J_z = \pm 2$. In a microcavity, excitons with spins of $J_z = \pm 2$ do not couple to light; hence they are called the dark states, while excitons with spins of $J_z = \pm 1$ do couple with the optical modes, and are therefore known as the bright states [251]. There are three main mechanisms for spin relaxation in semiconductors: the Elliott-Yafet mechanism [254, 255] and the Dyakonov-Perel mechanism [256] arising from the spin-orbit coupling, which result in the transition between bright and dark states; as well as the Bir-Aronov-Pikus mechanism [257], which arises from the spin-flip interaction and leads to the transition between the bright states $J_z = +1$ and $J_z = -1$ [251]. It was discovered by Maialle et al. that in a two-dimensional excitonic system, the spin relaxation is dominated by Bir-Aronov-Pikus mechanism, which makes the dark states negligible [258, 251]. Exciton polaritons in a quantum microcavity can therefore be described using a two-component pseudospin.

Right and left circularly-polarized light excites excitons with $J_z = 1$ and $J_z = -1$, respectively, while linearly-polarized light excites equal amounts of excitons with spins of $J_z = 1$ and $J_z = -1$ [259]. Since polaritons have a finite lifetime, they eventually decay releasing photons which escape the microcavity. The polarizations of the emitted photons contain complete information of the polariton pseudospins, which can be experimentally measured using polarimetry techniques. We can therefore define the components of the exciton-polariton pseudospin in terms of Stokes vector of light as

$$\begin{aligned} S_x &= \frac{|\psi^H|^2 - |\psi^V|^2}{|\psi^H|^2 + |\psi^V|^2} \\ S_y &= \frac{|\psi^D|^2 - |\psi^A|^2}{|\psi^D|^2 + |\psi^A|^2} \\ S_z &= \frac{|\psi^+|^2 - |\psi^-|^2}{|\psi^+|^2 + |\psi^-|^2}. \end{aligned} \tag{1.82}$$

where here, H, V denote the horizontal and vertical polarizations, D, A denote the diagonal and anti-diagonal polarizations and $+, -$ denote the right and left circular polarizations [189, 191, 260]. In the next Section, I will discuss theoretical models of exciton polaritons including pseudospin effects. I will also show how the spinor model leads to optical spin Hall effects and a topological insulating phase.

1.4.3 Exciton Polaritons under Artificial Gauge Field

Anisotropy in optical cavities can result in synthetic gauge fields for photons and polaritons [261]. In a birefringent material, the lower polaritonic branches exhibit constant polarization splitting between the linearly-polarized modes arising from the cavity anisotropy. On the other hand, when an external magnetic field is applied to the sample, there emerges Zeeman splitting on the excitonic energy, which splits the spin-up and spin-down exciton polaritons, which emit circularly-polarized modes. Furthermore, the polaritonic branches also exhibit k-dependent splitting between the transverse-electric (TE) and transverse-magnetic (TM) modes, which scales as $\sim k^2$ at small k and effectively results in photonic spin-orbit coupling [251, 262, 263, 261]. In Ref. [261], the authors proposed a model of the lower polariton branch in the basis of the circular polarizations. This model combines the polarization splitting arising from the TE-TM splitting β, the cavity anisotropy α and the Zeeman splitting Δ into a non-Abelian gauge field $\overrightarrow{\mathbf{G}}$, which can also be interpreted as a k-dependent effective magnetic field acting on the polariton pseudospins described by the two-by-two Pauli matrices

$$\begin{aligned} H &= \left(E_0 + \frac{\hbar^2 k^2}{2m}\right)\mathbf{I} + \overrightarrow{\mathbf{G}} \cdot \overrightarrow{\boldsymbol{\sigma}} \\ \overrightarrow{\mathbf{G}} &= \left(\alpha + \beta(k_x^2 - k_y^2), 2\beta k_x k_y, \Delta\right) \end{aligned} \tag{1.83}$$

with mean polariton energy E_0 and effective lower polariton mass m. This model has the energy band structure

$$\begin{aligned} E_\pm &= \left(E_0 + \frac{\hbar^2 k^2}{2m}\right) \pm \sqrt{(\alpha + \beta(k_x^2 - k_y^2))^2 + 4\beta^2 k_x^2 k_y^2 + \Delta^2} \\ &= \left(E_0 + \frac{\hbar^2 k^2}{2m}\right) \pm E. \end{aligned} \tag{1.84}$$

When the Zeeman splitting is zero, the exciton-polariton band structure has two spectral degeneracy in the forms of Dirac points at

$$\mathbf{k}^{DP} = \left(0, \pm\sqrt{\frac{\alpha}{\beta}}\right) \tag{1.85}$$

which are diabolical points that lead to conical diffraction of circularly-polarized Gaussian wavepacket in their vicinities [see Fig. 1.8(a)] [261, 124, 123]. When a non-zero Zeeman splitting is applied, the Dirac points are lifted and a gap is opened [see Fig. 1.8(b)]. Due to the TE-TM splitting, the exciton polaritons have also been predicted to exhibit optical spin Hall effect in Ref. [229], which was later experimentally demonstrated in Ref. [230]. Moreover, when both the TE-TM splitting and the Zeeman splitting are present, the polaritonic bands exhibit a non-zero Berry curvature [189]

$$\Omega_\pm^z = \mp\frac{2k^2\beta^2\Delta}{E^3} \tag{1.86}$$

and non-zero Chern number [189, 191, 219, 220, 231, 234]. Exciton-polariton topological insulator has been experimentally demonstrated in Ref. [232] using a lattice potential.

More recently, exciton polaritons have also been shown to exhibit non-trivial quantum

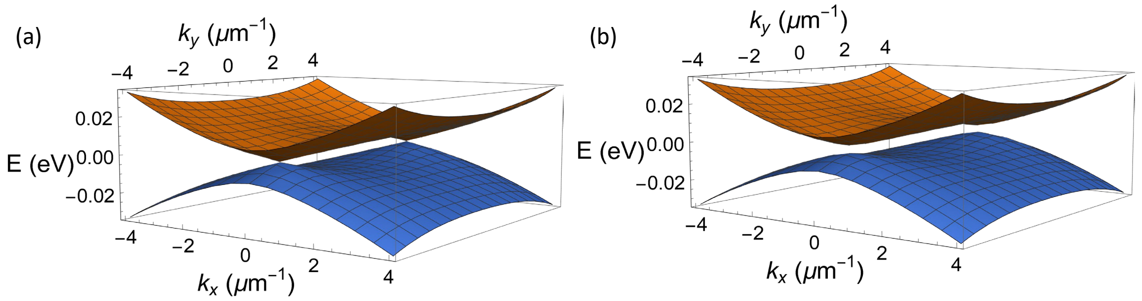

Figure 1.8: Mean-subtracted eigenenergy of the Hamiltonian in Eq. (1.83) in the (a) gapless and (b) gapped phase. Here, the orange surfaces correspond to $+E$ while the blue surfaces correspond to $-E$ from Eq. (1.84).

geometry [see Section 1.3] and the components of its QMT take the form [180, 189, 191]

$$\begin{aligned} g_{\pm,xx} =& \frac{\beta^2\left[(\alpha-\beta k^2)^2k_y^2+\Delta^2k^2\right]}{E^4} \\ g_{\pm,xy} =& g_{\pm,yx} = \frac{\beta^2 k_x k_y\left(\alpha^2-\beta^2k^4\right)}{E^4} \\ g_{\pm,yy} =& \frac{\beta^2\left[(\alpha+\beta k^2)^2k_x^2+\Delta^2k^2\right]}{E^4}. \end{aligned} \tag{1.87}$$

Although in this Thesis I mainly focus on the Zeeman splitting arising from the out-of-plane field, it has been shown in Ref. [233] that the optical activity also manifests as an effective field in the out-of-plane z-direction and can lift the degenercay at the Dirac point and open a topologically non-trivial gap.

More recently, the exciton polaritons have been proposed as a platform to study non-Hermitian physics [14, 15, 218]. Exciton polaritons are intrinsically non-Hermitian due to the presence of photonic and excitonic losses and gain from the pump. As discussed in Sec. 1.4.1 above, the effective potentials introduced by a pump into the exciton-polariton system are intrinsically complex-valued. As mentioned previously, the exciton polaritons decay and release photon emission. These photons contain complete information about the polaritons in the microcavity, and by measuring them, one can have direct access to the distribution of the exciton polaritons in both real and momentum space, their pseudospin (polarization) distribution as well as their complex-valued eigenenergy [15, 218]. Exciton polaritons thus present an experimentally accessible platform to study non-Hermitian physics. Moreover, unlike many systems where the exceptional points live in parameter space, where one needs to tune the parameters to encircle or reach the exceptional point [15, 264] some exciton-polariton systems [218, 265] exhibit exceptional points and Fermi arcs in momentum space. In the latter case, we can investigate the effects of these non-Hermitian degeneracies on the dynamics of the system, which is the main goal of my research. In the next Section, I will present the main models which I use to investigate the non-Hermitian physics of exciton polaritons.

1.5 Non-Hermitian Exciton-Polariton Models

Throughout this Thesis, I consider three non-Hermitian effective models describing the lower polariton branches in momentum space, and my work focuses on the momentum-dependence of the Hamiltonian. One of them is a non-Hermitian generalisation of the Dirac model in Eq. 1.17 and the other two are generalisations of the exciton-polariton model presented in Ref. [261], with each of them an experimentally realisable exciton-polariton system.

In this Thesis, I consider two-band non-Hermitian models described by the following Hamiltonians:

$$\begin{aligned}\hat{H}(\mathbf{k}) &= H_0(\mathbf{k})\mathbf{I} + \overrightarrow{\mathbf{H}}(\mathbf{k}) \cdot \overrightarrow{\boldsymbol{\sigma}} \\ \overrightarrow{\mathbf{H}}(\mathbf{k}) &= [H_x(\mathbf{k}), H_y(\mathbf{k}), H_z(\mathbf{k})] \\ \overrightarrow{\boldsymbol{\sigma}} &= [\sigma_x, \sigma_y, \sigma_z]\end{aligned} \tag{1.88}$$

where σ_i are the 2×2 Pauli matrices, and $\overrightarrow{\mathbf{H}}(\mathbf{k})$ describes the complex-valued effective magnetic field acting on the exciton-polariton pseudospins.

I also split the Hamiltonian into the Hermitian part $\hat{G}$ and the non-Hermitian part $\hat{\Gamma}$ such that

$$\hat{H}(\mathbf{k}) = \hat{G}(\mathbf{k}) + i\hat{\Gamma}(\mathbf{k}),$$

and separate the Hermitian and anti-Hermitian parts of the Hamiltonian as

$$\begin{aligned}\hat{G}(\mathbf{k}) &= G_0\mathbf{I} + \overrightarrow{\mathbf{G}}(\mathbf{k}) \cdot \overrightarrow{\boldsymbol{\sigma}} \\ \hat{\Gamma}(\mathbf{k}) &= \Gamma_0(\mathbf{k})\mathbf{I} + \overrightarrow{\mathbf{\Gamma}}(\mathbf{k}) \cdot \overrightarrow{\boldsymbol{\sigma}} \\ \overrightarrow{\mathbf{G}}(\mathbf{k}) &= [G_x(\mathbf{k}), G_y(\mathbf{k}), G_z(\mathbf{k})] \\ \overrightarrow{\mathbf{\Gamma}}(\mathbf{k}) &= [\Gamma_x(\mathbf{k}), \Gamma_y(\mathbf{k}), \Gamma_z(\mathbf{k})].\end{aligned} \tag{1.89}$$

The eigenenergies of this model take the form of $E_\pm = H_0 \pm E$ with $E = \sqrt{H_x^2 + H_y^2 + H_z^2}$, which is also the mean-subtracted eigenenergy. In this form, both $\hat{G}, \hat{\Gamma}$ are Hermitian operators and G_i, Γ_i for $i = 0, 1, 2, 3$ are real valued.

This general non-Hermitian Hamiltonian also has the left and right eigenstates in the form

$$\begin{aligned}|\psi_\pm^R\rangle &\propto \begin{pmatrix} H_z \pm E \\ H_+ \end{pmatrix} \\ \langle\psi_\pm^L| &\propto \begin{pmatrix} H_z \pm E, & H_- \end{pmatrix}\end{aligned} \tag{1.90}$$

where the factor varies on how I want to normalize the eigenstates, for instance as $\langle\psi_\pm^R|\psi_\pm^R\rangle = 1$, $\langle\psi_\pm^L|\psi_\pm^R\rangle = 1$ or $\langle\psi_\pm^L|\psi_\pm^L\rangle = 1$. Here, I also denote $H_\pm = H_x \pm iH_y$ for simplicity.

1.5.1 Non-Hermitian Dirac Model

Recall that in Section 1.2.2, we have seen that the low-energy physics of the Haldane model near the **K** and **K**′-points can be effectively described by the Dirac Hamlitonian [see Eq. (1.17)]

$$\hat{H}(\mathbf{k}) = \hbar v_F k_x \sigma_x + \hbar v_F k_y \sigma_y + m\sigma_z. \tag{1.91}$$

This Dirac model has a degeneracy called the Dirac point at $\mathbf{k} = 0$ when $m = 0$. If $m \neq 0$, the degeneracy would be lifted and a topologically non-trivial gap would be opened [see Fig. 1.9(a,b)].

The first simple 2×2 non-Hermitian model I consider is a simple generalisation of this Dirac model described by the Hamiltonian [8, 202]:

$$H = k_x \sigma_x + (k_y - i\kappa)\sigma_y + \Delta\sigma_z, \tag{1.92}$$

where I set $\hbar v_F = 1$ for simplicity. This is a toy model which is easy to solve, but it exhibits complex-valued energy structure and degeneracies similar to those found in realistic non-Hermitian exciton-polariton systems. Therefore, it provides useful intuition to understand the non-Hermitian physics of the polaritons. Here, I denote the z-component of the effective field as Δ instead of m, so it would not be confused with the exciton-polariton mass. At $\Delta = 0$, the imaginary effective field κ splits the Dirac point at $\mathbf{k}_{DP} = (0, 0)$ into a pair of exceptional points at $\mathbf{k}_{EP} = (\pm|\kappa|, 0)$ [see Fig. 1.9(c-e)]. The exceptional points are connected by the bulk Fermi arc [16] where the real parts of energies are degenerate, $\mathrm{Re}[E] = 0$. This bulk Fermi arc is similar to the surface Fermi arc in Weyl semi-metal in the Hermitian system, however, it manifests in the bulk band instead of the surface band structures [113, 266, 118]. The exceptional points are also connected by the imaginary Fermi arcs where the imaginary parts of energies are degenerate $\mathrm{Im}[E] = 0$ [267]. In this model, the Fermi arcs stretch along the k_x-axis, where the bulk Fermi arc is at $|k_x| < |k_{EP,x}|$ and the imaginary Fermi arcs lie along $|k_x| > |k_{EP,x}|$. When there is a non-zero out-of-plane field Δ, it shrinks the bulk Fermi arcs, and pulls the exceptional points towards each other $\mathbf{k}_{EP} = (\pm\sqrt{\kappa^2 - \Delta^2}, 0)$. A strong enough $\Delta^* = \pm|\kappa|$ merges the two exceptional points into a hybrid point, which is a non-Hermitian spectral degeneracy that is defective (meaning that the Hamiltonian is no longer diagonalizable and the eigenstates coalesce), but has zero spectral winding [see Section 1.1.1 for more detail] [6], and $|\Delta| > |\Delta^*|$ would annihilate the degeneracy and open a gap in the real energies, while the imaginary energies remain gapless, and the imaginary Fermi arcs now extends to the entire k_x-axis [see Fig. 1.9(f-h)]. Realistic exciton-polariton systems can exhibit exceptional points and Fermi arcs arising from the cavity anisotropy, TE-TM splitting and polarization-dependent photonic losses [218, 265]. This simple model can be considered as a low energy effective model of these exciton-polariton systems near a single exceptional points pair, and has been previously used to study non-Hermitian Berry curvature [202] as well as non-Hermitian quantum metric tensor [8].

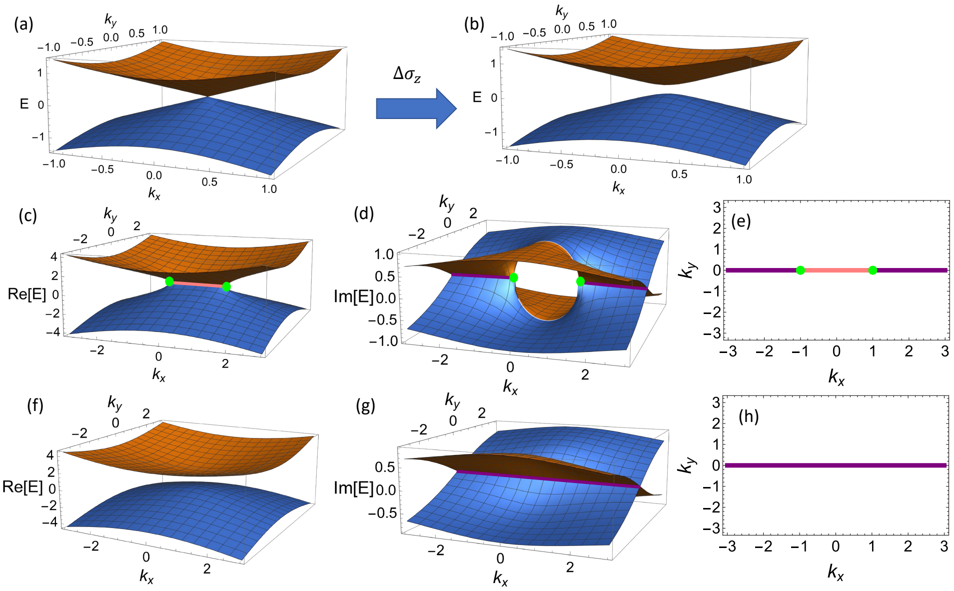

Figure 1.9: Band structure of the Dirac model in the (a) gapless and (b) gapped phases. Also showing the bands of the non-Hermitian Dirac model (1.92) in the (c,d) gapless and (f,g) gapped phases. Panels (e,h) show the exceptional points (green dots), bulk Fermi arcs (pink line) and imaginary Fermi arcs (purple lines) in momentum space in the gapless and gapped phases, respectively. The green dots and the pink and purple lines in (a,b,e) are added by hands.

1.5.2 Perovskite-Based Microcavity Exciton-Polariton Model

The second model I consider was developed to describe an exciton-polariton system in a perovskite-based microcavity experimentally investigated in Ref. [218]. The dispersion splitting arising from optical anisotropy plays a significant role in the effects described in this thesis. Perovskite materials exhibit stronger optical anisotropy in the magnitude of ~ 1 meV [218] compared to other materials, such as GaAs where the optical anisotropy is in the magnitude of $\sim 10\mu$eV [268]. Other materials can also be used to produce similar effects. This non-Hermitian model is very similar to the model in Eq. (1.83), and it includes the momentum-dependent mean polariton linewidth γ, as well as the polarization-dependent photonic losses a, b, which arise from the cavity anisotropy α and the TE-TM splitting β, respectively:

$$\begin{aligned} H &= \Big(E_0 + \frac{\hbar^2 k^2}{2m} - i\gamma(\mathbf{k})\Big)\mathbf{I} + (\overrightarrow{\mathbf{G}} + i\overrightarrow{\mathbf{\Gamma}}) \cdot \overrightarrow{\sigma} \\ \overrightarrow{\mathbf{G}} &= \Big(\alpha + \beta(k_x^2 - k_y^2), 2\beta k_x k_y, \Delta\Big) \\ \overrightarrow{\mathbf{\Gamma}} &= \Big(-a - b(k_x^2 - k_y^2), -2bk_x k_y, 0\Big). \end{aligned} \tag{1.93}$$

Since a, b represent the linewidth splitting, we can also denote $\tilde{\alpha} = \alpha - ia$ and $\tilde{\beta} = \beta - ib$, to simplify the notations for the later Chapters. The polarisation-dependent losses a, b are key to the effect which I will describe in later Chapters in this thesis. These two parameters arise from the fact that the reflectance of the Bragg reflector mirrors forming the microcavity dependents on wavelength (and hence energy) and polarisation. Therefore, the modes suffer different loss when the energy changes.

The polarization-dependent photonic losses split each Dirac point into a pair of exceptional points, which in polar coordinates are at $\mathbf{k}^{EP} = (k^{EP}, \phi^{EP})$

$$\begin{aligned} k^{EP} &= \sqrt{\left|\frac{\alpha - ia}{\beta - ib}\right|} \\ \phi^{EP} &= \pm\frac{\pi}{2} \pm \arg\left(\sqrt{\frac{\alpha - ia}{\beta - ib}}\right) \end{aligned} \tag{1.94}$$

where each ± is independent. Similarly to the non-Hermitian Dirac model (1.92), each pair of exceptional points is connected by the bulk Fermi arc, as well as the imaginary Fermi arcs [see Fig. 1.10]. Each exceptional point in a pair carries a non-zero, but opposite spectral winding [see Section 1.1.1] of $w = \pm 1/2$ around them [16], which has been experimentally measured in Ref. [218]. Similarly to the non-Hermitian Dirac model discussed earlier, the exceptional point pair can be merged into a hybrid point by a strong enough Zeeman splitting $|\Delta| = |\Delta^*|$ and lifted at $|\Delta| > |\Delta^*|$. For example, in a GaAs-based exciton-polariton system investigated in Ref. [191], which was described by the Hermitian case of the same effective model, the authors experimentally realised a Zeeman splitting at the magnitude of $2\Delta = 100.9 \pm 0.6\mu\text{eV}$. Here, the critical value Δ^* is $|\Delta^*| = |(b\alpha - a\beta)/\beta|$. Also similarly to the non-Hermitian Dirac model, when a gap is opened in the real parts of the energy, the imaginary part remains gapless.

1.5.3 Liquid-Crystal Based Exciton-Polariton Model

The third model I consider here was proposed in Ref. [265] to describe photonic modes in a tunable liquid-crystal-filled microcavity [234, 220].

$$\begin{aligned} H &= \left(E_0 + \frac{\hbar^2 k^2}{2m} - i\gamma_0\right)\mathbf{I} + (\overrightarrow{\mathbf{G}} + i\overrightarrow{\mathbf{\Gamma}}) \cdot \overrightarrow{\sigma} \\ \overrightarrow{\mathbf{G}} &= \left(\alpha - \beta(k_x^2 - k_y^2) - \beta' k^2, 2\beta k_x k_y, 0\right) \\ \overrightarrow{\mathbf{\Gamma}} &= (-\delta\Gamma, 0, 0). \end{aligned} \tag{1.95}$$

where β' arise from the difference between the TE-TM splittings of the two linearly polarized modes and $\delta\Gamma$ arises from the difference between the photonic losses of the two linearly polarized modes. Here, I switch the sign of β to follow the convention in Ref. [265]. At $\delta\Gamma = 0$, the exciton-polariton bands have two Dirac points if $\beta > \beta'$ and four Dirac points if $\beta < \beta'$, and non-zero photonic losses $\delta\Gamma$ split each Dirac point into a pair of exceptional points [265].

Although this model was originally developed to describe photonic modes instead of polaritons in Ref. [265], it is possible to grow a layer of active material (such as perovskite) when fabricating the sample which can then host the exciton polaritons in the liquid-

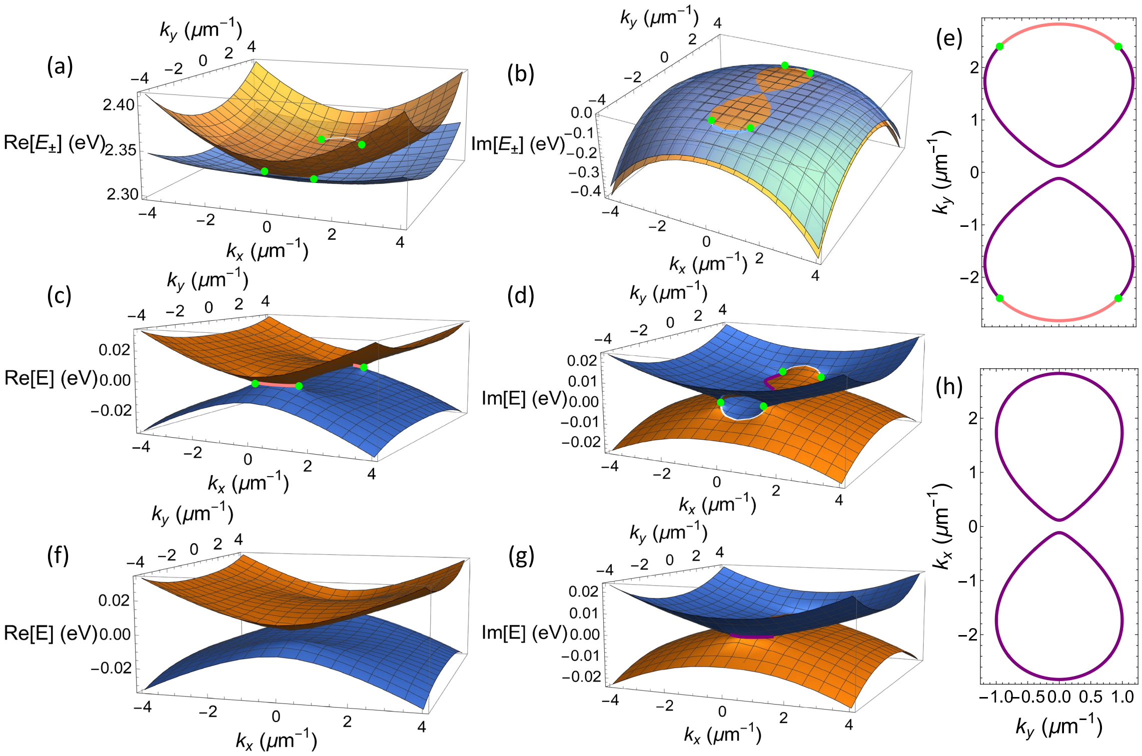

Figure 1.10: (a) Real and (b) imaginary parts of the band of the exciton-polariton model in Eq. (1.93). Also showing the real and imaginary parts of the mean-subtracted eigenenergies in the (c,d) gapless phase and (f,g) the gapped phase. (e,f) show the exceptional points (green dots) and the bulk (pink) and imaginary (purple) Fermi arcs in momentum space in the gapless and gapped phases, respectively. The green dots and the pink and purple lines in (a,b,c,d,f,g) are a guide to the eye.

crystal-filled microcavity. In this case, the exciton polaritons in the liquid-crystal-filled microcavity can be described by the Hamiltonian 1.95, but with different values of parameters. Furthermore, we can induce a Zeeman splitting $\Delta\sigma_z$ to the Hamiltonian in Eq. (1.95) by applying an external magnetic field. Similar to the previous model, at a large enough Zeeman splitting $|\Delta| = |\delta\Gamma|$, each pair of exceptional points are merged into a hybrid point, and $|\Delta| > |\delta\Gamma|$ would open a gap in the real energies. In Chapter 5 in this Thesis, I focus on the configuration with eight exceptional points (with $\beta' > \beta$), where the Fermi arcs and the exceptional points are located along the closed curve of

$$k(\phi) = \sqrt{\frac{\alpha}{\beta' + \beta\cos 2\phi}} \tag{1.96}$$

and the exceptional points are at

$$\phi^{EP} = \pm\arccos\left(\pm\sqrt{\frac{\gamma\beta + \beta'(\Delta^2 - \delta\Gamma^2) \pm \alpha\sqrt{\gamma\beta^2 + \beta'^2(\Delta^2 - \delta\Gamma^2)}}{2\beta\gamma}}\right) \tag{1.97}$$

where $\gamma = \alpha^2 - (\Delta^2 - \delta\Gamma^2)$ [see Fig. 1.11]. This model is more realistic than the non-

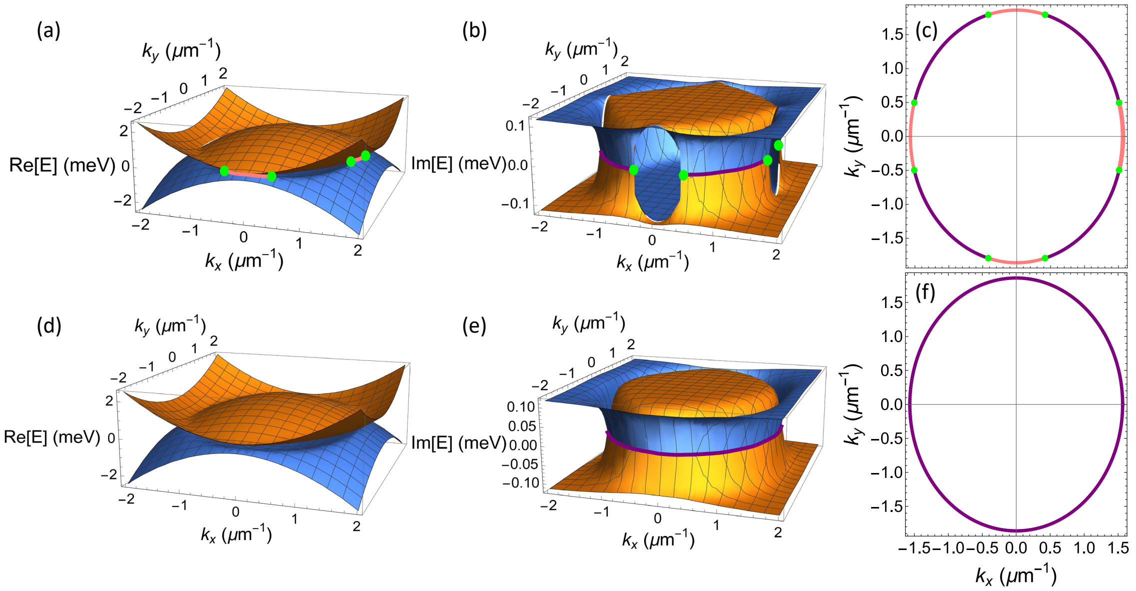

Figure 1.11: The real and imaginary parts of the liquid crystal-based exciton polaritons in the (a,b) gapless and (d,e) gapped phases. Also showing the EPs (green dots) and the bulk (pink) and imaginary (purple) Fermi arcs in momentum space in the (c) gapless and (d) gapped phases. The green dots and the pink and purple lines in (a,b,e) are a guide to the eye.

Hermitian Dirac model, but its Fermi arcs structures are still simpler than the perovskite-based exciton-polariton model (1.93). Therefore, it is easy enough to solve analytically, but still fully captures the physics of a realistic system.

The models presented here can also be used to describe purely photonic modes in optical cavities, but with different parameters. Therefore, the results presented in this thesis have applications in photonic systems as well.

The non-Hermitian models describing the perovskite-based polaritons (1.93) and liquid-crystal-based microcavity (1.95) are phenomelogical, but they are based on realistic assumptions and more importantly, they were both verified in experiments [218, 265]. The parameters in these two models have proper physical origins and most of them can be determined experimentally. In the following Chapters, I will use these three model to investigate non-Hermitian physics of exciton polaritons. The values of the parameters used are presented in Appendix A.

Chapter 2

Wavepacket Self-Acceleration

Disclaimer: This Chapter contains results adapted from my published work "Wave-packet dynamics in a non-Hermitian exciton-polariton system", *Phys. Rev. B* **108**, 115404 (2023).

2.1 Introduction

One major fact of the non-Hermitian Hamiltonian operator is the complex-valued eigenenergies. The imaginary part of the energy eigenvalues determines the growth or decay rate of the corresponding eigenstate and hence strongly affects the dynamics of the system, even in the absence of an external potential. For example, a recent study on a non-Hermitian Dirac model showed that a wavepacket can move in momentum space without an external force as a result of the growth and decay of its momentum components [8, 205]. The trajectories of the wavepackets under this self-acceleration are polarization-dependent and the centre-of-mass (COM) momenta for certain initial conditions follow the gradient of the imaginary part of the eigenenergy. Similar effects were also described in the context of a one-dimensional non-Hermitian lattice [269]. Non-trivial dynamical effects due to non-Hermiticity are therefore expected to arise in real systems with gain and loss.

In this Chapter, I investigate non-Hermitian wavepacket dynamics in a microcavity polariton system using a two-band model relevant to recent experiments [218] and focusing on observable effects. Apart from the previously predicted [8, 205] acceleration in the absence of an external force, I also find that for some initial conditions, the wavepackets tend to split into multiple components that propagate towards different directions. Moreover, these wavepackets tend to evolve into different eigenstates and propagate towards the maxima of the imaginary part of the corresponding eigenenergy. I further show that this non-unitary dynamics of the wavepacket COM is accurately captured by the non-Hermitian extension of the Ehrenfest theorem, where the non-Hermitian component of the Hamiltonian drives the effective force field. Finally, I investigate the interplay between the self-acceleration and the anomalous velocity arising from the Berry curvature and non-Hermitian anomalous Berry connection due to an external force [204].

I mainly focus my analysis on the non-Hermitian model based on the perovskite-based microcavity exciton-polariton system described by the Hamiltonian in Eq. (1.93), which has the band structure and imaginary Fermi arcs shown in Fig. 2.1(a-c). I also emphasise that, in my analysis, I expand the momentum-dependent mean polariton linewidth (see

Eq. (1.93)) to the fourth order in k as

$$\gamma(\mathbf{k}) \approx \gamma_0 + \gamma_2 k^2 + \gamma_4 k^4$$

to capture the non-monotonic behaviour observed in previous experiments [218]. The exciton-polariton linewidths are even functions of k, and the data from previous experiments in Ref. [218] show that at least the forth order in k is needed to capture the structure of the linewidth. As shown in Fig. 2.1(b) and highlighted in Fig. 2.1(d,e), $\operatorname{Im} E_+$ has two maxima lying on the k_y-axis, while $\operatorname{Im} E_-$ has two maxima on the k_x-axis. These points play an important role in the dynamics of the polariton wave packets as discussed in the next Section. I also present my analysis of two other similar models; the non-Hermitian Dirac model based on Eq. (1.92) and the non-Hermitian Chern insulator model from Ref. [270].

2.2 Wavepacket Dynamics

To understand the influence of the non-Hermiticity on the dynamics of exciton polaritons, inspired by previous works [8, 269], I investigate the dynamics of Gaussian wavepackets in the polariton system described by the model Hamiltonian Eq. (1.93). Since the Hamiltonian contains k-components only and no external potential, the time evolution of wavepackets in real and momentum spaces and the resulting pseudospin textures can be calculated exactly using the time-evolution operator

$$e^{-i\mathbf{H}t/\hbar} = e^{-iH_0 t/\hbar}\left(\mathbf{I}\cos\frac{Et}{\hbar} - i\frac{\overrightarrow{\mathbf{H}}}{E}\cdot\overrightarrow{\sigma}\sin\frac{Et}{\hbar}\right), \tag{2.1}$$

where $E = \sqrt{H_x^2 + H_y^2 + H_z^2}$ is the mean-subtracted eigenenergy, and this equation is valid anywhere in the momentum space except at the degeneracies.

The initial Gaussian wavepacket is a superposition of multiple $\mathbf{k}$-components of the pseudospin eigenstates whose individual contributions to the time evolution can be described by:

$$\begin{aligned} |\psi(\mathbf{k},t)\rangle &= e^{-i\mathbf{H}t/\hbar}|\psi(\mathbf{k},t=0)\rangle \\ |\psi^R_\pm(\mathbf{k},t)\rangle &= e^{-i\operatorname{Re}E_\pm(\mathbf{k})t}e^{\operatorname{Im}E_\pm(\mathbf{k})t}|\psi^R_\pm(\mathbf{k})\rangle, \end{aligned} \tag{2.2}$$

where the superscript R denotes the right-eigenstates (Eq. (1.90)). The variation in the imaginary part, as shown below, is responsible for some peculiar dynamical effects.

The COM position in real and momentum spaces is then calculated using the expectation values of k and x as [269]:

$$\begin{aligned} \langle\mathbf{k}(t)\rangle &= \frac{\int\langle\psi(\mathbf{k},t)|\mathbf{k}|\psi(\mathbf{k},t)\rangle d^2\mathbf{k}}{\int\langle\psi(\mathbf{k},t)|\psi(\mathbf{k},t)\rangle d^2\mathbf{k}} \\ \langle\mathbf{x}(t)\rangle &= \frac{\int\langle\psi(\mathbf{x},t)|\mathbf{x}|\psi(\mathbf{x},t)\rangle d^2\mathbf{x}}{\int\langle\psi(\mathbf{x},t)|\psi(\mathbf{x},t)\rangle d^2\mathbf{x}}. \end{aligned} \tag{2.3}$$

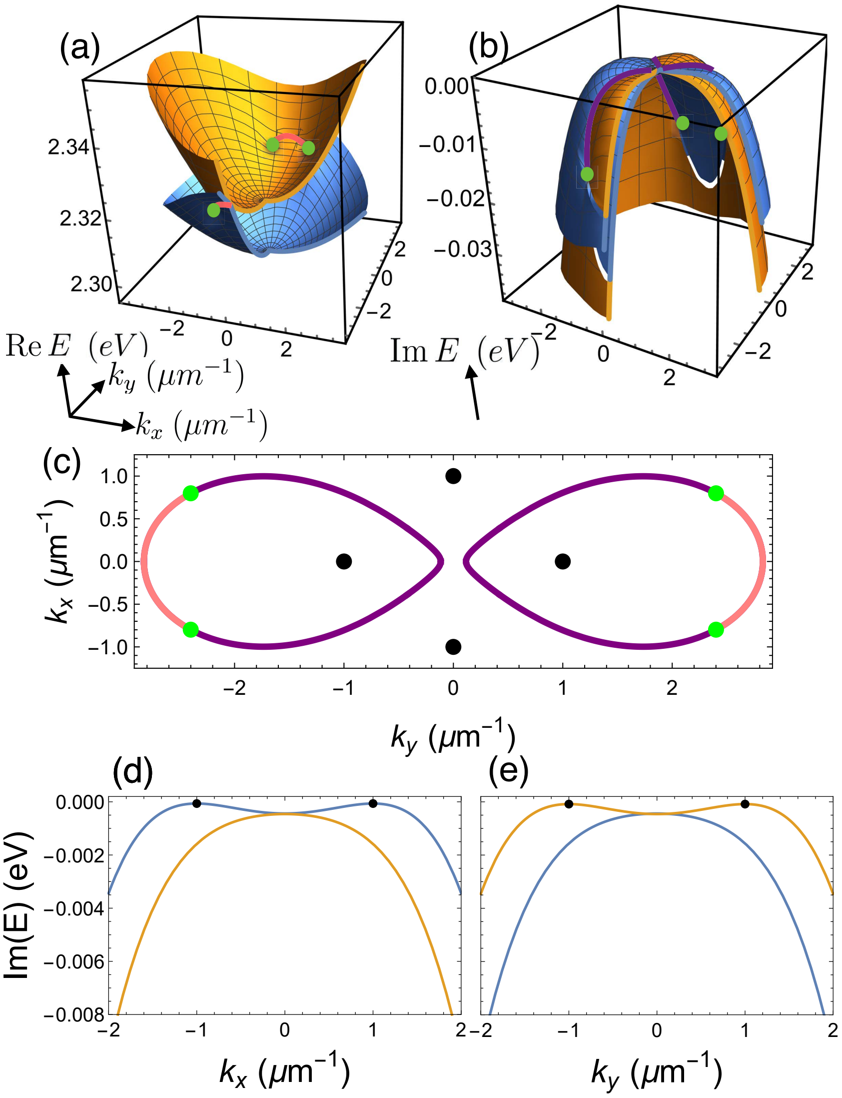

Figure 2.1: The (a) real and (b) imaginary parts of the polariton eigenenergies with cuts to show the degeneracies. Green dots mark the exceptional points, and the pink and purple arcs are guides to the eye indicating the bulk and the imaginary Fermi arcs, respectively. (c) The momentum-space structure of the bulk Fermi arcs, the imaginary Fermi arcs and the exceptional points shown in (a,b). (d,e) The imaginary parts of the eigenenergies $\operatorname{Im} E_+$ (orange line) and $\operatorname{Im} E_-$ (blue line) at $k_y = 0$ and $k_x = 0$, respectively. The black dots mark the maxima of $\operatorname{Im} E_\pm$. Reprinted with permission from [271] © American Physical Society.

This ensures that even though the time-evolution is non-unitary, I can still normalize the wavefunction at each point in time. These two quantities can be experimentally measured in polariton systems since experiments have access to the distribution of the polaritons in both real and momentum spaces.

2.2.1 Self-Acceleration and Splitting of Wavepackets

Example COM trajectories of the wavepackets in real and momentum spaces are presented in Fig. 2.2 which clearly shows the accelerating behaviour in the absence of an external field. The initial exciton-polariton wavepackets are Gaussians centred at $\mathbf{k} = (0, 3)\mu\text{m}^{-1}$ with widths of $2\mu\text{m}^{-1}$ in momentum space. The wavepakcets were initially placed in circularly (±), horizontally (H), vertically (V), diagonally (D) and anti-=diagonally (A) polarized modes, and the lines in Fig. 2.2 represent trajectories of the wavepackets with different initial polarizations. The same self-acceleration was previously theoretically predicted in other non-Hermitian systems [8, 269]. Furthermore, the trajectories are sensitive to the polarization of the initial wavepacket. However, regardless of the initial polarization, the self-accelerating wavepackets tend to move towards the same point in momentum space or towards the same direction in real space. This point in momentum space, which I denote $\mathbf{k}^*$, corresponds to the maximum of the imaginary part of the eigenenergy.

Intuitively, the acceleration arises from the inhomogeneous landscape of $\operatorname{Im} E_\pm$ in k space, in other words, a non-zero gradient of the imaginary part of eigenenergy $\nabla \operatorname{Im} E_\pm \neq 0$ [see Fig. 2.1(b,d,e)] [8]. Some k-components are decaying faster than others, causing the wavepacket to reshape and resulting in an effective displacement of the COM towards k-components with larger imaginary part (or lesser decay rates), until it reaches the value of k^*. However, the actual trajectory of the wavepacket does not follow $\nabla \operatorname{Im} E_\pm$, as I show here and in other two-band systems (see Sec. 2.2.3).

The acceleration of the wavepacket can be derived from the Ehrenfest theorem [17] where the dynamics of the expectation value of some operator $\hat{A}$ follows the equation of motion:

$$\frac{d}{dt}\langle \hat{A} \rangle = \langle \frac{d\hat{A}}{dt} \rangle + \frac{i}{\hbar}\langle [\hat{H}, \hat{A}] \rangle. \tag{2.4}$$

In Hermitian systems, the wavepacket will accelerate when the Hamiltonian is either time-dependent or does not commute with the momentum operator, e.g. when H has a spatial dependence. The Hamiltonian defined by Eq. (1.93) satisfies neither of these conditions. However, extending Ehrenfest theorem to non-Hermitian systems [272, 273] leads to the following equation of motion:

$$\frac{d}{dt}\langle \hat{A} \rangle = \langle \frac{d\hat{A}}{dt} \rangle + \frac{i}{\hbar}\langle \hat{H}^\dagger \hat{A} - \hat{A}\hat{H} \rangle - \frac{i}{\hbar}\langle \hat{A} \rangle \langle \hat{H}^\dagger - \hat{H} \rangle, \tag{2.5}$$

which describes the dynamics of the centre-of-mass momentum as:

$$\frac{d}{dt}\langle \mathbf{k} \rangle = \frac{2}{\hbar}\langle \mathbf{k}\hat{\Gamma} \rangle - \frac{2}{\hbar}\langle \mathbf{k} \rangle \langle \hat{\Gamma} \rangle. \tag{2.6}$$

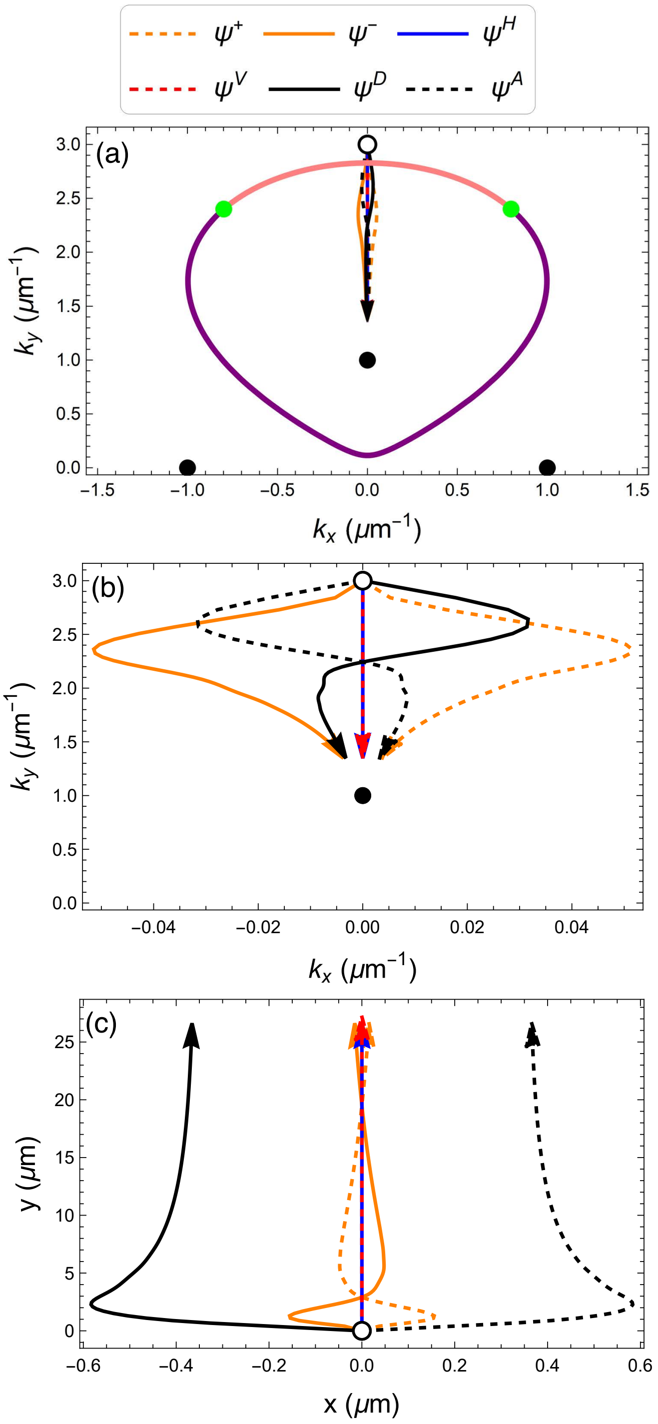

Figure 2.2: The polarization-dependent trajectories of the COM of the polariton wavepacket in (a,b) the momentum space and (c) in the real space, where (b) is the zoom-in of (a). Different colours represent different initial waveapckets, which are initially horizontally (ψ^H), vertically(ψ^V), diagonally (ψ^D), anti-diagonally (ψ^A) and circularly ($\psi^{\pm}$) polarized. Note that the trajectories of the horizontally polarized and the vertically-polarized modes overlap. The open dots denote the initial wavepacket centre of mass in both momentum and real space and the black dots denote the maxima of Im $E_{\pm}$ in momentum space. Reprinted with permission from [271] © American Physical Society.

Here, $\hat{\Gamma}$ is the anti-Hermitian component of the Hamiltonian, which results in extra terms that describe an acceleration of the wavepackets analogous to the effect of an external force. The effect is similar to an electromagnetic field applied to electronic wavepackets in a solid state system [100, 178, 179]. The extended Ehrenfest theorem clearly shows that the observed self-acceleration is due to the non-Hermitian terms.

If the initial polarization of the wavepacket is the right eigenstate $|\psi_{\pm}^{R}\rangle$, Eq. (2.6) can be further simplified as:

$$\frac{d}{dt}\langle \mathbf{k} \rangle = \frac{2}{\hbar}\langle \mathbf{k} \operatorname{Im} E_{\pm}\rangle - \frac{2}{\hbar}\langle \mathbf{k}\rangle\langle \operatorname{Im} E_{\pm}\rangle. \tag{2.7}$$

This expression highlights that the self-acceleration results from the imaginary parts of the eigenenergies. Moreover, I note that when $\operatorname{Im} E_{\pm}$ are constants, the two terms in Eq. (2.7) will cancel out. Hence, a non-zero gradient of $\operatorname{Im} E_{\pm}$ is necessary for the self-acceleration.

Note that the self-acceleration arising from Eq. (2.6) also depends on the current state of the system. Therefore, the dynamics of $\langle \mathbf{k} \rangle$ depends on the COM momentum, width, and polarization of the wavepacket, as well as time. This explains the previous findings that wavepackets with larger widths in momentum space show larger accelerations [8] and the polarization-dependent trajectories in Fig. 2.2 (see also Ref. [8]).

Although Eq. 2.6 describes complicated dynamics, its r.h.s. defines an effective k-dependent force field corresponding to the self-acceleration of an initial wavepacket. Two examples of the initial force fields, denoted as $d_t\langle \mathbf{k} \rangle$, are presented in Fig. 2.3(a,b), where the fields are calculated for a fixed-width Gaussian wavepacket centered at $\mathbf{k}$ with initial horizontal (H) or vertical (V) polarizations, respectively. The H-polarized wavepackets tend to accelerate towards two of $\mathbf{k}^*$ at $\mathbf{k} = (0, \pm 1)$ μm^{-1} [see Fig. 2.3(a)], while the vertically-polarized ones tend towards the other $\mathbf{k} = (\pm 1, 0)$ μm^{-1} [see Fig. 2.3(b)]. This reflects the results presented in Fig. 2.2 that the magnitude of the acceleration is minimised around $\mathbf{k}^*$.

The force field also changes with time as the momentum distribution and polarization evolve. An example is presented in Fig. 2.3(c-f) for the diagonally (D) polarized initial wavepacket in Fig. 2.2. The acceleration of the wavepacket oscillates and decays to zero as the wavepacket propagates towards $\mathbf{k}^* = (0, 1)$ μm^{-1}. The agreement between the acceleration calculated from the direct simulation (dots) and from Eq. (2.6) (line), clearly shows that the non-Hermitian extension of the Ehrenfest theorem accurately captures the COM dynamics, and therefore provides a semi-classical description of the wavepacket dynamics.

Surprisingly, when the wavepacket is initialized on the imaginary Fermi arc, it splits into two components that propagate away from each other as seen in Fig. 2.4(a-c). Furthermore, when the wavepacket is initialized at the origin, $\mathbf{k} = 0$, while overlapping with the two imaginary Fermi arcs, it splits into four components that accelerate away from each other along the $\pm k_x$ and $\pm k_y$ directions [see Fig. 2.4(d-f)].

The splitting of the wavepackets is due to the different imaginary parts (or decay rates) of the two eigenstates. It is natural for the wavepacket to evolve with time towards an eigenstate with the larger growth rate (or the smaller decay rate). In my model,

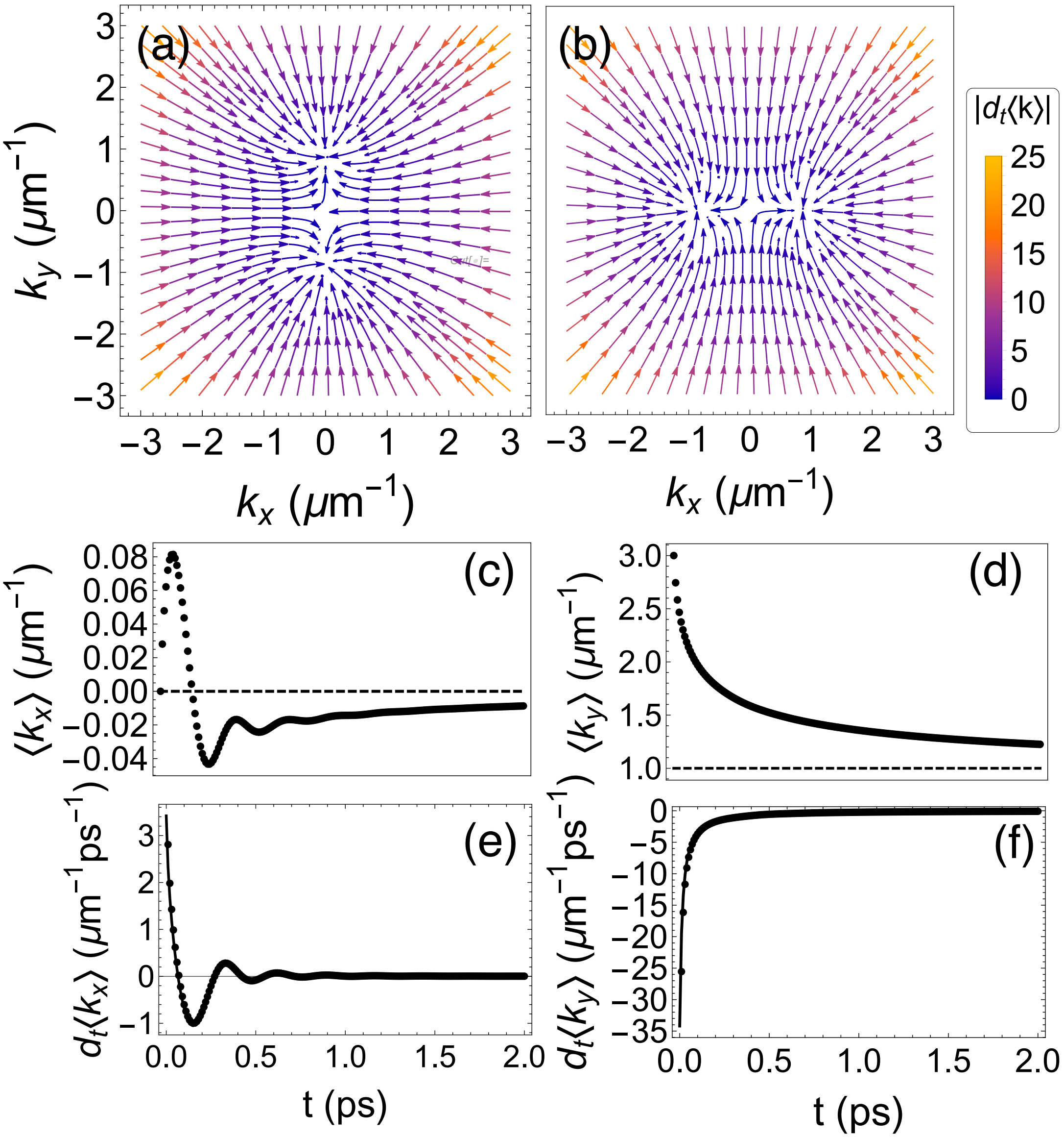

Figure 2.3: The time-derivative of the COM momenta $d_t\langle\mathbf{k}\rangle$ of (a) horizontally-polarized and (b) vertically-polarized wavepackets with different initial COM momenta $\mathbf{k}_0$ at $t = 0$ ps, respectively. (c,d) show the COM momenta of an initially diagonally-polarized wavepacket initially centred at $\mathbf{k}_0 = (0, 3)$, while the dotted lines denote $\mathbf{k}^*$. (e,f) show $d_t\langle\mathbf{k}\rangle$ of the same wavepacket. The black lines are $d_t\langle\mathbf{k}\rangle$ calculated from Eq. (2.6), which fully agree with the numerical results (black dots). Reprinted with permission from [271] © American Physical Society.

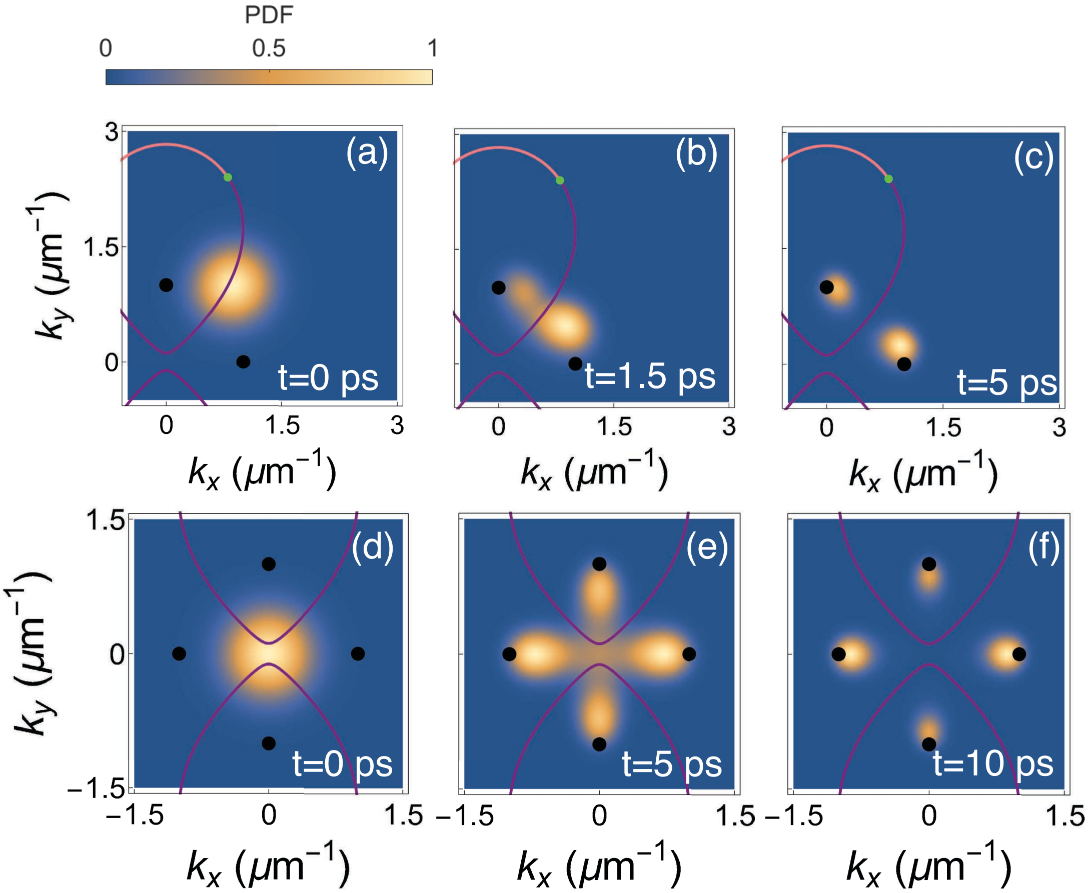

Figure 2.4: Splitting of the exciton-polariton wavepacket when initialized (a-c) on the imaginary Fermi arc, and (d-f) at the origin. The black dots denote k^*. The plots and the colorbar represent the evolution of the normalized probability density function (PDF). Note that this is not equal to the wavepacket amplitude $|\psi|^2$, which decreases over time due to the continuous decay. Reprinted with permission from [271] © American Physical Society.

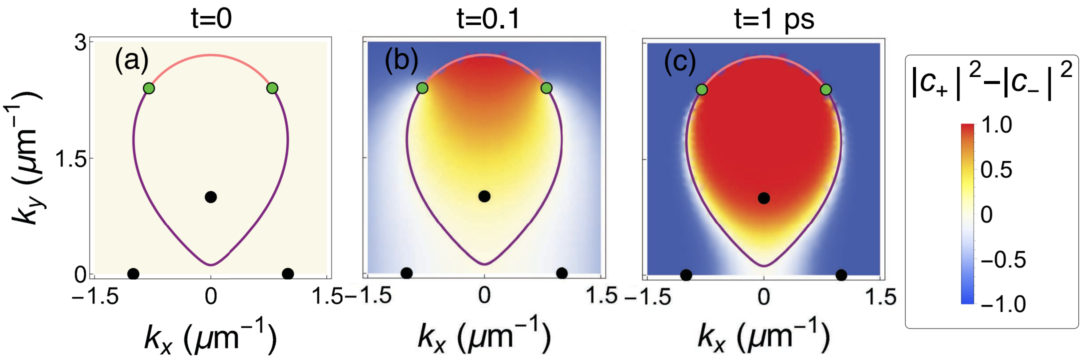

Figure 2.5: (a-c) Evolution of the wavepacket initially prepared as an equal superposition of the two right eigenstates $|\psi\rangle = c_+|\psi_+^R\rangle + c_-|\psi_-^R\rangle$. Shown is $(|c_+|^2 - |c_-|^2)/(|c_+|^2 + |c_-|^2)$. The green dots denote the exceptional points and the black dots denote $\mathbf{k}^*$. Reprinted with permission from [271] © American Physical Society.

$\operatorname{Im} E_+(\mathbf{k})$ is larger inside the region bounded by the Fermi arcs, while $\operatorname{Im} E_-(\mathbf{k})$ is larger outside. Therefore, the components of the wavepackets bounded by the Fermi arcs will evolve towards the upper eigenstate $|\psi_+^R(\mathbf{k})\rangle$, while those outside the region will evolve towards the lower eigenstate $|\psi_-^R(\mathbf{k})\rangle$. Hence, the wavepacket splits as shown in Fig. 2.4.

Therefore, when the system is in a superposition of the two right eigenstates $|\psi\rangle = c_+|\psi_+^R\rangle + c_-|\psi_-^R\rangle$, the coefficients can be determined using the bi-orthogonality condition as

$$c_\pm = \langle\psi_\pm^L|\psi\rangle.$$

By taking the normalized modulus squared $|c_\pm|^2/(|c_+|^2 + |c_-|^2)$, I was able to calculate the weight of each eigenstate in the wavepacket.

This analysis is supported by the time evolution of the normalized components of the upper and lower eigenstates shown in Fig. 2.5, corresponding to the case presented in Fig. 2.4(a-c). Since in this case, there is no external force, and the Hamiltonian has only momentum dependence. The time evolution operator can be calculated exactly in Eq. (2.1). One component quickly becomes dominant such that the components inside (outside) the region bounded by the Fermi arcs belong to the upper (lower) eigenstate. The situation is the same for the case presented in Fig. 2.4(d-f). Note that since the difference in the imaginary parts of the two eigenenergies, $\operatorname{Im}(\Delta E)$, is larger for large k [see Fig. 2.1], the components of the wavepackets with large k will evolve into the two eigenstates faster than the components near $\mathbf{k} = 0$.

Importantly, whenever the wavepackets split, the extended Ehrestfest theorem fails to capture their motion as the COM momenta will no longer correspond to the peak of the wavepackets. Here, despite the COM momenta being still described by Eq. (2.6), they can no longer be used to describe the wavepckets semi-classically in analogy to point particles.

2.2.2 Directional Propagation of Wavepackets

After the wavepacket evolves into the eigenstates with the larger $\operatorname{Im} E$, its COM will then propagate towards the maxima of the corresponding $\operatorname{Im} E$ in momentum space, as shown in Fig. 2.4(c,f). In real space, the wavepackets will asymptotically exhibit directional transport with a group velocity corresponding to the $(1/\hbar)\nabla_{\mathbf{k}} \operatorname{Re} E$ at $\mathbf{k}^*$ [269].

In the perovskite exciton-polariton model (1.93), $\operatorname{Im} E_+$ has two maxima at $(0, \pm k_+^*)$ inside the region bounded by the Fermi arcs, while $\operatorname{Im} E_-$ has two maxima at $(\pm k_-^*, 0)$ outside this region [see Fig. 2.1(c)]. Hence, wavepackets inside the region bounded by the Fermi arcs will asymptotically reach the points $\mathbf{k}^* = (0, \pm k_+^*)$ while those outside this region reach $\mathbf{k}^* = (\pm k_-^*, 0)$. Note that for $\Delta_z = 0$, we have $k_\pm^* = \sqrt{(\gamma_2 + b)/2\gamma_4}$

In real space, the wavepackets asymptotically reach their corresponding non-vanishing group velocities. The wavepackets inside the Fermi arcs will have $\langle \mathbf{v}_+ \rangle = (0, \pm v^*)$, while those outside will have $\langle \mathbf{v}_- \rangle = (\pm v_-^*, 0)$, where (for $\Delta_z = 0$)

$$v_\pm^* = \left(\frac{\hbar}{2m} - \frac{\beta}{\hbar}\right)\sqrt{\frac{2(\gamma_2 + b)}{\gamma_4}}. \tag{2.8}$$

Note that these asymptotic group velocities of the wavepackets only depend on the mean linewidth parameters $\gamma_{2,4}$, and the spin-orbit coupling parameters β and b. The anisotropy, however, determines the direction.

In the limit of a tightly focused wavepacket in real space, hence covering multiple $\mathbf{k}^*$ in momentum space, the wavepacket will split into four parts with each part funneling to the vicinity of $\mathbf{k}^*$ that it covered, as shown in Fig. 2.6(a-c). In real space, the wavepacket splits and spreads over time, eventually evolving into four broad wavepackets in the two eigenstates. Each of the smaller wavepackets exhibits directional transport with the corresponding non-vanishing asymptotic group velocities $\langle \mathbf{v}_\pm \rangle$ [see Fig. 2.6(a-f)].

In the presence of Zeeman splitting, i.e., $\Delta_z \neq 0$, the $\mathbf{k}^*$ points can be found numerically by solving $\partial_{\mathbf{k}} \operatorname{Im}[H_0 \pm E] = 0$, which yields the local minima at $\mathbf{k} = 0$ and the local maxima at $\mathbf{k}^*$. Increasing Δ_z will move them towards $\mathbf{k} = 0$ [see Fig. 2.6(g,h)]. Since the $\mathbf{k}^*$ points stay on the k_x and k_y axes, Δ_z will only change the magnitude of the final group velocities, but not the directions. The final group velocities depend on Δ_z non-monotonically, as seen in Fig. 2.6(i,j).

Note that when the system is isotropic, both α and a vanish and the exceptional points will move to the origin and merge into a single Hermitian-like degeneracy with two distinct eigenstates. In this case, the four maxima at $\mathbf{k}^*$ will join to form a ring around the origin with radius $k = \sqrt{(\gamma_2 + b)/2\gamma_4}$. Hence, the wavepacket will propagate and evolve towards this ring.

It is worth mentioning that the above results are derived under the assumption that the polariton wavepacket is initialized as a superposition of the two eigenstates, $|\psi\rangle = c_+|\psi_+^R\rangle + c_-|\psi_-^R\rangle$, and has nonzero $|c_\pm|$ at all of $\mathbf{k}^*$. In contrast, if the initial state is in one of the eigenstate $|\psi_\pm^R\rangle$, the wavepacket will only propagate towards the corresponding $\max(\operatorname{Im} E_\pm)$. Furthermore, if the components of the eigenstate $|c_\pm|^2$ in the initial state is zero at the corresponding $\max(\operatorname{Im} E_\pm)$, the wavepackets will not asymptotically funnel to $\max(\operatorname{Im} E_\pm)$

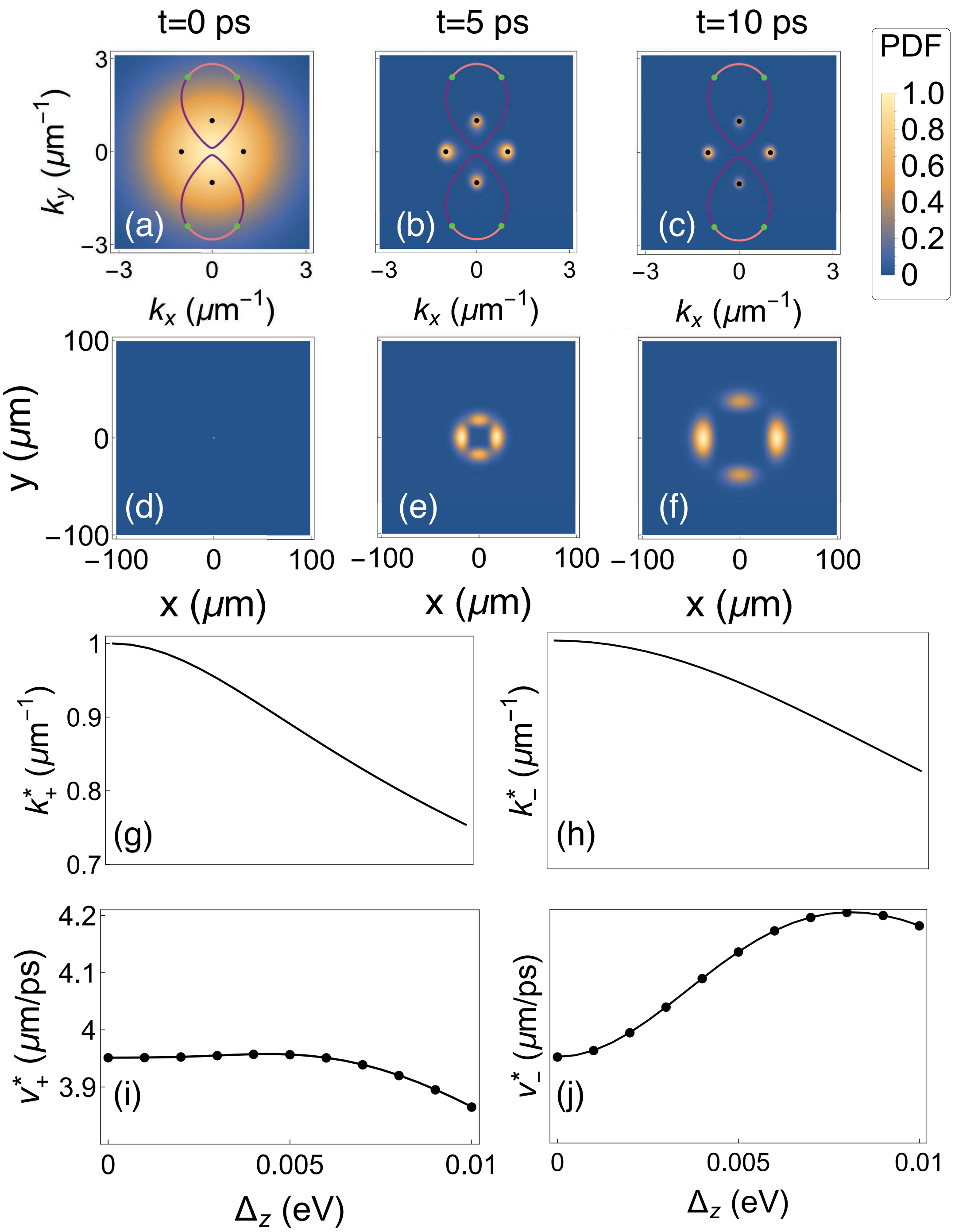

Figure 2.6: (a-c) Momentum space, and (d-f) real space time evolution of a spatially tightly focused initial wavepacket. (g,h) Coordinates of the $\mathbf{k}^*$ points as a function of Zeeman splitting Δ_z where $\mathbf{k}^* = (0, \pm k_+^*), (\pm k_-^*, 0)$. (i,j) Asymptotic group velocities where $\langle \mathbf{v}_+ \rangle = (0, \pm v_+^*)$ and $\langle \mathbf{v}_- \rangle = (\pm v_-^*, 0)$. The black lines in (i,j) represent the group velocities $\mathbf{v} = (1/\hbar)\nabla_{\mathbf{k}} \operatorname{Re} E_\pm$ calculated from $\mathbf{k}^*$ in (g,h), which show excellent agreement with the results from numerical simulation of wavepacket dynamics (black dots). In the numerical simulation, I calculate the COM position of the wavepacket in time, then compute the asymptotic group velocity. Reprinted with permission from [271] © American Physical Society.

For example, when $\Delta_z = 0$, the upper eigenstate at the points $\mathbf{k}^* = (0, \pm k_+^*)$ inside the region bounded by the Fermi arcs is H-polarized. Therefore, if the initial state is V-polarized and has no H component, the polaritons at $\mathbf{k}^* = (0, \pm k_+^*)$ cannot evolve into $|\psi_+^R\rangle$, as shown in Fig. 2.7(a-c). Consequently, the wavepacket will never funnel to the corresponding $\mathbf{k}^*$ points [see Fig. 2.7(d-f)]. Instead, the wavepacket will funnel to the other extrema at $\mathbf{k}^* = (\pm k_-^*, 0)$ and exhibit directional transport in real space at the constant velocities $\langle \mathbf{v}_- \rangle$. This also explains why the extended Ehrenfest theorem predicts $d_t\langle \mathbf{k} \rangle \approx 0$ only at $\mathbf{k}^* = (\pm k_-^*, 0)$ [or $\mathbf{k}^* = (0, \pm k_+^*)$] for the V-polarized [or H-polarized] wavepackets in Fig. 2.3(a,b).

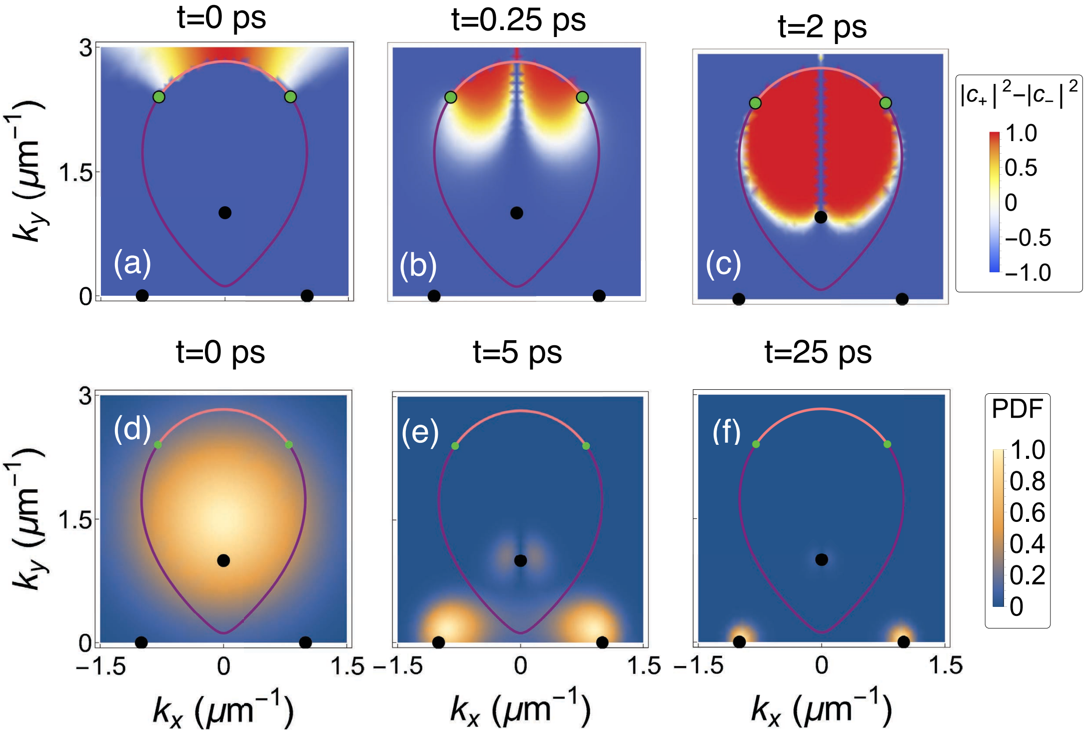

Figure 2.7: (a-c) Time evolution of $(|c_+|^2 - |c_-|^2)/(|c_+|^2 + |c_-|^2)$ when the initial wavepacket is vertically-polarized. (d-f) Shows the time evolution of the wavepacket with black dots marking $\mathbf{k}^* = \max(\operatorname{Im} E_\pm)$ and the green dots marking the exceptional points. Reprinted with permission from [271] © American Physical Society.

2.2.3 Wavepacket Trajectories in Other Two-Band Systems

Previous studies [8, 205] have suggested that the wavepacket COM momenta in a non-Hermitian Dirac model follow the gradient of the imaginary part of the eigenenergies $\nabla \operatorname{Im} E$. In particular, Silberstein et al. derived an approximated semi-classical equation of motion describing the self-acceleration of a wavepacket COM as

$$\hbar \dot{k}_c = 2w^2 \nabla_k \operatorname{Im}[E_n]|_{k=k_c} \tag{2.9}$$

where w is the width of the wavepacket in the k-space [205]. This equation was derived for a one-dimensional system, but can be easily generalized to higher dimensions. Although this seems to accurately describe the trajectories of the exciton-polariton wavepackets described by the model in Eq. (1.93), this is not always the case. In this Section, I will demonstrate the disagreement between Eq. (2.9) and wavepacket dynamics under self-acceleration by analysing two different non-Hermitian two-band models to highlight the discrepancy and the need for a new theory of this dynamical effect.

In this Section, I present the analysis of the wavepacket dynamics in two additional exemplary models, a non-Hermitian Dirac model and a non-Hermitian Chern insulator. These two models have similar band structures near the origin, but their wavepacket dynamics and asymptotic behaviour are qualitatively different.

One of the models I consider here is the non-Hermitian Dirac model described by the Hamiltonian in Eq. (1.92). In the gapless phase with $\Delta = 0$, its band structure has two excpetional points at $\mathbf{k}^{EP} = (\pm\kappa, 0)$ and the eigenenergies structure is shown in Fig. 2.8(a,b).

In the non-Hermitian Dirac model, E_+ has the larger imaginary part at $k_y < 0$ while E_- has the larger imaginary part at $k_y > 0$ [see Fig. 2.8(a,b)]. Therefore, as time evolves, the wavepackets at $k_y < 0$ tend to evolve into the upper eigenstate, while the wavepackets at $k_y > 0$ tend to evolve into the lower eigenstate. Furthermore, at $\Delta = 0$, $\max(\operatorname{Im} E)$ lies on the k_y-axis. Therefore, the wavepackets in this model propagate towards a line of extrema $\mathbf{k}^*$, unlike the wavepackets in the exciton-polariton model in Eq. (1.93) described in the previous Section. From Fig. 2.8(e,f), It can be seen that, unlike the trajectories of the exciton-polariton wavepackets, the centre-of-mass momenta of the Dirac wavepackets seem to only follow $\nabla \operatorname{Im} E_\pm$ initially. As time evolves, the trajectories of the wavepackets start to deviate from $\nabla \operatorname{Im} E_\pm$. More importantly, the trajectories of the wavepackets, as well as the $\mathbf{k}^*$ points they propagate to, highly depend on their initial momenta. Figure 2.8(h) shows that the trajectories of the wavepackets with different set of initial centre-of-mass momenta will not follow the same paths towards the same $\mathbf{k}^*$ as the wavepackets in Fig. 2.8(f).

The other non-Hermitian model considered in this Section is the non-Hermitian Chern insulator described by the Hamiltonian [270]:

$$\mathbf{H} = (m + \cos k_x + \cos k_y)\sigma_x + (i\gamma + \sin k_x)\sigma_y + \sin k_y \sigma_z \tag{2.10}$$

that has eigenenergies

$$E_\pm = \pm\Big((m + \cos k_x + \cos k_y)^2 + (i\gamma + \sin k_x)^2 + \sin^2 k_y\Big)^{1/2}. \tag{2.11}$$

The phase diagram and edge states of this model have been extensively studied in Ref. [270]. At $m = -2$, $\gamma = 1$, there is a pair of exceptional points in the Brillouin zone at $\mathbf{k} = (0, \pm\pi/3)$ and the band structure is similar to that of the non-Hermitian Dirac model. However, unlike the Dirac model, $\operatorname{Im} E_\pm$ reaches maximum at a $\mathbf{k}^*$ in the middle of the Brillouin zone, which is also the middle of the bulk Fermi arc [see Fig. 2.8(c,d)].

The wavepackets with different initial centre-of-mass momenta in this model also follow different paths [see Fig. 2.8(g)]. Here, the wavepackets are initialised in the less dissipative eigenstate. However, unlike the non-Hermitian Dirac model, where the

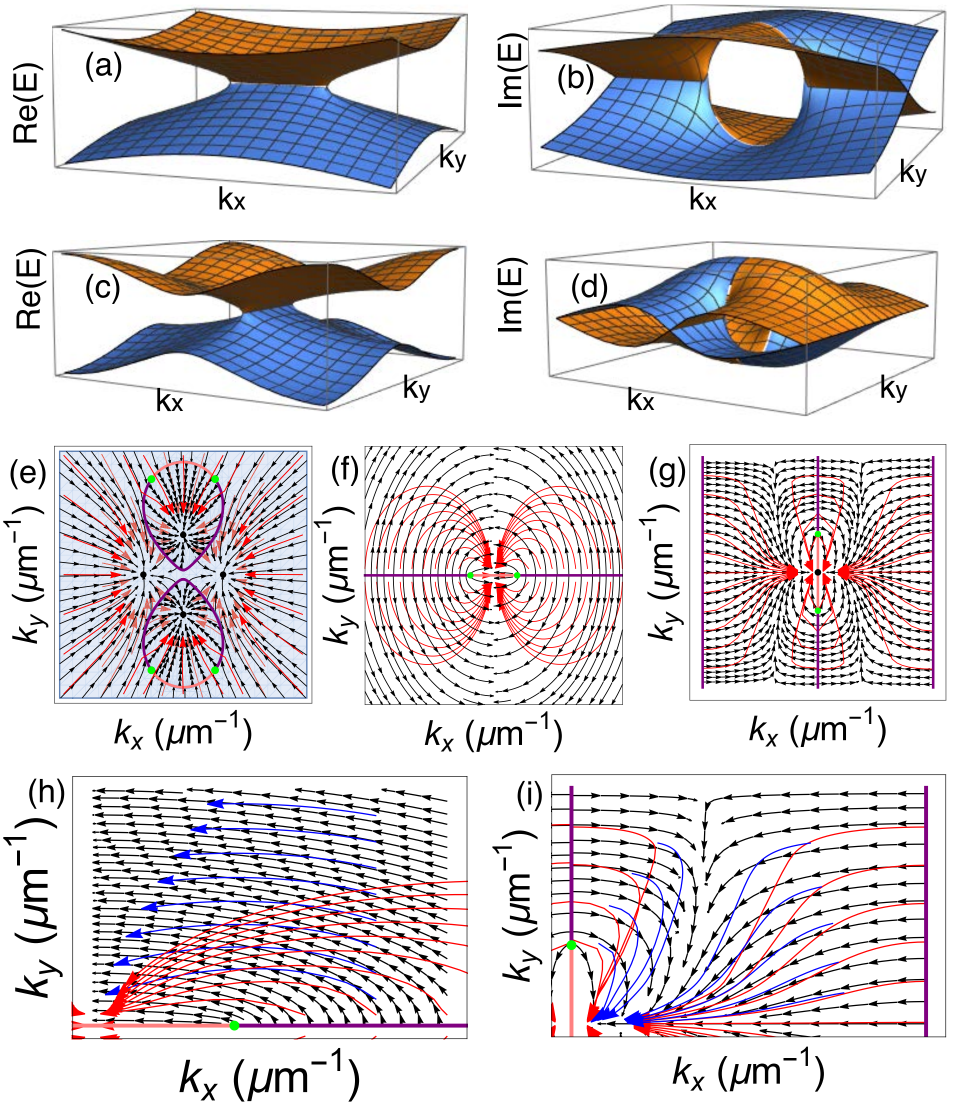

Figure 2.8: (a,b) The real and imaginary parts of the eigenenergies of the non-Hermitian Dirac model, Eq. (1.92). (c,d) The real and imaginary parts of the eigenenergies of the non-Hermitian Chern insulator, Eq. (2.10) in a gapless phase with exceptional points. (e-i) Wavepacket trajectories (red) with $\nabla\,\mathrm{Im}\,E$ (black) with the Fermi arcs and exceptional points of the (e) polariton model (1.93), (f) the non-Hermitian Dirac model (1.92) and (g) the non-Hermitian Chern insulator (2.10). (h,i) Wavepacket trajectories with different sets of initial COM momenta (blue arrows) in the non-Hermitian Dirac model and non-Hermitian Chern insulator, respectively, showing that they do not follow the same paths indicated by the red arrows. Reprinted with permission from [271] © American Physical Society.

asymptotic behaviour of the wavepacket centre-of-mass momenta is sensitive to the initial conditions, the wavepackets in the non-Hermitian Chern insulator seem to propagate to the same $\mathbf{k}^*$ asymptotically.

The above analysis of the non-Hermitian Dirac model and the non-Hermitian Chern insulator shows that the centre-of-mass momenta of a wavepacket only follow $\nabla \operatorname{Im} E$ of its corresponding eigenstate on a short time scale. The trajectories of the wavepackets will deviate increasingly from $\nabla \operatorname{Im} E$ with time. Furthermore, in cases where there are multiple maxima of $\operatorname{Im} E_{\pm}$, both the paths that the wavepackets take and the $\mathbf{k}^*$ points that the wavepackets propagate towards to will be sensitive to the initial conditions of the wavepackets. This is perhaps because the derivation of Eq. (2.9) only includes Taylor expansion around the COM momenta up to the 2nd order [205]. Higher-order terms will be needed to capture the trajectories of wavepackets under self-acceleration, but this is beyond the scope of this thesis.

2.3 Conclusion and outlook

To conclude, I have investigated the dynamics of wavepackets in a non-Hermitian exciton-polariton system. I found that the wavepackets tend to evolve into the eigenstate with the larger imaginary part of the energy $\operatorname{Im} E$, then propagate towards the momentum corresponding to the $\max(\operatorname{Im} E)$. This results in splitting, self-acceleration, and directional transport of the wavepackets in the absence of an external force. These effects arise from the imbalance of decay rates (or gain) between the eigenstates due to the non-Hermitian components of the Hamiltonian. I also show that the non-Hermitian extension of the Ehrenfest theorem results in a semi-classical equation of motion for non-Hermitian wavepacket dynamics.

Although here I focus on polaritons, these results are general and applicable to other two-dimensional two-band systems as well as one-dimensional or three dimensional multi-band systems, including purely photonic systems. However, experimentally, the coupling between photons and excitons results in a larger effective mass and slower propagation speeds, potentially allowing us to observe the predicted dynamics at a picosecond scale using a streak camera [274]. In addition, the presence of distinct extrema of the polariton linewidth at a finite momentum, which arises from photon-exciton coupling, is responsible for the acceleration, splitting and directional propagation in absence of an external force described in this Chapter. The self-acceleration shows the possibility to control the particle flows via tuning of the landscape of the imaginary-valued eigenenergy in momentum space, which might have application in future photonic or hybrid light-matter based low-energy technologies.

Chapter 3

Non-Hermitian Quantum Geometric Tensor and Wavepacket Dynamics

Disclaimer: This Chapter is based on my published works "Generalised quantum geometric tensor in a non-Hermitian exciton-polariton system [Invited]", *Optical Materials Express* **14**, 3, 664-686 (2024) and "Quantum geometric tensor and wavepacket dynamics in two-dimensional non-Hermitian systems", *Phys. Rev. Research* **7**, L012067 (2025). The analytic forms of the LR QGT was also previously presented in my Honours Thesis "Non-Hermitian Topology of Microcavity Exciton Polaritons" [Honours Thesis, Australian National University], Australian National University Open Research Repository http://hdl.handle.net/1885/256023 (2021). Although in my Honours Thesis, I also discussed the role of the RR QGT in dynamics of exciton-polariton wavepackets, I later found the previous results to be incorrect, and present the corrected results in this Chapter.

3.1 Introduction

As previously discussed in Chapter 1, the QGT plays an important role in the wavepacket dynamics as it accounts for the field-induced positional shift [178, 179] or the nonadiabatic corrections to the group velocity [180]. However, it is difficult to generalise these results to non-Hermitian system due to the different ways to define the components of the QGT, namely the right-right (RR) and left-right (LR), as the results of the different left and right eigenstates. In this Chapter, I address this ambiguity in the QGT definition by investigating the wavepacket dynamics in a two-band non-Hermitian system using the first-order perturbative theory and generalising the semi-classical equation of motion in Ref. [178] to non-Hermitian systems.

In the first half of this Chapter, I derive a semi-classical equation of the center-of-mass motion of a wavepacket, which explicitly shows the contributions of both the LR and RR components of the QGT. I then compare the analytical results with a numerical simulation using a non-Hermitian model of a perovskite-based exciton-polariton system described by Hamiltonian in Eq. 1.93. The model is chosen because the exciton-polariton system, in principle, allows for experimental verification of my theoretical predictions.

In the second half of this Chapter, I show how the components of the two non-Hermitian generalisations of QGT (i.e., the RR and LR QGT) can be experimentally measured in an exciton-polariton system by generalising the approach proposed by Bleu et al. in Ref. [189]. The method in Ref. [189] was recently applied to measure the QGT of non-Hermitian systems [199, 9]. However, the approach is based solely on right eigenstates that are experimentally accessible, and hence may not apply to generic non-Hermitian systems, where the LR QGT may play a significant role. In this Chapter, I show how the components of the LR QGT can also be experimentally measured by measuring only the right eigenstates and demonstrate this methodology using the non-Hermitian model of a perovskite-based exciton-polariton system.

3.2 Wavepacket Dynamics and Non-Hermitian Quantum Geometric Tensors

In the previous section, I studied wavepacket dynamics in the absence of an external force. In this Section, I will include the effects from an external force in the wavepacket dynamics. It should be noted that the derivation presented here is quite general, it is highly relevant to the cavity exciton-polariton system that I refer to throughout my Thesis. Although the exciton polaritons are neutrally charged, hence one cannot apply an external force using an electric field as in the case of electronic wavepackets in solid state systems [178, 179]. Instead, an external force can be realised through a cavity wedge. Because the fabrication process is never perfect, there will inevitably be a small variation or wedge in the cavity length. Such a wedge translates to a linear energy gradient experienced by polaritons and therefore gives rise to an effective external force needed to study the effects that will be discussed in this Section [275].

3.2.1 Interplay between Self-Acceleration and External Force

In Ref. [205], Silberstein et al. derived a semi-classical equation of motion for a wavepacket in a non-Hermitian system, showing both the effects from the RR Berry curvature and the non-Hermitian anomalous Berry connection [as shown in Eq. (1.64)], as well as self-acceleration arising from the finite size of the wavepackets in the absence of an external force:

$$\dot{\mathbf{k}}_c = 2w^2 \nabla_{\mathbf{k}} \operatorname{Im}[E]|_{\mathbf{k}=\mathbf{k}_c}, \tag{3.1}$$

where w denotes the width of the wavepacket, $|\psi(\mathbf{k}, t = 0)\rangle \propto \exp(-\frac{(\mathbf{k}-\mathbf{k}_c(t=0))^2}{4w^2})$, in momentum space. In this Section, I will present my results on a semi-classical equation of motion describing the interplay between the self-acceleration and the effects of a force. I derive the equation of motion by extending the formalism in Ref. [205] to include both the external force and self-acceleration while assuming that the two bands are well separated, so that the single-band approximation holds, which neglects the mixing between the two eigenstates due to the perturbation[276, 269, 8, 277]. For more information on the derivation, please refer to Appendix B.

The resulting equations, up to the second order in the wavepacket widths, along the

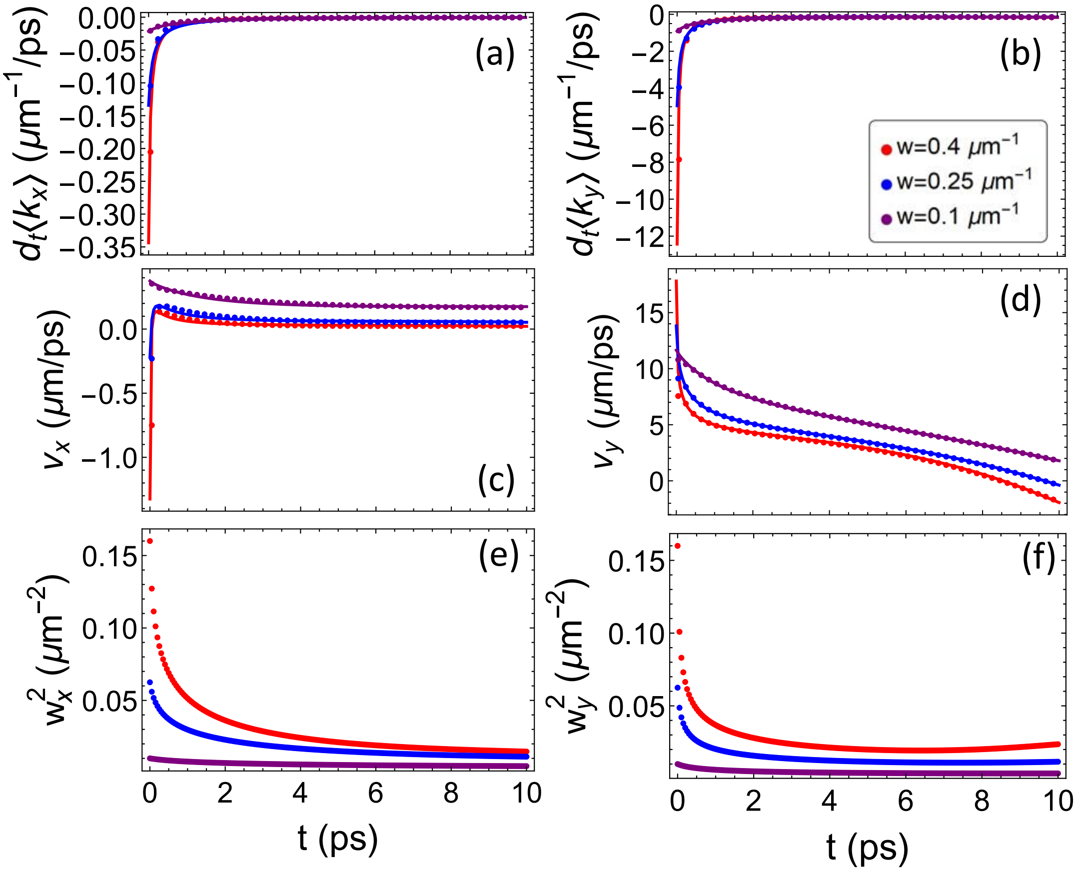

Figure 3.1: (a,b) Time derivatives of the COM momenta and (c,d) the group velocities computed numerically using the split-step method [278, 279] (dots) and semi-analytically using Eq. (3.2) (lines). (e,f) The numerically extracted wavepacket widths. The values of w in the legend correspond to the initial wavepacket widths. Reprinted with permission from [61] © Optica Publishing Group.

i-th direction are

$$\begin{aligned}\hbar(\dot{k}_c)_i =&F_i + 2w_i^2\partial_{k_i}\operatorname{Im}[E_\pm + \mathbf{F}\cdot(\mathbf{A}_\pm^{RR}-\mathbf{A}_\pm^{LR})]\\ \hbar(\dot{r}_c)_i =&\partial_{k_i}\operatorname{Re}[E_\pm + \mathbf{F}\cdot(\mathbf{A}_\pm^{RR}-\mathbf{A}_\pm^{LR})] - (\mathbf{F}\times\Omega_\pm^{RR})_i\\ &+\sum_j\Bigg(\frac{w_j^2}{2}\partial_{k_j}^2\left(\partial_{k_i}\operatorname{Re}\left[E_\pm + \mathbf{F}\cdot(\mathbf{A}_\pm^{RR}-\mathbf{A}_\pm^{LR})\right] - (\mathbf{F}\times\Omega_\pm^{RR})_i\right)\\ &+2w_j^2\left[\partial_{k_j}\operatorname{Im}\left[E_\pm + \mathbf{F}\cdot(\mathbf{A}_\pm^{RR}-\mathbf{A}_\pm^{LR})\right]\partial_{k_j}\left(\operatorname{Re}\left[(\mathbf{A}_\pm^{RR})_i\right]-\partial_{k_i}\varphi\right)\right]\Bigg)\end{aligned} \tag{3.2}$$

where φ is the complex phase of the wavepacket and w_j is the wavepacket width along the j-th direction in momentum space. The latter parameter can be computed as

$$w_j^2 = \frac{\int(k_j-(\mathbf{k}_c)_j)^2\langle\psi(\mathbf{k},t)|\psi(\mathbf{k},t)\rangle d^2\mathbf{k}}{\int\langle\psi(\mathbf{k},t)|\psi(\mathbf{k},t)\rangle d^2\mathbf{k}}.$$

To test the approximation in Eq. (3.2), I simulate the dynamics of Gaussian wavepackets using the exciton-polariton model in Eq. (1.93). The Zeeman splitting is set to $\Delta = 0.008$ eV to open a gap. For the values of the rest of the parameters used in the simulation, please refer to Appendix A. The wavepacket was initially prepared in the upper right eigenstates of the Hamiltonian (1.93) with different initial widths w, and initial COM at $\mathbf{k}_c = (0.05, 2.5)\mu\text{m}^{-1}$, $\mathbf{r}_c = (0,0)\mu$m and an external force $\mathbf{F} = (0, -10^{-4})$ eV/μm, which is chosen to be small enough so the first-order approximation is valid [180, 205]. The complex phase φ from Eq. (3.2) is difficult to compute but I assume that the terms proportional to the external force are small and approximate the terms as $\partial_{k_i}\varphi \approx -\partial_{k_i} \operatorname{Re} E_+ t/\hbar + (\mathbf{r}_0)_i$ where $\mathbf{r}_0$ disappear in the derivatives. Note that in contrast with Hermitian systems, the wavepacket size (in momentum space) changes as it evolves, which makes it difficult to compute Eq. (3.2) completely analytically. I therefore adopt a semi-analytic approach and numerically extract w_j^2 [see Figs. 3.1(e,f)], then use it to compute the time derivatives of the COM momenta [see Figs. 3.1(a,b)] and the group velocities [see Figs. 3.1(c,d)].

The results presented in Fig. 3.1 show that the semi-analytic approach using Eq. (3.2) gives good approximations for the wavepacket dynamics. More importantly, it clearly shows that the anomalous drift is strongly modified by the size of the wavepacket.

In the following Section, I will consider another effect in wavepacket dynamics from the external force, which arises from the quantum metric instead of the finite wavepacket size. As shown in Section 1.3.2, the quantum metric tensor describes the perturbative correction to the anomalous velocity in the wavepacket dynamics. I will expand the previous results in Eq. (1.64) to the second order in force using non-Hermitian perturbation theory [280]. This will uncover how the semi-classical theory in Eq. (1.51) is modified by non-Hermiticity. Furthermore, it will also clear the ambiguity arising from the different ways to define the quantum metric, namely LR and RR.

3.2.2 Wavepacket Dynamics in Non-Hermitian Perturation Theory

In this Section, I will show my results on how the generalised QGT describes the wavpacket dynamics, which arises from the first-order non-Hermitian perturbation theory. First, I consider a perturbation to a two-dimensional (2D) Hamiltonian in the form of

$$\tilde{H} = H - \mathbf{F} \cdot \mathbf{r}, \tag{3.3}$$

where $\mathbf{F}$ represents a weak external force field and $\mathbf{r}$ is the position operator. The term $-\mathbf{F} \cdot \mathbf{r}$ can be seen as a perturbation to the unperturbed Hamiltonian H which only has k-dependence. I then consider a Gaussian wavepacket in the state

$$|W\rangle = \int w(\mathbf{k}, t) e^{i\mathbf{k}\cdot\mathbf{r}} |\tilde{u}_0^R(\mathbf{k})\rangle d^2\mathbf{k}, \tag{3.4}$$

where $|\tilde{u}_n^R\rangle$ is a right eigenstate of the Hamiltonian $\tilde{H}$ (3.3). I also denote the n-th right eigenstate of the Hamiltonian H without external force as $|u_n^R\rangle$.

In this Section, I focus on a generic two-band system with gain and loss and denote $|\tilde{u}_0^R\rangle$ to be the eigenstate with the larger growth (or the smaller decay) rate. The wavepacket will eventually evolve into the eigenstate with the largest $\operatorname{Im} E_n$ due to the loss or gain (see previous Chapter) [205, 276]. Therefore, in order to employ a single-band approximation, I need to ensure that the wavepacket stays in the eigenstate that has the larger $\operatorname{Im} E_n$, i.e. larger gain (or smaller loss).

I then apply the perturbation theory [280] by expanding the eigenstate to the first order correction in $\mathbf{F}$ as,

$$|\tilde{u}_0^R(\mathbf{k})\rangle = |u_0^R(\mathbf{k})\rangle - \frac{\mathbf{F}\cdot\mathbf{A}_{10}^{LR}}{\epsilon_0 - \epsilon_1}|u_1^R(\mathbf{k})\rangle \tag{3.5}$$

where $|u_1^R(\mathbf{k})\rangle$ is the other eigenstate (with larger loss), $\mathbf{A}_{10}^{LR} = \langle u_1^L | i\partial_{\mathbf{k}} u_0^R\rangle$ is the LR inter-band Berry connection, and $\epsilon_{0,1}$ are the complex-valued energy eigenvalues of the unperturbed Hamiltonian H. I emphasise that the inter-band Berry connection in the perturbative correction has to be defined in the "left-right" (LR), instead of the conventional "right-right" (RR), formalism due to bi-orthogonality in non-Hermitian systems [280].

Assuming that the wavepacket is narrowly centered at its center of mass in momentum space $|w(\mathbf{k},t)|^2 \approx \delta(\mathbf{k}-\mathbf{k}_c)$, I then follow the formalism presented in Refs. [204, 206] and derive the equation of motion of the wavepacket COM in position space up to the first-order perturbative correction (see Appendix C.2 for details) as:

$$\hbar\dot{\mathbf{r}}_c = \partial_{\mathbf{k}} \operatorname{Re}\left[\epsilon_0 + \mathbf{F}\cdot(\tilde{\mathbf{A}}_{00}^{RR} - \tilde{\mathbf{A}}_{00}^{LR})\right] - \mathbf{F}\times\tilde{\mathbf{\Omega}}_0^{RR} \tag{3.6}$$

where,

$$\begin{aligned}\tilde{\mathbf{A}}_{00}^{RR} =& \mathbf{A}_{00}^{RR} + \operatorname{Re}\left[\frac{2Q_0^{RR}\cdot\mathbf{F}}{\epsilon_1-\epsilon_0}\right] \\ &- \operatorname{Im}\left[\partial_{\mathbf{k}}\left(\frac{\mathbf{F}\cdot(\mathbf{A}_{00}^{RR}-\mathbf{A}_{00}^{LR})}{\epsilon_1-\epsilon_0}\right)\right]\end{aligned} \tag{3.7}$$

$$\tilde{\mathbf{A}}_{00}^{LR} = \mathbf{A}_{00}^{LR} + \frac{2g^{LR}\cdot\mathbf{F}}{\epsilon_1-\epsilon_0} \tag{3.8}$$

$$\tilde{\mathbf{\Omega}}_0^{RR} = \mathbf{\Omega}_0^{RR} + \nabla_{\mathbf{k}}\times\operatorname{Re}\left[\frac{2Q_0^{RR}\cdot\mathbf{F}}{\epsilon_1-\epsilon_0}\right], \tag{3.9}$$

where g_0^{LR} and Q_0^{RR} denote the LR quantum metric tensor and the RR QGT of the 0-th band, respectively. As I will show in the next Section, in a two-band system, which is the focus of this Chapter, the LR quantum metric tensors of the two bands are the same. Therefore I drop the index 0 in Eq. (3.8) and denote $g^{LR} = g_0^{LR}$. These expressions form the main result in this Chapter: Eq. (3.6) is the non-Hermitian generalisation of Eq. (1.51), where the QMT g describes the perturbative correction, Eqs. (3.7, 3.8, 3.9), explicitly show the first-order perturbation corrections to Eq. (1.64), which describe the wavepacket dynamics in terms of the RR Berry curvature $\mathbf{\Omega}_0^{RR}$ and the non-Hermitian anomalous Berry connection $\operatorname{Re}[\mathbf{A}_{00}^{RR} - \mathbf{A}_{00}^{LR}]$. In the following, I will show that the second-order (in $\mathbf{F}$) corrections have contributions from the QMT, Berry curvature, and anomalous non-Hermitian Berry connection.

Let us first examine the correction to the Berry curvature $\tilde{\mathbf{\Omega}}_0^{RR}$ by comparing Eq. (3.6) to Eq. (1.51). The second-order field-induced correction clearly transforms as $g_0/(\epsilon_1 - \epsilon_0) \to \mathrm{Re}[Q_0^{RR}/(\epsilon_1 - \epsilon_0)]$ when the non-Hermiticity is introduced. Note, however, that this is not simply $g_0 \to g_0^{RR}$ due to the complex denominator. In fact, there is an additional non-Hermitian correction which comes from the RR Berry curvature $\mathbf{\Omega}_0^{RR}$ itself, as shown below:

$$\mathrm{Re}\left[\frac{2Q_0^{RR}\cdot\mathbf{F}}{\Delta\epsilon}\right] = \mathrm{Re}\left[\frac{1}{\Delta\epsilon}\right] 2g_0^{RR}\cdot\mathbf{F} - \mathrm{Im}\left[\frac{1}{\Delta\epsilon}\right]\mathbf{F}\times\mathbf{\Omega}_0^{RR} \tag{3.10}$$

This new term depends on the imaginary part of the complex energy gap, which naturally vanishes in the Hermitian limit or along the imaginary Fermi arc, where $\mathrm{Im}\,\Delta\epsilon = 0$ [218, 276].

The second-order field-induced corrections to the anomalous non-Hermitian Berry connection have two components, i.e. $\mathrm{Re}[\mathbf{F}\cdot(\tilde{\mathbf{A}}_{00}^{RR} - \tilde{\mathbf{A}}_{00}^{LR})] = I_0 + I_1 + I_2$, where $I_0 = \mathbf{F}\cdot(\mathbf{A}_{00}^{RR} - \mathbf{A}_{00}^{LR})]$ is the first-order term. The first correction is proportional to the difference of the RR and LR QMTs and has the form

$$I_1 = 2\mathbf{F}\cdot\mathrm{Re}\left[\frac{g_0^{RR} - g_0^{LR}}{\Delta\epsilon}\right]\cdot\mathbf{F}, \tag{3.11}$$

while the second term is proportional to the anomalous Berry connection and has the form

$$I_2 = -\mathbf{F}\cdot\mathrm{Im}\left[\partial_{\mathbf{k}}\left(\frac{\mathbf{F}\cdot(\mathbf{A}_{00}^{RR} - \mathbf{A}_{00}^{LR})}{\Delta\epsilon}\right)\right]. \tag{3.12}$$

Note that both the real and imaginary parts of the LR QMT and Berry connections contribute to the corrections due to the complex denominator (see Appendix C.3 for the explicit forms of I_1 and I_2). This novel non-Hermitian effect shows that the LR QMT should indeed be defined as a complex-valued quantity [10, 201, 203]. This is in contrast to the corrections to the Berry curvature, Eq. (3.9), which originate from the real-valued RR QMT and Berry curvature.

To examine the corrections closely, I integrate Eq. 3.6 to get (see Appendix C.2 for the derivation):

$$\mathbf{r}_c = \left[-\partial_{\mathbf{k}}\varphi + \tilde{\mathbf{A}}_{00}^{RR}\right]_{\mathbf{k}=\mathbf{k}_c}, \tag{3.13}$$

$$\varphi = -\frac{1}{\hbar}\int_{t_0}^{t}\mathrm{Re}\left[\epsilon_0 - \mathbf{F}\cdot\tilde{\mathbf{A}}_{00}^{LR}\right]_{\mathbf{k}=\mathbf{k}_c} dt'. \tag{3.14}$$

The positional shift [178] of the COM, given by Eq. (3.13), is due to the gradient of the phase φ and the corrected RR Berry connection. The latter, which is given by Eq. (3.7), has two field-induced corrections. The first depends on the RR QGT, Q_0^{RR}, which is the same term that appears in field-induced correction to the Berry curvature $\tilde{\mathbf{\Omega}}_0^{RR}$ in Eq. (3.9). The second correction depends on the anomalous non-Hermitian Berry connection, $\mathbf{A}_{00}^{RR} - \mathbf{A}_{00}^{LR}$, which also appears in the field-induced correction to the energy

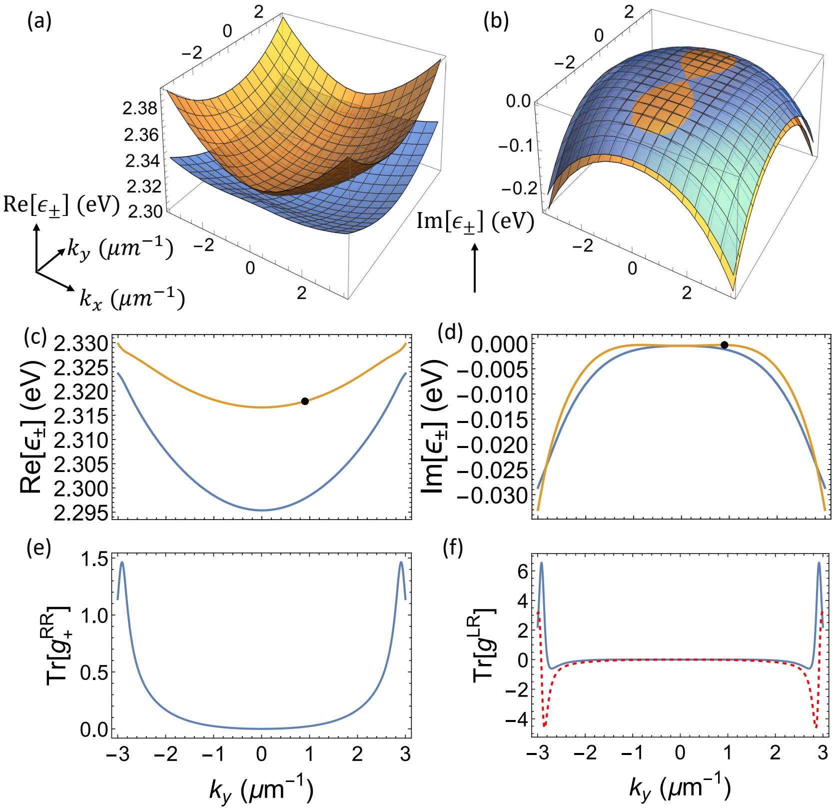

Figure 3.2: The (a) real and (b) imaginary parts of the eigenenergies of the exciton polaritons in a gapped phase with $\Delta_z = 0.007$ eV. (c, d) The cross-sections of the real and imaginary parts of the eigenenergies along the k_y-axis, respectively. The orange line and surface represent the upper band, the blue line and surface represent the lower band, and the black dots represent the initial momentum of the wavepacket center-of-mass. (e, f) The RR quantum metric and Berry curvature. (g, h) The real and imaginary parts of the LR quantum metric. The blue and red lines in (e, g, h) show the xy-components and the yy-components respectively, since these are the only components that appears in the dynamics when the force is in the y-direction. Reprinted with permission from [281] © American Physical Society.

in Eq. (1.64). There is also a field-induced correction to the geometric (Berry) phase [94, 204, 206], Eq. (3.14), which is proportional to the LR QMT, g_0^{LR} [see Eq. (3.8)].

In the Hermitian limit, the eigenenergies become real-valued, $\mathbf{A}_{00}^{LR} = \mathbf{A}_{00}^{RR}$, and $Q_0^{RR} = Q_0^{LR}$ becoming Hermitian as well. Therefore, the correction to the LR and RR Berry connections both take the forms of $\mathbf{A}_{00} \to \mathbf{A}_{00} + 2(g \cdot \mathbf{F})/(\Delta\epsilon)$, and I recover the previous results given by Eq. (1.51) [178, 179, 180].

3.2.3 Non-Hermitian Quantum Geometric Tensors in a Non-Hermitian Exciton-Polariton System

In this Section, I will present the analytic forms of the RR and LR QGTs derived for the non-Hermitian model of perovskite-based exciton-polariton system described by the Hamiltonian in Eq. (1.93). To demonstrate the relevance of the QGT components to the description of dynamical effects, I then simulate the wavepacket dynamics in this system and present the results in the next Section.

The components of the RR QGT of this non-Hermitian exciton-polariton model can be found analytically as

$$\begin{aligned}
g_{\pm,xx}^{RR} =& \frac{4|\tilde{\beta}|^2 \left(k_y^2 |H_+|^2 |\tilde{\alpha} - \tilde{\beta} k^2|^2 - 2k_y \operatorname{Im}[G_{\pm,x}] + \Delta^2 k^2 |\Delta \pm E|^2\right)}{|E|^2 \left(|H_+|^2 + |\Delta \pm E|^2\right)^2} \\
g_{\pm,xy}^{RR} =& \frac{4|\tilde{\beta}|^2 \left(k_x k_y |H_+|^2 \left(|\tilde{\alpha}|^2 - |\tilde{\beta}|^2 k^4\right) + \operatorname{Re}\left[k_y G_{\pm,x}^* + i k_x G_{\pm,y}\right]\right)}{|E|^2 \left(|H_+|^2 + |\Delta \pm E|^2\right)^2} \\
g_{\pm,yy}^{RR} =& \frac{4|\tilde{\beta}|^2 \left(k_x^2 |H_+|^2 |\tilde{\alpha} + \tilde{\beta} k^2|^2 - 2k_x \operatorname{Im}[G_{\pm,y}] + \Delta^2 k^2 |\Delta \pm E|^2\right)}{|E|^2 \left(|H_+|^2 + |\Delta \pm E|^2\right)^2} \\
\Omega_{\pm}^{z,RR} =& \frac{8|\tilde{\beta}|^2 \left(2k_x k_y k^2 |H_+|^2 (b\alpha - a\beta) - \operatorname{Im}\left[k_y G_{\pm,x}^* + i k_x G_{\pm,y}\right] - \Delta^2 k^2 |\Delta \pm E|^2\right)}{|E|^2 \left(|H_+|^2 + |\Delta \pm E|^2\right)^2}
\end{aligned} \tag{3.15}$$

where I denote $G_{\pm,x} = H_+(\tilde{\alpha} - \tilde{\beta} k^2)(k_x - ik_y)\Delta(\Delta \pm E^*)$, $G_{\pm,y} = H_+(\tilde{\alpha} + \tilde{\beta} k^2)(k_x - ik_y)\Delta(\Delta \pm E^*)$. As discussed in Section 1.5.2, Δ represents the Zeeman splitting, α represents the cavity anisotropy, β represents the TE-TM splitting, while a, b represent the polarization-dependent photonic losses arising from the anisotropy and TE-TM splitting, respectively. I also denote $\tilde{\alpha} = \alpha - ia$ and $\tilde{\beta} = \beta - ib$ for simplicity. Interestingly, the $|E|^2$ in the denominator ensures that all components of the RR QGT diverge at the spectral degeneracies, where $E = 0$, unlike in previous work on non-Hermitian Su-Schrieffer-Heeger models [203]. At $\Delta = 0$, the divergence is $\sim k^{-1}$, in agreement with previous results following a similar approach [199].

The $\Delta = 0$ case, with no out-of-pane field, features a symmetrical distribution with components from the opposite bands aligned with each other. However, it is important to highlight that the Berry curvatures of the two bands are the same, i.e., $\Omega_+^{RR} = \Omega_-^{RR}$, instead of having the opposite signs [see Eqs. (1.36)].

For larger Δ, such that the exceptional points are annihilated and the gap is opened, the components of the RR QMT take on finite values. Unlike in the $\Delta = 0$ case, the upper and lower bands are not exactly equal nor opposite to each other, violating the identities for the Hermitian limit [see Eqs. (1.36)]. These features arise from the $|\Delta \pm E|$ factors in Eqs. (3.15), which originated from the non-orthogonality of the right-eigenstates [280, 201].

Similarly, the components of the LR QGT of this model take the forms

$$\begin{aligned}
g^{LR}_{\pm,xx} =& \frac{\tilde{\beta}^2\left[(\tilde{\alpha}-\tilde{\beta}k^2)^2k_y^2+\Delta^2k^2\right]}{E^4}\\
g^{LR}_{\pm,xy} =& \frac{\tilde{\beta}^2k_xk_y\left(\tilde{\alpha}^2-\tilde{\beta}^2k^4\right)}{E^4}\\
g^{LR}_{\pm,yy} =& \frac{\tilde{\beta}^2\left[(\tilde{\alpha}+\tilde{\beta}k^2)^2k_x^2+\Delta^2k^2\right]}{E^4}\\
\Omega^{z,LR}_{\pm} =& \mp\,\frac{2k^2\tilde{\beta}^2\Delta}{E^3}.
\end{aligned} \tag{3.16}$$

Unlike in the RR QGT, the identities $g_{+,\mu\nu}=g_{-,\mu\nu}$, $\Omega_{+,\mu\nu}=-\Omega_{-,\mu\nu}$ are recovered for the LR QGT, since the components of the LR QGT can be expressed as

$$\begin{aligned}
g^{LR}_{n,\mu\nu} &= \frac{1}{2}\sum_{m\neq n}\left[\frac{\langle\psi^L_m|\partial_\mu H|\psi^R_n\rangle\langle\psi^L_n|\partial_\nu H|\psi^R_m\rangle}{(E_m-E_n)^2}+\frac{\langle\psi^L_m|\partial_\nu H|\psi^R_n\rangle\langle\psi^L_n|\partial_\mu H|\psi^R_m\rangle}{(E_m-E_n)^2}\right]\\
\Omega^{LR}_{n,\mu\nu} &= i\sum_{m\neq n}\left[\frac{\langle\psi^L_m|\partial_\mu H|\psi^R_n\rangle\langle\psi^L_n|\partial_\nu H|\psi^R_m\rangle}{(E_m-E_n)^2}-\frac{\langle\psi^L_m|\partial_\nu H|\psi^R_n\rangle\langle\psi^L_n|\partial_\mu H|\psi^R_m\rangle}{(E_m-E_n)^2}\right]
\end{aligned} \tag{3.17}$$

similarly to the Hermitian case in Eq. (1.35) [201, 280].

Compared to the components of $Q^{RR}_{\pm,\mu\nu}$, the components of $Q^{LR}_{\pm,\mu\nu}$ take very similar forms to the ones in the Hermitian limit [189] but with $(\alpha,\beta)\rightarrow(\tilde{\alpha},\tilde{\beta})$. Similarly, one can also recover the RL $g^{RL}_{\pm,\mu\nu}$ and $\Omega^{z,RL}_{\pm}$ by taking the Hermitian results and replacing $(\alpha,\beta)\rightarrow(\tilde{\alpha}^*,\tilde{\beta}^*)$.

I also note that, unlike the RR QGT $Q^{RR}_{\pm,\mu\nu}$ at $\Delta=0$, the quantum metric $g^{LR}_{\pm,\mu\nu}$ diverges as $\sim k^{-2}$ at each exceptional point while the Berry curvature $\Omega^{z,LR}_{\pm}$ diverges as $\sim k^{-3/2}$, in agreement with previous work which used the same formalism [200]. Furthermore, although both $\Omega^{z,LR}_{\pm}$ and $\Omega^{z,RR}_{\pm}$ diverge at the exceptional points, the LR Berry curvature $\Omega^{z,LR}=0$ elsewhere but the RR Berry curvature $\Omega^{z,RR}_{\pm}$ is finite. The delta-function behavior of the former is reminiscent of the Berry curvature near Dirac points in the Hermitian limit [189].

3.2.4 Wavepacket Dynamics in the Perovskite-Based Exciton-Polariton System

To verify that the first order perturbation theory developed in the previous Sections improves the accuracy of the semi-classical equation of motion Eq. (3.6), I simulate the wavepacket dynamics numerically using split-step methods [278, 279]. The parameters of the model (1.93) used for the simulations are specified in Appendix A. I initialise the wavepacket at $\mathbf{k}=(0,0.9)\mu\mathrm{m}^{-1}$ in the upper eigenstate which has the larger $\operatorname{Im}E$ (or less loss) [see the dot in Figs. 3.2(c,d)]. The two bands are separated at this point in momentum space and $\partial_{k_x}\operatorname{Re}\epsilon_0=0$. Experimentally, the wavepacket can be prepared using resonant optical excitation of exciton polaritons, where the exciting laser wavelength is adjusted to match the energy and the excitation angle is tuned to match the momentum of the target state [191].

An external force $\mathbf{F} = (0, 5 \times 10^{-4})$ eV/μm is applied accelerating the wavepacket along the $+k_y$-axis towards smaller (real) energy spacing. As the bands get closer, the mixing between the two eigenstates will be more profound and can result in oscillation due to the Zitterbewegung effect [235, 282]. However, since the wavepacket evolves into the less dissipative eigenstate, the inter-band mixing will gradually disappear and so will the oscillation. I also ensure that the wavepacket does not cross the imaginary Fermi arc [218], where the imaginary parts of the eigenenergies cross, otherwise the single-band approximation will fail [276] as the loss rates of the eigenstates will switch. The numerical results are presented as dots in Figs. 3.3.

In this simple case, Eq. (3.6) becomes:

$$v_x = \frac{1}{\hbar}\partial_{k_x} \operatorname{Re}\left[F_y\left(\tilde{A}^{RR}_{00,y} - \tilde{A}^{LR}_{00,y}\right)\right] - \frac{F_y}{\hbar}\tilde{\Omega}^{RR}_{0,xy} \tag{3.18}$$

$$v_y = \frac{1}{\hbar}\partial_{k_y} \operatorname{Re}\left[\epsilon_0 + F_y\left(\tilde{A}^{RR}_{00,y} - \tilde{A}^{LR}_{00,y}\right)\right]. \tag{3.19}$$

The explicit forms of $\tilde{A}^{RR}_{00,y} - \tilde{A}^{LR}_{00,y}$ and $\tilde{\Omega}^{RR}_{0,xy}$ are presented in Appendix C.3.

The solution of the first-order perturbation theory in Eq. (3.6) gives a better fit to the numerical results than the solution of the non-perturbative theory in Eq. (1.64). This is apparent from the discrepancy between the numerical and analytical solutions plotted in Figs. 3.3 (c,d). Although the non-adiabatic correction is rather small in this particular example, a larger force or a smaller energy gap will result in a much larger correction, meaning that the previously derived equation of motion without perturbative corrections (1.64) will no longer be adequately describing the dynamics. In this case, however, I might also need to extend the treatment beyond the first-order perturbation theory and consider higher order corrections. On the other hand, if the wavepacket propagates for a longer time, it would cross the imaginary Fermi arc, and the semi-classical equations of motion will no longer be valid, since the wavepacket would evolve into the opposite right eigensate and the single-band approximation would fail [276].

I also provide further analysis on the deviation between the analytical and numerical results [283]. The previous theory in Ref. [204] includes up to the first order in the external force, while the theory presented in Section 3.2.2, which arises from the first-order perturbation theory, includes up to the 2nd order in force. Therefore, I expect that the deviation from the first-order theory has a leading order of F^2, while the deviation from the second-order theory has a leading order of F^3.

In Fig. 3.4, I present the deviation in the wavepacket centre-of-mass positions at $t = 1.25$ ps plotted against the external force in log-log scale. At lower F, the deviation from the first-order theory is quadratic. However, the quadratic function fails to capture the data at higher F and instead, a quartic function is required. This suggests that the higher-order terms becomes stronger at high F, and start to dominate over the deviation between the first-order theory and the simulation. On the other hand, the deviation from the second-order theory in x does, indeed, exhibit cubic behaviour.

The first-order and the second-order theory gives almost the same result for the deviation in y, which can be fitted with a linear function in F. I believe that this is because the

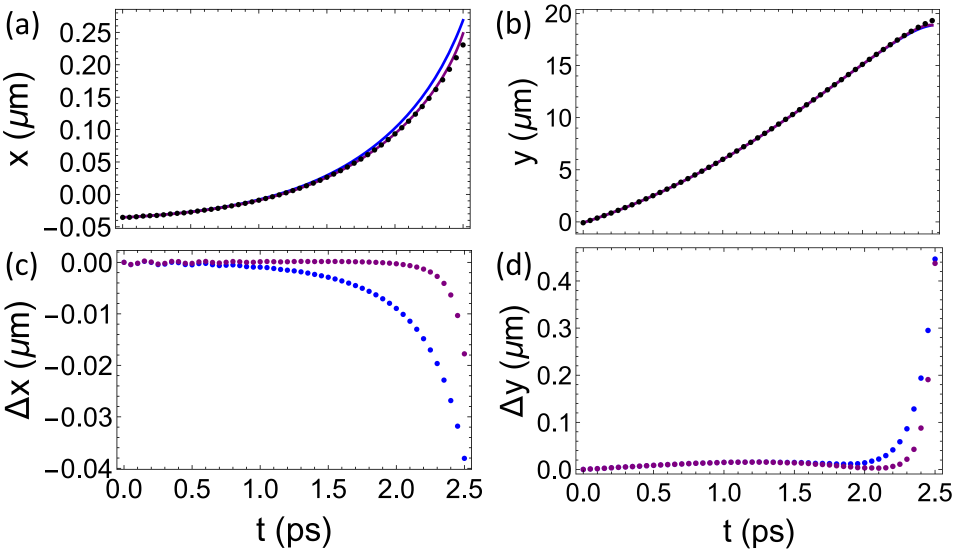

Figure 3.3: (a, d) The real-space trajectory of exciton-polariton wavepackets initially placed in the upper eigenstate in 3 different gapped phases with $\Delta_z = 0.007$ eV. Shown are the simulated results (black dots), the solution of semi-classical equation of motion derived previously Eq. (1.64) (blue lines) and the solution of the semi-classical equation of motion derived here Eq. (3.6) (purple lines). (c, d) The difference between the analytical results and the numerical simulation with blue dots denote deviation from Eq. (1.64) and the purple dots denote deviation from Eq. (3.6). Reprinted with permission from [281] © American Physical Society.

main correction comes from the correction to the anomalous Hall drift in the x-direction since the force is in the y-direction. It would require a new theory to capture the correction to the non-Hermitian anomalous Berry connection, which is beyond the scope of this Thesis.

3.3 Measuring Non-Hermitian Quantum Geometric Tensor

In Sections 3.2.2 and 3.2.4, I have demonstrated the important roles that the RR and the LR QGTs play in the wavepacket dynamics in non-Hermitian systems. Now, I will show that the components of the RR and LR QGTs can be experimentally measured by generalising the approach presented in Ref. [189] for Hermitian systems. Simultaneous measurements of the QGT components and wavepacket dynamics provide a way to verify my theoretical prediction encapsulated in Eq. (3.6).

In the following, I consider a general two-band non-Hermitian Hamiltonian previously presented in Eq. 1.88

$$\hat{H}(\mathbf{k}) = H_0(\mathbf{k})\mathbf{I} + \overrightarrow{\mathbf{H}}(\mathbf{k}) \cdot \overrightarrow{\boldsymbol{\sigma}} \tag{3.20}$$

with $\overrightarrow{\mathbf{H}}(\mathbf{k}) = [H_x(\mathbf{k}), H_y(\mathbf{k}), H_z(\mathbf{k})]$. The methodology for a measurement of the QGT

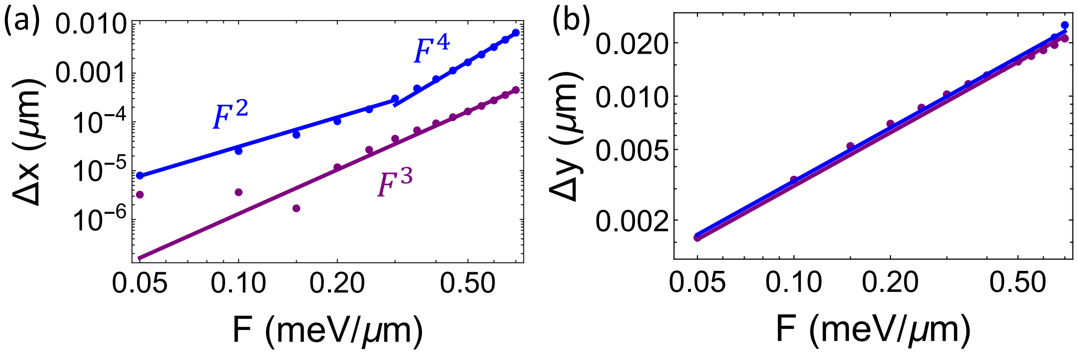

Figure 3.4: The deviation in position along x (a) and along y (b) between the numerical simulation and the first order theory (blue dots), and the second order theory (purple dots), respectively, as a function of increasing external force F at constant $t = 1.25$ ps . The deviation from the first-order theory in x was fitted with a quadratic function at lower F and with a quartic function at higher F, while the deviation from the second-order theory (this work) is fitted with the cubic function in F. The deviations in y in (b) from both theories are linear in F (blue and purple lines, respectively). Reprinted with permission from [281] © American Physical Society.

components using the angles of the Stokes vectors of the emitted photons, $\theta = \arccos S_z$ and $\phi = \arctan(S_y/S_x)$, in Hermitian case

$$\begin{aligned} g_{n,ij} =& \frac{1}{4}\Big(\partial_i\theta\partial_j\theta + \sin^2\theta\partial_i\phi\partial_j\phi\Big) \\ \Omega_{n,ij} =& \frac{1}{2}\sin\theta\Big(\partial_i\phi\partial_j\theta - \partial_j\phi\partial_i\theta\Big) \end{aligned} \tag{3.21}$$

was proposed in Ref. [189]. Here, I will show how $Q^{RR}_{\pm,\mu\nu}$ and $Q^{LR}_{\pm,\mu\nu}$ can be constructed from experimentally accessible observables.

3.3.1 Right-right Quantum Geometric Tensor

The pseudospin components of a photonic or exciton-polariton system (see Section 1.4.2) can be measured from the polarization of emitted light, i.e. from the Stokes vector. In exciton-polariton systems, I only have access to the polarization of the right eigenstates which corresponds to the Stokes vectors as follows:

$$S^{RR}_{j,\pm} = \frac{\langle\psi^R_\pm|\sigma_j|\psi^R_\pm\rangle}{\langle\psi^R_\pm|\psi^R_\pm\rangle} \tag{3.22}$$

where $j = \{x, y, z\}$.

By expanding $S^{RR}_{j,\pm} = \langle\psi^R_\pm|\sigma_j|\psi^R_\pm\rangle/\langle\psi^R_\pm|\psi^R_\pm\rangle$, the components of the pseudospins of the

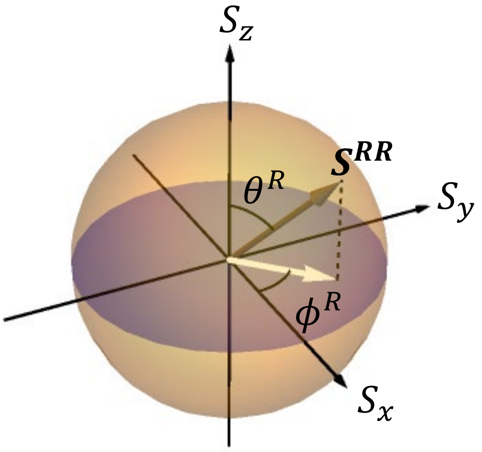

Figure 3.5: Showing the pseudospin of the right eigenstate and its angle on the Bloch sphere.

right eignstates take the general form

$$\begin{aligned} S^{RR}_{x,\pm} &= \frac{2\,\mathrm{Re}[H_+(H_z^* \pm E^*)]}{|H_z \pm E|^2 + |H_+|^2} \\ S^{RR}_{y,\pm} &= \frac{2\,\mathrm{Im}[H_+(H_z^* \pm E^*)]}{|H_z \pm E|^2 + |H_+|^2} \\ S^{RR}_{z,\pm} &= \frac{|H_z \pm E|^2 - |H_+|^2}{|H_z \pm E|^2 + |H_+|^2} \end{aligned} \tag{3.23}$$

and are all real-valued.

This definition coincides with how pseudospins are usually measured in exciton-polariton systems using the intensities of different polarizations [189, 191, 218]. It also gives experimentally measured real-valued pseudospins [191, 218, 199]. Moreover, it matches the non-antipodal behaviour of the pseudospins on the Bloch sphere, which reflects the non-orthogonality of the eigenstates [218].

From these experimentally measured components, I define the angles on the Bloch sphere as $\theta^R_\pm = \arccos S^{RR}_{z,\pm}$, $\phi^R_\pm = \arctan\left(S^{RR}_{y,\pm}/S^{RR}_{x,\pm}\right)$ [see Fig. 3.5]. Then, using the formalism presented in Ref. [189], the spinor wavefunction defined using these two angles recovers the right eigenstates and their conjugates

$$\begin{aligned} \begin{pmatrix} e^{-i\phi^R_\pm}\cos\frac{\theta^R_\pm}{2} \\ \sin\frac{\theta^R_\pm}{2} \end{pmatrix} &= \frac{1}{\sqrt{\langle\psi^R_\pm|\psi^R_\pm\rangle}}\sqrt{\frac{H_+^*}{H_+}}|\psi^R_\pm\rangle = |\bar{\psi}^R_\pm\rangle \\ \begin{pmatrix} e^{i\phi^R_\pm}\cos\frac{\theta^R_\pm}{2} & \sin\frac{\theta^R_\pm}{2} \end{pmatrix} &= \frac{1}{\sqrt{\langle\psi^R_\pm|\psi^R_\pm\rangle}}\sqrt{\frac{H_+}{H_+^*}}\langle\psi^R_\pm| = \langle\bar{\psi}^R_\pm|. \end{aligned} \tag{3.24}$$

In this approach, the right eigenstates $|\bar{\psi}^R_\pm\rangle$ are normalized as $\langle\bar{\psi}^R_\pm|\bar{\psi}^R_\pm\rangle = 1$. Plugging

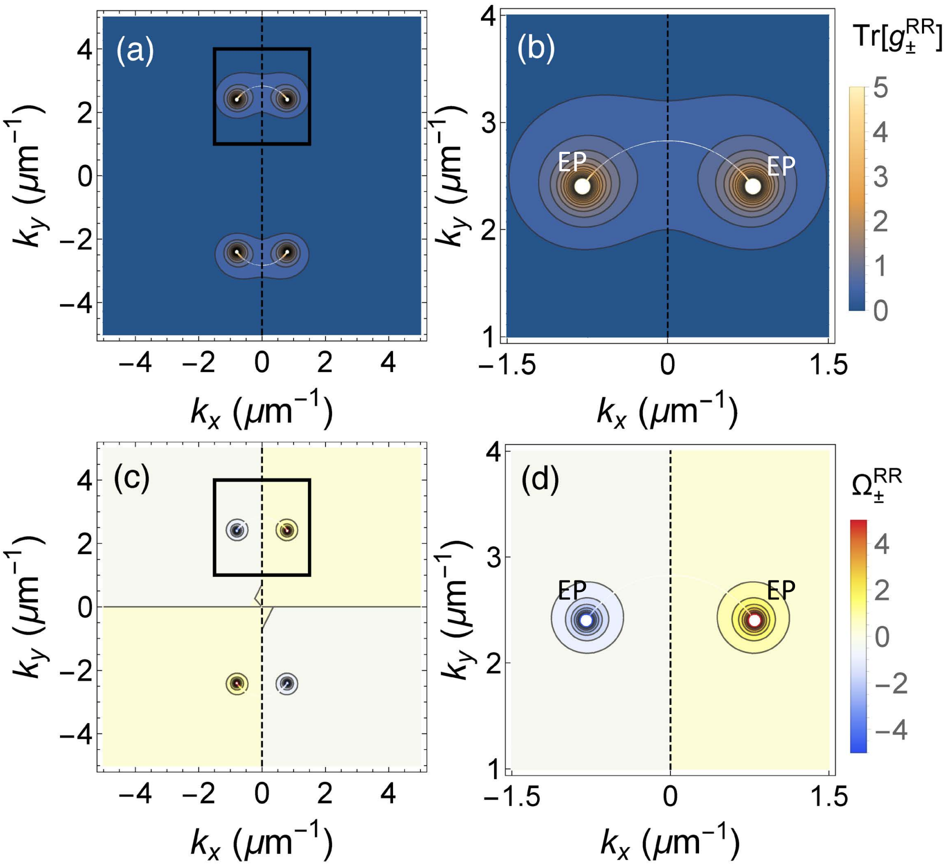

Figure 3.6: The trace of (a) the RR QMT and (c) the RR Berry curvature calculated from the eigenstates (left-half panel) and from the pseudospin components (right-half panel) at $\Delta = 0$ eV. Also showing the zoom-in near the exceptional points of $\mathrm{Tr}[g_{\pm}^{RR}]$ and $\Omega_{\pm}^{z,RR}$ in (b) and (d), respectively. Reprinted with permission from [61] © Optica Publishing Group.

the left-hand side back to the definition of the RR QGT in Eq. (1.57), the components of the RR QGT can be written as:

$$\begin{aligned} g_{\pm,\mu\nu}^{RR} &= \frac{1}{4}\Big(\partial_\mu\theta_\pm^R\partial_\nu\theta_\pm^R + \sin^2\theta_\pm^R\partial_\mu\phi_\pm^R\partial_\nu\phi_\pm^R\Big) \\ \Omega_{\pm,z}^{z,RR} &= \frac{1}{2}\sin\theta_\pm^R\Big(\partial_{k_x}\phi_\pm^R\partial_{k_y}\theta_\pm^R - \partial_{k_y}\phi_\pm^R\partial_{k_x}\theta_\pm^R\Big). \end{aligned} \tag{3.25}$$

This is the same result as the Hermitian case, Eqs. (1.54), showing that the formalism from Ref. [189] can be directly applied to non-Hermitian systems yielding the RR QMT and Berry curvature [199, 9].

To emulate the proposed experiment, I calculate the components of the RR QMT from the polariton pseudospins using Eqs. (3.25) and the parameters of the model (1.93) defined in Appendix A. The resulting distributions are plotted in Fig. 3.6 for the $\Delta = 0$ case and in Fig. 3.7 for the $\Delta \neq 0$ case. These distributions are then compared with those derived directly from the eigenstates in Eq. (1.57), which are plotted on the l.h.s.

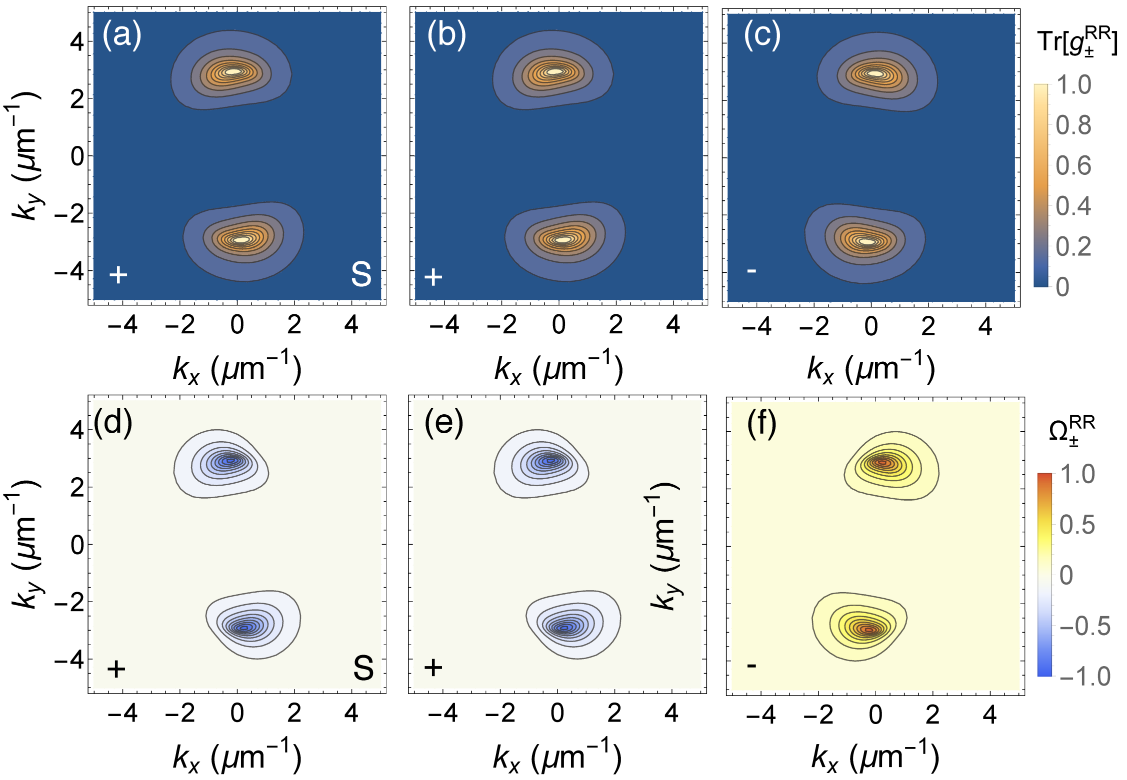

Figure 3.7: The traces of the right-right quantum geometric tensors of (b) the upper and (c) the lower bands. Also showing right-right Berry curvatures of (e) the upper and (f) the lower bands in a gapped phase with $\Delta = 0.0075$ eV, slightly larger than $|\Delta_c| = 0.00599$ eV. The results calculated from the eigenstates (b,e) show excellent agreement with the ones calculated from the pseudospins (a,d). Reprinted with permission from [61] © Optica Publishing Group.

of the panels (a-d) in Fig. 3.6 and on panels (b, e) in Fig. 3.7. We can see that the quantities calculated using these two different methods agree very well, which confirms the applicability of the formalism presented in Section 3.3 for non-Hermitian systems.

Figure 3.6 (a, b) shows the trace of the RR QMT and the RR Berry curvature calculated using Eqs. (3.15), which clearly shows the divergence of the components at the exceptional points. Note that the divergence of the Berry curvature is opposite for exceptional points in the same pair, which is reminiscent of their opposing spectral winding [218]. Note also that, unlike the Hermitian case [189], the divergence of the RR QMT components will persist for small values of Δ as long as the exceptional points persist. Interestingly, unlike the Hermitian case or the gapless case, $\Delta = 0$, in the gapped phase with $\Delta \neq 0$ [see Fig. 3.7], the components of the RR QGT are no longer symmetric in the momentum space as a result from the non-orthogonality of the right eigenstates.

In exciton-polariton systems, only the components of $\mathbf{S}_\pm^{RR}$ [218] and $Q_{\pm,\mu\nu}^{RR}$ [199] have been experimentally measured so far, and the left eigenstates are not directly accessible. Here,I present an approach enabling the reconstruction of the components of $\mathbf{S}_\pm^{LR}$ and $Q_{\pm,\mu\nu}^{LR}$, by measuring the pseudospins of the right eigenstates. In the following section, I will demonstrate LR generalisations of both, the non-Hermitian Berry curvature and quantum metric tensor using the non-Hermitian exciton-polariton model (1.93).

3.3.2 Left-Right Quantum Geometric Tensor

Measuring the LR QGT is not straightforward since the pseudospins of both the left and the right eigenstates are required. However, at least for the system considered here, experiments only have direct access to the right eigenstates. Fortunately, in a two-band system, the left eigenstates are closely related to the right eigenstate by the bi-orthonormality condition $\langle\psi^L_\pm|\psi^R_\pm\rangle = 1$ and $\langle\psi^L_\pm|\psi^R_\mp\rangle = 0$. The bi-orthogonality means that the left and right eigenstates with different indices are antipodal on the Bloch sphere, as shown in Fig. 3.8. The right and left eigenstates are actually mirrored images of each other where the plane of symmetry is formed by the real and imaginary parts of the effective field $\overrightarrow{\mathbf{H}} = \overrightarrow{\mathbf{G}} + i\overrightarrow{\mathbf{\Gamma}}$. Hence, the relation between the eigenstate pseudospins are simply:

$$\mathbf{S}^{LL}_\pm = -\mathbf{S}^{RR}_\mp, \tag{3.26}$$

where the components of $\mathbf{S}^L_\pm$ are defined as $S^{LL}_{j,\pm} = \langle\psi^L_\pm|\sigma_j|\psi^L_\pm\rangle/\langle\psi^L_\pm|\psi^L_\pm\rangle$.

The angles of the pseudospins of the left eigenstates in the Bloch sphere can then be written in terms of the right eigenstates as $\phi^L_\pm = \pi + \phi^R_\mp$, $\theta^L_\pm = \pi - \theta^R_\mp$. Hence, the left eigenstates can be reconstructed using the pseudospin textures (or the Bloch sphere angles) of the right eigenstates as:

$$\left(-e^{i\phi^R_\mp}\sin\tfrac{\theta^R_\mp}{2} \quad \cos\tfrac{\theta^R_\mp}{2}\right) = \frac{1}{\sqrt{\langle\psi^L_\pm|\psi^L_\pm\rangle}}\sqrt{\frac{H^*_-}{H_-}}\langle\psi^L_\pm| = \langle\bar{\psi}^L_\pm| \tag{3.27}$$

where $\langle\bar{\psi}^L_\pm|\bar{\psi}^L_\pm\rangle = 1$.

Given both the right and left eigenstates, I can then construct the spin components of the bi-orthogonal $\mathbf{S}^{LR}_\pm$ which I use to construct the LR QGT, $Q^{LR}_{\pm,\mu\nu}$. Similarly to the RR version [see Eqs. (3.22)], the pseudospin components are

$$S^{LR}_{j,\pm} = \frac{\langle\bar{\psi}^L_\pm|\sigma_j|\bar{\psi}^R_\pm\rangle}{\langle\bar{\psi}^L_\pm|\bar{\psi}^R_\pm\rangle}. \tag{3.28}$$

where $j = \{x, y, z\}$, following the bi-orthogonal formalism in Refs. [194, 195, 196, 197, 200]. Note that the components of $\mathbf{S}^{LR}_\pm$ are complex-valued, but they are constructed here from the real-valued components of $\mathbf{S}^R_\pm$ using Eqs. (3.27) and (3.28).

By expanding $S^{LR}_{j,\pm} = \langle\psi^L_\pm|\sigma_j|\psi^R_\pm\rangle/\langle\psi^L_\pm|\psi^R_\pm\rangle$, the LR pseudospins take the general forms as:

$$\begin{aligned}
S^{LR}_{x,\pm} &= \frac{2H_x(H_z \pm E)}{(H_z \pm E)^2 + H_x^2 + H_y^2} \\
S^{LR}_{y,\pm} &= \frac{2H_y(H_z \pm E)}{(H_z \pm E)^2 + H_x^2 + H_y^2} \\
S^{LR}_{z,\pm} &= \frac{(H_z \pm E)^2 - H_x^2 - H_y^2}{(H_z \pm E)^2 + H_x^2 + H_y^2}.
\end{aligned} \tag{3.29}$$

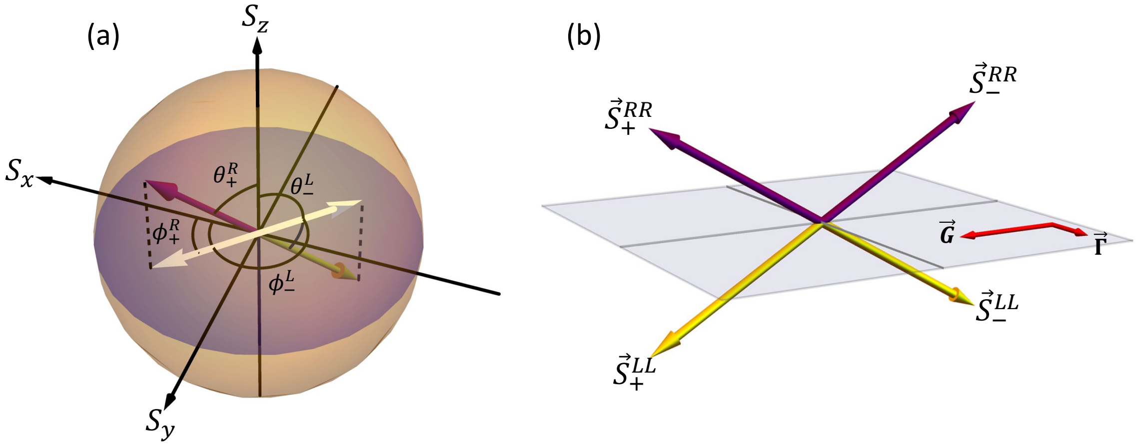

Figure 3.8: The pseudospin of the right (purple) and left (yellow) eigenstates with their projections (white) on the $[S_x, S_y]$-plane plotted with (a) the Bloch sphere. (b) Same as (a) but showing all four pseudospins oriented with respect to the real and imaginary parts of the effective magnetic field (red). The pseudospin $\mathbf{S}_\pm^R$ points in the opposite direction to $\mathbf{S}_\mp^L$, while the real and imaginary parts of the effective magnetic field define the mirror symmetry plane. Reprinted with permission from [61] © Optica Publishing Group.

In the Hermitian limit, $\operatorname{Re} H_+ = H_x$, while $\operatorname{Im} H_+ = H_y$, and $\mathbf{S}_\pm^{LR}$ becomes $\mathbf{S}_\pm^{RR}$. However, in a non-Hermitian system, the effective magnetic fields H_j are generally complex-valued, therefore the components of $\mathbf{S}_\pm^{LR}$ can be complex-valued as well. As a consequence, the angles $\phi_\pm^{LR}$, $\theta_\pm^{LR}$ also become complex valued.

Explicitly, the components of $\mathbf{S}_\pm^{LR}$ can be written in terms of the measured real-valued pseudospin angles $\phi_\pm^R$ and $\theta_\pm^R$, which can be reconstructed from the experiments [189, 191] as

$$\begin{aligned}
S_{x,\pm}^{LR} &= \frac{e^{-i\phi_\pm^R} \cos\frac{\theta_\mp^R}{2} \cos\frac{\theta_\pm^R}{2} - e^{i\phi_\mp^R} \sin\frac{\theta_\mp^R}{2} \sin\frac{\theta_\pm^R}{2}}{S_{0,\pm}} \\
S_{y,\pm}^{LR} &= \frac{ie^{-i\phi_\pm^R} \cos\frac{\theta_\mp^R}{2} \cos\frac{\theta_\pm^R}{2} + ie^{i\phi_\mp^R} \sin\frac{\theta_\mp^R}{2} \sin\frac{\theta_\pm^R}{2}}{S_{0,\pm}} \\
S_{z,\pm}^{LR} &= \frac{-e^{i(\phi_\mp^R - \phi_\pm^R)} \cos\frac{\theta_\pm^R}{2} \sin\frac{\theta_\mp^R}{2} - \cos\frac{\theta_\mp^R}{2} \sin\frac{\theta_\pm^R}{2}}{S_{0,\pm}} \\
S_{0,\pm} &= -e^{i(\phi_\mp^R - \phi_\pm^R)} \cos\frac{\theta_\pm^R}{2} \sin\frac{\theta_\mp^R}{2} + \cos\frac{\theta_\mp^R}{2} \sin\frac{\theta_\pm^R}{2} = \langle \bar{\psi}_\pm^L | \bar{\psi}_\pm^R \rangle
\end{aligned} \tag{3.30}$$

From these complex-valued pseudospin components, the corresponding complex angles on the Bloch sphere [189] , $\theta_\pm^{LR} = \arccos S_{z,\pm}^{LR}$ and $\phi_\pm^{LR} = \arctan\left(S_{y,\pm}^{LR} / S_{x,\pm}^{LR}\right)$, can be calculated as:

$$
\begin{aligned}
\phi^{LR}_{\pm} &= -i\tanh^{-1}\left(1+\frac{2}{e^{i(\phi^R_{\mp}+\phi^R_{\pm})}\tan\frac{\theta^R_{\mp}}{2}\tan\frac{\theta^R_{\pm}}{2}-1}\right)\\
\theta^{LR}_{\pm} &= \cos^{-1}\left(\frac{2}{1-e^{i(\phi^R_{\pm}-\phi^R_{\mp})}\cot\frac{\theta^R_{\mp}}{2}\tan\frac{\theta^R_{\pm}}{2}}-1\right).
\end{aligned}
\tag{3.31}
$$

Using these $\theta^{LR}_{\pm}$, $\phi^{LR}_{\pm}$, the bi-orthonormal left and right eigenstates are reconstructed as:

$$
\begin{aligned}
\begin{pmatrix} e^{-i\phi^{LR}_{\pm}}\cos\frac{\theta^{LR}_{\pm}}{2} \\ \sin\frac{\theta^{LR}_{\pm}}{2} \end{pmatrix} &= \frac{1}{\sqrt{\langle L_{\pm}|R_{\pm}\rangle}}\sqrt{\frac{h_-}{h_+}}|R_{\pm}\rangle = |\psi^R_{\pm}\rangle\\
\begin{pmatrix} e^{i\phi^{LR}_{\pm}}\cos\frac{\theta^{LR}_{\pm}}{2} & \sin\frac{\theta^{LR}_{\pm}}{2} \end{pmatrix} &= \frac{1}{\sqrt{\langle L_{\pm}|R_{\pm}\rangle}}\sqrt{\frac{h_+}{h_-}}\langle L_{\pm}| = \langle \psi^L_{\pm}|.
\end{aligned}
\tag{3.32}
$$

These can also be written in terms of the original angles, $\theta^R_{\pm}$ and $\phi^R_{\pm}$, by normalizing Eqs. (3.24) and (3.27) with respect to $\sqrt{\langle\bar{\psi}^L_{\pm}|\bar{\psi}^R_{\pm}\rangle}$, whose form is presented as $S^L_{0,\pm}R$ in Eqs. (3.30).

I emphasise that the denominators in Eq. (3.28) are necessary to recover the bi-orthonormality condition of the left and right eigenstates $\langle\psi^L_{\pm}|\psi^R_{\pm}\rangle = 1$, which are required for the LR QGT. Plugging the left-hand-side of $|\psi^R_{\pm}\rangle$, $\langle\psi^L_{\pm}|$ in the LR QGT definition in Eq. (1.58), the components of the LR QGT can be expressed as:

$$
\begin{aligned}
g^{LR}_{\pm,\mu\nu} =& \frac{1}{4}\left(\partial_\mu\theta^{LR}_{\pm}\partial_\nu\theta^{LR}_{\pm}+\sin^2\theta^{LR}_{\pm}\partial_\mu\phi^{LR}_{\pm}\partial_\nu\phi^{LR}_{\pm}\right)\\
\Omega^{z,LR}_{\pm} =& \frac{1}{2}\sin\theta^{LR}_{\pm}\left(\partial_{k_x}\phi^{LR}_{\pm}\partial_{k_y}\theta^{LR}_{\pm}-\partial_{k_y}\phi^{LR}_{\pm}\partial_{k_x}\theta^{LR}_{\pm}\right).
\end{aligned}
\tag{3.33}
$$

This form is similar to the Hermitian case Eqs. (1.54) and the RR QGT given by Eq. (1.57), but uses the complex angles $\theta^{LR}_{\pm}$ and $\phi^{LR}_{\pm}$. Interestingly, the LR QGT can also be written explicitly in terms of the Bloch angles of the right eigenstates as

$$
Q^{LR}_{\pm,\mu\nu} = \frac{e^{i(\phi^R_{\mp}+\phi^R_{\pm})}\left(\partial_\mu\theta^R_{\mp}+i\sin\theta^R_{\mp}\partial_\mu\phi^R_{\mp}\right)\left(\partial_\nu\theta^R_{\pm}+i\sin\theta^R_{\pm}\partial_\nu\phi^R_{\pm}\right)}{4\left[e^{i\phi^R_{\mp}}\cos(\theta^R_{\pm}/2)\sin(\theta^R_{\mp}/2)-e^{i\phi^R_{\pm}}\cos(\theta^R_{\mp}/2)\sin(\theta^R_{\pm}/2)\right]^2}.
\tag{3.34}
$$

Unfortunately, it is hard to extract a simple expression of the LR QMT and Berry curvature from this expression.

The components of $\mathbf{S}^{LR}_{j,\pm}$ and the angles $\theta^{LR}_{\pm}$, $\phi^{LR}_{\pm}$ are generally complex-valued. Unlike the RR pseudospin, which corresponds to the polarisation of the photon emission in real photonic or polaritonic systems, the LR versions of the pseudospins are not directly measurable. However, since they can be calculated from the experimentally measurable polariton pseudospins, Eq. (3.33) provides a way to experimentally determine the components of $Q^{LR}_{\pm,\mu\nu}$.

As noted previously, the components of $\mathbf{S}_\pm^{LR}$ can be constructed from the pseudospins of the right eigenstates, which can also be experimentally measured. The $\mathbf{S}_\pm^{LR}$ calculated from both the eigenstates and from the experimentally measurable pseudospin $\mathbf{S}_\pm^{R}$ is shown in Fig. 3.9, showing excellent agreement. The latter method provides a way to experimentally measure the components of the LR QGT, $Q_{\pm,\mu\nu}^{LR}$, in an exciton-polariton system.

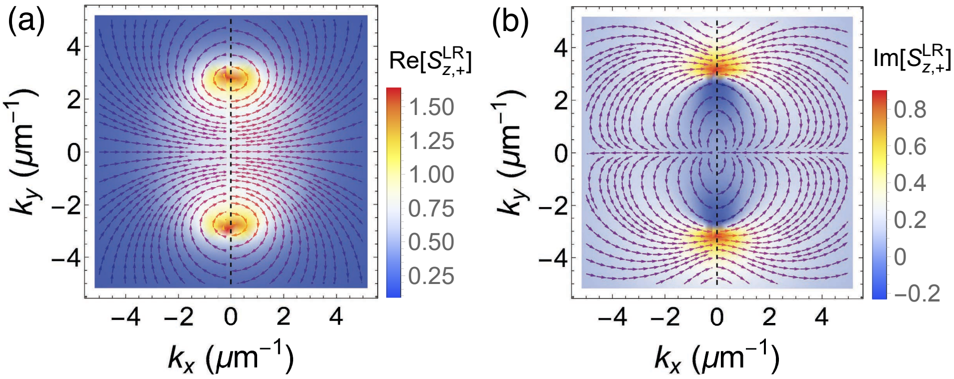

Figure 3.9: (a) Real part and (d) imaginary parts of $\mathbf{S}_+^{LR}$ calculated from the eigenstates (left-half panel) and the pseudospins $\mathbf{S}_\pm^{R}$ (right-half panel), respectively. The color denotes the out-of-plane components $S_{z,+}^{LR}$ while the arrows denote the in-plane components $(S_{x,+}^{LR}, S_{y,+}^{LR})$. To open the a gap, $\Delta = 0.0075$ eV was chosen. Reprinted with permission from [61] © Optica Publishing Group.

To visualize these in momentum space, I plot the real and imaginary parts of the trace of the LR QGT and the LR Berry curvature in Fig. 3.10 and compare with those derived from the pseudospins using Eq. (3.33). The plots clearly show that the formalism presented in Eqs. (3.33) and (3.34) works well for the LR QGT.

3.3.3 Non-Hermitian Anomalous Berry Connection

Just like the LR and RR QGTs, the NH anomalous Berry connection $\mathbf{A}_\pm^{RR} - \mathbf{A}_\pm^{LR}$ can be written in terms of the complex-valued angles of $\mathbf{S}_\pm^{LR}$, namely $\theta_\pm^{LR}$ and $\phi_\pm^{LR}$, as

$$\begin{aligned}\mathbf{A}_\pm^{RR} - \mathbf{A}_\pm^{LR} =& \frac{\cosh \operatorname{Im}\phi_\pm^{LR} \sinh \operatorname{Im}\theta_\pm^{LR} - i \sin \operatorname{Re}\theta_\pm^{LR} \sinh \operatorname{Im}\phi_\pm^{LR}}{2\cosh \operatorname{Im}\theta_\pm^{LR} \cosh \operatorname{Im}\phi_\pm^{LR} + 2\cos \operatorname{Re}\theta_\pm^{LR} \sinh \operatorname{Im}\phi_\pm^{LR}} \nabla_{\mathbf{k}}\theta_\pm^{LR} \\ &+ \left(\frac{e^{\operatorname{Im}\phi_\pm^{LR}} \left(\cos \operatorname{Re}\theta_\pm^{LR} + \cosh \operatorname{Im}\theta_\pm^{LR}\right)}{2\cosh \operatorname{Im}\theta_\pm^{LR} \cosh \operatorname{Im}\phi_\pm^{LR} + 2\cos \operatorname{Re}\theta_\pm^{LR} \sinh \operatorname{Im}\phi_\pm^{LR}} - \cos^2 \frac{\theta_\pm^{LR}}{2} \right) \nabla_{\mathbf{k}}\phi_\pm^{LR}.\end{aligned} \tag{3.35}$$

Since both $\phi_\pm^{LR}$ and $\theta_\pm^{LR}$ can be constructed by measuring the Stokes vector $\mathbf{S}_\pm^{R}$, this shows that $\mathbf{A}_\pm^{RR} - \mathbf{A}_\pm^{LR}$ [see Fig. 3.11] can be experimentally measured, and is also gauge-invariant [205].

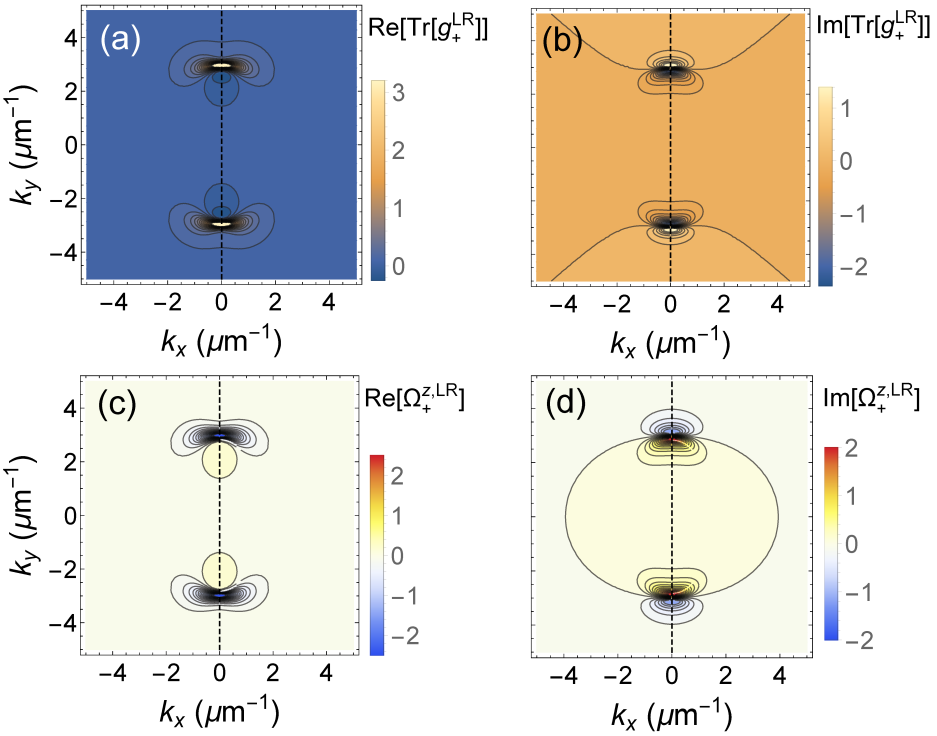

Figure 3.10: The real and imaginary parts of the trace of the (a), (b) LR QMT and the (c), (d) LR Berry curvature of the upper band, respectively. The left-half of each panel is calculated from the eigenstates and the right half is calculated from the pseudospins. The Zeeman splitting is large enough ($\Delta = 0.0075$ eV) such that the exciton-polariton bands are the gapped. Reprinted with permission from [61] © Optica Publishing Group.

3.4 Conclusion

In this Chapter, I derive the first-order perturbative corrections to the semi-classical equation of motion describing the centre-of-mass motion of a wavepacket in a non-Hermitian two-band system in the presence of a force field. My results show that both the left-right (LR) and right-right (RR) quantum geometric tensor (QGT) play a role in the dynamics. In particular, the RR QGT describes the non-Hermitian generalisation of the field-induced positional shift, while the LR QGT describes the field-induced correction to the Berry phase. Interestingly, my results also suggest a novel second-order anomalous Hall drift correction arising from the RR Berry curvature, and the positional-shift correction arising from the difference between the RR and LR QMT and the anomalous Berry connection. More importantly, these results show that the imaginary part of the LR QMT and Berry connections play a direct role in the second-order field-induced corrections, unlike the first-order case. Therefore, these results settle the dispute on whether the LR or the RR QGT should be used to describe the dynamics of non-Hermitian systems, and instead suggest that both LR and RR QGTs represent physical quantities and play a significant role in the dynamics.

I further confirmed the accuracy of the analytical results by simulating the center-of-mass dynamics of a wavepacket in the non-Hermitian system with a gapped spectrum,

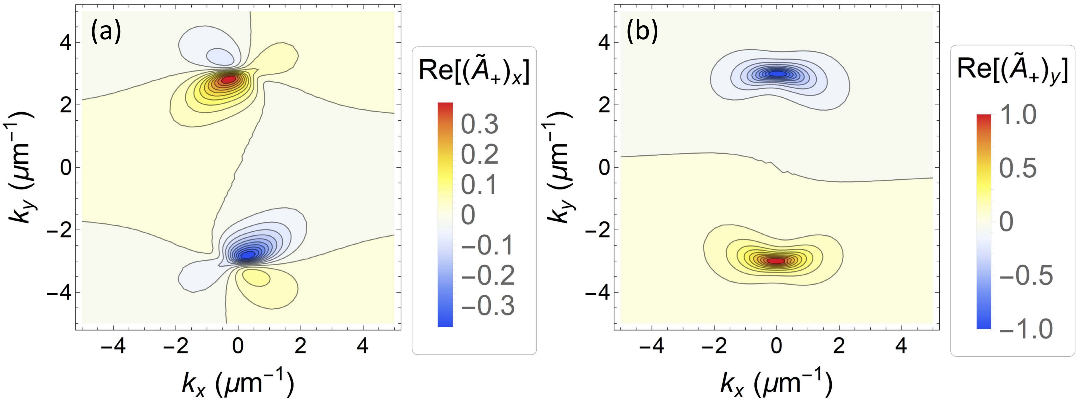

Figure 3.11: Non-Hermitian anomalous Berry connection $\tilde{\mathbf{A}} = \mathbf{A}^{\mathbf{RR}} - \mathbf{A}^{\mathbf{LR}}$ of the upper band of the exciton-polariton system described by Eq. (1.93). The x and y components are presented separately. Reprinted with permission from [61] © Optica Publishing Group.

which can be realised in microcavity exciton-polaritons exposed to a strong out-of-plane magnetic field [232, 234] or hosted in liquid-crystal cavities [220].

I also show that the components of both the RR and LR QGT as well as the NH anomalous Berry connection can be experimentally measured in a microcavity exciton-polariton system. In particular, I proposed a method for inferring the left eigenstates from the directly accessible right eigenstates, which enable the measurement of the observables defined in the LR conventions.

My work also opens up possibilities for further investigation of the QGT in non-Hermitian systems. In particular, the results presented in this Chapter should be relevant for the physics of second-harmonic generation [177], non-linear response theory [175, 176], quantum information [184, 185] and flat-band superconductivity [181, 182, 183], where the quantum metric tensor plays a significant role.

Chapter 4

Non-Hermitian Zitterbewegung Effects

Disclaimer: This Chapter contains results from my previous published work "Zitterbewegung effect and quantum geometry in non-Hermitian exciton-polariton systems", *Appl. Phys. Lett.* **127**, 253101 (2025).

4.1 Introduction

In this Chapter, I present a non-Hermitian generalization of the Zitterbewegung effect for wavepackets. The Zitterbewegung effect, as first proposed by Erwin Schrodinger in 1930 [284], refers to the trembling motion of relativistic electrons described by the Dirac equation due to interference between states with positive and negative energies [122]. Fascinatingly, it was later discovered that the Zitterbewegung effect can also arise from the precession of the phase of the wavefunction [285], and it can also be realised in non-relativistic quantum systems exhibiting spin precession and spin-orbit coupling [286, 287]. More recently, it has been shown that the Zitterbewegung effect can occur in a wide range of physical systems with spin-orbit coupling such as semiconductor quantum wells [288, 289], graphene [290, 291], ultracold atoms [292], trapped ions [293, 294], photonics [295, 296, 297, 298] and exciton-polariton systems [235, 236].

It was shown that spin dynamics in non-Hermitian systems exhibits qualitatively different behavior to its Hermitian counterpart [273, 299, 300, 272, 301, 302, 303, 304]. The non-Hermiticity induces a nonlinear term in the mean-field equation of motion describing the expectation value of the spin operator, and the system becomes sensitive to the initial condition. Since the spin dynamics is closely related to the Zitterbewegung effect, non-Hermiticity is expected to play a significant role in modifying the wavepacket dynamics. In this Chapter, I present results of my study on the generalised Zitterbewegung effect, which is a consequence of the distinct spin dynamics in non-Hermitian systems.

I consider the general two-band non-Hermitian Hamiltonian written in terms of real and imaginary effective fields $\overrightarrow{\mathbf{G}}$, $\overrightarrow{\mathbf{\Gamma}}$ as previously discussed in Chapter. 1 [see Eq. (1.88)]

$$\hat{H}(\mathbf{k}) = (G_0(\mathbf{k}) + i\Gamma_0(\mathbf{k}))\mathbf{I} + (\overrightarrow{\mathbf{G}}(\mathbf{k}) + i\overrightarrow{\mathbf{\Gamma}}(\mathbf{k})) \cdot \overrightarrow{\boldsymbol{\sigma}}, \tag{4.1}$$

where the individual terms are discussed in Section 1.5.

I first present an overview of the pseudospin dynamics in Hermitian and non-Hermitian systems. I then derive a semi-classical equation of motion that describes the generalized Zitterbewegung effect in the non-Hermitian systems and compare the analytical theory with numerical simulation using the non-Hermitian model (1.93) describing a perovskite-based exciton-polariton system. I also present the semi-classical equation of motion in a simpler non-Hermitian Dirac model described by Eq. (1.92) to gain some intuition on the dynamics. The main results are general and can be used to describe wavepacket dynamics in any non-Hermitian two-band system described by the Hamiltonian in the form of Eq. (1.88).

4.2 Pseudospin Dynamics

In Hermitian systems, the effective magnetic field $\overrightarrow{\mathbf{G}}$ results in the precession of the pseudospins with the frequency $2E/\hbar$, where $E = \sqrt{\overrightarrow{\mathbf{G}} \cdot \overrightarrow{\mathbf{G}}}$ is the mean-subtracted eigenenergy [see Fig. 4.1]. This can be seen from the equation of motion that describes the pseudospin $\overrightarrow{\mathbf{S}}$ dynamics in a two-band Hermitian system described by Eq. 4.1 with $\overrightarrow{\mathbf{\Gamma}} = 0$,

$$\frac{d}{dt}\overrightarrow{\mathbf{S}} = \frac{2}{\hbar}\Big(\overrightarrow{\mathbf{S}} \times \overrightarrow{\mathbf{G}}\Big), \tag{4.2}$$

which has a general solution of the form

$$\overrightarrow{\mathbf{S}}(t) = \frac{(\overrightarrow{\mathbf{G}} \cdot \overrightarrow{\mathbf{S}}_0)}{E^2}\overrightarrow{\mathbf{G}} - \frac{\overrightarrow{\mathbf{G}} \times (\overrightarrow{\mathbf{G}} \times \overrightarrow{\mathbf{S}}_0)}{E^2}\cos\left(\frac{2Et}{\hbar}\right) - \frac{\overrightarrow{\mathbf{G}} \times \overrightarrow{\mathbf{S}}_0}{E}\sin\left(\frac{2Et}{\hbar}\right) \tag{4.3}$$

with the initial condition $\overrightarrow{\mathbf{S}}(t=0) = \overrightarrow{\mathbf{S}}_0$.

In a two-band non-Hermitian system, the imaginary effective magnetic field gives rise to additional terms in the equation of motion and the dynamics of the pseudospins can be described by the equation

$$\frac{d}{dt}\overrightarrow{\mathbf{S}} = \frac{2}{\hbar}\Big(\overrightarrow{\mathbf{S}} \times \overrightarrow{\mathbf{G}} - (\overrightarrow{\mathbf{\Gamma}} \cdot \overrightarrow{\mathbf{S}})\overrightarrow{\mathbf{S}} + \overrightarrow{\mathbf{\Gamma}}\Big) \tag{4.4}$$

with the additional nonlinear terms as the results of the non-Hermiticity [273, 299, 300, 301, 302, 303, 304]. This equation also closely resembles the Landau-Lifshitz-Gilbert equation describing a damped spin precession [20, 21],

$$\frac{d}{dt}\overrightarrow{\mathbf{S}} = \frac{2}{\hbar}\Big(\overrightarrow{\mathbf{S}} \times \overrightarrow{\mathbf{G}} - (\lambda\overrightarrow{\mathbf{G}} \cdot \overrightarrow{\mathbf{S}})\overrightarrow{\mathbf{S}} + \lambda\overrightarrow{\mathbf{G}}\Big), \tag{4.5}$$

but the damping term $\lambda\overrightarrow{\mathbf{G}}$ (where λ is a damping constant) is replaced by another imaginary-valued effective field $\overrightarrow{\mathbf{\Gamma}}$. This is because the pseudospins here are defined in the RR formalism, and therefore are always real-valued and normalized [see Chapter 3 for more details].

Although I am unable to solve the differential equations in Eq. (4.4) analytically, I

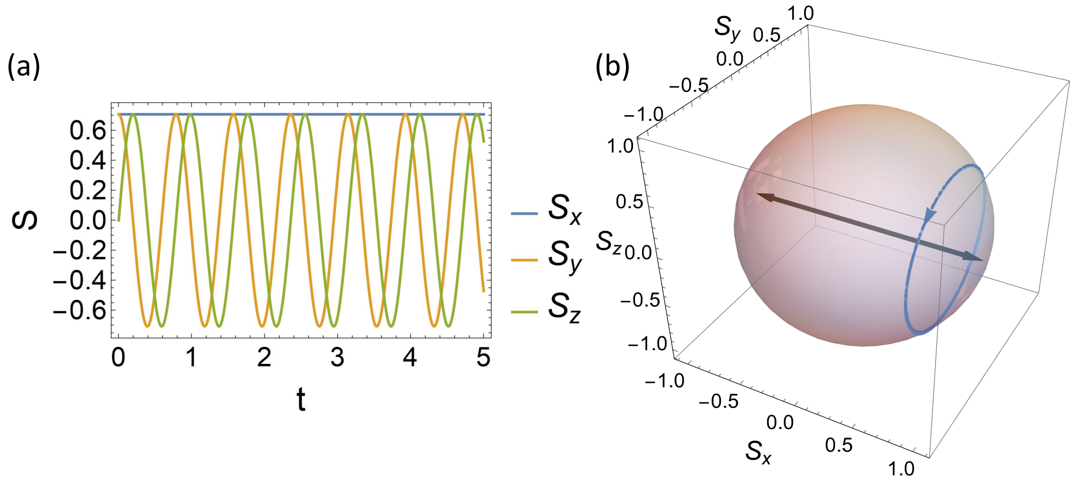

Figure 4.1: Pseudospin dynamics in a Hermitian system described by the model Hamiltonian (4.1) with $\mathbf{\Gamma} = 0$, plotted in (a) as time dependence of the components of the Stokes vector, and (b) as trajectories on the Bloch sphere. Here, the blue arrow denotes the trajectory of the pseudospin and the black arrows denote the pseudospins of the two eigenstates. Reproduced from [305], with the permission of AIP Publishing.

can compute the time evolution of the pseudospins using the time evolution operator

$$S_j = \frac{\langle\psi_0|e^{i\hat{H}^\dagger t/\hbar}\sigma_j e^{-i\hat{H}t/\hbar}|\psi_0\rangle}{\langle\psi_0|e^{i\hat{H}^\dagger t/\hbar}e^{-i\hat{H}t/\hbar}|\psi_0\rangle} \tag{4.6}$$

where $|\psi_0\rangle$ denotes the initial spinor wavefunction. The time evolution operator can be defined using the usual form of matrix exponential in terms of the components of the effective magnetic field H_j [272]:

$$e^{-i\frac{\hat{H}}{\hbar}t} = e^{-i\frac{H_0}{\hbar}t}\mathbf{I}\cdot\begin{pmatrix}\cos\frac{Et}{\hbar} - \frac{iH_z}{E}\sin\frac{Et}{\hbar} & -i\frac{H_x - iH_y}{E}\sin\frac{Et}{\hbar} \\ -i\frac{H_x + iH_y}{E}\sin\frac{Et}{\hbar} & \cos\frac{Et}{\hbar} + \frac{iH_z}{E}\sin\frac{Et}{\hbar}\end{pmatrix} \tag{4.7}$$

which is valid everywhere except at the exceptional points, where the two eigenstates coalesce and the Hamiltonian operator is no longer diagonalizable [6]. At the exceptional points, the dynamics can be determined by solving the differential equation in Eq. (4.4).

As an illustrative example, I consider a simple case with zero z-component of the effective magnetic field, i.e. $G_z = \Gamma_z = 0$, and the initial pseudospin pointing up on the Bloch sphere $\mathbf{S}(t=0) = (0,0,1)$. In this case, the dynamics of the pseudospins has the form

$$\begin{aligned} S_x =& \frac{2\,\mathrm{Im}\left[\sqrt{H_+H_-^*}\right]\sin\frac{2\,\mathrm{Re}[E]t}{\hbar}+2\,\mathrm{Re}\left[\sqrt{H_+H_-^*}\right]\sinh\frac{2\,\mathrm{Im}[E]t}{\hbar}}{(|H_-|-|H_+|)\cos\frac{2\,\mathrm{Re}[E]t}{\hbar}+(|H_-|+|H_+|)\cosh\frac{2\,\mathrm{Im}[E]t}{\hbar}} \\ S_y =& \frac{-2\,\mathrm{Re}\left[\sqrt{H_+H_-^*}\right]\sin\frac{2\,\mathrm{Re}[E]t}{\hbar}-2\,\mathrm{Im}\left[\sqrt{H_+H_-^*}\right]\sinh\frac{2\,\mathrm{Im}[E]t}{\hbar}}{(|H_-|-|H_+|)\cos\frac{2\,\mathrm{Re}[E]t}{\hbar}+(|H_-|+|H_+|)\cosh\frac{2\,\mathrm{Im}[E]t}{\hbar}} \\ S_z =& \frac{(|H_-|+|H_+|)\cos\frac{2\,\mathrm{Re}[E]t}{\hbar}+(|H_-|-|H_+|)\cosh\frac{2\,\mathrm{Im}[E]t}{\hbar}}{(|H_-|-|H_+|)\cos\frac{2\,\mathrm{Re}[E]t}{\hbar}+(|H_-|+|H_+|)\cosh\frac{2\,\mathrm{Im}[E]t}{\hbar}}, \end{aligned} \tag{4.8}$$

where I denote $H_\pm = H_x \pm iH_y$ to simplify the expressions. I should also emphasize that although there is not a simple closed form for solution like in the Hermitian case (4.3), the pseudospin dynamics in this general non-Hermitian system is always analytically trackable and deterministic. I chose the simple case with $H_z = 0$ simply because the expression would become more complicated otherwise, and the behaviour is not qualitatively different between the $H_z \neq 0$ and $H_z = 0$ cases.

Here, similar to the Hermitian case, the pseudospins oscillate with the frequency of $2\,\mathrm{Re}\,E/\hbar$. Although, the oscillations are no longer harmonic due to the denominators. Furthermore, the amplitude of oscillation is decaying as a result of $\mathrm{Im}\,E$. However, it is difficult to analytically compute the decay rate.

The pseudospin dynamics also shows distinct behaviour in special cases, such as at the exceptional point or on the bulk or imaginary Fermi arcs. On the imaginary Fermi arcs, there is no decay in the amplitude of the pseudospin precession. The pseudospins therefore oscillate anharmonically [see Figs. 4.2(c,f)]. While at the exceptional points or on the bulk Fermi arc, there is no oscillation, and the pseudospin will align with the pseudospin of the less dissipative eigenstate [see Figs. 4.2(b,e)]. On the other hand, when away from both the imaginary and the bulk Fermi arc, the pseudospin will oscillate while also decaying towards the less dissipative eigenstate [see Figs. 4.2(a,d)].

4.3 Zitterbewegung Effects

The Zitterbewegung effects can be realised in a two-band system Eq. (4.1) with a Gaussian wavepacket initially prepared a superposition of the two eigenstates, and the spatial distribution of the wavepacket is narrowly focused in momentum space, $|\psi(\mathbf{k})|^2 \propto \delta(\mathbf{k}-\mathbf{k}_c)$. In the Hermitian case, the dynamics of the wavepacket centre of mass can be described by the equation of motion [235]

$$\hbar(\dot{\mathbf{r}}_H)_i = \partial_{k_i} G_0 + \partial_{k_i}\overrightarrow{\mathbf{G}}\cdot\overrightarrow{\mathbf{S}}\Big|_{\mathbf{k}=\mathbf{k}_c}, \tag{4.9}$$

where $\mathbf{k}_c$ denotes the centre-of-mass momentum of the wavepacket. The spin (or pseudospin) precession and non-vanishing $\partial_{\mathbf{k}}\overrightarrow{\mathbf{G}}$ arising from spin-orbit coupling result in the oscillation of the wavepacket centre-of-mass motion [235].

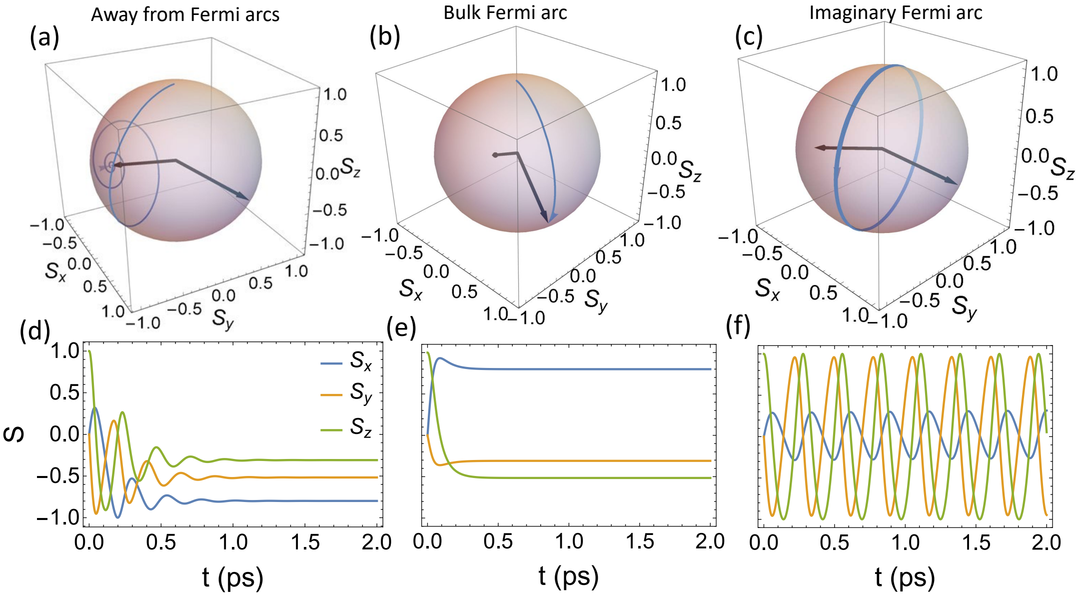

Figure 4.2: The pseudospin dynamics as (a-c) trajectories on the Bloch sphere and (d-f) respective time-dependences of the Stokes vector components. The initial wavefunction is chosen to be uniformly distributed in the momentum space, while each panel shows the pseudospin dynamics on a single point in momentum space: (a,d) away from the Fermi arcs at $\mathbf{k} = (1.5, 1.5)\mu\text{m}^{-1}$, (b,e) on the bulk Fermi arc at $\mathbf{k} = (0.5, 2.685)\mu\text{m}^{-1}$ and (c,f) on the imaginary Fermi arc at $\mathbf{k} = (0.9, 1.22)\mu\text{m}^{-1}$. The blue arrows represent the trajectories of the pseudospins and the black arrows represent the pseudospins of the two eigenstates. The initial pseudospin configuration is chosen to be $\mathbf{S} = (0, 0, 1)$ as an example. Reproduced from [305], with the permission of AIP Publishing.

In non-Hermitian systems, the non-Hermiticity of the Hamiltonian operators not only modifies the pseudospin dynamics, but also gives rise to novel effects not found in the usual Hermitian systems. In a non-Hermitian system, the dynamics of the wavepacket can be described using the equation of motion:

$$\begin{aligned}\hbar(\dot{\mathbf{r}})_i =& \hbar(\dot{\mathbf{r}}_H)_i + \frac{2t}{\hbar}(\vec{\mathbf{\Gamma}} \cdot \partial_{k_i}\vec{\mathbf{G}}) - \frac{2t}{\hbar}\Big(\vec{\mathbf{\Gamma}} \cdot (\partial_{k_i}\vec{\mathbf{\Gamma}} \times \vec{\mathbf{S}})\Big) - \frac{2t}{\hbar}(\vec{\mathbf{\Gamma}} \cdot \vec{\mathbf{S}})(\partial_{k_i}\vec{\mathbf{G}} \cdot \vec{\mathbf{S}}) \\ &+ 2(\vec{\mathbf{\Gamma}} \cdot \mathrm{Re}[\vec{\mathbf{B}}_i]) - 2\Big(\vec{\mathbf{\Gamma}} \cdot (\mathrm{Im}[\vec{\mathbf{B}}_i] \times \vec{\mathbf{S}})\Big) - 2(\vec{\mathbf{\Gamma}} \cdot \vec{\mathbf{S}})(\mathrm{Re}[\vec{\mathbf{B}}_i] \cdot \vec{\mathbf{S}}),\end{aligned} \tag{4.10}$$

where $\mathbf{B}$ is defined as

$$\vec{\mathbf{B}}_i = -\frac{1}{2E^2}\left(\cos\frac{2Et}{\hbar} - 1\right)(\vec{\mathbf{H}} \times \partial_{k_i}\vec{\mathbf{H}}) + \frac{1}{2E^3}\left(\sin\frac{2Et}{\hbar} - \frac{2Et}{\hbar}\right)\Big((\vec{\mathbf{H}} \times \partial_{k_i}\vec{\mathbf{H}}) \times \vec{\mathbf{H}}\Big). \tag{4.11}$$

As will be shown in the later Sections, the non-Hermitian corrections in Eq. (4.10) give rise to novel behaviours including both damping and enhancing of the oscillation amplitude of the wavepacket COM, as well as frequency doubling. Although the components of $\mathbf{B}$

can be non-zero even in Hermitian systems, all of the corrections in terms of $\overrightarrow{\mathbf{B}}$ are also proportional to the components of $\overrightarrow{\boldsymbol{\Gamma}}$, which will vanish in the Hermitian limit. I also note that in the special case with $H_z = 0$, i.e. no effective out-of-plane magnetic field, the non-Hermitian correction can be simplified as

$$\overrightarrow{\mathbf{B}}_i = \sqrt{g^{LR}_{k_i k_i}} \Big[-\Big(\cos\frac{2Et}{\hbar} - 1 \Big)\hat{\mathbf{z}} + \Big(\sin\frac{2Et}{\hbar} - \frac{2Et}{\hbar} \Big)\Big(-\frac{H_y}{E}\hat{\mathbf{x}} + \frac{H_x}{E}\hat{\mathbf{y}} \Big) \Big] \tag{4.12}$$

where $g^{LR}_{\mathbf{kk}} = (g^{LR}_{k_x k_x}, g^{LR}_{k_y k_y})$ represents the diagonal elements of the left-right quantum metric tensor (LR QMT) [see Section 1.3 for more information]

$$\begin{aligned} g^{LR}_{n,\mu\nu} =& \frac{1}{2}\Big(\langle \partial_\mu \psi^L_n | \partial_\nu \psi^R_n \rangle + \langle \partial_\nu \psi^L_n | \partial_\mu \psi^R_n \rangle \Big) \\ &+ \langle \partial_\mu \psi^L_n | \psi^R_n \rangle \langle \psi^L_n | \partial_\nu \psi^R_n \rangle \end{aligned} \tag{4.13}$$

which satisfies that $g^{LR}_+ = g^{LR}_- = g^{LR}$ in a two-band system. Note that in the case with $H_z = 0$, the diagonal components of LR QMT take the form of

$$g^{LR}_{\mathbf{kk}} = \frac{(H_x \partial_{\mathbf{k}} H_y - H_y \partial_{\mathbf{k}} H_x)^2}{4E^4}. \tag{4.14}$$

The LR QMT arises naturally from the additional terms that involve the momentum-derivatives of the Hamiltonian operator. On the other hand, the RR QMT needs to be constructed using both the Hamiltonian and its Hermitian conjugate, which do not appear together in the derivation. For details in derivation of Eqs. (4.10, 4.12), please refer to the Appendix D.

4.4 Zitterbewegung Effects in a Perovskite-Based Exciton-Polariton System

To provide a concrete example of the dynamics, I numerically simulate the dynamics of a Gaussian wavepacket that has a narrow but finite width in momentum space in a perovskite micarocavity exciton-polariton system described by the Hamiltonian (1.93). The initial state is prepared in a right-handed circularly polarized wavepacket

$$|\psi_0\rangle = e^{-\frac{(\mathbf{k}-\mathbf{k}_c)^2}{4w^2}} \begin{pmatrix} 1 \\ 0 \end{pmatrix}, \tag{4.15}$$

which then evolves in discrete time $dt = 0.01$ ps in momentum space. I then calculate the centre-of-mass position and the group velocity via the discrete Fourier transform every 4 steps. Since there is no external force in this case, the split-step method used in the previous Section was not needed. I also change the values of the centre-of-mass momentum $\mathbf{k}_c$ to simulate the wavepackets initially placed on the imaginary and bulk Fermi arcs, and away from the Fermi arcs to demonstrate the effects captured by Eq. (4.12) in different cases.

When the wavepacket is placed on the bulk Fermi arc, the group velocity will decay to a constant with no oscillation [see Fig. 4.3 (a-e)]. When the wavepacket is away from the Fermi arcs, the group velocity will oscillate anharmonically with a decreasing amplitude, and eventually will decay to a constant group velocity [see Fig. 4.3 (f-j)]. When the wavepacket is placed initially on the imaginary Fermi arc, it will oscillate anharmonically in time and the amplitude will grow due to the terms proportional to $2t/\hbar^2$ in Eq. (4.12) [see Fig. 4.3 (k-o)]. However, this only holds under the assumption that the wavepacket is infinitely narrow and its probability density distribution is described by a Dirac delta function in momentum space, and therefore experiences no self-acceleration. When the self-acceleration is present, the wave packet will move away from the imaginary Fermi arcs, and the amplitude of the oscillation will decay.

4.5 Zitterbewegung Effect in a Non-Hermitian Dirac Model

I note that the semi-classical equation in Eqs. (4.10, 4.12) are fairly complicated and difficult to gain intuition from. However, for the gapless two-band non-Hermitian Dirac model described by the Hamiltonian in Eq. (1.92) with $\Delta = 0$, I can simplify the equations of motion on the bulk and imaginary Fermi arcs. In this Section, I set $\hbar = 1$ for simplicity.

The diagonal elements of the left-right quantum metric tensor (1.66) for the non-Hermitian Dirac model take the forms

$$\begin{aligned} g_{xx}^{LR} &= \frac{(k_y - i\kappa)^2}{4E^4} \\ g_{yy}^{LR} &= \frac{k_x^2}{4E^4} \end{aligned} \tag{4.16}$$

where $E = \sqrt{k_x^2 + (k_y - i\kappa)^2}$, where κ denotes an imaginary effective field in the y-direction. Note that $\sqrt{g_{xx}^{LR}}$ is purely imaginary and $\sqrt{g_{yy}^{LR}}$ is purely real on both the bulk and imaginary Fermi arcs. Using these identities, I can write down a simple form of the equation of motion (4.12) on the imaginary Fermi arc:

$$\begin{aligned} \frac{d}{dt}\langle \hat{x} \rangle =& S_x + 2t\kappa S_x S_y + 2\,\mathrm{Im}\left[\sqrt{g_{xx}^{LR}}\right]\Bigg(-(\cos 2\,\mathrm{Re}[E]t - 1)\kappa S_x \\ & - \left(\frac{\sin 2\,\mathrm{Re}[E]t}{\mathrm{Re}[E]} - 2t\right)\kappa^2 S_x S_y \Bigg) \\ \frac{d}{dt}\langle \hat{y} \rangle =& S_y - 2t\kappa(1 - S_y^2)) + 2\,\mathrm{Re}\left[\sqrt{g_{yy}^{LR}}\right]\Bigg(\left(\frac{\sin 2\,\mathrm{Re}[E]t}{\mathrm{Re}[E]} - 2t\right)(-\kappa k_x - \kappa^2 S_z + \kappa k_x S_y^2) \\ & - (\cos 2\,\mathrm{Re}[E]t - 1)\kappa S_y S_z \Bigg), \end{aligned} \tag{4.17}$$

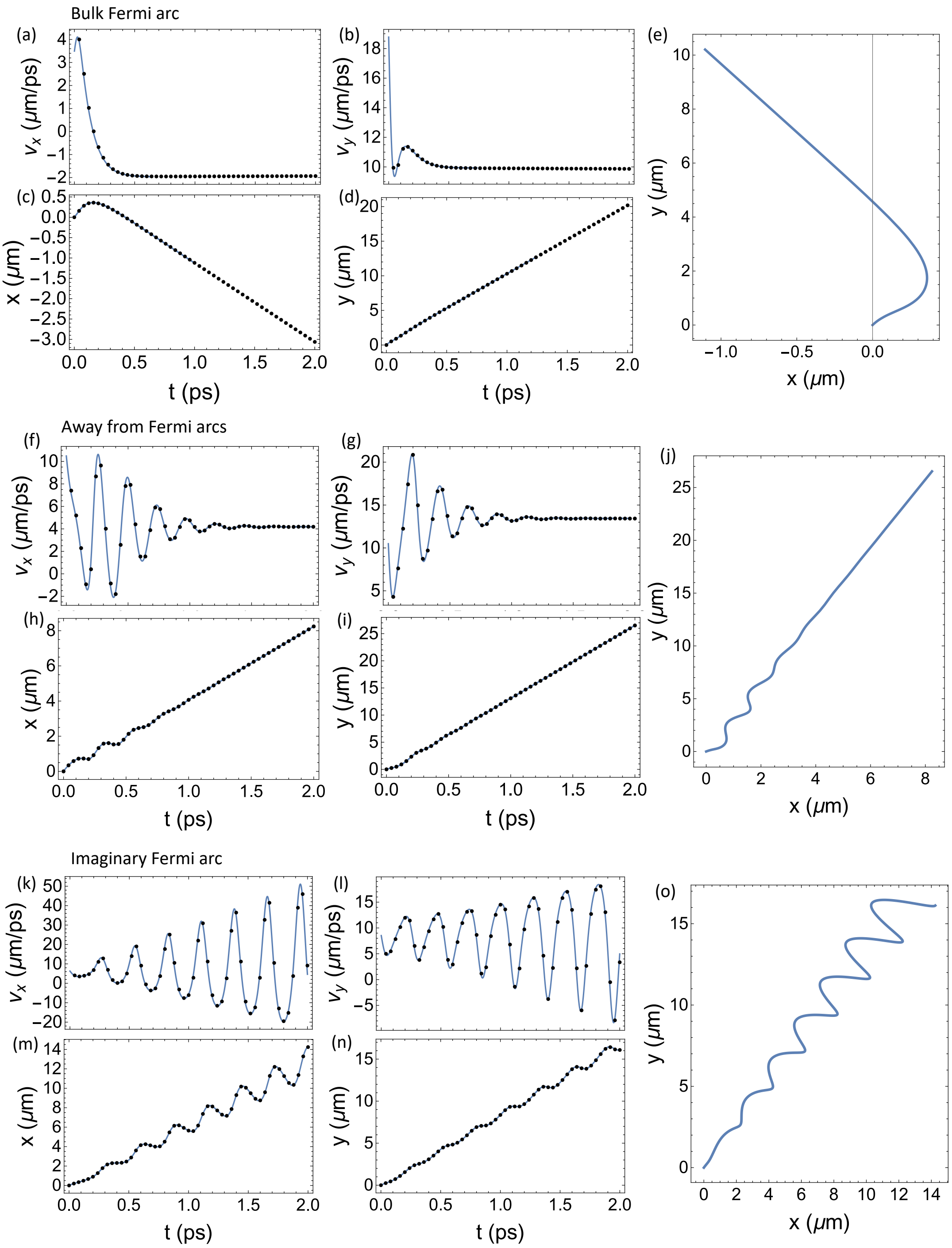

Figure 4.3: The group velocities (a,b,f,g,k,l) and centre-of-mass positions (c,d,h,i,m,n) of a Gaussian wavepacket initially centred at (a-d) $\mathbf{k} = (0.5, 2.685)\mu\mathrm{m}^{-1}$ (on the bulk Fermi arc), (f-i) $\mathbf{k} = (1.5, 1.5)\mu\mathrm{m}^{-1}$ (away from the Fermi arcs) and (k-n) $\mathbf{k} = (0.9, 1.22)\mu\mathrm{m}^{-1}$ (on the imaginary Fermi arc) as a function of time. The corresponding trajectories in real space are shown in (e,j,o). The lines represent analytical results derived from Eq. (4.12) and the black dots represent the numerical results for a Gaussian wavepacket with the initial with of $w = 0.005\mu\mathrm{m}^{-1}$ in momentum space. Reproduced from [305], with the permission of AIP Publishing.

and on the bulk Fermi arc

$$\begin{aligned}\frac{d}{dt}\langle\hat{x}\rangle =& S_x + 2t\kappa S_x S_y + 2\,\mathrm{Im}\left[\sqrt{g_{xx}^{LR}}\right]\Bigg(-(\cosh 2\,\mathrm{Im}[E]t - 1)\kappa S_x \\ & - \left(\frac{\sinh 2\,\mathrm{Im}[E]t}{\mathrm{Im}[E]} - 2t\right)\kappa^2 S_x S_y\Bigg) \\ \frac{d}{dt}\langle\hat{y}\rangle =& S_y - 2t\kappa(1 - S_y^2)) + 2\,\mathrm{Re}\left[\sqrt{g_{yy}^{LR}}\right]\Bigg(\left(\frac{\sinh 2\,\mathrm{Im}[E]t}{\mathrm{Im}[E]} - 2t\right)(-\kappa k_x - \kappa^2 S_z + \kappa k_x S_y^2) \\ & - (\cosh 2\,\mathrm{Im}[E]t - 1)\kappa S_y S_z\Bigg).\end{aligned} \tag{4.18}$$

The equations of motion in these two special cases highlight the oscillation driven by Re$[E]$ and decay in the amplitude of the oscillation as a direct result of Im$[E]$.

Similarly to the exciton-polariton model in the previous Section, I also simulate the wavepacket dynamics to confirm the validity of the semi-classical equation of motions in the non-Hermitian Dirac model. Here, the initial state is set to

$$|\psi_0\rangle = e^{-\frac{(\mathbf{k}-\mathbf{k}_c)^2}{4w^2}}\begin{pmatrix} 0.5 - 0.5i \\ \frac{1}{\sqrt{2}} \end{pmatrix}, \tag{4.19}$$

with $w = 0.005$ μm^{-1}. The wavepacket is also narrow in the k-space and has initial pseudospin texture of $\overrightarrow{\mathbf{S}} = (1/\sqrt{2}, 1/\sqrt{2}, 0)$. This initial state was chosen because if the S_x (S_y) component of the initial wavepacket is zero, v_x (v_y) is also zero, as can be seen from Eqs. (4.17, 4.18). Similarly to the results obtained in the perovskite-based exciton-polariton model, the simulation shows strong agreement with the analytical theory as well as qualitatively different behaviour on the bulk and imaginary Fermi arcs, and away from the Fermi arcs [see Fig. 4.4].

Interestingly, the $O(S^2)$-terms in Eqs. (4.17) can also give rise to the oscillation frequency doubling which is not seen in the usual Hermitian cases. To highlight this, I plot the Fourier transforms of the group velocities in the frequency space for the initial wavepacket centered on the imaginary Fermi arc. I use the discrete Fourier transform in Wolfram Mathematica, with discretization of $\Delta T = 0.05$ for the time step and $N = 4000$ for the total number of time steps, where $t = n\Delta T$, $n = 1, ..., N$. I then plot the results from the discrete Fourier transform with the frequency defined as $\omega = n\Delta\omega$, where $\Delta\omega = 2\pi/(N\Delta T)$, $n = 1, ..., N$. This procedure results in two copies of the frequency spectrum, but since they are symmetric, I only plot one set of them in Fig. 4.5. Each of v_x and v_y shows 3 peaks in the dimensionless frequency space at $\omega \approx 7.6969$, $\omega \approx 15.551$ and $\omega \approx 23.311$, corresponding to oscillation at frequencies of $2\,\mathrm{Re}[E] = 7.7460$, $4\,\mathrm{Re}[E] = 15.4919$ and $6\,\mathrm{Re}[E] = 23.2379$. Here, the frequency-tripling term arises from the product between the S^2-terms and either $\cos 2\,\mathrm{Re}[E]t$ or $\sin 2\,\mathrm{Re}[E]t$.

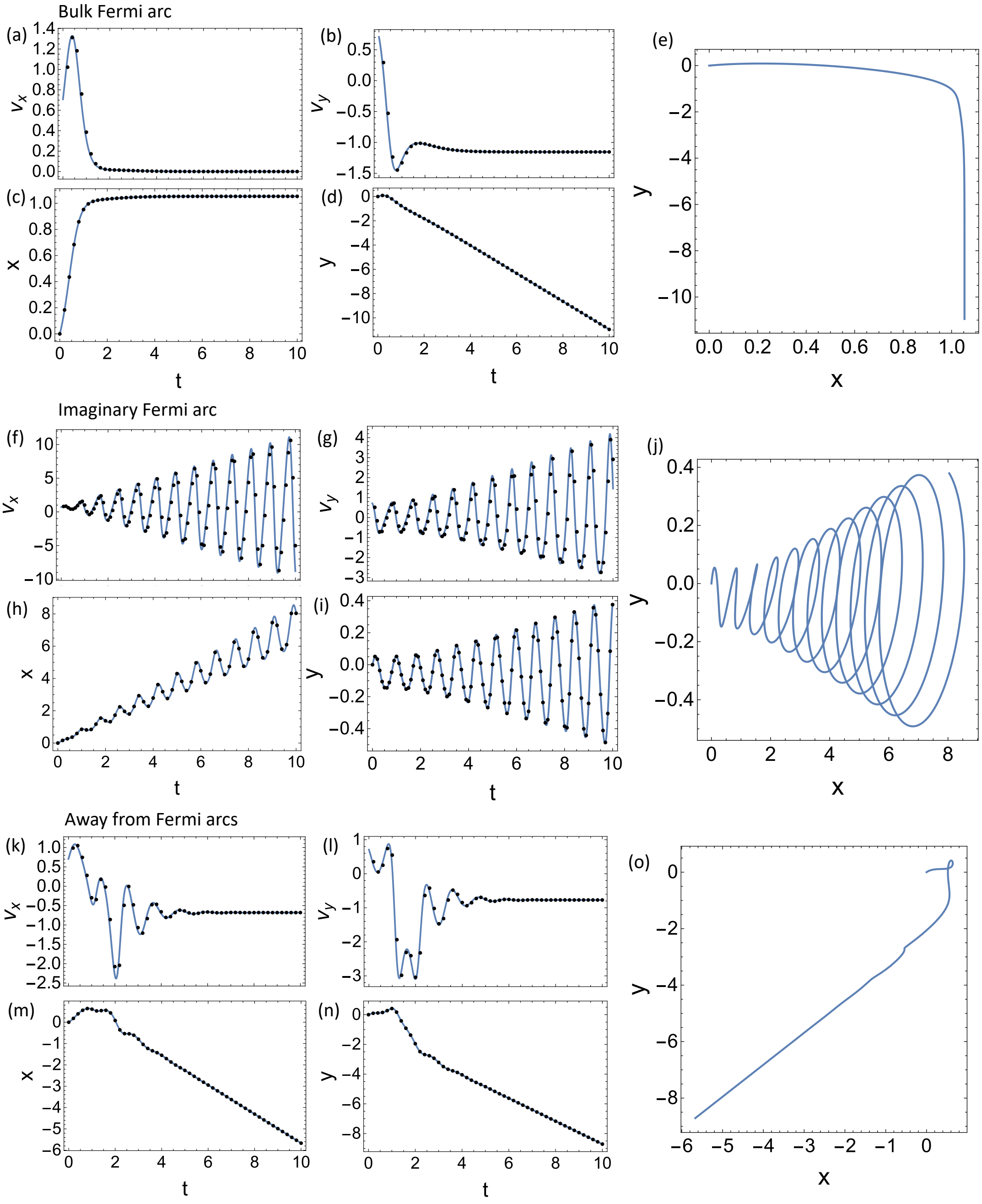

Figure 4.4: The group velocities (a,b,f,g,k,l) and centre-of-mass positions (c,d,h,i,m,n) of a Gaussian wavepacket initially centred at (a-d) $\mathbf{k} = (0.5, 0)$ (on the bulk Fermi arc), (f-i) $\mathbf{k} = (4, 0)$ (on the imaginary Fermi arc) and (k-n) $\mathbf{k} = (2, 2)$ (away from the Fermi arcs) as a function of time. The corresponding trajectories in real space are shown in (e,j,o). The lines represent analytical results derived from Eq. (4.12) and the black dots represent the numerical results for a Gaussian wavepacket with initial with of $w = 0.005$ in momentum space. Reproduced from [305], with the permission of AIP Publishing.

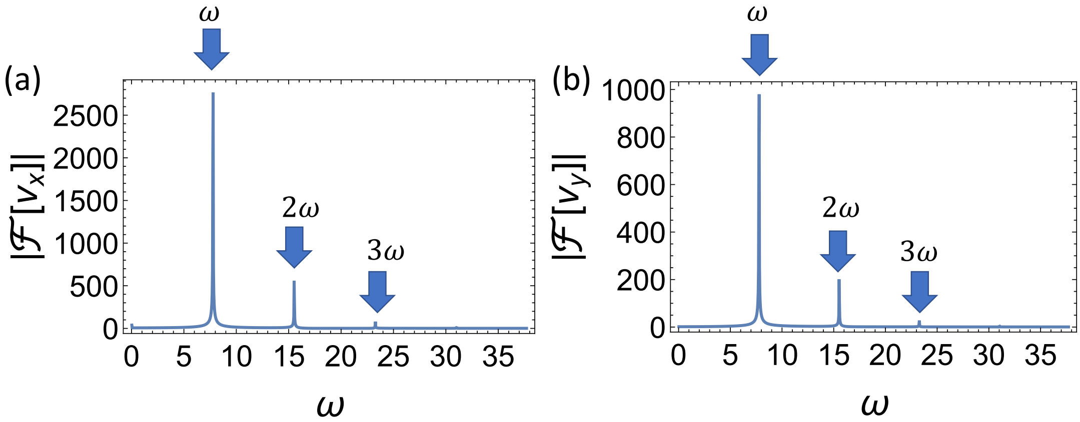

Figure 4.5: The Fourier transform of the group velocities v_x and v_y on the imaginary Fermi arc at $\mathbf{k} = (4, 0)$ in the non-Hermitian Dirac model. Here, the primary frequency ω is shown on both plots along with doubled and tripled frequencies. Reproduced from [305], with the permission of AIP Publishing.

4.6 Conclusion

In this work, I derive an equation of motion for the wavepacket centre of mass which describes a non-Hermitian generalization of Zitterbewegung effect. I show that the motion of the wavepacket is sensitive to its initial centre-of-mass momentum (when the wavepacket is centred at the exceptional points or on the Fermi arcs), similar to the nonlinear dynamics of a non-Hermitian Bose-Einstein dimer [273, 299, 300]. I also demonstrate the excellent agreement of the analytical theory with numerical simulation of wavepackets using a model describing a perovskite-based exciton-polariton system. Interestingly, in a special case where there is no effective field in the z-direction, part of the non-Hermitian corrections can be written in terms of the diagonal components of the LR quantum metric (see Section 1.3). This is similar to previous work in Ref. [282], which describes the wavepacket centre-of-mass motion in terms of the quantum metric, and in Ref. [306], which describes an exotic Zitterbewegung-like motion in terms of the left-right interband Berry connection. The results presented in this Chapter demonstrate the rich novel dynamical effects in non-Hermitian systems, while the deeper connection between the dynamics and the non-Hermitian QMT remains an interesting open question for further investigation. Furthermore, since the LR QMT in Eq. (4.12) arises from novel non-Hermitian terms, it will also be interesting to uncover its interplay with the terms proportional to the QMT in the semi-classical equation presented in Ref. [282].

Chapter 5

Emergent Psuedospin Defects

Disclaimer: This Chapter contains results from my previous published work "Wave-packet dynamics in a non-Hermitian exciton-polariton system", *Phys. Rev. B* **108**, 115404 (2023) and "Emergent momentum-space topological pseudospin defects in non-Hermitian systems ", arXiv preprint arXiv:2509.14605 (2025).

5.1 Introduction

Generation of topological defects has attracted a great amount of attention since they exhibit potential for storing and transmitting information in photonic and spintronic systems [133, 136, 137]. In this Chapter, I present a novel way to generate momentum-space point defects in the pseudospin textures of exciton polaritons. These defects arise from non-Hermiticity of the exciton-polariton system and are protected by topological winding.

First, I describe the emergent pseudospin defects using the perovskite-based exciton-polariton model (1.93), and argue that these defects can be experimentally measured in this system. I then probe the dynamics of the defects using two simpler non-Hermitian models, the non-Hermitian Dirac model described by Eq. (1.92) and a liquid crystal-based exciton-polariton model described by Eq. (1.95).

The defining feature of the topological point defects in these models is that they are associated with degeneracy lines (imaginary Fermi arcs) of the imaginary part of the eigenenergy spectrum, and their dynamics is fully deterministic. This allows for accurate analytical description of their dynamics and sets the non-Hermitian systems apart from Hermitian systems, where typically the spontaneous emergence of the topologically protected point defects occurs in position space and is associated with the development of instabilities and turbulence due to nonlinearity [307, 308, 309, 310].

5.2 Pseudospin Dynamics in a Perovskite-Based Exciton-Polariton System

As previously described in Chapter 2, the polariton Gaussian wavepackets in the system described by Eq. (1.93) tend to evolve into different eigenstates in different regions in momentum space. Since these regions are separated by the Fermi arcs [see Fig. 2.5], it is natural to investigate what happens close to these arcs. As shown in Fig. 5.1(a-b), the pseudospin textures of the upper and lower eigenstates have opposing in-plane components but the same out-of-plane components everywhere in momentum space (when $\Delta = 0$ in Eq. (1.93)) [218]. While the pseudospin texture of each eigenstate is anti-parallel on both sides of the bulk Fermi arc, the pseudospin of one eigenstate can transition smoothly to the texture of the other when crossing the bulk Fermi arc. On the other hand, the pseudospin textures of the upper and lower eigenstates are anti-parallel across the imaginary Fermi arcs. As the initially spin-up Gaussian wavepacket evolves, my calculation predicts emergent point defects on these imaginary Fermi arcs in momentum space. I should also emphasise that this effect does not require an external force, and the Hamiltonian operator has only a momentum dependence. Hence, the momentum-space pseudospin textures can simply be calculated as

$$S_j(\mathbf{k}) = \frac{\langle \psi_0(\mathbf{k})| e^{\frac{i\hat{H}^\dagger(\mathbf{k})t}{\hbar}} \sigma_j e^{-\frac{i\hat{H}(\mathbf{k})t}{\hbar}} |\psi_0(\mathbf{k})\rangle}{\langle \psi_0(\mathbf{k})| e^{\frac{i\hat{H}^\dagger(\mathbf{k})t}{\hbar}} e^{-\frac{i\hat{H}(\mathbf{k})t}{\hbar}} |\psi_0(\mathbf{k})\rangle}, \tag{5.1}$$

where $|\psi_0(\mathbf{k})\rangle$ denotes the initial state of the wavepacket and σ_j denotes the j-th 2×2 Pauli matrix. Here, the momentum-space Gaussian distribution of the wavepacket is canceled out, while the pseudospin texture of $|\psi_0(\mathbf{k})\rangle$ plays the dominant role. For the values of the parameters used in this Chapter, please refer to Appendix A.

In this Section, I study the dynamics of these emergent pseudospin defects. Remarkably, the evolution of the pseudospin textures and the emergence of the defects depend only on the initial polarization of the wavepacket, and not on the spatial or momentum components. Therefore, the pseudospin textures can evolve independently from the probability density function of the wavepacket, simplifying the calculations.

5.2.1 Pseudospin Defects

The pseudospin defects on the imaginary Fermi arcs are non-singular point defects similar to skyrmions [137, 136, 139, 138, 165, 164, 134, 62, 150, 135, 311] [see Section 1.2.3]. Some of the pseudospin defects (the ones circled by the black contour) that the simulation shows [see Fig. 5.1(d-h)] are core-up and core-down defects but with $S_z = 0$ at the edges. As previously discussed in Section 1.2.3, these defects have vorticities of $\nu = -1$ and the z-components of their pseudospins perform a $\pi/2$-rotation instead of a π-rotation [164], and thus have polarities $p = +1/2$ ($p = -1/2$). Hence, these defects have skyrmion numbers $N_{sk} = -1/2$ ($N_{sk} = +1/2$). I, therefore, conclude that these defects are core-up and core-down anti-merons, i.e., anti-skyrmions with half-integer winding numbers. The $[S_x, S_y]$-textures of the anti-merons are similar to that of the anti-skyrmions presented in Fig. 1.6(c, d) in Section 1.2.3, while their S_z-textures perform $\pi/2$-rotation from the centre to the edge similarly to the merons shown in Fig. 1.6(e, f).

In the vicinity of the exceptional points in the upper-half plane ($k_y \geq 0$), core-up and core-down anti-merons form on the right-hand side ($k_x \geq 0$) and left-hand side ($k_x \leq 0$) of the exceptional points pair, respectively. On the lower-half plane, the configuration is flipped. Note that this configuration is consistent with the configuration of the spectral

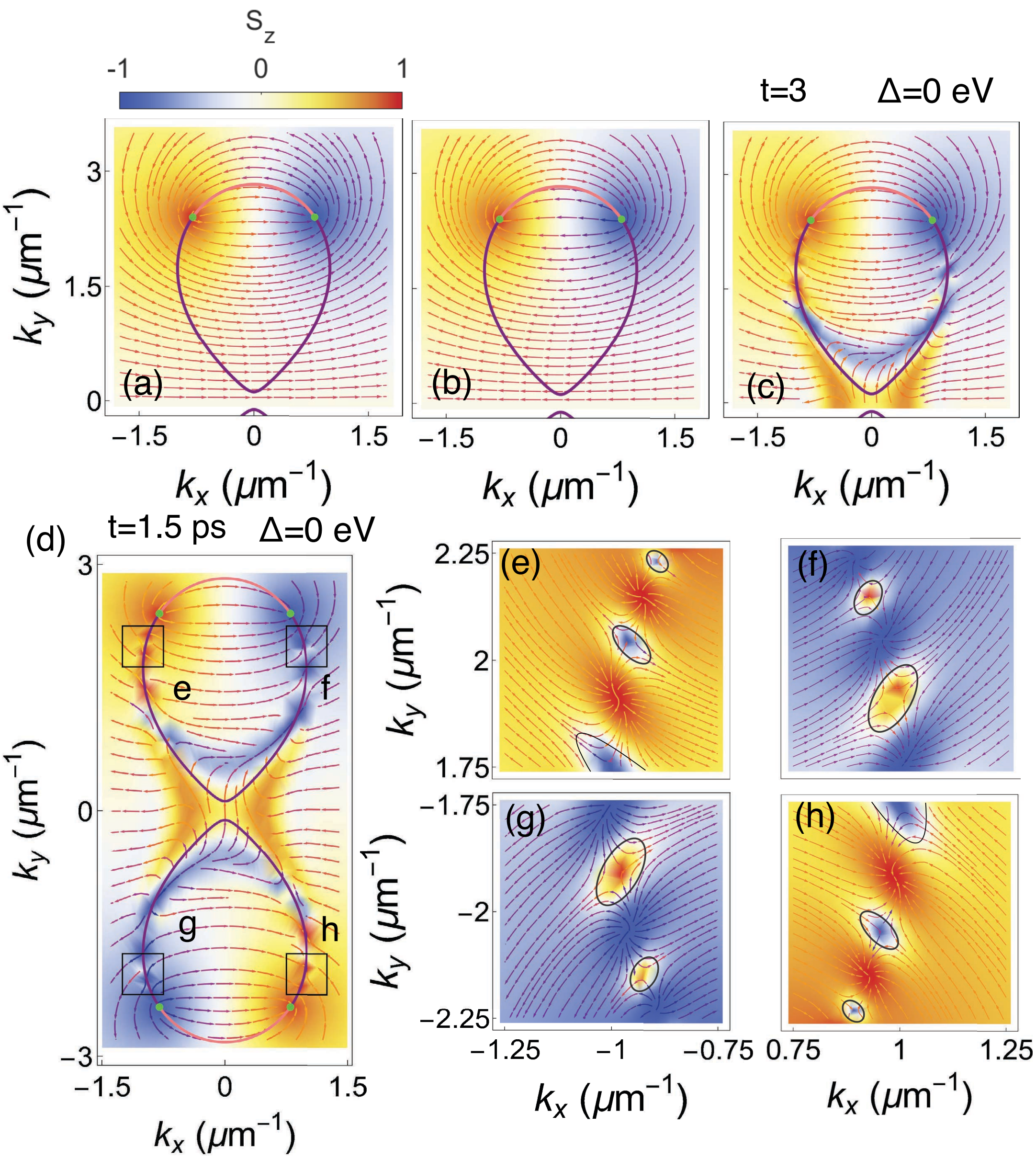

Figure 5.1: The pseudospin textures of (a) the upper eigenstate, (b) the lower eigenstate and (c) a polariton wavepacket at $t = 3$ ps with $\Delta = 0$. (d) The pseudospin textures of the polariton wavepacket at $t = 1.5$ ps. (e-h) Zoom-in of the areas marked in panel (d) near the pseudospin defects on the imaginary Fermi arcs. The color represents the values of S_z while the arrows represent the in-plane pseudospins (S_x, S_y). The imaginary and bulk Fermi arcs are marked by the purple and the pink curves, respectively, and the exceptional points are marked by the green dots.

winding [see Section 1.1.1] around the exceptional points in this system, where each exceptional points pair carries the opposite spectral winding, and the two exceptional points with opposite momenta also carry the opposite windings [218].

My simulation also predicts pseudospin vortices (the ones not circled by the black contour) with core polarization $S_z = +1$ ($S_z = -1$) forming between the core-down (core-up) anti-merons on the imaginary Fermi arcs [see Fig. 5.1(d-h)]. The in-plane pseudospins wind around the vortex cores, giving them vorticities of $w = +1$. However, the $S_z = \pm 1$ at their cores does not transform into $S_z = \mp 1$ or $S_z = 0$ on the edge. Consequently, they do not have exactly $p = \pm 1$ like a skyrmion or $p = \pm 1/2$ like a meron, and therefore do not have strictly integer-valued or half-integer-valued skyrmion numbers.

5.2.2 Pseudospin Defects in the Presence of Zeeman Splitting

Although the non-zero Zeeman splitting Δ in the model of Eq. (1.93) will not drastically change the in-plane textures $[S_x, S_y]$ of the defects, it has a huge impact on the out-of-plane S_z-textures of the eigenstates and the defects. As Δ increases, one eigenstate gains more positive S_z component, while the other eigenstate gains the component of the opposite sign. As shown in Fig. 5.2, S_z becomes more negative on one side of the imaginary Fermi arc, and more positive on the other side with increasing $|\Delta|$. Consequently, some of the defects slightly drift away from the imaginary Fermi arcs.

The initial polarization of the wavepacket and the sign of the Zeeman splitting Δdetermine which defects will be pushed away from the imaginary Fermi arc. For example, for an initially circularly polarized wavepacket ψ^+, the core-up anti-merons and vortices stay on the imaginary Fermi arcs. The core-down defects drift outward (inward) of the region bounded by the Fermi arcs [see Fig. 5.2(a-c)] for positive Δ as they gain more negative (positive) S_z in this region. If the wavepacket initially has the opposite polarization ψ^-, the opposite happens, and the core-down defects would stay on the arc while the core-up defects drift away.

Another consequence of the Zeeman splitting is that the core-up and core-down defects also gain more positive and negative S_z contribution, respectively. If $|\Delta|$ continues to increase, eventually the pseudospin on the edge of the anti-merons will no longer lie on the xy-plane. Consequently, S_z in these defects will no longer perform $\pi/2$ rotations with respects to the xy-plane, and they lose their anti-meron character. This is different from the self-acceleration, splitting and directional transport of the wavepackets, which can persist at large $|\Delta|$.

5.2.3 Pseudospin Defects in Real Space

The pseudospin anti-merons on the imaginary Fermi arc in momentum space can also be seen in the real space. When the wavepacket density distribution overlaps with the anti-merons in momentum space, the anti-meron textures also emerge in the real space [see Fig. 5.3]. The emergence of these anti-merons is a direct consequence of the imaginary Fermi arc and the non-unitary evolution (which will be discussed in more detail in the

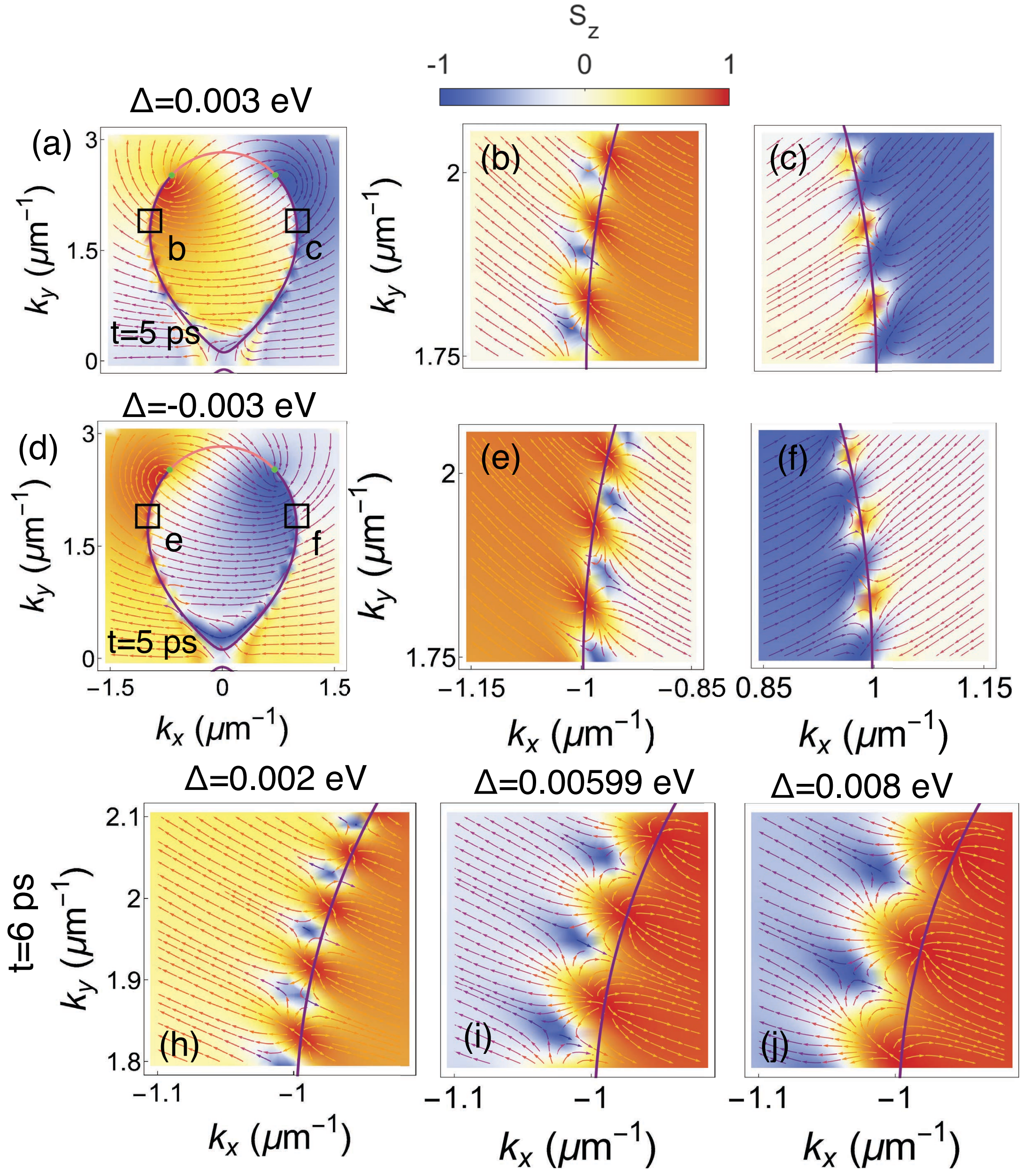

Figure 5.2: Pseudospin textures for (a-c) positive and (d-f) negative values of Zeeman splitting showing how the core-down defects drifts away from the imaginary Fermi arc. (h-j) Textures in the (a) gapless phase with nonzero Δ (i) the phase where the two exceptional points merge and (j) the gapped phase. The wavepackets are initially circularly polarized. The imaginary and bulk Fermi arcs are marked by the purple and the pink curves, respectively, and the exceptional points in the gapless phase are marked by the green dots.

next Sections). This is in contrast to the previous studies of purely Hermitian two-dimensional systems, where the topological defects emerge due to the cavity anisotropy and TE-TM splitting [164, 166, 165, 167].

My results show a new way to generate topological defects in the psuedospin structures that arise from the growth and decay of wavepackets in a non-Hermitian system. These defects also represent a clear signature of the effects of the imaginary Fermi arc on polariton dynamics in the real space. Furthermore, my results might be a useful tool for detecting the locations of the imaginary Fermi arcs in momentum space. Moreover, my preliminary estimates indicate that these defects can be observed experimentally in a polariton system based, for example, on a perovskite semiconductor embedded in a high-quality microcavity [218], which I will discuss in the next Section.

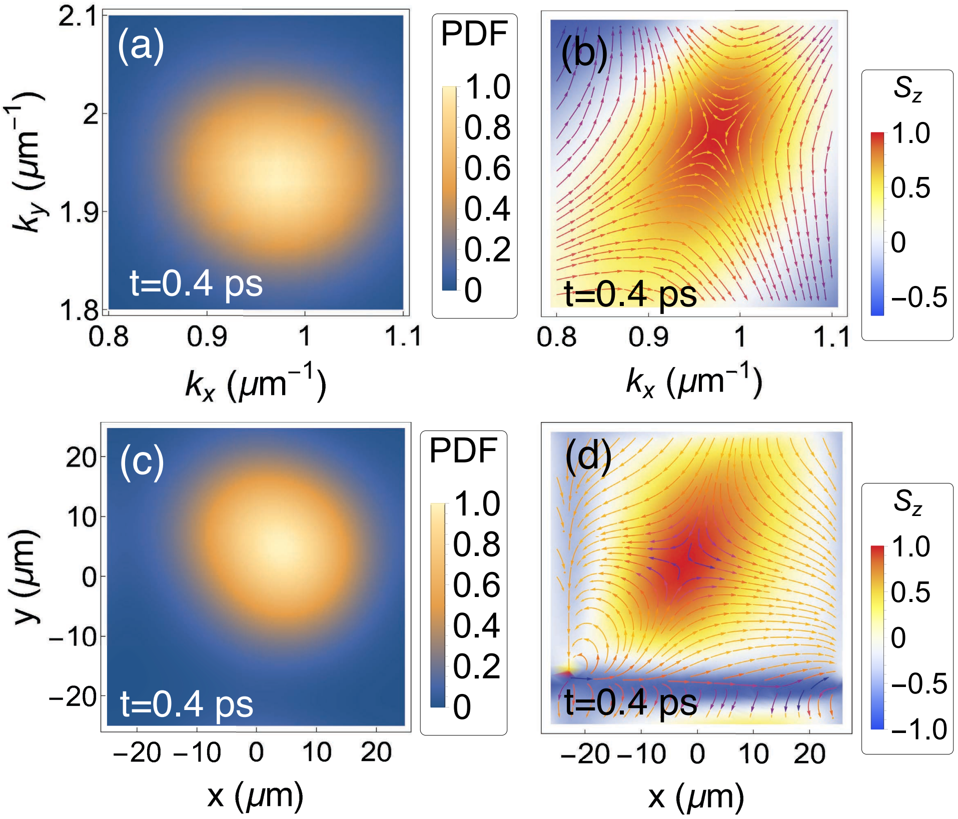

Figure 5.3: The probability density function (PDF) of an exciton-polariton wavepacket and its pseudospin textures in (a,b) the momentum and (c,d) the real space.

5.2.4 Proposed Experimental Measurement of the Pseudospin Defects

In experiments, the time evolution of probability density distribution and the pseudospin textures can be measured using a streak camera which can take a snapshot of the wavepackets in both real and momentum space at a resolution of ≈ 2 ps [274]. Since the measurements are made by taking multiple snapshots and then averaging over the time resolution, I aim to investigate whether the pseudospin defects on the imaginary Fermi arc will still appear when the fields are averaged.

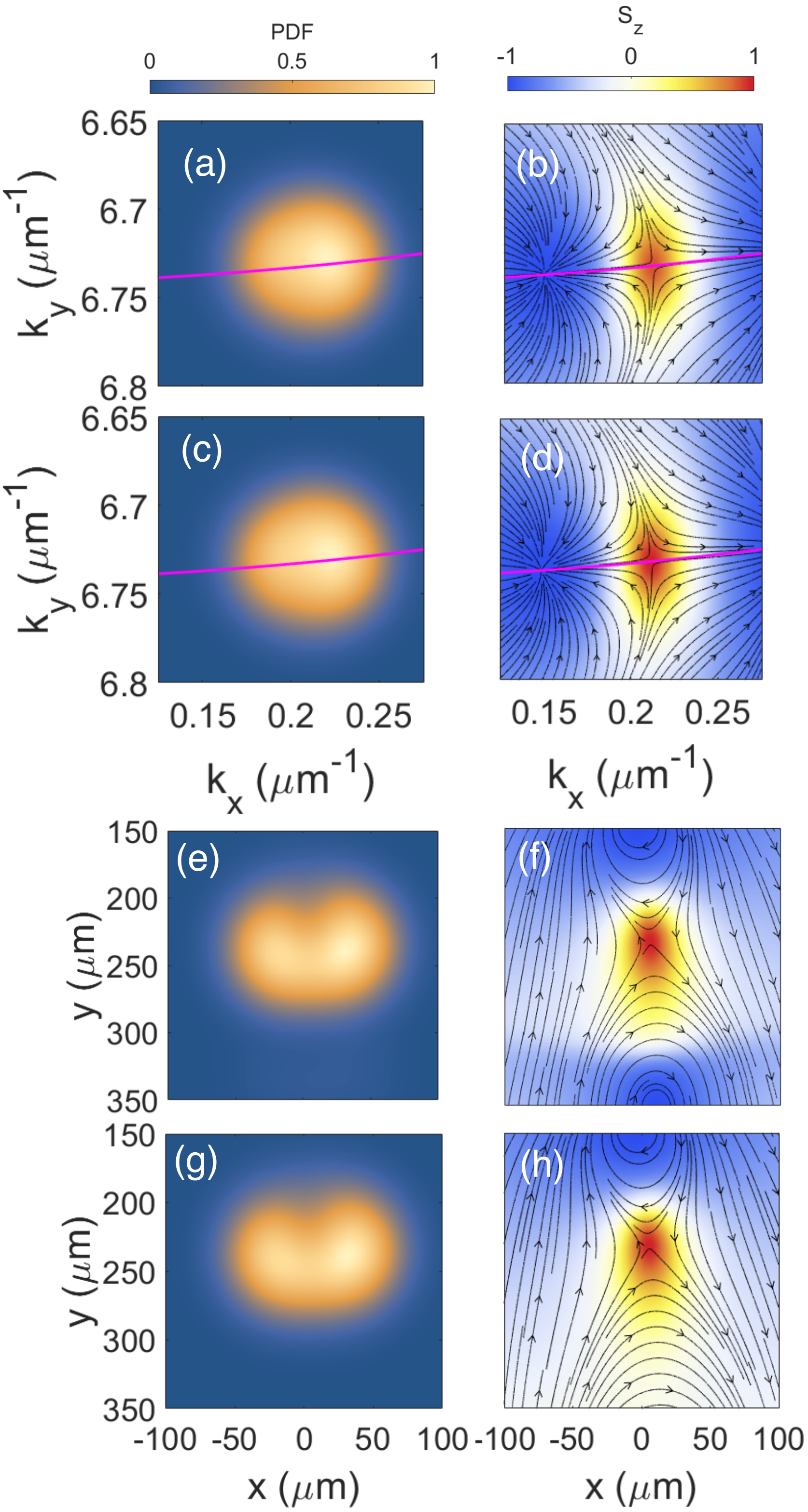

Figure 5.4: The averaged wavepacket and pseudospin textures of the exciton-polariton in momentum space (a,b) and in the real space (e,f). The probability density function (PDF) and the pseudospin take similar forms to the wavepacket and pseudospin textures at $t = 5$ ps in (c,d) and (g,h). The purple line denotes the imaginary Fermi arc.

Since the pseudospin of the wavepackets cannot be measured in the regions with small probability density (since the signal-to-noise ratio will be very low), I need to make sure that the polariton density at the location of the pseudospin defects is non-negligible. Previous work [8] shows that the larger the wavepackets are, the faster they will move away from the initial centre-of-mass positions. Therefore, I need a wavepacket that is well localised in momentum space, so it will stay near the defect for a long time. However, the wavepacket cannot be too focused since I still need to measure the pseudospin texture of the entire defect.

Furthermore, although it is unknown whether the change in the pseudospin textures will reach a steady state, my numerical calculations indicate that the change of the pseudospin slows down with time. Therefore, the best way to detect the pseudospin defects is to take measurements over a long time, taking care to not exceed the time after which the wavepacket moves away from the imaginary Fermi arc.

To simulate an experiment, I choose a circularly-polarized polariton Gaussian wavepacket with a width of $w = 0.02\ \mu\mathrm{m}^{-1}$ in momentum space with the initial centre-of-mass momentum of $\langle \mathbf{k} \rangle = (0.215, 6.73)\ \mu\mathrm{m}^{-1}$ and considered a realistic set of parameters presented in Ref. [218] [also in Appendix A]. The initial wavepacket is chosen so that its size is small enough so it will stay on the imaginary Fermi arc for a long time, yet not too small to be realised in experiment. The wavepacket has a width of $w_r = 1/\sigma_k = 50\ \mu\mathrm{m}$ in real space, which can be achieved in the experiments. I found that that the wavepacket at $t = 5$ ps is still on the imaginary Fermi arc and contains the pseudospin defect, but is starting to move away at $t = 15$ ps. Therefore, I chose to take the average of the wavepackets every 2 ps from $t = 5$ ps to $t = 15$ ps to see if the averaged wavepacket will exhibit the pseudospin defects.

The right/left-hand circular (±), horizontal (H), vertical (V), diagonal (D), and anti-diagonal (A) polarizations, defined by $|\psi^{\pm}|^2$, $|\psi^{H,V}|^2$ and $|\psi^{D,A}|^2$, respectively, are therefore calculated every 2 ps from $t = 5$ ps to $t = 15$ ps. I then take the average of these quantities $\langle|\psi^{\pm}|^2\rangle_{ave}$, $\langle|\psi^{H,V}|^2\rangle_{ave}$, $\langle|\psi^{D,A}|^2\rangle_{ave}$ and use them to compute the pseudopin textures defined by Eqs. (1.82). I observe that the wavepacket and its time-averaged pseudospin textures take forms similar to those at $t = 5$ ps in momentum space [see Fig. 5.4(a-d)]. Therefore the snapshot of the wavepacket at $t = 5$ ps will dominate the time-averaged measurement in momentum space. This is because the wavepackets at later times have much lower probability densities due to the continuing decay (negative imaginary part of eigenenergies) of the exciton polaritons. On the other hand, in the real space, the averaged wavepacket and pseudospin textures do not completely agree with those at $t = 5$ ps as seen in Fig. 5.4(e-h). However, the pseudospin anti-meron structure at the centre of the wavepacket still persists after the averaging. With these results, I conclude that the pseudospin anti-merons generated by non-Hermitian wavepacket dynamics can be measured experimentally in both momentum space and real space.

Note that, the perovskite-based exciton-polariton system described by Eq. (1.93) and considered in this Section has a rather complicated Fermi arcs structure which makes it difficult to investigate the behaviour of the pseudospin defects. In the following Sections, I will present further studies on the emergent pseudospin defects using simpler models. I consider two other models, the non-Hermitian Dirac model described by the Hamiltonian in Eq. (1.92) and the non-Hermitian liquid-crystal microcavity exciton-polariton model Eq. (1.95), where the structure of the Fermi arc is simpler, and the dynamics of the pseudospin defects can be described analytically under some initial conditions. Although the photonic disorder in the liquid-crystal-based microcavity contributes to the broadening of the cavity modes, both the polarisation textures [167] as well as the complex-energy landscape [265] can be successfully fully explored using this system.

5.3 Pseudospin Defects in a Non-Hermitian Dirac Model

The second model that I consider in this Chapter is the non-Hermitian Dirac model described by Eq. (1.92). The bulk and imaginary Fermi arcs of this model lie on the k_x-axis, separated by the exceptional points at $\mathbf{k}_{EP} = (\pm\sqrt{\kappa^2 - \Delta^2}, 0)$ if $|\kappa| < |\Delta|$, as shown in Fig. 1.9. For $|\Delta| > |\kappa|$, the bulk Fermi arc vanishes and the imaginary Fermi arc extends to the entire k_x-axis. This simple Fermi arc structure makes it easier to analytically investigate the defect dynamics, which will be discussed later.

As previously discussed in this Chapter, the dynamics of a wavepacket in the system governed by a non-Hermitian Hamiltonian, leads to the formation of pseudospin defects on the imaginary Fermi arcs. Example snapshots of the pseudospin texture in the non-Hermitian Dirac model are plotted in Fig. 5.5, showing staggering core-up and core-down defects being generated along the imaginary Fermi arcs in the gapless phase [Figs. 5.5(a-c)]. At $\Delta = 0$, the core-up (core-down) defects along the positive (negative) k_x-axis have the vorticity of $\nu = -1$ and polarity of $p = 1/2$ ($p = -1/2$), making them anti-merons. On the other hand, the core-down (core-up) defects along the positive (negative) k_x-axis have the vorticity of $\nu = 1$ but they do not have a well-defined edge and do not have integer nor half-integer valued polarity. I refer to them as pseudospin vortices. In Figs. 5.5(d-i), as Δ increases, the exceptional points approach each other and annihilate, opening an energy gap [see Section 1.5.1]. Through this process, the core-down defects stay on the imaginary Fermi arcs, while the core-up defects are pushed off the arcs. At the same time, the pseudospin textures gain $S_z = \pm 1$ on the two sides of the imaginary Fermi arcs. Subsequently, the anti-merons no longer have the polarity of $p = \pm 1/2$, and become pseudospin anti-vortices.

In the case where the initial wavefunction of the system $\psi(0)$ is in a homogeneous spin-up, $S_z = 1$, (spin-down, $S_z = -1$) configuration, I can show analytically that the centres of the emergent core-up (core-down) pseudospin point defects are located at $\mathbf{k}^*(t) = (\pm k^*_{x,n}(t), 0)$ where

$$k^*_{x,n} = \sqrt{k^2_{EP,x} + E^2_n(t)}. \tag{5.2}$$

Here, $*$ indicates the momentum space coordinates of the defects and $E_n(t)$ satisfies the quantization condition $E_n(t) = n\pi\hbar/t$, where $n \in \mathbb{Z}$ is an integer index of the defects. The evolution of the wavefunction (and therefore the associated pseudospin, Eq. (5.1)) is described by $\psi(t) = \hat{T}\psi(0)$, where $\hat{T} = \exp(-iHt/\hbar)$, which is linear and deterministic. The quantization condition corresponds to the moments of time when the time evolution operator $\hat{T}$, given by

$$\hat{T} = \begin{pmatrix} \cos\frac{Et}{\hbar} - \frac{i\Delta}{E}\sin\frac{Et}{\hbar} & -i\frac{k_x - i(k_y - i\kappa)}{E}\sin\frac{Et}{\hbar} \\ -i\frac{k_x + i(k_y - i\kappa)}{E}\sin\frac{Et}{\hbar} & \cos\frac{Et}{\hbar} + \frac{i\Delta}{E}\sin\frac{Et}{\hbar} \end{pmatrix} \tag{5.3}$$

coincides with the identity matrix, i.e. $\hat{T}$ maps $S_z = \pm 1$ to itself.

Similarly, when $\hat{T}$ is an anti-diagonal matrix, it maps $S_z = \pm 1$ to $S_z = \mp 1$ and generates the defects with the core orientation opposite to the initial condition. At $\Delta = 0$, this condition is satisfied along the imaginary Fermi arcs at $\mathbf{k}^*(t) = (\pm k^*_{x,m}(t), 0)$ with $k^*_{x,m}$ given by Eq. (5.2) but with the quantization condition $E_m = ((2m+1)/2)\pi\hbar/t$, where m is an integer.

When $\Delta \neq 0$ in Eq. (5.3), for the initial spin-up (spin-down) configuration, only the defects with $S_z = 1$ ($S_z = -1$) will stay on the imaginary Fermi arcs with their location in momentum space $\mathbf{k}^*$ determined by Eq. (5.2), while the defects with $S_z = -1$ ($S_z = 1$) will be pushed away from these arcs. This is because, when $\Delta \neq 0$, the condition for $\hat{T}$ to be anti-diagonal is satisfied for $E = \pm i\Delta \tan Et/\hbar$. The position of the defects $\mathbf{k}^*$ needs to be determined numerically and may no longer be on the imaginary Fermi arcs. In the rest of this Chapter, I consider the initial spin-down configuration and focus the analysis on the dynamics of the core-down ($S_z = -1$) defects, since only these defects can be described analytically for all values of Δ. If the initial condition was $S_z = 1$, the core-up defects would behave similarly. This explains why the defects emerge on the imaginary Fermi arcs or in their vicinity. It also shows that the number of the defects is determined by the mean-subtracted eigenenergy and time.

Note that in the fully gapped phase, the pair of pseudospin defects generated at opposite momenta $\mathbf{k}^* = (\pm k^*_{x,n}(t), 0)$ with the same index n have the same polarity p, but opposite vorticity ν, therefore they also have the opposite skyrmion numbers [see Eq. (1.18)]. The neighboring defects at $\mathbf{k}^*_n$ and $\mathbf{k}^*_{n+1}$ also have opposite vorticity ν, but they have opposite polarity p, and therefore the same skyrmion numbers. The typical pseudospin textures associated with such defects and their time evolution is presented in Fig. 5.5 for the three different phases: gapless with two exceptional points; gapless with a hybrid point at the origin, and fully gapped, with no degeneracy in the real part of the eigenenergy.

In the fully gapped phase, $|\Delta| > |\kappa|$, the two defects with opposite skyrmion numbers propagate along the imaginary Fermi arc until they annihilate with each other at the time $t = n\pi\hbar/\sqrt{\Delta^2 - \kappa^2}$ at $k_x = 0$, as shown in Fig. 5.6(c). However, in the gapless phase with $|\Delta| \leq |\kappa|$, the defects cannot pass through the degeneracy so the defects accumulate at $\mathbf{k}^* \to \mathbf{k}_{EP}$ as $t \to \infty$, as seen in Figs. 5.6(a,b). As the pairs of defects with opposite skyrmion numbers cannot move past the degeneracy, they do not annihilate, and the number of pseudospin defects will simply accumulate. With time, the defects become increasingly densely packed and move closer to the degeneracy, but never dissipate nor annihilate. Thus, the non-Hermitian spectral degeneracies, i.e. the hybrid and exceptional points, provide topological protection to the pseudospin defects on the imaginary Fermi arcs.

Note that despite the accumulation and increasing density of the defects with time,

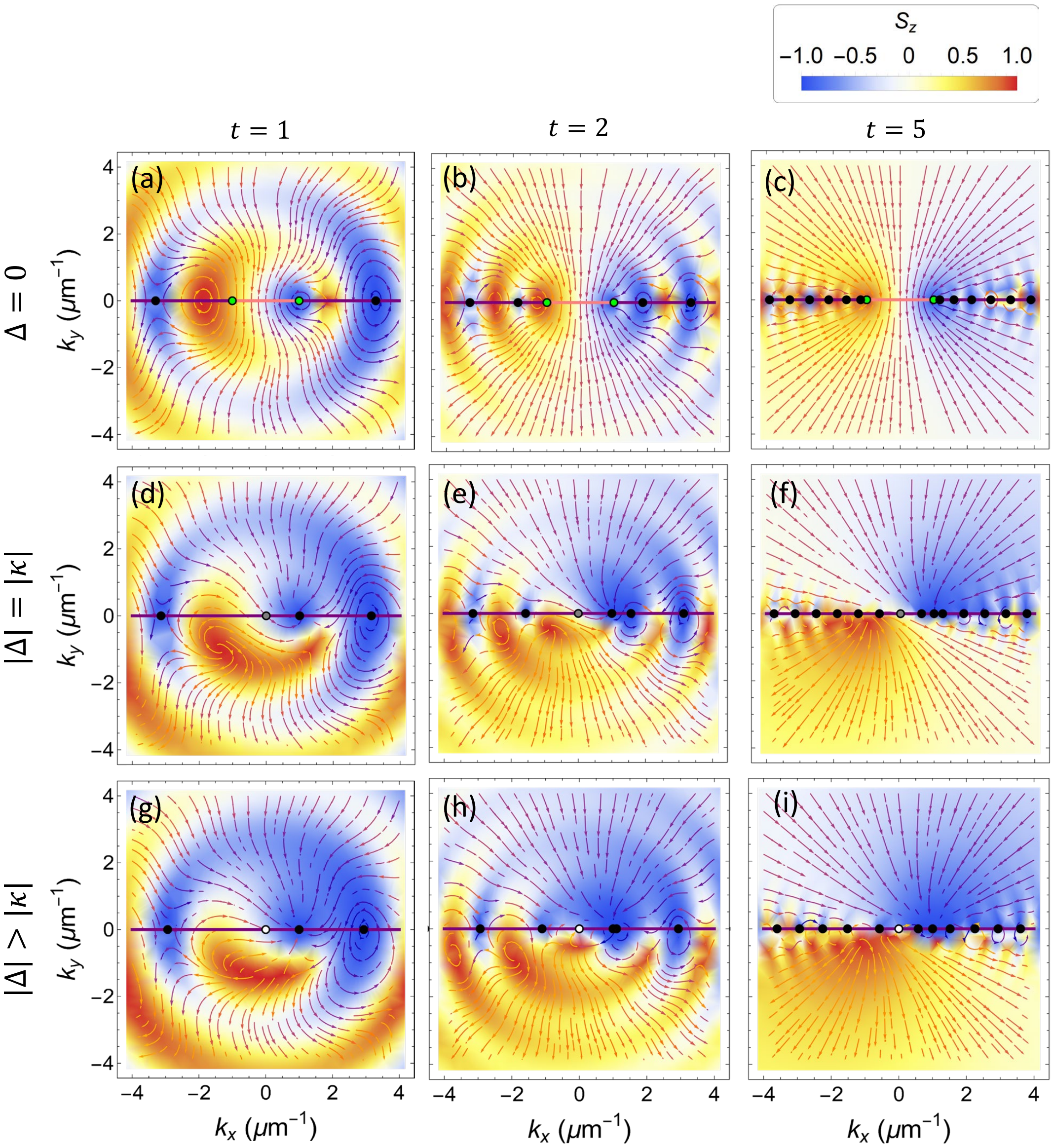

Figure 5.5: Snapshots of the defects arising in the non-Hermitian Dirac model, Eq. (1.92), ($\kappa = 1$) in (a-c) a gapless phase with two exceptional points (green dots) for $\Delta = 0$, (d-f) a gapless phase with a hybrid point (gray dots) for $\Delta = 1$ and (g-i) a gapped phase for $\Delta = 1.5$. The initial condition is a spin-down state. Only the core-down defects are highlighted by the black dots for simplicity. The core-up defects migrate away from the imaginary Fermi arc as Δ increases. The bulk and imaginary Fermi arcs are denoted by the pink and the purple lines, respectively. The points where min(Re[E]), which are attractors for these defects, are marked by the white dots.

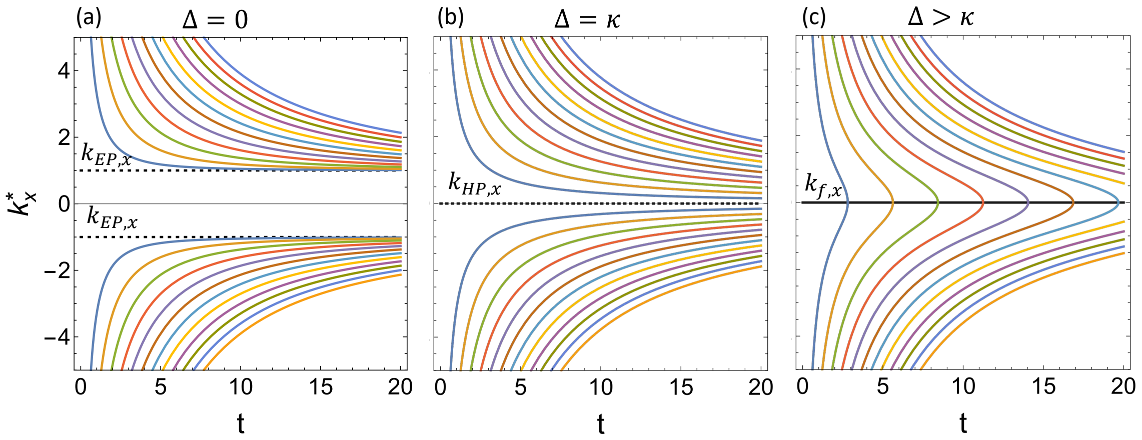

Figure 5.6: Position of the core-down defects on the imaginary Fermi arcs as a function of time in (a) a gapless phase with two exceptional points for $\Delta = 0$, (b) another gapless phase with a hybrid point for $\Delta = 1$ and (c) a fully gapped phase for $\Delta = 1.5$. Different colors correspond to different n (only up to $n = 12$ are shown). Momenta of the exceptional points ($k_{EP,x}$) in (a) and the hybrid point ($k_{HP,x}$) in (b) are marked with horizontal dashed lines, and $min(\text{Re}[E])$ is marked with a solid line ($k_{f,x}$).

the total (zero) skyrmion number in the system remains unchanged because the defects with opposite skyrmion numbers are always generated in pairs.

I note that, since the imaginary Fermi arc in the non-Hermitian Dirac model extends to $k_x = \pm\infty$, the defects are generated at $k_x^* \to \infty$ at $t \to 0$ (see Fig. 5.6 and Eq. (5.2)). Therefore, this simple model cannot provide useful insights into the early-time dynamics of the defects. In what follows, I consider a more realistic and experimentally relevant non-Hermitian model, whose Fermi arcs are confined within finite regions in the momentum space, enabling richer defect dynamics.

5.4 Pseudospin Defects in a Liquid Crystal-Based Exciton-Polariton System

In this Section, I consider the liquid crystal model previously discussed in Section 1.5.3 . In this model, the exceptional points, as well as both the bulk and imaginary Fermi arcs form an ellipse in momentum space [see Fig. (1.11)]. Similarly to the two models discussed in Sections 5.2 and 5.3, the pseudospin defects emerge on the imaginary Fermi arcs at $\mathbf{k}^* = (k_F(\phi^*), \phi^*)$ where $k_F(\phi)$ is an ellipse in the k-space defining the positions of the exceptional points, the hybrid points and the bulk and imaginary Fermi arcs. The location of the pseudospin defects on the imaginary Fermi arcs can be defined by the polar angle ϕ^*, where

$$
\begin{aligned}
\phi^* =& \frac{1}{2} \arctan B_\pm / A_\pm + m\pi \\
A_\pm =& \frac{\beta' \delta E}{\beta(\gamma + E_n^2)} \pm \frac{\alpha \sqrt{\beta^2(\gamma + E_n^2) + \beta'^2 \delta E}}{\beta(\gamma + E_n^2)} \\
B_\pm =& \pm \frac{\sqrt{\delta E}}{|\beta(\gamma + E_n^2)|} \sqrt{-2\alpha\beta' \sqrt{\beta^2(\gamma + E_n^2) + \beta'^2 \delta E} - (\beta^2\gamma + \beta'^2\gamma') - E_n^2(\beta^2 - \beta'^2)}.
\end{aligned}
\tag{5.4}
$$

Here $n \in \mathbb{N}$, $m \in \mathbb{Z}$, $\gamma' = \alpha^2 + (\Delta^2 - \delta\Gamma^2)$, $\delta E = \Delta^2 - \delta\Gamma^2 - E_n^2$, $E_n = n\pi\hbar/t$, and the sign permutations for ± in ϕ^* are independent, resulting in four values.

In contrast with the non-Hermitian Dirac model, where the defects emerge at infinity, the imaginary Fermi arcs in the exciton-polariton system have a finite length and the defects emerge at finite values of $\mathbf{k}$. The pair of defects are generated at $\mathbf{k}_i^* = (k_F(\phi_i), \phi_i)$ periodically at $t = nT_i$, where

$$
\begin{aligned}
T_i =& \pi\hbar \sqrt{\frac{\beta'^2 - \beta^2}{\alpha^2\beta^2 + (\beta'^2 - \beta^2)(\Delta^2 - \delta\Gamma^2)}}, \text{ and} \\
\phi_i =& \pm \arccos\left(\pm \sqrt{\frac{\beta' - \beta}{2\beta'}} \right).
\end{aligned}
\tag{5.5}
$$

The index n in T_i corresponds to the same index in ϕ^* from Eq. (5.4) and the two ±-signs in ϕ_i are independent, giving four values of ϕ_i [see Fig. 5.7].

In the fully gapped phase, a pair of defects with the same index n and polarity p, but opposite vorticity ν will emerge at the same ϕ_i, then each defect will propagate along the imaginary Fermi arcs towards $\mathbf{k}^* = (k_F(m\pi/2), m\pi/2)$, where m is an integer, and annihilate with another defect carrying the opposite skyrmion number at $t = nT_f$ where

$$
T_f = \frac{\pi\hbar}{\sqrt{\Delta^2 - \delta\Gamma^2}}. \tag{5.6}
$$

Note that the periods for creation T_i and annihilation T_f are different, so the defects will still accumulate with time.

In the gapless phase with either exceptional points or hybrid points, similarly to the non-Hermitian Dirac model (1.92), the defects with opposite skyrmion number will propagate along the imaginary Fermi arcs towards the non-Hermitian degeneracies, which protect them from annihilation. Notably, along the imaginary Fermi arcs, the real part of the eigenenergy Re[E] reaches its maxima exactly at $\phi = \phi_i$, and its minima at the degeneracy in the gapless phase, or at $\phi = m\pi/2$ in the fully gapped phase [see Fig. 5.8].

The qualitative change in the behavior of the pseudospin defects in the gapless and the gapped phase is also reflected in the skyrmion number in momentum space. In Fig. 5.9, I plot the skyrmion number calculated within the region in momentum space between $\phi = \arccos\sqrt{(\beta' - \beta)/(2\beta')}$, which is one of the ϕ_i where the defects are generated, and

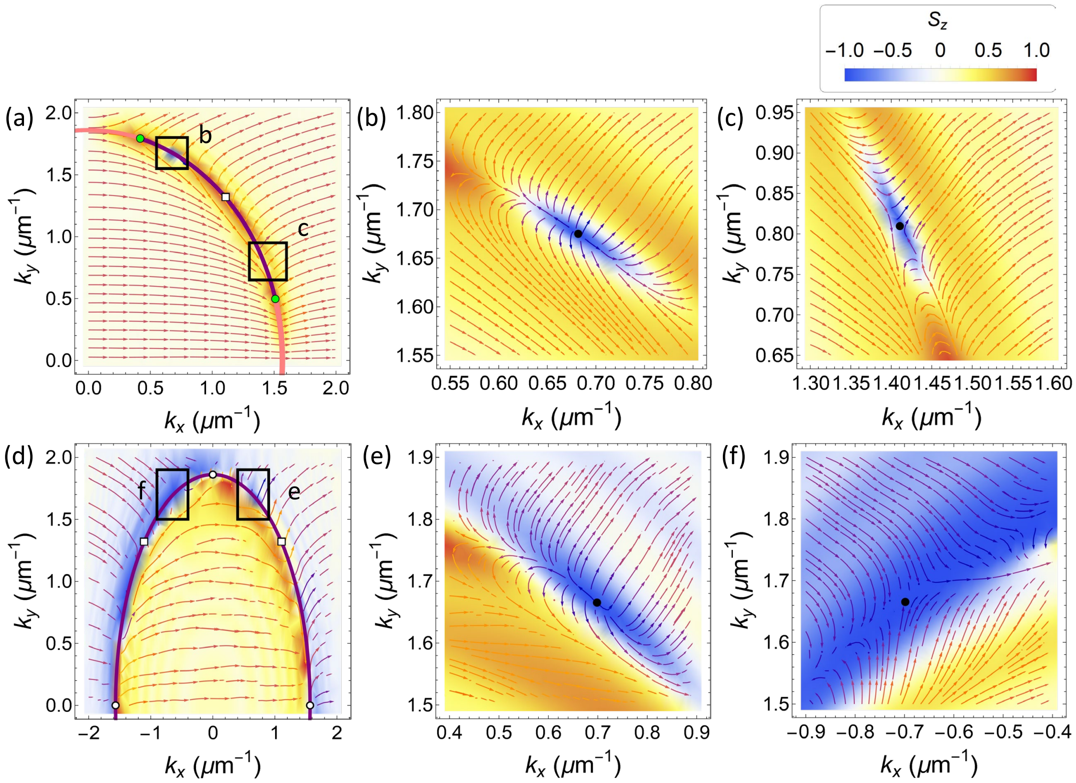

Figure 5.7: (a) A pair of point defects with the opposite vorticity, ν, in the gapless phase with $\Delta = 0$ eV, at $t = 15$ ps . (b,c) The close-up on the two defects with (b) $\nu = 1$ and (c) $\nu = -1$ shown in (a). (d) A pair of point defects with the opposite vorticity, ν, at in the fully gapped phase with $\Delta = 15 \times 10^{-4}$ eV, at $t = 10$ ps. (e,f) The close-up of the two defects with (e) $\nu = 1$ and (f) $\nu = -1$ shown in (d) that propagate towards $\phi = \pi/2$ before annihilating. The white square with black outline in (a,d) correspond to $\max(\mathrm{Re}[E])$ where the defects emerge from. The green dots with black outline in (a) and the white dots with black outline in (d) correspond to the $\min(\mathrm{Re}[E])$, where the defects propagate towards, which also correspond to the degeneracies in the gapless phase.

$\phi = 0$, which is an attractor for th defects. I chose this region to account for only one of the defects in each of the emerging (annihilating) pairs with the opposite skyrmion numbers. In the gapless phases, the total skyrmion number in this momentum-space region increases monotonically [blue and red line in Fig. 5.9] as a result of more and more defects accumulating near the spectral degeneracy. However, once a gap is opened, I can see periodic dips in the skyrmion number [purple lines in Fig. 5.9] that correspond to the annihilation events. The dips become more pronounced as the gap increases.

Interestingly, the imaginary Fermi arcs in this system play a role similar to that of domain walls [173, 312], but instead of spin-up and spin-down regions, they separate regions that align with the upper and the lower eigenstates. For an initial spin-down configuration, the overlap between the wavefunction and the upper (lower) eigenstates can be calculated using bi-orthogonality as

$$c_{\pm} = \langle \psi^{L}_{\pm} | \psi(t) \rangle. \tag{5.7}$$

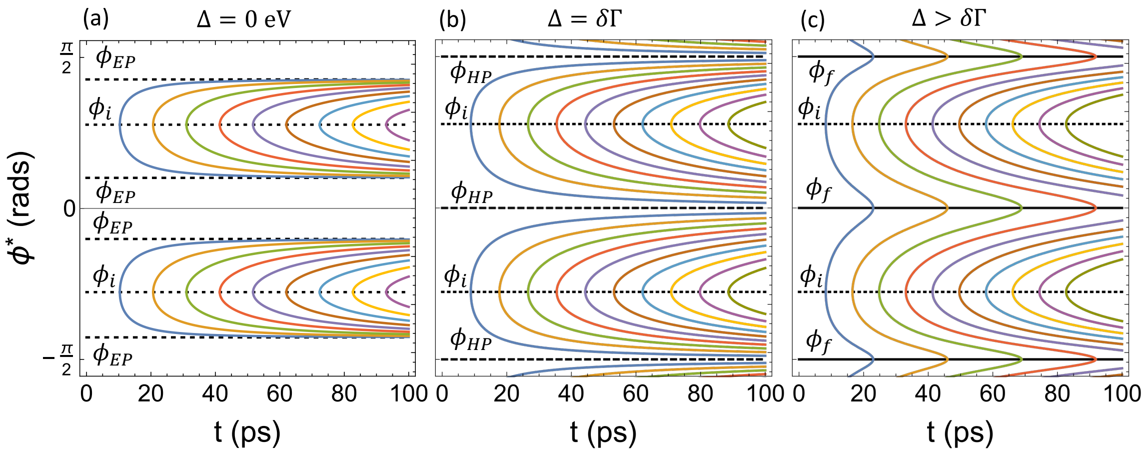

Figure 5.8: Azimuthal angles (in momentum space) of the core-down defects on the imaginary Fermi arcs plotted as a function of time in (a) a gapless phase with exceptional points (denoted as ϕ_{EP}) for $\Delta = 0$ eV, (b) another gapless phase with hybrid points (denoted as ϕ_{HP}) for $\Delta = \delta\Gamma = 1.2 \times 10^{-4}$ eV and (c) a fully gapped phase for $\Delta = 1.5 \times 10^{-4}$ eV, where the defects are annihilated at ϕ_f. Here, different colors correspond to different integer index of the defect, n.

For an initially spin-down configuration, $c_\pm$ are proportional to

$$\begin{aligned} c_\pm &\propto \begin{pmatrix} H_z \pm E & H_x - iH_y \end{pmatrix} \cdot \begin{pmatrix} \cos\frac{Et}{\hbar} - \frac{iH_z}{E}\sin\frac{Et}{\hbar} & -i\frac{H_x - iH_y}{E}\sin\frac{Et}{\hbar} \\ -i\frac{H_x + iH_y}{E}\sin\frac{Et}{\hbar} & \cos\frac{Et}{\hbar} + \frac{iH_z}{E}\sin\frac{Et}{\hbar} \end{pmatrix} \cdot \begin{pmatrix} 0 \\ 1 \end{pmatrix} \\ &= e^{\mp i\frac{Et}{\hbar}}(H_x - iH_y) \\ &= e^{\mp i\frac{\mathrm{Re}[E]t}{\hbar} \pm \frac{\mathrm{Im}[E]t}{\hbar}}(H_x - iH_y). \end{aligned} \tag{5.8}$$

Therefore, under the normalization condition $|\psi|^2 = |c_+|^2 + |c_-|^2 = 1$, the overlap between the wavefunction with the right eigenstates take the forms as

$$\begin{aligned} \frac{|c_\pm|^2}{|\psi|^2} &= \frac{|H_x - iH_y|^2 e^{\frac{2\mathrm{Im}[E]t}{\hbar}}}{|H_x - iH_y|^2\left(e^{\frac{2\mathrm{Im}[E]t}{\hbar}} + e^{-\frac{2\mathrm{Im}[E]t}{\hbar}}\right)} \\ &= \frac{e^{\pm\frac{2\mathrm{Im}[E]t}{\hbar}}}{2\cosh\frac{2\mathrm{Im}[E]t}{\hbar}}. \end{aligned} \tag{5.9}$$

As shown in Fig. 5.10, the normalized $|c_\pm|^2$ across the imaginary Fermi arcs take very similar shapes to the typical domain wall configuration.

In the case of spin-domain walls in conventional systems, skyrmions can be generated as a result of Kelvin-Helmholtz instability, as discussed in Refs. [173, 174, 312]. However, in contrast with the quantum hydrodynamics, where the domain wall emerges due to the nonlinear interactions, in the linear system considered here the pseudo-spin domains and point defects emerge due to the non-Hermiticity and the resulting complex structure of the momentum-space eigenenergies. The possibility that this non-Hermiticity may lead

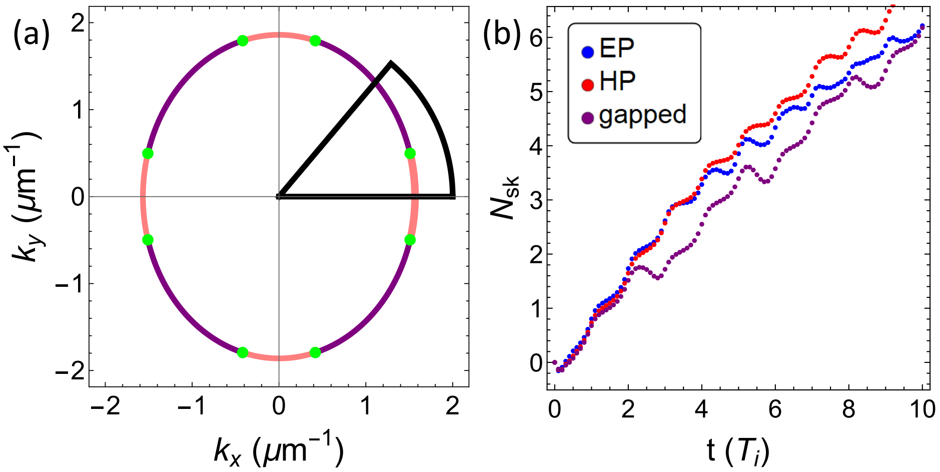

Figure 5.9: (a) The region of integration plotted with exceptional points and Fermi arcs. (b) The skyrmion number calculated in the region between $k \in [0, 2]$ and $\phi \in [0, \arccos\left(\sqrt{\frac{\beta'-\beta}{2\beta'}}\right) \approx 0.87]$ for $\Delta = 0$ (blue line), $\Delta = \delta\Gamma$ (red line) and $\Delta > \delta\Gamma$ (purple line). Here, t is in the units of T_i, which varies with Δ.

to effectively nonlinear dynamics of spin and pseudospin [273, 299, 300, 301, 302, 303, 304] requires further investigation.

5.5 Conclusion

In conclusion, I describe the process of generation, annihilation, and dynamics of emergent momentum-space pseudospin defects in a non-Hermitian two-band system. The spectrum can be tuned between a gapless and a gapped phase using a magnetic field, the former characterized by the presence of non-Hermitian degeneracies (exceptional and hybrid points). Using the simple case where the wavefunction is initially in a spatially homogeneous circularly-polarized state, I show analytically that the defects are generated in pairs, at the maxima of the mean-subtracted eigenenergy, then propagate towards the minima of the mean-subtracted eigenenergy. I also show that the defects with opposite vorticity will be annihilated if there is a real gap in the spectrum, but in the gapless phases, they will be protected by the non-Hermitian degeneracy. This whole process of generation and annihilation of defects preserves the total (zero) skyrmion number in the system. In contrast with quantum hydrodynamics of turbulent systems, the location and trajectories of the skyrmions in momentum space are fully deterministic and are determined by the location of eigenenergy degeneracy lines (imaginary Fermi arcs) in momentum space.

Since the pseudospin texture in an exciton-polariton system can be experimentally measured [167, 189, 191, 218], the measurement of the pseudospin defects will provide a clear signature of the effects of the imaginary Fermi arcs on the dynamics of the system. Furthermore, by measuring the pseudospin and the skyrmion number in a certain region

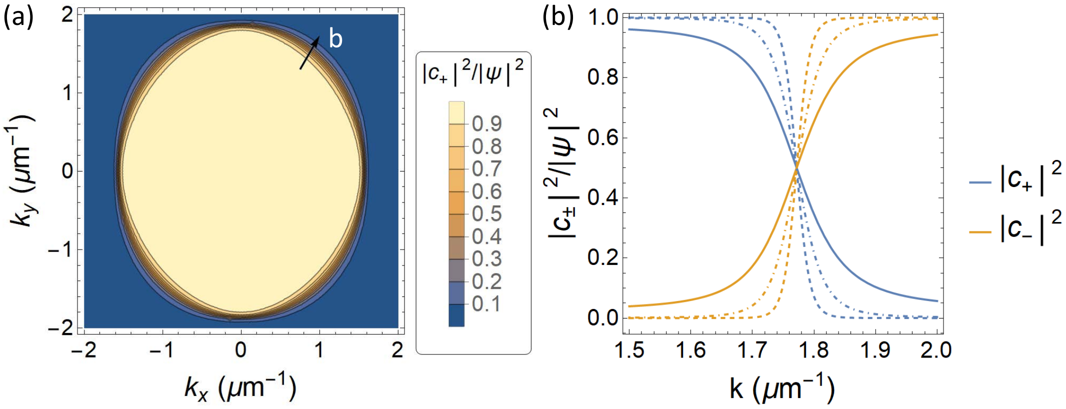

Figure 5.10: (a) The normalized overlap of the wavefunction with the upper eigenstate at $t = 5$ ps. (b) The cross section of normalized $|c_\pm|^2$ along the k-direction at $\phi = \pi/3$ marked with the black arrow in (a) at $t = 5$ ps (solid lines), $t = 10$ ps (dotted dashed lines) and $t = 20$ ps (dashed lines).

of the momentum space at different times, one can potentially detect the signature of the transition between the gapped and the gapless phase.

I also show that an imaginary Fermi arc forms a domain wall separating the regions where the pseudospins align with the two different eigenstates of the non-Hermitian system. It is therefore tempting to draw parallels with previous studies connecting the generation of skyrmions in a Hermitian spinor system to the domain wall instabilities [173, 174, 312], but a closer link between these effects remains to be uncovered. The study presented in this Chapter highlights the rich physics of non-Hermitian systems and the role played by the imaginary Fermi arcs in the new, experimentally observable dynamical effects. Furthermore, these defects are dynamics, which is in contrast to the static ones generated in the conventional Hermitian systems, that usually requires an applied electromagnetic field to move. Topological defects have potential application in quantum communication [136, 137]. Although, the generation and motion of the emergent defects discussed in this Chapter are purely determined by the underlying Hamiltonian, if one can find a way to control the motion of the defects or to stabilise them, this could potentially enable future applications in quantum communication.

Chapter 6

Momentum-Space Non-Hermitian Skin Effect

6.1 Introduction

As discussed before in Section 1.1.2, the non-Hermitian skin effect (NHSE), where all eigenstates localise on the edge of the system as a results of the point-gap topology of the eigenspectrum, plays an important role in non-Hermitian physics. However, it is difficult to realise the NHSE in real space. In one-dimensional periodic (lattice) systems, the NHSE either requires non-reciprocal coupling between the lattice sites [1, 3, 35, 44] or an induced flux [51, 52, 53]. In a system without discrete translational symmetry (i.e. a lattice), realisation of NHSE requires an imaginary gauge transformation [58], a combination between the Rashba-Dresselhaus spin-orbit coupling and dissipation [59], or, as recently shown, precise control over the boundary conditions [57]. These conditions are difficult to realise in an exciton-polariton system, which I focus on in this Thesis. However, in this Chapter, I will show that a similar localisation can be induced in momentum space of a continuous system. This k-space NHSE arises from an imaginary potential, which can be realised and controlled in a realistic exciton-polariton experiment.

In this Chapter, I will first review the NHSE induced by an imaginary gauge transformation in a continuous system with no discrete translational symmetry. I will then show that a similar effect can be realised in momentum space via an imaginary gauge transformation in momentum space, which corresponds to an imaginary offset in a spatial variable. I then illustrate this effect using a simple toy model which can be solved analytically. After this, I demonstrate that the k-space NHSE can similarly be realised using an asymmetric imaginary potential in real space, which corresponds to an optically-induced potential in an exciton-polariton system. Finally, I discuss the interplay between the NHSE and the nonlinearity by including a nonlinear interaction term in the Hamiltonian.

6.2 Continuous NHSE without Discrete Translational Symmetry

In this Section, I will review NHSE in real space induced by an imaginary gauge transformation. Let us first consider a one-dimensional (1D), single-band (spinless), non-Hermitian Hamiltonian describing a particle of mass m, subject to an imaginary vector potential A_0, which is well-known to exhibit NHSE [48, 57, 58, 60]

$$H = \frac{[p - iA_0]^2}{2m} + V(x) \tag{6.1}$$

where x (p) is the position (momentum) operator, and $V(x)$ is the (real-valued) confining potential. Here, the imaginary gauge transformation does not include charge, because exciton polaritons are neutrally charged. The imaginary gauge transform modifies the eigenstates as:

$$\psi_n(x) = e^{-A_0 \cdot x/\hbar} \phi_n^{(0)}(x), \tag{6.2}$$

where the $\phi_n^{(0)}(x)$ are the eigenstates of the Hermitian Hamiltonian (with $A_0 \to 0$) denoted by H_0, and n are positive integer that denotes the level.

The exponential factor $e^{-A_0 x/\hbar}$ in Eq. (6.2) demonstrates the action of the constant imaginary vector potential: it skews the eigenstates in real space towards the sign of A_0, as shown in Figs. 6.1(a,b) for a harmonic trap in the form of

$$V(x) = \frac{1}{2} m\omega^2 x^2, \tag{6.3}$$

where ω is the trapping frequency. Note that in Fig. 6.1, the exponential localisations of the wavefunctions towards the edges of the traps are demonstrated by plotting the amplitude of the right eigenstates. The edge localisation also occurs in a box-like trapping potential, such as shown in Figs. 6.1(d, e) for a super-Gaussian trap

$$V(x) = V_0 \left(1 - \exp\left[-\left(\frac{x^2}{a^2}\right)^{20}\right]\right), \tag{6.4}$$

where V_0 and a denote the depth and the width of the trap, respectively, and in other trapping configuration as long as there are bound states. Hence, Eq. (6.2) represents a simple continuous model exhibiting the non-Hermitian skin effect [48, 56, 58, 60], where a macroscopic number of eigenstates are localised towards the edge of the confining potential.

The topological origin of the NHSE is established through the non-trivial spectral winding and the sensitivity of the spectra to the boundary conditions [see Section 1.1] [1, 44, 54]. In prototypical tight-binding models, the NHSE is accompanied by the sharp difference between spectra under the periodic boundary condition (PBC) and the open-boundary condition (OBC). The OBC spectrum lies within the area enclosed by the PBC spectrum that has a non-trivial spectral winding in the complex plane[see Section 1.1.1] [6, 44, 49, 54].

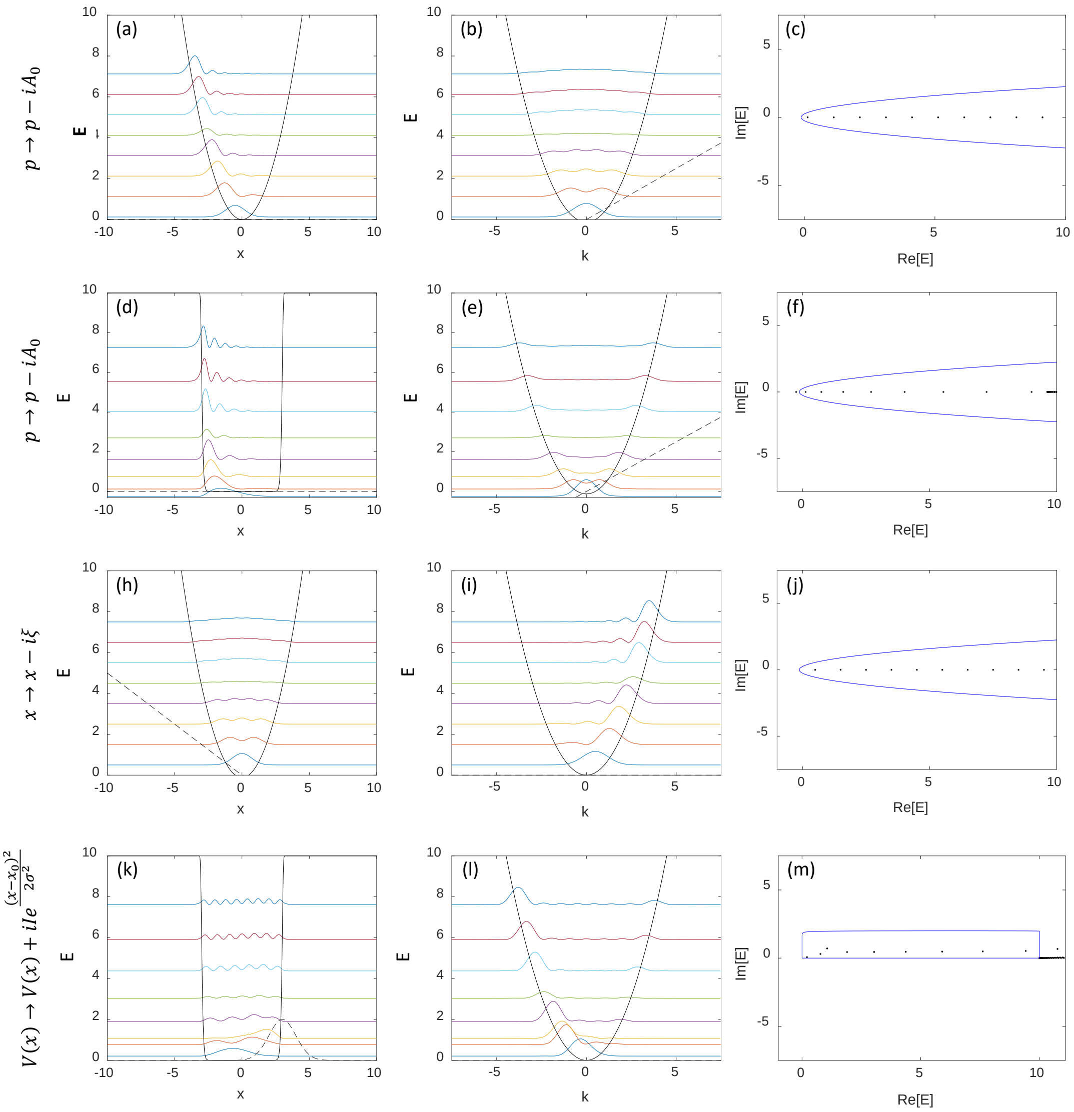

Figure 6.1: Continuous non-Hermitian skin effect (NHSE) in real space (a-f) induced by an imaginary gauge transformation and in momentum space induced by (h-j) an imaginary offset in x and (k-m) an imaginary Gaussian on the edge of the harmonic, Eq. (6.3), or the box-like, Eq. (6.4), trap. Panels (c,f) show the unconfined spectra (blue lines), which demonstrate point-gap topology and the confined spectra (black dots), which is similar to the sensitivity to the boundary condition in the NHSE in the lattice systems. Panels (j,m) shows the complex-valued potential (blue lines) with no kinetic energy and the spectra of both the kinetic and the potential energies (black dots) which shows behaviour similar with (c,f) but with x and k interchanged. The solid (dashed) lines in panels (a,d,h,k) show the real (imaginary) part of the potential energy in real space, and similarly the solid (dashed) lines in panels (b,e,i,l) show the real (imaginary) part of the kinetic energy in k space. In panels (a,b,d,e,h,i,k,l), E denotes the real part of the energies of the eigenstates.

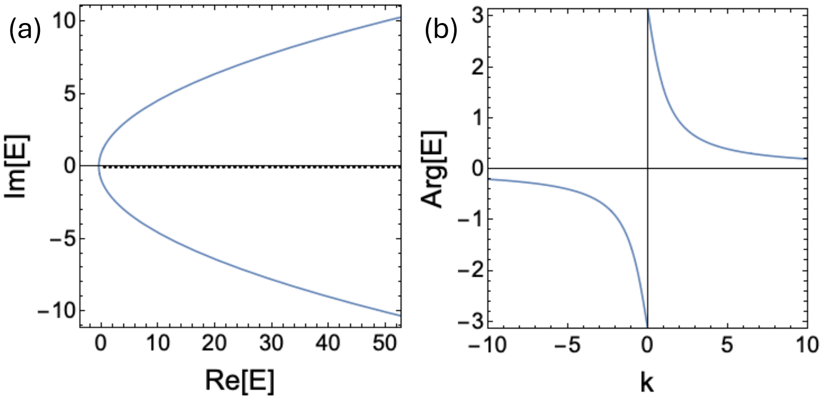

Figure 6.2: (a) The confined (blue line) and unconfined spectrum (black dots) of the Hamiltonian (6.1) with harmonic potential defined by Eq. (6.3). (b) The complex angle of the free spectrum, where the discontinuous jump at $k = 0$ results in non-zero spectral winding.

In the continuous version of NHSE, the PBC eigenspectrum is replaced with the unconfined eigenspectrum, i.e. eigenenergy there is no confining potential, $E_{PBC} \to E_{V=0}$ and use the momentum range of $k \in (-\infty, \infty)$ instead of a periodic one. The confinement due to the potential $V(x)$ plays the role of OBC [59, 51]. The unconfined spectrum is simply

$$E_{V=0} = \frac{[p - iA_0]^2}{2m}, \quad p \in (-\infty, \infty), \tag{6.5}$$

a parabola in the complex plane, while the trapped spectrum remains unchanged by the imaginary gauge transformation $E = E_{A_0=0}$ [58, 60]. For an illustrative example, consider a quantum harmonic oscillator with potential from Eq. (6.3), the harmonically trapped spectrum is

$$E_n = (n + 1/2)\hbar\omega, \quad n \in \mathbb{N} \tag{6.6}$$

which is purely real-valued. The two spectra are plotted in the complex plane in Fig. 6.1(c), showing the stark difference between the two, in the same way the OBC and PBC spectra are different in the NHSE in the lattice systems discussed previously in Section 1.1.2. Hence, the difference between the confined and the unconfined spectra here plays the same role as the sensitivity to the boundary conditions, and indicates the presence of the NHSE in a continuous system without discrete translational symmetry.

Next, I can calculate the spectral winding [see Section 1.1.1 for more details] of the unconfined spectrum around some base energy E_b for the range $k = (-\infty, \infty)$ following the topological index defined for tight-binding models [6, 44, 49] as follows:

$$w = \frac{1}{2\pi} \int_k \nabla_k [\arg(E_{V=0} - E_b)] \cdot dk = \mathrm{sgn}(A_0). \tag{6.7}$$

The nontrivial winding can be analytically calculated using the fundamental theorem of calculus, and depends on the sign of A_0, which determines the direction of localisation. A non-zero value of A_0 would results in both the localisation of the eigesntates at the boundary as well as non-zero spectral winding. This is equivalent to the point-gap topology, where the PBC spectrum forms a closed loop on the complex plane, in tight-binding models, which generalises the bulk-boundary correspondence to non-Hermitian systems, and in this case extends to continuous systems [see Fig. 6.2].

Physically realising an imaginary vector potential that leads to the emergence of the NHSE in real space is not straightforward, especially in continuous systems [51, 59, 58]. In this work, I generalise the skin effect to momentum space by switching the roles of position and momentum operators, and provide further insights into more complex forms of imaginary vector potentials and their effect on the eigenstates in position and momentum spaces. To gain more intuition, the dependence of localisation of the eigenstates in momentum space on various parameters is examined in the following Section.

6.3 Continuous Momentum-Space NHSE

When the roles of x and p in Eq. (6.1) are interchanged, the localisation (skin effect) occurs in the momentum space and is induced by an imaginary vector potential $A(p)$. To demonstrate the effect, I provide a simple example, a one-dimensional harmonic oscillator with a linear imaginary potential given by $V(x) = m\omega^2(x^2 - i\xi x)/2$. The Hamiltonian can be written in momentum space as

$$H_p = \frac{p^2}{2m} + \frac{1}{2}m\omega^2\left(i\hbar\frac{\partial}{\partial p} - i\frac{\xi}{2}\right)^2 + \frac{1}{8}m\omega^2\xi^2. \tag{6.8}$$

In this form, the imaginary vector potential (in momentum space) is $A(p) = \xi/2$, analogous to A_0 in Eq. (6.1) with the addition of a constant energy offset (last term in Eq. 6.8). The confined energies are:

$$E_n = (n + 1/2)\hbar\omega + m\omega^2\xi^2/8, \tag{6.9}$$

with the corresponding momentum, p, eigenstates:

$$\psi_n(p) = e^{\xi p/2\hbar}\psi_n^{(0)}(p) \tag{6.10}$$

where $\psi_n^{(0)}(p)$ are the eigenstates of the Hermitian harmonic oscillator (with $\xi = 0$). The exponential factor explicitly shows the localisation, and hence, the skin effect in momentum space. The complex spectra are exactly the same as the Hermitian case, except for the energy offset. In the previous Section, it is demonstrated that the exponential localisation of all eigenstates at the edge corresponds to the non-zero spectral winding, a non-Hermitian topological invariant, of the unconfined spectrum in a continuous system (or the PBC spectrum in a lattice system). This shows the skin effect to be intimately related to the topology of the complex-valued eigenenergies. Here, the imaginary offset in x similarly results in the exponential localisation of all momentum-space eigenstates, showing the NHSE in momentum space.

To understand the connection of the simple model (6.8) to the prototypical Hatano-

Nelson model [48], which is the simplest tight-binding model demonstrating the NHSE, consider the Hamiltonian H_p (6.8) discretised in momentum space:

$$\begin{aligned} H_p =& \sum_n \Big(\frac{n^2(\Delta p)^2}{2m} + \frac{m\hbar^2\omega^2}{(\Delta p)^2}\Big)|n\rangle\langle n| \\ &+ \Big(-\frac{m\hbar^2\omega^2}{2(\Delta p)^2} - \frac{m\hbar\omega^2\xi}{4\Delta p}\Big)|n\rangle\langle n+1| \\ &+ \Big(-\frac{m\hbar^2\omega^2}{2(\Delta p)^2} + \frac{m\hbar\omega^2\xi}{4\Delta p}\Big)|n+1\rangle\langle n|. \end{aligned} \tag{6.11}$$

In this form, the imaginary vector potential ξ clearly induces asymmetric nearest-neighbor hopping (second and third lines), which is the key component to the NHSE of the Hatano-Nelson model described by Eq. (1.8) [48]. The kinetic term, $p^2/(2m)$ plays the role of the "trapping" potential which simply adds an onsite potential.

I further investigate the topological nature of the localisation by examining the sensitivity of the spectrum (6.11) to the boundary conditions. Since the NHSE and the imaginary gauge transformation are now in momentum space, the unconfined spectra (corresponding to the PBC) can be obtained by setting $m \to \infty$ to remove the confinement, which is described by the parabola of the kinetic energy. Hence, the unconfined eigenspectra are simply the potential, i.e. $E = V(x)$, which is also a parabola in the complex plane. The confined eigenspectrum (corresponding to the OBC) is given by Eq. (6.9), which is again confined on the real axis. The two eigenspectra are plotted in Figs. 6.1(j,m), clearly showing the stark difference between the unconfined and confined spectra, corresponding to the point-gap topology in 1D tight-binding model that exhibits NHSE [see Section 1.1].

Interestingly, the localisation in momentum space can persist even if the confining potential (real part of V) is not harmonic and the imaginary potential (imaginary part of V) is not linear. An example is shown in Fig. 6.1(k-m), where the confining potential is an inverted super-Gaussian (6.4) and the imaginary part is an off-centered Gaussian

$$V(x) = V_0\left(1 - e^{-\left(\frac{x^2}{a^2}\right)^{20}}\right) + Iie^{-(x-x_0)^2/(2\sigma^2)}, \tag{6.12}$$

where I, x_0 and σ denote the height, the centre, and the width of the imaginary-valued Gaussian. In this case, the real-space eigenstate distributions remain symmetric but the momentum-space eigenstates are localised towards the direction of the offset of the imaginary part [see Fig. 6.1(k-m)].

Furthermore, the complex eigenspectrum is also sensitive to the boundary conditions as shown in Fig. 6.1(j,m). The unconfined eigenspectrum forms a closed loop in the complex plane with a finite area and a non-zero topological winding number defined using Eq. (6.7) but with $k \to x$ and $E_{V=0} \to V(x)$. The sign of the winding depends on the relative position of the center of imaginary Gaussian potential with respect to the center of the confining potential. When the imaginary Gaussian is centered on the trap, there is no localisation and the winding (6.7) of the unconfined spectrum is zero [see Fig. 6.3].

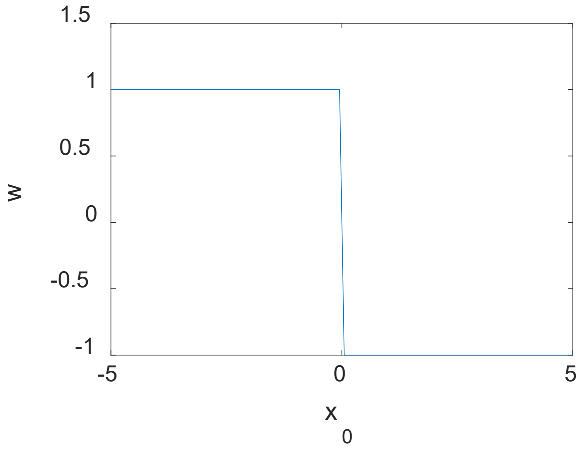

Figure 6.3: The winding plotted against the centre-of-mass position of the imaginary Gaussian inside an inverted super-Gaussian trap similar to the one shown in Fig. 6.1(k). Here, the super-Gaussian trap defined by Eq. (6.12) has a depth of $V_0 = 10$ and a width of $a = 5$. The imaginary Gaussian has a width of $\sigma = 1$ and a height of $I = 1$.

6.4 Proposal for Experimental Realisation in an Exciton-Polariton System

In this section, I present an effective model that is based on an experimentally realisable quasi-1D exciton-polariton system [313]. The effective one-dimensional Hamiltonian can be written in the following form:

$$H = \frac{p^2}{2m} + V(x), \tag{6.13}$$

and the trapping potential consists of a potential well arising from the structure of the sample [314] and an additional complex-valued Gaussian-shaped potential barrier induced by the optical pump that creates an incoherent excitonic reservoir in the system (see Section 1.4 for details). Although the etching of the sample that creates the trapping potential locally changes the polariton linewidth, this effect will be symmetric, and does not result in NHSE in momentum space. In this Section, the units are set to be arbitrary unit for simplicity.

$$V(x) = V_0(x) + (R + iI)e^{-(x-x_0)^2/(2\sigma^2)}. \tag{6.14}$$

Here, $V_0(x)$ is the trapping potential that arises from the structure of the microcavity and and is shaped as a finite square well with height V_0 [315, 314] and width a, which I

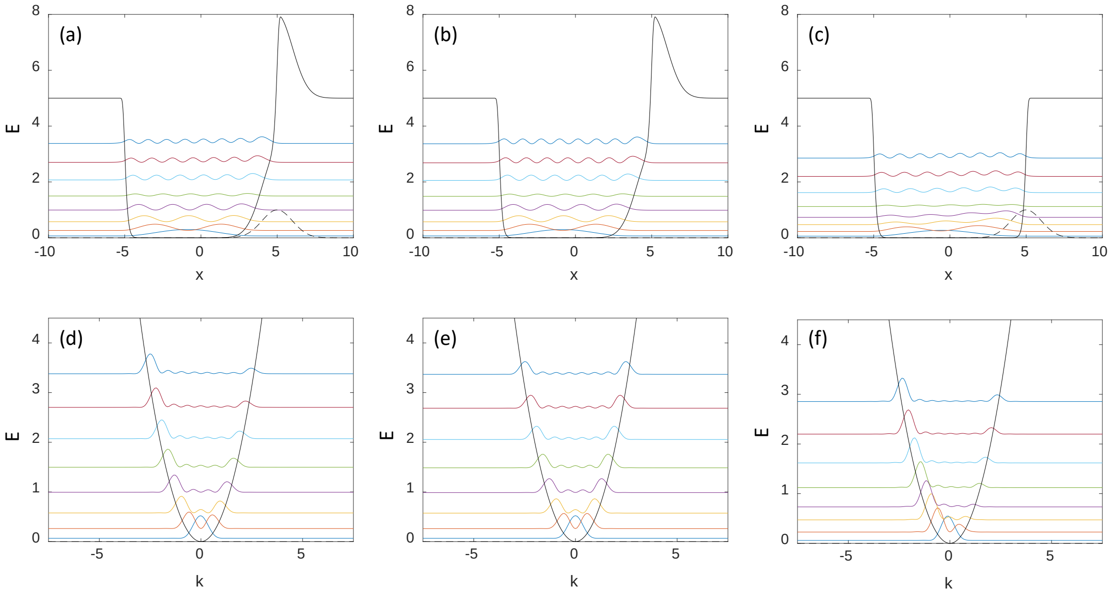

Figure 6.4: The amplitudes of the 8 lowest energy right eigenstates in a finite square well with height $V_0 = 5$ and width $a = 5$ with a complex-valued Gaussian barrier in real and momentum space. (a, d) showing the eigenstates with both real and imaginary Gaussian, (b, e) showing the eigenstates with only the real Gaussian and (c, f) showing the eigenstates with only the imaginary Gaussian. Here, the heights of the real and imaginary Gaussian are $R = 3$ and $I = 1$, and the width of the Gaussian is $\sigma = 1$. The black solid (dashed) lines represent the real (imaginary) parts of the kinetic energy and potential energy. In the simulation, I set the grid to be periodic at $x = \pm 40$. This enables the Fourier transform, but also minimises the effects from the grid boundary since it is significantly far away from the edge of the trap.

approximate using a super-Gaussian

$$V_0(x) = V_0\left(1 - e^{-\left(\frac{x^2}{a^2}\right)^{20}}\right), \tag{6.15}$$

which is shaped similarly to a finite square well, but with smoothed edge, which is more realistic. Parameters R and I in Eq. (6.14) represent the height of the real and imaginary parts of the Gaussian-shaped potential barrier, respectively. The height of the square well is set to $V_0 = 5$ while the width is $a = 5$.

In Fig. 6.4, I plot the 8 lowest-energy eigenstates to show the effects from the real and imaginary part of the Gaussian potential barrier centred on the edge of the trap. Fig. 6.4 shows that although a real Gaussian would shift the centre-of-mass of the eigenstates in real space [Figs. 6.4(a-b)], an imaginary Gaussian is required to induce localisation of the eigenstates in momentum space [Fig. 6.4 (d, f)] and in the absence of the imaginary Gaussian, the eigenstates stay symmetric in momentum space [Fig. 6.4 (e)].

I also vary the height, the width and the centre of the imaginary part of the Gaussian

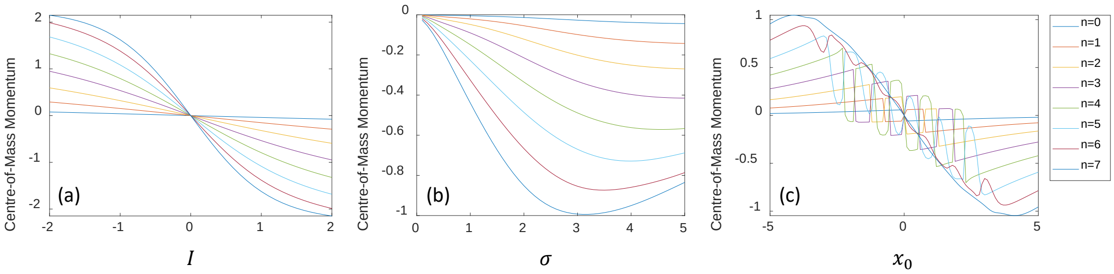

Figure 6.5: The centre of mass momenta of the 8 lowest energy eigenstates plotted with (a) different heights, I, (b) different widths, σ, and (c) different centre-of-mass position, x_0 of the imaginary Gaussian (see Eq. (6.14)). The height and width of the Gaussian are set at $I = 0.5$ in (b, c), $\sigma = 2.5$ in (a,c) and centred at $x_0 = 5$ in (a,b) unless specified otherwise. The trap takes the form of the inverse super-Gaussian in Eq. (6.15) with $V_0 = 10$ and $a = 5$.

pump to investigate how these parameters affect the centre-of-mass momentum of the eigenstates. While Fig. 6.5(a) shows that the strength of localisation increases with the height of the imaginary Gaussian, the dependence on the width and the centre seem to be more complicated. The eigenstates seem to reach the strongest asymmetry around $\sigma = 3$, which suggests that localisation of the eigenstates is the strongest for the more anti-symmetric imaginary potential [Fig. 6.5(b)]. Similarly, from Fig. 6.5(c), it seems that although the centre of the imaginary Gaussian and the centre-of-mass momenta of the eigenstates are not simply related, as long as the Gaussian is not centred on $x = 0$, the eigenstates will become asymmetric and localise in momentum space.

6.5 Effects of Nonlinearity

I then explore the effects of nonlinearity on the localisation or the non-Hermitian effect by exploring an exciton-polariton condensate based on the Gross-Pitaevskii formalism. For polaritons, this nonlinearity arises from the matter component and reflects the repulsive interaction between excitons [13, 12, 316]. To model the effect of this repulsive polariton-polariton interaction, a nonlinear term $g|\psi|^2$ is introduced to the effective Hamiltonian (6.8).

In this section, I introduce a nonlinear term to the more simple effective Hamiltonian model, Eq. (1.77), to gain some insights on the effects of interactions that may be applicable to an exciton-polariton setting:

$$H = \frac{\hbar^2 k^2}{2m} + \frac{1}{2} m\omega^2 (x - i\xi)^2 + g|\psi|^2 \tag{6.16}$$

This equation is similar to the Hamiltonian resulting in the Gross-Pitaevskii equation for the polariton wavefunction [245, 246], but with a complex-valued potential.

Although I am unable to determine the entire eigenspectrum due to the additional nonlinear term, The ground state can be numerically found by employing imaginary time evolution [317] and split-step methods [278, 279].

The corresponding Gross-Pitaevskii equation for the polariton wavefunction in real time

$$i\hbar \frac{d}{dt}\psi = -\frac{\hbar^2}{2m}\nabla^2\psi + \frac{1}{2}m\omega^2(x - i\xi)^2\psi + g|\psi|^2\psi \tag{6.17}$$

can be rewritten in imaginary time $\tau = it$

$$-\hbar \frac{d}{d\tau}\psi = -\frac{\hbar^2}{2m}\nabla^2\psi + \frac{1}{2}m\omega^2(x - i\xi)^2\psi + g|\psi|^2\psi. \tag{6.18}$$

In this case, for an initial wavefunction in a superpositions of different eigenstates (or steady states in the nonlinear case), $\psi(0) = \sum_n c_n\psi_n$, evolution in imaginary time at $\tau \to \infty$ ensures that all the higher energy states will decay and the wavefunction will evolve into the lowest energy eigenstate (or steady state)

$$\begin{aligned} \psi(\tau) &= e^{-\frac{H\tau}{\hbar}}\psi(0) \\ &= \sum_n c_n e^{-\frac{E_n\tau}{\hbar}}\psi_n \\ &\xrightarrow{\tau\to\infty} c_0\psi_0. \end{aligned} \tag{6.19}$$

In order to tackle the nonlinear terms, I implement split-step methods in imaginary time, and evolve the wavefunction under the linear and nonlinear parts of Hamiltonian separately,

$$\psi(x, \tau + \Delta\tau) = e^{-g|\psi(x,\tau)|^2\Delta\tau/\hbar}e^{-H_l\Delta\tau/\hbar}\psi(x, \tau) \tag{6.20}$$

where $H_l = -\frac{\hbar^2}{2m}\nabla^2 + \frac{1}{2}m\omega^2(x - i\xi)^2$ denotes the linear part of the Hamiltonian, which was discretised into an $N \times N$ matrix, with N being the size of the grid, and $e^{-H_l\Delta\tau/\hbar}$ computed using the matrix exponential in MatLab. The results of the simulation with different g are plotted in Fig. 6.6. Here, I also normalise the wavefunction at each step, so even if the lowest energy level is below zero, the algorithm would not diverge.

The repulsive interaction broadens the ground-state wavefunctions in the real space [see fig. 6.6(a)] and narrows wavefunctions in momentum space [see fig. 6.6(ab]. This is expected even in the Hermitian case. Interestingly, as the strength of g increases, it also shifts the centre-of-mass momentum of the ground-state wavefunction, and therefore strengthens the localisation in momentum space [see fig. 6.6(c, d)]. This is unlike the NHSE in the real space where the repulsive interaction is expected to widen the wavefunction, therefore weakening the localisation. Although, the strengthening of the k-space NHSE could be attributed to the energy blue-shift induced by nonlinaerity.

6.6 Conclusion

In this Chapter, I discuss localisation of eigenstates in momentum space induced by a complex-valued potential. I uncover that this effect is equivalent to the real-space NHSE with position and momentum space interchanged, and it presents an easier way to implement NHSE in a realistic experimental setup. I also propose a way to realise this effect using an exciton-polariton system in a trapping potential. Finally, I discuss the

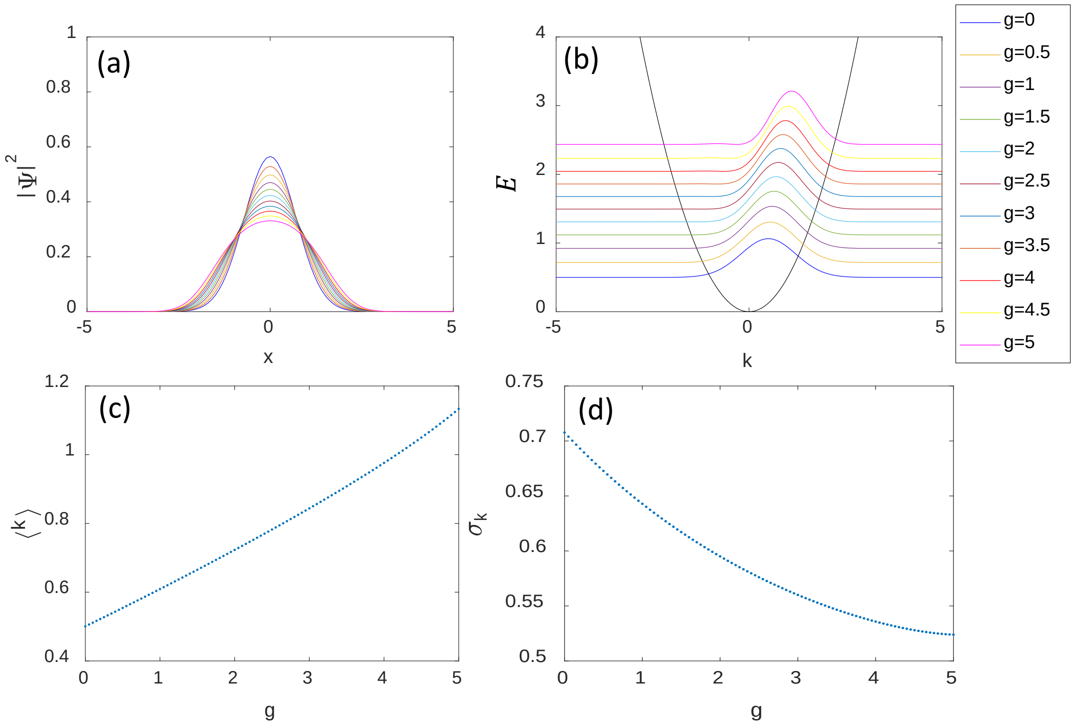

Figure 6.6: The amplitudes of the ground-state wavefunctions in (a) real and (b) momentum space. The black solid lines in panels (a) and (b) represents the real part of the potential and kinetic energy, respectively, and the wavefunctions in (b) are plotted at the values of energy that are shifted with respects to the ground-state eigenenergies. Panels (c, d) show the centre-of-mass momenta and widths in momentum space of the ground-state wavefunction with different values of g. Here, I set $\xi = 0.5$.

effect of nonlinear interaction and show that while the nonlinearity broadens the ground states in the real space, it enhances the localisation in the momentum space. This suggests an interesting new approach to investigating the interplay between the non-Hermitian and nonlinear effects, where nonlinearity enhances the localisation, instead of weakening it.

Experimental verification of the theory presented here faces several difficulties. For example,the influence of nonlinearity is difficult to isolate from other effects. In experiments, the nonlinear interaction is induced by increasing the pump strength beyond the condensation threshold [13, 12]. However, since the complex-valued optically induced potential is also proportional to the pump, increasing the pump strength also enhances the imaginary Gaussian potential. In this case, it would be difficult to distinguish between the effects arising from the interaction and the effects arising from a stronger imaginary potential. Additionally, since the ratio between the real and imaginary parts of the optically-induced potential is fixed and is determined by the material, it would also be experimentally impossible to turn off either the real or the imaginary part of the potential. Nevertheless, experiments are currently ongoing in the ANU Polariton BEC Group to verify these theoretical predictions.

Chapter 7

Conclusion and Outlook

In this Thesis, I have presented the results of the research I conducted during my PhD with the help of my research group and collaborators. My initial focus was to generalise the quantum geometric tensors to non-Hermitian systems and to investigate their consequence on the dynamics of the wavepackets. The unexpected complexities and vastness of new dynamical effects in non-Hermitian systems forced me to detour to also describe other dynamical effects including the self-acceleration of wavepackets. This then led me to look into the pseudospin dynamics in non-Hermitian systems, resulting in my research on the defect dynamics and the generlised Zitterbewegung effect. In the following section, I will summarise the key findings of my research.

7.1 Summary of Major Findings

In summary, my research has uncovered novel dynamics of wavepackets and pseudospins arising from topology and quantum geometry in non-Hermitian systems. Using exciton-polariton systems as an experimentally relevant example, I investigated how non-Hermiticity affects the wavepacket and pseudospin dynamics as well as topological edge states.

In Chapter 2, I investigated the self-acceleration of the wavepackets in non-Hermitian exciton-polariton systems. In particular, I describe the dynamics and splitting of the exciton-polariton wavepackets in momentum space even in the absence of a real-space potential, and showed that these effects arise from the finite wavepakcet size and the non-zero gradient of the imaginary energy landscape in momentum space. I also identified the extrema of the imaginary energy as attractors of the wavepacket centre-of-mass motion.

In Chapter 3, I investigated how the inclusion of an external force modifies the wavepacket dynamics in non-Hermitian systems. First, I included a small external force and investigated the interplay between the self-acceleration arising from the finite wavepacket size and the acceleration arising from the external potential. I then analytically derived a semi-classical equation of motion of wavepackets in non-Hermitian two-dimensional systems using perturbation theory. My semi-classical theory explicitly shows that both the right-right (RR) and left-right (LR) quantum geometric tensors (QGTs) play significant roles in the wavepacket dynamics. In particular, the RR QGT appears as the correction to the wavepacket centre-of-mass position, the LR QGT appears as the correction to the phase of the wavepackets. I also showed how the components of the

LR QGT can be constructed from the exciton-polariton pseudospins, which enables its direct measurement. I emphasise that both the components of QGT and the wavepacket dynamics can be independently measured experimentally, and hence can provide direct experimental tests of the validity of the role of non-Hermiticity on quantum geometry.

In Chapter 4, I presented a generalisation of the Zitterbewegung effect for wavepackets in non-Hermitian systems. I first reviewed the pseudospin dynamics in non-Hermitian systems, which is qualitatively different from the Hermitian case. I then derived an analytical semi-classical theory for the wavepacket centre of mass motion, highlighting new dynamical effects arising from both the pseudospin behaviour and from the non-Hermitian parts of the Hamiltonian. I also demonstrated that in the special case where there is no out-of-plane component of the effective magnetic field, the non-Hermitian corrections can be expressed in terms of the LR quantum metric tensor, showing how this generalised Zitterbewegung effect is related to quantum geometry. This effect can also, in principle, be verified experimentally in an exciton-polariton system.

In Chapter 5, I described the emergent pseudospin defects on the imaginary Fermi arcs in momentum space of a two-band non-Hermitian system. I highlighted that these defects are entirely deterministic, and can emerge even in the absence of nonlinear interactions or turbulence. I also showed that in a simple case, where the system is initially spatially homogeneous and circularly polarized, the defects can be described analytically both in the gapless and gapped phases. These phases are defined by the absence or presence of a gap in the real part of the eigenenergy spectrum, respectively. I then showed that in the gapless phases, the defects are protected by the non-Hermitian spectral degeneracy (exceptional points and hybrid points), whereas in the gapped phases, they will be annihilated with each other. Finally, I suggested that the signatures of these defects can be experimentally measured using non-Hermitian exciton-polariton systems.

And finally, in Chapter 6, I demonstrated that non-Hermitian skin effects can be induced in momentum space by an imaginary potential in the real space. I first illustrated this effect using a simple modified quantum harmonic oscillator model which can be analytically solved. I then considered a more realistic exciton-polariton system in the presence of a trapping potential, which comes from the sample structure, and a complex-valued Gaussian-shaped potential barrier, which arises from the pump. I showed that the imaginary parts of the Gaussian potential can induce the localisation of the trapped states in momentum space. Finally, I showed that, in principle, the presence of nonlinear interaction can strengthen the localisation of the eienstates in momentum space. However, in actual experiments, it would be difficult to separate the effects arising from the potential from the ones arising from the interaction.

These results demonstrate the new physics and novel dynamical effects in non-Hermitian systems as well as the potential of exciton polaritons as an experimental platform for studies of non-Hermitian physics. There are still many things to investigate further. In the next section, I will present a non-exhaustive list of future directions.

7.2 Future Directions

7.2.1 Non-Adiabatic Wavepacket Dynamics

In Chapter 4, I presented an analytical semi-classical theory of the wavepacket in terms of the pseudospin precession in the absence of an external force. In Chapter 3, I also presented a different analytical semi-classical theory of the wavepackets in the presence of a force using perturbation theory. One potential future direction is to include an external force in the derivation of the non-Hermitian Zitterbewegung effect.

Usually, the semi-classical theory of wavepackets in non-Hermitian systems fails when a wavepacket centre-of-mass momentum crosses the Fermi arcs. As discussed in Chapters 2 and 5, the quantum state in non-Hermitian systems evolves into the least dissipative eigenstate, and the Fermi arcs separate the regions where the quantum state evolves into different eigenstates. Therefore, the wavepacket would first evolve into one eigenstate on one side of the Fermi arcs, before it evolves into a different eigenstate when it crosses the Fermi arcs. In the semi-classical theory, the wavepacket is usually assumed to stay in the same eigenstates, which would fail to capture this non-adiabatic behaviour. I believe that a theory that captures both the acceleration due to an external force and the pseudospin precession would address this problem and demonstrate the novel effects of the wavepackets in non-Hermitian systems without the above constraints.

7.2.2 Generalisation of Non-Hermitian Skin Effects

In Chapter 6, I showed that the non-Hermitian skin effect can occur in the momentum space, where the imaginary parts of the potential in real space induce localisation of the eigenstates in momentum space and the kinetic energy plays the role of a trapping potential. Although I was able to show numerically that an asymmetric imaginary potential induces the localisation in momentum space, it is still unclear what the necessary conditions are for the the existence of the edge,'skin' modes in momentum space.

My main assumption in Chapter 6 is that for the momentum-space NHSE in continuum, the complex-valued potential term is analogous to the eigenspectrum under periodic boundary conditions (PBC) while the eigenspectrum of the full Hamiltonian is analogous to the eigenspectrum under open boundary conditions (OBC). This was an intuitive generlisation from the NHSE in real space in a continuous, non-periodic systems where the unconfined spectrum, the eigenspectrum from the kinetic terms alone, plays the role of the PBC eigenspectrum while the eigenspectrum of the full Hamiltonian plays the role of the OBC eigenspectrum. However, this assumption has not yet been properly proven. Therefore, I believe that another key future direction is to generalise the previous theories in Refs. [55, 57], which predict the existence of non-Hermitian skin modes using non-Bloch band theory, to predict the skin modes in momentum space, as well as find a new way to define the point-gap topology and non-Hermitian bulk-boundary correspondence.

7.2.3 Interplay between Nonlinearity and Non-Hermiticity

In Chapter 6, I highlighted that the inclusion of repulsive nonlinear interaction strengthens the non-Hermitian skin effects in momentum space, and weakens the non-Hermitian skin effects the real space. One other potential future direction is to investigate the interplay between nonlinearity and the non-Hermitian topology. Using the Bogoliubov spectrum of incoherently pumped exciton-polariton condensate [244], it is possible to investigate if the inclusion of nonlinearity would break the point-gap topology in a system that exhibits skin modes in the real space. On the other hand, one can also investigate how the inclusion of the nonlinearity affects the unconfined spectrum of a continuous, non-periodic system that exhibits skin modes in momentum space.

Chapter 8

Appendix

A Values of Parameters

In this Section, I present the values of the parameters that I used for the figures and simulations in this thesis. I keep most of the parameters constant and change the values of the Zeeman splitting to open or close a gap.

For the perovskite-based exciton-polariton model, I choose the parameters such that the exceptional points are well separated and the bulk Fermi arcs are clearly visible. I set $\gamma_2 = 0$ μm^{2}eV, $\gamma_4 = 3.75 \times 10^{-4}$ μm^{4}eV, and choose the mean energy, linewidth and effective polariton mass to be $E_0 - i\gamma_0 = 2.306 - 4.5 \times 10^{-4}i$ eV and $\hbar^2/2m \approx 2.3 \times 10^{-3}$ μm^{2}eV. The X-Y splitting parameters are $\alpha = 8 \times 10^{-3}$ eV and $a = 10^{-5}$, while the TE-TM splitting parameters are $\beta = 10^{-3}$ μm^{2}eV and $b = 7.5 \times 10^{-4}$ μm^{2}eV. The Zeeman splitting $\Delta_z = 0$ unless stated otherwise. Using this set of parameters, the exceptional points are located at $k \approx 2.5$ μm^{-1} and each pair is separated by ≈ 1.6 μm^{-1} in momentum space. For comparison, in the perovskite-based exciton-polariton system described in Ref. [218], the exceptional points are located at $k \approx 6.7$ μm^{-1} and each pair is separated by ≈ 0.24 μm^{-1} in momentum space, making the Fermi arc difficult to see.

The only exception was in Section 5.2.4, where I used the values from the realistic perovskite-based sample in Ref. [218] to show that the pseudospin defects can be experimentally meausred. Here, I set the parameters for the mean polariton energy and linewidths to be $E_0 = 2.306$ eV, $\gamma_0 = 4.58 \times 10^{-4}$ eV, $\hbar^2/(2m) = 2.3 \times 10^{-3}$ eVμm^2, $\gamma_2 = 1.45 \times 10^{-7}$ eVμm^2 and $\gamma_4 = 8.59 \times 10^{-8}$ eVμm^4. While the parameters related to the anisotropy are set at $\alpha = 8 \times 10^{-3}$ eV and $a = 4.28 \times 10^{-6}$ eV, and the parameters related to the TE-TM splitting are set at $\beta = 1.76 \times 10^{-4}$ eVμm^2 and $b = 6.4 \times 10^{-6}$ eVμm^2.

For the liquid-crystal microcavity exciton polaritons, I used the parameters from fitting with a real experimental sample. The effective masses in the x and y directions are $m_X = 1.34 \times 10^{-5} m_0$ and $m_Y = 1.08 \times 10^{-5} m_0$, where m_0 is the bare electron mass. The linewidths Γ_0 and $\delta\Gamma$ take the values of $\Gamma_0 = 1.92$ meV and $\delta\Gamma = 0.12$ meV. While the anisotropy and TE-TM splittings take values of $\alpha = 1.35$ meV, $\beta = 0.08$ meVμm^2 and $\beta' = 0.47$ meVμm^2.

B Appendix for Self-Acceleration and Force in Chapter 3

In this Appendix, I will present the derivation of the semi-classical equation of motion presented in Section 3.2.1. I will first briefly review the methods the Silberstein et al. used in Ref. [205] before showing my own results.

B.1 Review of Methods used by Silberstein et al.

Similarly with the derivation in Section 1.3.2, let us consider a Hamiltonian under an external force

$$\hat{H} = \hat{H}_0 - \mathbf{F} \cdot \mathbf{r}, \tag{B1}$$

where $\hat{H}_0$ has left and right eigenstates $|u_n^{L,R}\rangle$ as well as eigenenergies E_n. Suppose that there exists a wavepacket placed in the n-th right eigenstate of $\hat{H}_0$

$$|W\rangle = \int w_{n,\mathbf{k}} e^{i\mathbf{k}\cdot\mathbf{r}} |u_n^R\rangle d^2\mathbf{k} \tag{B2}$$

where $w_{n,\mathbf{k}}$ denotes the WP distribution. However, unlike in the derivation in Hermitian case presented in Section 1.3.2, the norm $N = \langle W|W\rangle$ is no longer constant due to the growth or decay of $|u_n^R\rangle$, therefore, the group velocity needs to be calculated as

$$\dot{\mathbf{r}}_c = \frac{1}{N}\frac{d}{dt}\langle W|\hat{\mathbf{r}}|W\rangle + \frac{\dot{N}}{N}\mathbf{r}_c. \tag{B3}$$

More importantly, since the system is no longer conserved, the Euler-Lagrange equation is no longer valid [205].

The centre-of-mass position of the wavepacket can be calculated similarly to the derivation in Section 1.3.2

$$\begin{aligned} \mathbf{r}_c &= \frac{1}{N}\left(\int i w_{n,\mathbf{k}}^* \partial_\mathbf{k} w_{n,\mathbf{k}} \langle u_n^R|u_n^R\rangle d^2\mathbf{k} + \int |w_{n,\mathbf{k}}|^2 \langle u_n^R|i\partial_\mathbf{k} u_n^R\rangle d^2\mathbf{k}\right) \\ &= -\partial_\mathbf{k}\varphi - \frac{i}{2}\frac{\partial_\mathbf{k} I_{nn}}{I_{nn}} + \mathbf{A}_n^{RR}\bigg|_{\mathbf{k}=\mathbf{k}_c}. \end{aligned} \tag{B4}$$

Here, I set $\langle u_n^R|u_n^R\rangle = I_{nn} \neq 1$, and the RR Berry connection is defined as

$$\mathbf{A}_n^{RR} = \frac{\langle u_n^R|i\partial_\mathbf{k} u_n^R\rangle}{\langle u_n^R|u_n^R\rangle}, \tag{B5}$$

which was also the case in Ref. [205]. In this definition, we can also identify the second term in the last line of Eq. (B4) as

$$\frac{i}{2}\frac{\partial_{\mathbf{k}I}}{I} = \mathrm{Im}[\mathbf{A}_n^{RR}]. \tag{B6}$$

This results in the wavepacket centre-of-mass position as

$$\mathbf{r}_c = -\partial_{\mathbf{k}}\varphi + \operatorname{Re}[\mathbf{A}_n^{RR}]\Big|_{\mathbf{k}=\mathbf{k}_c}. \tag{B7}$$

Alternatively, one can also set $I_{nn} = 1$. In this case the wavepacket centre-of-mass position is

$$\mathbf{r}_c = -\partial_{\mathbf{k}}\varphi + \mathbf{A}_n^{RR}\Big|_{\mathbf{k}=\mathbf{k}_c}. \tag{B8}$$

where the RR Berry connection is real-valued.

Under single-band approximation, Silberstein et al. show that the time evolution of the wavepacket can be calculated from the coefficients using Schrodinger equation

$$\begin{aligned} i\hbar\dot{w}_{n,\mathbf{k}} &= E_n w_{n,\mathbf{k}} + \mathbf{F}\cdot\langle u_n^L|\hat{\mathbf{r}}|u_n^R\rangle \\ &= E_n w_{n,\mathbf{k}} + \mathbf{F}\cdot\mathbf{A}_n^{LR}. \end{aligned} \tag{B9}$$

By using this relation and assuming the wavepacket to be infinitely narrow wavepacket in momentum space $|w_{n,\mathbf{k}}|^2 = \delta(\mathbf{k}-\mathbf{k}_c)$, Silbersein et al. derived the relation

$$\frac{1}{N}\int |w_{n,\mathbf{k}}|^2 I_{nn}(\mathbf{k}) f(\mathbf{k}) d^2\mathbf{k} = 2f(\mathbf{k})\operatorname{Im}[E_n + \mathbf{F}\cdot\mathbf{A}_n^{RR}] + \mathbf{F}\cdot\Big(\partial_{\mathbf{k}} f - 2\operatorname{Im}[E_n]\Big)\Big|_{\mathbf{k}=\mathbf{k}_c}. \tag{B10}$$

Using this relation, we can derive each term in Eq. (B3) one by one. The dynamics in the weight of the wavepakcet N takes the form as

$$\frac{\dot{N}}{N} = \frac{2}{\hbar}\operatorname{Im}\Big[E_n + \mathbf{F}\cdot(\mathbf{A}_n^{RR} - \mathbf{A}_n^{LR})\Big]. \tag{B11}$$

The first term in in Eq. (B3) can be similarly calculated as

$$\begin{aligned} \frac{1}{N}\frac{d}{dt}\langle W|(\hat{\mathbf{r}})_i|W\rangle =& \frac{1}{N}\frac{i}{\hbar}\Bigg(\int I_{nn}(\mathbf{k})(\dot{w}_{n,\mathbf{k}}^*\partial_{k_i} w_{n,\mathbf{k}} + w_{n,\mathbf{k}}^*\partial_{k_i}\dot{w}_{n,\mathbf{k}})d^2\mathbf{k} \\ &+ \int \langle u_n^R|\partial_{k_i} u_n^R\rangle(\mathbf{k})(\dot{w}_{n,\mathbf{k}}^* w_{n,\mathbf{k}} + w_{n,\mathbf{k}}^*\dot{w}_{n,\mathbf{k}})d^2\mathbf{k}\Bigg) \\ =& \frac{2}{\hbar}(\mathbf{r}_c)_i\operatorname{Im}[E_n + \mathbf{F}\cdot(\mathbf{A}_n^{RR} - \mathbf{A}_n^{LR})] + \frac{1}{\hbar}\partial_{k_i}\operatorname{Re}[E_n] \\ &- \frac{1}{\hbar}\sum_j F_j \operatorname{Re}[\partial_{k_i}(\mathbf{A}_n^{LR})_j) - \partial_{k_j}(\mathbf{A}_n^{RR})_i]\Big|_{\mathbf{k}=\mathbf{k}_c}. \end{aligned} \tag{B12}$$

This yields the equation of motion

$$\hbar\dot{\mathbf{r}} = \partial_{\mathbf{k}}\operatorname{Re}[E_n + \mathbf{F}\cdot(\mathbf{A}_n^{RR} - \mathbf{A}_n^{LR})] - \mathbf{F}\times\operatorname{Re}[\mathbf{\Omega}_n^{RR}]\Big|_{\mathbf{k}=\mathbf{k}_c}. \tag{B13}$$

Silberstein et al. also derived a semi-classical equation of motion describing self-acceleration arising from the finite wavepacket size. Similarly to Eq. (B3), the time derivative of the centre-of-mass momentum takes the form as

$$\dot{\mathbf{k}}_c = \frac{1}{N}\frac{d}{dt}\langle W|\hat{\mathbf{k}}|W\rangle + \frac{\dot{N}}{N}\mathbf{k}_c. \tag{B14}$$

Consider a one-dimensional system, using the Taylor expansion of an integral in the form of

$$\begin{aligned}\int |w_{n,k}|^2 I_{nn}(k) f(k) d^2k &\approx \int |w_{n,k}|^2 I_{nn}(k)\Big[f(k_c) + \partial_k f|_{k_c=k}(k-k_c) + \frac{1}{2}\partial_k^2 f|_{k_c=k}(k-k_c)^2\Big]d^2k \\ &= Nf(k_c) + \frac{1}{2}N\sigma^2\frac{1}{2}\partial_k^2 f|_{k_c=k},\end{aligned} \tag{B15}$$

where

$$\sigma^2 = \frac{1}{N}\int |w_{n,k}|^2 I_{nn}(k-k_c)^2 d^2k$$

denotes the width of the waveacket. In the absence of an external force, the two terms in Eq. (B14) can be expanded into

$$\begin{aligned}\frac{1}{N}\frac{d}{dt}\langle W|\hat{k}|W\rangle &\approx \frac{2}{\hbar}k\,\mathrm{Im}[E_n] + \left(\frac{\sigma^2}{\hbar}k\partial_k^2\,\mathrm{Im}[E_n] + \frac{2\sigma^2}{\hbar}\partial_k\,\mathrm{Im}[E_n]\right)\Bigg|_{k=k_c} \\ \frac{\dot{N}}{N} &\approx \frac{2}{\hbar}\,\mathrm{Im}[E_n] + \frac{\sigma^2}{\hbar}\partial_k^2\,\mathrm{Im}[E_n]\Bigg|_{k=k_c}\end{aligned} \tag{B16}$$

which results in self-acceleration arising from the finite-size effects

$$\dot{k}_c = 2\sigma^2\partial_k\,\mathrm{Im}[E]|_{k=k_c}. \tag{B17}$$

B.2 Derivation of the Interplay between Self-Acceleration and Force

Similar to the derivation for self-acceleration in previous Section, we can expand $\dot{N}/N$ Eq. (B11) and $\mathbf{r}_c$ in Eq. (B7) to the second order as

$$\begin{aligned}\frac{\dot{N}}{N} &= \frac{1}{N}\int |w_{n,\mathbf{k}}|^2 I_{nn}\frac{2}{\hbar}\,\mathrm{Im}\Big[E_n + \mathbf{F}\cdot(\mathbf{A}_n^{RR} - \mathbf{A}_n^{LR})\Big]d^2\mathbf{k} \\ &\approx \frac{2}{\hbar}\,\mathrm{Im}\Big[E_n + \mathbf{F}\cdot(\mathbf{A}_n^{RR} - \mathbf{A}_n^{LR})\Big] + \sum_j \frac{\sigma_j^2}{\hbar}\partial_{k_j}^2\,\mathrm{Im}\Big[E_n + \mathbf{F}\cdot(\mathbf{A}_n^{RR} - \mathbf{A}_n^{LR})\Big]\Bigg|_{k=k_c}, \\ \mathbf{r}_c &\approx -\partial_{\mathbf{k}}\varphi + \mathrm{Re}[\mathbf{A}]_n^{RR} + \frac{1}{2}\sum_j \sigma_j^2\partial_{k_j}^2\Big(-\partial_{\mathbf{k}}\varphi + \mathrm{Re}[\mathbf{A}]_n^{RR}\Big)\Bigg|_{\mathbf{k}=\mathbf{k}_c}\end{aligned} \tag{B18}$$

where σ_j denotes the wavepacket width in the j-direction. Similarly, $\frac{1}{N}\frac{d}{dt}\langle W|\hat{k}|W\rangle$ can be expanded as

$$\begin{aligned}\frac{1}{N}\frac{d}{dt}\langle W|\hat{k}_i|W\rangle \approx{}& \frac{2}{\hbar}k_i \operatorname{Im}\Big[E_n + \mathbf{F}\cdot(\mathbf{A}_n^{RR}-\mathbf{A}_n^{LR})\Big] + \bigg(\sum_j \frac{\sigma_j^2}{\hbar} k_i \partial_{k_j}^2 \operatorname{Im}\Big[E_n + \mathbf{F}\cdot(\mathbf{A}_n^{RR}-\mathbf{A}_n^{LR})\Big] \\ &+ \frac{2\sigma_i^2}{\hbar}\partial_{k_i}\operatorname{Im}\Big[E_n + \mathbf{F}\cdot(\mathbf{A}_n^{RR}-\mathbf{A}_n^{LR})\Big]\bigg)\bigg|_{k=k_c}\end{aligned} \tag{B19}$$

which yields

$$(\dot{\mathbf{k}}_c)_i = \frac{2\sigma_i^2}{\hbar}\partial_{k_i}\operatorname{Im}\Big[E_n + \mathbf{F}\cdot(\mathbf{A}_n^{RR}-\mathbf{A}_n^{LR})\Big]\bigg|_{k=k_c}. \tag{B20}$$

Similarly, $\hbar\dot{\mathbf{r}}_c$ can be expanded as

$$\begin{aligned}\frac{1}{N}\frac{d}{dt}\langle W|(\hat{\mathbf{r}})|W\rangle \approx{}& \frac{1}{\hbar}\partial_{\mathbf{k}}\operatorname{Re}[E_n + \mathbf{F}\cdot(\mathbf{A}_n^{RR}-\mathbf{A}_n^{LR})] - \frac{1}{\hbar}\mathbf{F}\times\operatorname{Re}[\mathbf{\Omega}_n^{RR}] \\ &+ \frac{2}{\hbar}\Big(-\partial_{\mathbf{k}}\varphi + \operatorname{Re}[\mathbf{A}_n^{RR}]\Big)\operatorname{Im}[E_n + \mathbf{F}\cdot(\mathbf{A}_n^{RR}-\mathbf{A}_n^{LR})] \\ &+ \frac{1}{2}\sum_j \sigma_j^2\partial_{k_j}^2\bigg(\frac{1}{\hbar}\partial_{\mathbf{k}}\operatorname{Re}[E_n + \mathbf{F}\cdot(\mathbf{A}_n^{RR}-\mathbf{A}_n^{LR})] - \frac{1}{\hbar}\mathbf{F}\times\operatorname{Re}[\mathbf{\Omega}_n^{RR}]\bigg) \\ &+ \frac{1}{2}\sum_j \sigma_j^2\partial_{k_j}^2\bigg(\frac{2}{\hbar}\Big(-\partial_{\mathbf{k}}\varphi + \operatorname{Re}[\mathbf{A}_n^{RR}]\Big)\operatorname{Im}[E_n + \mathbf{F}\cdot(\mathbf{A}_n^{RR}-\mathbf{A}_n^{LR})]\bigg)\bigg|_{\mathbf{k}=\mathbf{k}_c} \\ ={}& \frac{1}{\hbar}\partial_{\mathbf{k}}\operatorname{Re}[E_n + \mathbf{F}\cdot(\mathbf{A}_n^{RR}-\mathbf{A}_n^{LR})] - \frac{1}{\hbar}\mathbf{F}\times\operatorname{Re}[\mathbf{\Omega}_n^{RR}] \\ &+ \frac{2}{\hbar}\Big(-\partial_{\mathbf{k}}\varphi + \operatorname{Re}[\mathbf{A}_n^{RR}]\Big)\operatorname{Im}[E_n + \mathbf{F}\cdot(\mathbf{A}_n^{RR}-\mathbf{A}_n^{LR})] \\ &+ \frac{1}{2}\sum_j \sigma_j^2\partial_{k_j}^2\bigg(\frac{1}{\hbar}\partial_{\mathbf{k}}\operatorname{Re}[E_n + \mathbf{F}\cdot(\mathbf{A}_n^{RR}-\mathbf{A}_n^{LR})] - \frac{1}{\hbar}\mathbf{F}\times\operatorname{Re}[\mathbf{\Omega}_n^{RR}]\bigg) \\ &+ \frac{1}{\hbar}\sum_j\bigg(\sigma_j^2\partial_{k_j}^2\Big(-\partial_{\mathbf{k}}\varphi + \operatorname{Re}[\mathbf{A}_n^{RR}]\Big)\bigg)\operatorname{Im}[E_n + \mathbf{F}\cdot(\mathbf{A}_n^{RR}-\mathbf{A}_n^{LR})] \\ &+ \frac{1}{\hbar}\sum_j\sigma_j^2\Big(-\partial_{\mathbf{k}}\varphi + \operatorname{Re}[\mathbf{A}_n^{RR}]\Big)\partial_{k_j}^2\operatorname{Im}[E_n + \mathbf{F}\cdot(\mathbf{A}_n^{RR}-\mathbf{A}_n^{LR})] \\ &+ \frac{2}{\hbar}\sum_j\sigma_j^2\partial_{k_j}\Big(-\partial_{\mathbf{k}}\varphi + \operatorname{Re}[\mathbf{A}_n^{RR}]\Big)\partial_{k_j}\operatorname{Im}[E_n + \mathbf{F}\cdot(\mathbf{A}_n^{RR}-\mathbf{A}_n^{LR})]\bigg|_{\mathbf{k}=\mathbf{k}_c}.\end{aligned} \tag{B21}$$

By combining each term, this eventually yields

$$\begin{aligned}\hbar\dot{\mathbf{r}}_c =&\partial_{\mathbf{k}}\,\mathrm{Re}[E_n+\mathbf{F}\cdot(\mathbf{A}_n^{RR}-\mathbf{A}_n^{LR})]-\mathbf{F}\times\mathrm{Re}[\mathbf{\Omega}_n^{RR}]\\&+\sum_j\frac{1}{2}\sigma_j^2\partial_{k_j}^2\Big(\partial_{\mathbf{k}}\,\mathrm{Re}[E_n+\mathbf{F}\cdot(\mathbf{A}_n^{RR}-\mathbf{A}_n^{LR})]-\mathbf{F}\times\mathrm{Re}[\mathbf{\Omega}_n^{RR}]\Big)\\&+\sum_j 2\sigma_j^2\partial_{k_j}\Big(-\partial_{\mathbf{k}}\varphi+\mathrm{Re}[\mathbf{A}_n^{RR}]\Big)\partial_{k_j}\Big(\mathrm{Im}[E_n+\mathbf{F}\cdot(\mathbf{A}_n^{RR}-\mathbf{A}_n^{LR})]\Big),\end{aligned} \tag{B22}$$

which is my results in Eq. (3.2). Although, in the main text, I denote the width to be w instead to avoid confusion with the Pauli matrices.

C Appendix for Quantum Geometric Tensor and Wavepacket Dynamics in Chapter 3

C.1 Identities of the Quantum Geometric Tensors

In this section, we provide identities related to the left-right and the right-right quantum geometric tensor to aide the derivations in the next section. The components of the left-right quantum geometric tensor (LR QGT) is defined as

$$Q_{n,ij}^{LR}=\langle\partial_{k_i}u_n^L|\partial_{k_j}u_n^R\rangle-\langle\partial_{k_i}u_n^L|u_n^R\rangle\langle u_n^L|\partial_{k_j}u_n^R\rangle, \tag{C1}$$

where the left and right eigenstates satisfy the normalization $\langle u_n^L|u_n^R\rangle=\langle u_n^R|u_n^R\rangle=1$. We can also define the intra-band and inter-band Berry connections as $\mathbf{A}_{nm}^{\alpha\beta}=\langle u_n^\alpha|i\partial_{\mathbf{k}}u_m^\beta\rangle$ with $\alpha,\beta=L,R$.

The LR QGT can be written in terms of the inter-band Berry connection [201] by inserting $\sum_m|u_m^R\rangle\langle u_m^L|=\mathbf{I}$ to get

$$\begin{aligned}Q_{n,ij}^{LR}=&\sum_m\langle\partial_{k_i}u_n^L|u_m^R\rangle\langle u_m^L|\partial_{k_j}u_n^R\rangle-\langle\partial_{k_i}u_n^L|u_n^R\rangle\langle u_n^L|\partial_{k_j}u_n^R\rangle\\=&\sum_{m\neq n}\langle\partial_{k_i}u_n^L|u_m^R\rangle\langle u_m^L|\partial_{k_j}u_n^R\rangle\\=&\sum_{m\neq n}\langle -i\partial_{k_i}u_n^L|u_m^R\rangle\langle u_m^L|i\partial_{k_j}u_n^R\rangle\\=&\sum_{m\neq n}\langle u_n^L|i\partial_{k_i}u_m^R\rangle\langle u_m^L|i\partial_{k_j}u_n^R\rangle\\=&\sum_{m\neq n}(A_{nm}^{LR})_i(A_{mn}^{LR})_j.\end{aligned} \tag{C2}$$

We use the identity $\langle\partial_{k_i}u_m^L|u_n^R\rangle=-\langle u_m^L|\partial_{k_i}u_n^R\rangle$ on the third line, based on:

$$\begin{aligned}\partial_{k_i}\langle u_n^L|u_m^R\rangle&=0\\\langle\partial_{k_i}u_n^L|u_m^R\rangle+\langle u_n^L|\partial_{k_i}u_m^R\rangle&=0\\-\langle\partial_{k_i}u_n^L|u_m^R\rangle&=\langle u_n^L|\partial_{k_i}u_m^R\rangle.\end{aligned} \tag{C3}$$

Note that this also implies that $(\mathbf{A}^{LR}_{nm})^* = \mathbf{A}^{RL}_{mn}$. In a two-band system, the LR QGT simplifies to

$$Q^{LR}_{n,ij} = A^{LR}_{nm,i} A^{LR}_{mn,j}.$$

As in the main text, the LR quantum metric tensor (QMT) corresponds to the symmetric part of the LR QGT, therefore, its components can be written as

$$g^{LR}_{n,ij} = \sum_{m\neq n} \frac{1}{2}(A^{LR}_{nm})_i (A^{LR}_{mn})_j + \frac{1}{2}(A^{LR}_{nm})_j (A^{LR}_{mn})_i. \tag{C4}$$

Similarly, the components of the right-rght quantum geometric tensor (RR QGT) is defined as

$$Q^{RR}_{n,ij} = \langle \partial_{k_i} u^R_n | \partial_{k_j} u^R_n \rangle - \langle \partial_{k_i} u^R_n | u^R_n \rangle \langle u^R_n | \partial_{k_j} u^R_n \rangle. \tag{C5}$$

Where we can use the completeness relation $\sum_m |u^L_m\rangle\langle u^R_m| = \mathbf{I}$ and rewrite the RR QGT as

$$\begin{aligned}
Q^{RR}_{n,ij} =& \sum_m \langle \partial_{k_i} u^R_n | u^L_m \rangle \langle u^R_m | \partial_{k_j} u^R_n \rangle - \langle \partial_{k_i} u^R_n | u^L_m \rangle \langle u^R_m | u^R_n \rangle \langle u^R_n | \partial_{k_j} u^R_n \rangle \\
=& \langle \partial_{k_i} u^R_n | u^L_n \rangle \langle u^R_n | \partial_{k_j} u^R_n \rangle - \langle \partial_{k_i} u^R_n | u^L_n \rangle \langle u^R_n | \partial_{k_j} u^R_n \rangle \\
&+ \sum_{m\neq n} \langle \partial_{k_i} u^R_n | u^L_m \rangle \langle u^R_m | \partial_{k_j} u^R_n \rangle - \langle \partial_{k_i} u^R_n | u^L_m \rangle \langle u^R_m | u^R_n \rangle \langle u^R_n | \partial_{k_j} u^R_n \rangle \\
=& \sum_{m\neq n} \langle -i\partial_{k_i} u^R_n | u^L_m \rangle \langle u^R_m | i\partial_{k_j} u^R_n \rangle - \langle -i\partial_{k_i} u^R_n | u^L_m \rangle \langle u^R_m | u^R_n \rangle \langle u^R_n | i\partial_{k_j} u^R_n \rangle \\
=& \sum_{m\neq n} (A^{RL}_{nm})_i (A^{RR}_{mn})_j - I_{mn} (A^{RL}_{nm})_i (A^{RR}_{nn})_j
\end{aligned} \tag{C6}$$

where we denote $I_{mn} = \langle u^R_m | u^R_n \rangle$, which arise from the non-orthogonality of the right eigenstates. For a two-band system, the RR QGT simplifies to

$$Q^{RR}_{n,ij} = A^{RL}_{nm,i} A^{RR}_{mn,j} - I_{mn} A^{RL}_{nm,i} A^{RR}_{nn,j}.$$

C.2 Derivation of Equation of Motion

In this section, we will present our derivation of the equation of motion presented in the main text. First, we consider a non-Hermitian Hamiltonian under a constant force $\mathbf{F}$ in the real space

$$\tilde{H}(\mathbf{k}) = H(\mathbf{k}) - \mathbf{F}\cdot\mathbf{r} \tag{C7}$$

where $\tilde{H}$ has left and right eigenstates $|\tilde{u}^{L/R}_n\rangle$ and corresponding eigenenergies $\tilde{\epsilon}_n$, and $H(\mathbf{k})$ has left and right eigenstates denoted as $|u^{L/R}_n\rangle$ and corresponding eigenenergies ϵ_n.

We begin by considering a wavepacket in the eigenstate $|\tilde{u}^R_0\rangle$, which has the largest imaginary parts of the eigenenergies (the smallest decaying rate)

$$|W\rangle = \int w(\mathbf{k},t) e^{i\mathbf{k}\cdot\mathbf{r}} |\tilde{u}^R_0\rangle d\mathbf{k}. \tag{C8}$$

We then expand $|W\rangle$ to first order using the perturbation theory in Ref. [280]

$$|W\rangle = \int w(\mathbf{k},t)e^{i\mathbf{k}\cdot\mathbf{r}}\left(|u_0^R\rangle + \frac{\mathbf{F}\cdot\mathbf{A}_{10}^{LR}}{\epsilon_1-\epsilon_0}|u_1^R\rangle\right)d\mathbf{k} \tag{C9}$$

where the index 1 denotes the other band in the non-Hermitian two-band system. From this point forward, we denote $\int_{\mathbf{k}} = \int d\mathbf{k}$ and $w(\mathbf{k},t) = w$ for brevity.

To show that the RR QGT describes the field-induced positional shift [178, 179], we first calculate the centre-of-mass (COM) position of the wave packet $|W\rangle$, $\mathbf{r}_c = \frac{\langle W|\hat{\mathbf{r}}|W\rangle}{\langle W|W\rangle}$. When we expand the numerator in $\mathbf{r}_c$ to first order perturbation, it can be rewritten as

$$\begin{aligned}\langle W|\hat{\mathbf{r}}|W\rangle = \int_{\mathbf{k}}\Bigg[& iw^*\partial_{\mathbf{k}}w\left(1+\frac{\mathbf{F}\cdot\mathbf{A}_{10}^{LR}}{\epsilon_1-\epsilon_0}I_{01}+\frac{\mathbf{F}\cdot\mathbf{A}_{01}^{RL}}{\epsilon_1^*-\epsilon_0^*}I_{10}\right)+|w|^2\Bigg(\langle u_0^R|i\partial_{\mathbf{k}}u_0^R\rangle \\ &+\langle u_1^R|i\partial_{\mathbf{k}}u_0^R\rangle\frac{\mathbf{F}\cdot\mathbf{A}_{01}^{RL}}{\epsilon_1^*-\epsilon_0^*}+\langle u_0^R|i\partial_{\mathbf{k}}u_1^R\rangle\frac{\mathbf{F}\cdot\mathbf{A}_{10}^{LR}}{\epsilon_1-\epsilon_0}+i\partial_{\mathbf{k}}\left(\frac{\mathbf{F}\cdot\mathbf{A}_{10}^{LR}}{\epsilon_1-\epsilon_0}\right)I_{01}\Bigg)\Bigg].\end{aligned} \tag{C10}$$

Suppose that the wave packet takes the form $w = |w|e^{i\varphi}$, the first 3 terms in Eq. (C10) can be rewritten as

$$\begin{aligned}\int_{\mathbf{k}} iw^*\partial_{\mathbf{k}}w\left(1+\frac{\mathbf{F}\cdot\mathbf{A}_{10}^{LR}}{\epsilon_1-\epsilon_0}I_{01}+\frac{\mathbf{F}\cdot\mathbf{A}_{01}^{RL}}{\epsilon_1^*-\epsilon_0^*}I_{10}\right) &= \int_{\mathbf{k}}(-|w|^2\partial_{\mathbf{k}}\varphi+i|w|\partial_{\mathbf{k}}|w|)\Bigg(1+\frac{\mathbf{F}\cdot\mathbf{A}_{10}^{LR}}{\epsilon_1-\epsilon_0}I_{01} \\ &\quad+\frac{\mathbf{F}\cdot\mathbf{A}_{01}^{RL}}{\epsilon_1^*-\epsilon_0^*}I_{10}\Bigg) \\ &= \int_{\mathbf{k}}|w|^2\Bigg(-\partial_{\mathbf{k}}\varphi\left(1+\frac{\mathbf{F}\cdot\mathbf{A}_{10}^{LR}}{\epsilon_1-\epsilon_0}I_{01}+\frac{\mathbf{F}\cdot\mathbf{A}_{01}^{RL}}{\epsilon_1^*-\epsilon_0^*}I_{10}\right) \\ &\quad-\frac{i}{2}\partial_{\mathbf{k}}\left(\frac{\mathbf{F}\cdot\mathbf{A}_{10}^{LR}}{\epsilon_1-\epsilon_0}I_{01}+\frac{\mathbf{F}\cdot\mathbf{A}_{01}^{RL}}{\epsilon_1^*-\epsilon_0^*}I_{10}\right)\Bigg).\end{aligned} \tag{C11}$$

We can then plug Eq, (C11) back to Eq. (C10) which yields

$$\begin{aligned}\langle W|\hat{\mathbf{r}}|W\rangle &= \int_{\mathbf{k}}|w|^2\Bigg(-\partial_{\mathbf{k}}\varphi\left(1+\frac{\mathbf{F}\cdot\mathbf{A}_{10}^{LR}}{\epsilon_1-\epsilon_0}I_{01}+\frac{\mathbf{F}\cdot\mathbf{A}_{01}^{RL}}{\epsilon_1^*-\epsilon_0^*}I_{10}\right)-\frac{i}{2}\partial_{\mathbf{k}}\left(\frac{\mathbf{F}\cdot\mathbf{A}_{10}^{LR}}{\epsilon_1-\epsilon_0}I_{01}+\frac{\mathbf{F}\cdot\mathbf{A}_{01}^{RL}}{\epsilon_1^*-\epsilon_0^*}I_{10}\right) \\ &\quad+\langle u_0^R|i\partial_{\mathbf{k}}u_0^R\rangle+\langle u_1^R|i\partial_{\mathbf{k}}u_0^R\rangle\frac{\mathbf{F}\cdot\mathbf{A}_{01}^{RL}}{\epsilon_1^*-\epsilon_0^*}+\langle u_0^R|i\partial_{\mathbf{k}}u_1^R\rangle\frac{\mathbf{F}\cdot\mathbf{A}_{10}^{LR}}{\epsilon_1-\epsilon_0}+i\partial_{\mathbf{k}}\left(\frac{\mathbf{F}\cdot\mathbf{A}_{10}^{LR}}{\epsilon_1-\epsilon_0}\right)I_{01}\Bigg) \\ &= \int_{\mathbf{k}}|w|^2\Bigg(-\partial_{\mathbf{k}}\varphi\left(1+\frac{\mathbf{F}\cdot\mathbf{A}_{10}^{LR}}{\epsilon_1-\epsilon_0}I_{01}+\frac{\mathbf{F}\cdot\mathbf{A}_{01}^{RL}}{\epsilon_1^*-\epsilon_0^*}I_{10}\right)+\frac{i}{2}\left(\partial_{\mathbf{k}}\frac{\mathbf{F}\cdot\mathbf{A}_{10}^{LR}}{\epsilon_1-\epsilon_0}\right)I_{01}-\frac{i}{2}\frac{\mathbf{F}\cdot\mathbf{A}_{10}^{LR}}{\epsilon_1-\epsilon_0}\partial_{\mathbf{k}}I_{01} \\ &\quad-\frac{i}{2}\partial_{\mathbf{k}}\left(\frac{\mathbf{F}\cdot\mathbf{A}_{01}^{RL}}{\epsilon_1^*-\epsilon_0^*}\right)I_{10}-\frac{i}{2}\frac{\mathbf{F}\cdot\mathbf{A}_{01}^{RL}}{\epsilon_1^*-\epsilon_0^*}\partial_{\mathbf{k}}I_{10}+\langle u_0^R|i\partial_{\mathbf{k}}u_0^R\rangle+\langle u_1^R|i\partial_{\mathbf{k}}u_0^R\rangle\frac{\mathbf{F}\cdot\mathbf{A}_{01}^{RL}}{\epsilon_1^*-\epsilon_0^*} \\ &\quad+\langle u_0^R|i\partial_{\mathbf{k}}u_1^R\rangle\frac{\mathbf{F}\cdot\mathbf{A}_{10}^{LR}}{\epsilon_1-\epsilon_0}\Bigg)\end{aligned} \tag{C12}$$

Suppose that the wave packet is narrow, we can approximate $|w|^2 \approx \delta(\mathbf{k}-\mathbf{k}_c)$, where $\mathbf{k}_c$ is the COM momentum. The equation can be rewritten as

$$\begin{aligned}
\langle W|\hat{\mathbf{r}}|W\rangle =& -\partial_{\mathbf{k}}\varphi + \mathbf{A}^{RR}_{00} + \frac{\mathbf{F}\cdot\mathbf{A}^{LR}_{10}}{\epsilon_1-\epsilon_0}\Big(-\partial_{\mathbf{k}}\varphi I_{01} + \mathbf{A}^{RR}_{01} - \frac{i}{2}\partial_{\mathbf{k}}I_{01}\Big) + \frac{\mathbf{F}\cdot\mathbf{A}^{RL}_{01}}{\epsilon_1^*-\epsilon_0^*}\Big(-\partial_{\mathbf{k}}\varphi I_{10} + \mathbf{A}^{RR}_{10} \\
&- \frac{i}{2}\partial_{\mathbf{k}}I_{10}\Big) + \frac{i}{2}I_{01}\Big(\partial_{\mathbf{k}}\frac{\mathbf{F}\cdot\mathbf{A}^{LR}_{10}}{\epsilon_1-\epsilon_0}\Big) - \frac{i}{2}I_{10}\Big(\partial_{\mathbf{k}}\frac{\mathbf{F}\cdot\mathbf{A}^{RL}_{01}}{\epsilon_1^*-\epsilon_0^*}\Big)\Big|_{\mathbf{k}=\mathbf{k}_c} \\
=& -\partial_{\mathbf{k}}\varphi + \mathbf{A}^{RR}_{00} + \frac{\mathbf{F}\cdot\mathbf{A}^{LR}_{10}}{\epsilon_1-\epsilon_0}\Big(-\partial_{\mathbf{k}}\varphi I_{01} + \mathbf{A}^{RR}_{01} - i\partial_{\mathbf{k}}I_{01}\Big) + \frac{\mathbf{F}\cdot\mathbf{A}^{RL}_{01}}{\epsilon_1^*-\epsilon_0^*}\Big(-\partial_{\mathbf{k}}\varphi I_{10} + \mathbf{A}^{RR}_{10}\Big) \\
&+ \frac{i}{2}\partial_{\mathbf{k}}\Big(I_{01}\frac{\mathbf{F}\cdot\mathbf{A}^{LR}_{10}}{\epsilon_1-\epsilon_0}\Big) - \frac{i}{2}\partial_{\mathbf{k}}\Big(I_{10}\frac{\mathbf{F}\cdot\mathbf{A}^{RL}_{01}}{\epsilon_1^*-\epsilon_0^*}\Big)\Big|_{\mathbf{k}=\mathbf{k}_c}.
\end{aligned} \tag{C13}$$

We then also note that the term $\mathbf{A}^{RR}_{01} - i\partial_{\mathbf{k}}I_{01}$ can be identified as $(\mathbf{A}^{RR}_{10})^*$ since

$$\begin{aligned}
-i\partial_{\mathbf{k}}I_{01} &= \langle -i\partial_{\mathbf{k}}u^R_0|u^R_1\rangle - \langle u^R_0|i\partial_{\mathbf{k}}u^R_1\rangle \\
&= (\mathbf{A}^{RR}_{10})^* - \mathbf{A}^{RR}_{01} \\
(\mathbf{A}^{RR}_{10})^* &= \mathbf{A}^{RR}_{01} - i\partial_{\mathbf{k}}I_{01}.
\end{aligned} \tag{C14}$$

Additionally, the term $I_{01}\mathbf{A}^{LR}_{10}$ can also be identified as $\mathbf{A}^{RR}_{00} - \mathbf{A}^{LR}_{00}$ since

$$\begin{aligned}
\mathbf{A}^{RR}_{00} &= \langle u^R_0|i\partial_{\mathbf{k}}u^R_0\rangle \\
&= \langle u^R_0|u^R_0\rangle\langle u^L_0|i\partial_{\mathbf{k}}u^R_0\rangle + \langle u^R_0|u^R_1\rangle\langle u^L_1|i\partial_{\mathbf{k}}u^R_0\rangle \\
&= \mathbf{A}^{LR}_{00} + I_{01}\mathbf{A}^{LR}_{10} \\
I_{01}\mathbf{A}^{LR}_{10} &= \mathbf{A}^{RR}_{00} - \mathbf{A}^{LR}_{00}.
\end{aligned} \tag{C15}$$

We then expand the denominator in $\mathbf{r}_c$ to first order in $\mathbf{F}$ using geometric series

$$\begin{aligned}
\frac{1}{\langle W|W\rangle} &= \Big(1 + \frac{\mathbf{F}\cdot\mathbf{A}^{LR}_{10}}{\epsilon_1-\epsilon_0}I_{01} + \frac{\mathbf{F}\cdot\mathbf{A}^{RL}_{01}}{\epsilon_1^*-\epsilon_0^*}I_{10}|_{\mathbf{k}=\mathbf{k}_c}\Big)^{-1} \\
&\approx \Big(1 - \frac{\mathbf{F}\cdot\mathbf{A}^{LR}_{10}}{\epsilon_1-\epsilon_0}I_{01} - \frac{\mathbf{F}\cdot\mathbf{A}^{RL}_{01}}{\epsilon_1^*-\epsilon_0^*}I_{10}\Big)\Big|_{\mathbf{k}=\mathbf{k}_c}.
\end{aligned} \tag{C16}$$

We can finally combine $\langle W|\hat{\mathbf{r}}|W\rangle$ from Eq. (C13) and $\langle W|W\rangle$ from Eq. (C16) and obtain $\mathbf{r}_c$ up to the first order perturbation

$$
\begin{aligned}
\mathbf{r}_c =& \frac{\langle W|\hat{\mathbf{r}}|W\rangle}{\langle W|W\rangle} \\
=& \Big(- \partial_{\mathbf{k}}\varphi + \mathbf{A}_{00}^{RR}\Big)\Big(1 - \frac{\mathbf{F}\cdot\mathbf{A}_{10}^{LR}}{\epsilon_1 - \epsilon_0} I_{01} - \frac{\mathbf{F}\cdot\mathbf{A}_{01}^{RL}}{\epsilon_1^* - \epsilon_0^*} I_{10}\Big) + \frac{\mathbf{F}\cdot\mathbf{A}_{10}^{LR}}{\epsilon_1 - \epsilon_0}\Big(- \partial_{\mathbf{k}}\varphi I_{01} + (\mathbf{A}_{10}^{RR})^*\Big) \\
& + \frac{\mathbf{F}\cdot\mathbf{A}_{01}^{RL}}{\epsilon_1^* - \epsilon_0^*}\Big(- \partial_{\mathbf{k}}\varphi I_{10} + \mathbf{A}_{10}^{RR}\Big) + \frac{i}{2}\partial_{\mathbf{k}}\Big(\frac{\mathbf{F}\cdot(\mathbf{A}_{00}^{RR} - \mathbf{A}_{00}^{LR})}{\epsilon_1 - \epsilon_0}\Big) - \frac{i}{2}\partial_{\mathbf{k}}\Big(\frac{\mathbf{F}\cdot(\mathbf{A}_{00}^{RR} - \mathbf{A}_{00}^{LR})^*}{\epsilon_1^* - \epsilon_0^*}\Big)|_{\mathbf{k}=\mathbf{k}_c} \\
=& - \partial_{\mathbf{k}}\varphi + \mathbf{A}_{00}^{RR} + \frac{\mathbf{F}\cdot\mathbf{A}_{10}^{LR}}{\epsilon_1 - \epsilon_0}\Big((\mathbf{A}_{10}^{RR})^* - I_{01}\mathbf{A}_{00}^{RR}\Big) + \frac{\mathbf{F}\cdot\mathbf{A}_{01}^{RL}}{\epsilon_1^* - \epsilon_0^*}\Big(\mathbf{A}_{10}^{RR} - I_{10}\mathbf{A}_{00}^{RR}\Big) \\
& + \frac{i}{2}\partial_{\mathbf{k}}\Big(\frac{\mathbf{F}\cdot(\mathbf{A}_{00}^{RR} - \mathbf{A}_{00}^{LR})}{\epsilon_1 - \epsilon_0}\Big) - \frac{i}{2}\partial_{\mathbf{k}}\Big(\frac{\mathbf{F}\cdot(\mathbf{A}_{00}^{RR} - \mathbf{A}_{00}^{LR})^*}{\epsilon_1^* - \epsilon_0^*}\Big)|_{\mathbf{k}=\mathbf{k}_c} \\
=& - \partial_{\mathbf{k}}\varphi + \mathbf{A}_{00}^{RR} + 2\,\mathrm{Re}\left[\frac{\mathbf{F}\cdot(Q_0^{RR})^*}{\epsilon_1 - \epsilon_0}\right] - \mathrm{Im}\left[\partial_{\mathbf{k}}\Big(\frac{\mathbf{F}\cdot(\mathbf{A}_{00}^{RR} - \mathbf{A}_{00}^{LR})}{\epsilon_1 - \epsilon_0}\Big)\right]|_{\mathbf{k}=\mathbf{k}_c}.
\end{aligned}
\tag{C17}
$$

Since the RR QGT is a Hermitian tensor $(Q_{0,ij}^{RR})^* = Q_{0,ji}^{RR}$, we can rewrite the third term using the identity $\mathbf{F}\cdot(Q_0^{RR})^* = Q_0^{RR}\cdot\mathbf{F}$, which yields the result

$$
\mathbf{r}_c = -\partial_{\mathbf{k}}\varphi + \mathbf{A}_{00}^{RR} + 2\,\mathrm{Re}\left[\frac{Q_0^{RR}\cdot\mathbf{F}}{\epsilon_1 - \epsilon_0}\right] - \mathrm{Im}\left[\partial_{\mathbf{k}}\Big(\frac{\mathbf{F}\cdot(\mathbf{A}_{00}^{RR} - \mathbf{A}_{00}^{LR})}{\epsilon_1 - \epsilon_0}\Big)\right]|_{\mathbf{k}=\mathbf{k}_c} \tag{C18}
$$

which shows that the RR QGT together with the anomalous Berry connection $\mathbf{A}_{00}^{RR} - \mathbf{A}_{00}^{LR}$ describe the field-induced positional shift.

To derive how the LR QGT appears in the equation of motion, we follow the same formalism presented in Refs. [204, 206]. We start from the time-dependent Schrodinger equation of the wave packet

$$
i\hbar\partial_t\Big(we^{i\mathbf{k}\cdot\mathbf{r}}|\tilde{u}_0^R\rangle\Big) = (H - \mathbf{F}\cdot\mathbf{r})\Big(we^{i\mathbf{k}\cdot\mathbf{r}}|\tilde{u}_0^R\rangle\Big). \tag{C19}
$$

We then multiply both sides with $\langle\tilde{\psi}| = \sum_n \tilde{c}_n^L\langle\tilde{u}_n^L|$, where $|\tilde{u}_n^L\rangle$ denote the n-th left eigenstate of the Hamiltonian $\tilde{H} = H - \mathbf{F}\cdot\mathbf{r}$,

$$
\sum_n \tilde{c}_n^L\langle\tilde{u}_n^L|i\hbar\partial_t we^{i\mathbf{k}\cdot\mathbf{r}}|\tilde{u}_0^R\rangle = \sum_n \tilde{c}_n^L\langle\tilde{u}_n^L|(H - \mathbf{F}\cdot\mathbf{r})we^{i\mathbf{k}\cdot\mathbf{r}}|\tilde{u}_0^R\rangle. \tag{C20}
$$

Note that for any $\tilde{c}_n^L$, all terms proportional to $\sum_{n\neq 0}\tilde{c}_n^L\langle\tilde{u}_n^L|$ will vanish since

$$
\begin{aligned}
\sum_{n\neq 0}\tilde{c}_n^L\langle\tilde{u}_n^L|i\hbar\partial_t we^{i\mathbf{k}\cdot\mathbf{r}}|\tilde{u}_0^R\rangle &= \sum_{n\neq 0}\tilde{c}_n^L we^{i\mathbf{k}\cdot\mathbf{r}}\langle\tilde{u}_n^L|(H - \mathbf{F}\cdot\mathbf{r})|\tilde{u}_0^R\rangle \\
&= \sum_{n\neq 0}\tilde{c}_n^L we^{i\mathbf{k}\cdot\mathbf{r}}\tilde{\epsilon}_n\langle\tilde{u}_n^L|\tilde{u}_0^R\rangle \\
&= 0,
\end{aligned}
\tag{C21}
$$

and only the terms proportional to $\langle \tilde{u}_0^L|$ survive.

We can then expand both sides of Eq. (C20) and remove the overall factor of $\tilde{c}_0^L$ as

$$\begin{aligned}
\langle \tilde{u}_0^L| i\hbar\partial_t \Big(w e^{\mathbf{ik\cdot r}} |\tilde{u}_0^R\rangle \Big) =& \Big(\langle u_0^L| + \frac{\mathbf{F}\cdot\mathbf{A}_{01}^{LR}}{\epsilon_1-\epsilon_0}\langle u_1^L| \Big) i\hbar\partial_t \Big(w e^{\mathbf{ik\cdot r}} \Big(|u_0^R\rangle + \frac{\mathbf{F}\cdot\mathbf{A}_{10}^{LR}}{\epsilon_1-\epsilon_0}|u_1^R\rangle \Big)\Big) \\
=& \Big(\langle u_0^L| + \frac{\mathbf{F}\cdot\mathbf{A}_{01}^{LR}}{\epsilon_1-\epsilon_0}\langle u_1^L| \Big) \Big(i\hbar(\partial_t w)e^{\mathbf{ik\cdot r}}|u_0^R\rangle - \hbar(\partial_t \mathbf{k}\cdot\mathbf{r})e^{\mathbf{ik\cdot r}}|u_0^R\rangle + i\hbar w e^{\mathbf{ik\cdot r}}\partial_t|u_0^R\rangle \\
&+ i\hbar(\partial_t w)e^{\mathbf{ik\cdot r}}\frac{\mathbf{F}\cdot\mathbf{A}_{10}^{LR}}{\epsilon_1-\epsilon_0}|u_1^R\rangle - \hbar(\partial_t \mathbf{k}\cdot\mathbf{r})e^{\mathbf{ik\cdot r}}\frac{\mathbf{F}\cdot\mathbf{A}_{10}^{LR}}{\epsilon_1-\epsilon_0}|u_1^R\rangle \\
&+ i\hbar w e^{\mathbf{ik\cdot r}}\Big(\partial_t\frac{\mathbf{F}\cdot\mathbf{A}_{10}^{LR}}{\epsilon_1-\epsilon_0}\Big)|u_1^R\rangle + i\hbar w e^{\mathbf{ik\cdot r}}\frac{\mathbf{F}\cdot\mathbf{A}_{10}^{LR}}{\epsilon_1-\epsilon_0}\partial_t|u_1^R\rangle \Big) \\
\approx& i\hbar(\partial_t w)e^{\mathbf{ik\cdot r}} - \hbar w(\partial_t\mathbf{k}\cdot\mathbf{r})e^{\mathbf{ik\cdot r}} + i\hbar w e^{\mathbf{ik\cdot r}}\langle u_0^L|\partial_t|u_0^R\rangle \\
&+ i\hbar w e^{\mathbf{ik\cdot r}}\frac{\mathbf{F}\cdot\mathbf{A}_{10}^{LR}}{\epsilon_1-\epsilon_0}\langle u_0^L|\partial_t|u_1^R\rangle + i\hbar w e^{\mathbf{ik\cdot r}}\frac{\mathbf{F}\cdot\mathbf{A}_{01}^{LR}}{\epsilon_1-\epsilon_0}\langle u_1^L|\partial_t|u_0^R\rangle
\end{aligned} \tag{C22}$$

$$\begin{aligned}
\langle \tilde{u}_0^L|(H-\mathbf{F}\cdot\mathbf{r})\Big(w e^{\mathbf{ik\cdot r}}|\tilde{u}_0^R\rangle\Big) =& \Big(\langle u_0^L| + \frac{\mathbf{F}\cdot\mathbf{A}_{01}^{LR}}{\epsilon_1-\epsilon_0}\langle u_1^L| \Big)(H-\mathbf{F}\cdot\mathbf{r})\Big(w e^{\mathbf{ik\cdot r}} \Big(|u_0^R\rangle + \frac{\mathbf{F}\cdot\mathbf{A}_{10}^{LR}}{\epsilon_1-\epsilon_0}|u_1^R\rangle \Big)\Big) \\
=& \Big(\langle u_0^L| + \frac{\mathbf{F}\cdot\mathbf{A}_{01}^{LR}}{\epsilon_1-\epsilon_0}\langle u_1^L| \Big)\Big(w e^{\mathbf{ik\cdot r}}\epsilon_0|u_0^R\rangle - w e^{\mathbf{ik\cdot r}}(\mathbf{F}\cdot\mathbf{r})|u_0^R\rangle \\
&+ w e^{\mathbf{ik\cdot r}}\frac{\mathbf{F}\cdot\mathbf{A}_{10}^{LR}}{\epsilon_1-\epsilon_0}\epsilon_1|u_1^R\rangle - w e^{\mathbf{ik\cdot r}}\frac{\mathbf{F}\cdot\mathbf{A}_{10}^{LR}}{\epsilon_1-\epsilon_0}(\mathbf{F}\cdot\mathbf{r})|u_1^R\rangle \Big) \\
\approx& w e^{\mathbf{ik\cdot r}}\epsilon_0 - w e^{\mathbf{ik\cdot r}}(\mathbf{F}\cdot\mathbf{r})
\end{aligned} \tag{C23}$$

where we discard all the higher-order terms and only keep up to first order perturbation

Assuming the wave packet is infinitely narrow in momentum space, the dynamics of its centre-of-mass momentum is governed by the external force $\dot{\mathbf{k}}_c = \mathbf{F}/\hbar$, which allow us to rewrite the right hand side of the Eq. (C22) as

$$\begin{aligned}
\langle \tilde{u}_0^L| i\hbar\partial_t \Big(w e^{\mathbf{ik\cdot r}} |\tilde{u}_0^R\rangle \Big) =& i\hbar(\partial_t w)e^{i\mathbf{k}\cdot\mathbf{r}} - w(\mathbf{F}\cdot\mathbf{r})e^{i\mathbf{k}\cdot\mathbf{r}} + w e^{i\mathbf{k}\cdot\mathbf{r}}\mathbf{F}\cdot\langle u_0^L|i\partial_{\mathbf{k}}|u_0^R\rangle \\
&+ w e^{i\mathbf{k}\cdot\mathbf{r}}\frac{\mathbf{F}\cdot\mathbf{A}_{10}^{LR}}{\epsilon_1-\epsilon_0}\mathbf{F}\cdot\langle u_0^L|i\partial_{\mathbf{k}}|u_1^R\rangle + w e^{i\mathbf{k}\cdot\mathbf{r}}\frac{\mathbf{F}\cdot\mathbf{A}_{01}^{LR}}{\epsilon_1-\epsilon_0}\mathbf{F}\cdot\langle u_1^L|i\partial_{\mathbf{k}}|u_0^R\rangle \\
=& i\hbar(\partial_t w)e^{i\mathbf{k}\cdot\mathbf{r}} - w(\mathbf{F}\cdot\mathbf{r})e^{i\mathbf{k}\cdot\mathbf{r}} + w e^{i\mathbf{k}\cdot\mathbf{r}}(\mathbf{F}\cdot\mathbf{A}_{00}^{LR}) \\
&+ w e^{i\mathbf{k}\cdot\mathbf{r}}\frac{\mathbf{F}\cdot\mathbf{A}_{10}^{LR}}{\epsilon_1-\epsilon_0}(\mathbf{F}\cdot\mathbf{A}_{01}^{LR}) + w e^{i\mathbf{k}\cdot\mathbf{r}}\frac{\mathbf{F}\cdot\mathbf{A}_{01}^{LR}}{\epsilon_1-\epsilon_0}(\mathbf{F}\cdot\mathbf{A}_{10}^{LR}).
\end{aligned} \tag{C24}$$

After equating Eq. (C23) with Eq. (C24), we can remove the overall factor of $e^{i\mathbf{k}\cdot\mathbf{r}}$

and remove the terms that appear on both sides, yielding

$$w\epsilon_0 = i\hbar(\partial_t w) + w(\mathbf{F}\cdot\mathbf{A}^{LR}_{00}) + w\frac{\mathbf{F}\cdot\mathbf{A}^{LR}_{10}}{\epsilon_1-\epsilon_0}(\mathbf{F}\cdot\mathbf{A}^{LR}_{01}) + w\frac{\mathbf{F}\cdot\mathbf{A}^{LR}_{01}}{\epsilon_1-\epsilon_0}(\mathbf{F}\cdot\mathbf{A}^{LR}_{10}), \tag{C25}$$

after rearrangement, this gives a differential equation of w

$$\begin{aligned}\partial_t w &= -\frac{i}{\hbar}w\left(\epsilon_0 - (\mathbf{F}\cdot\mathbf{A}^{LR}_{00}) - \frac{\mathbf{F}\cdot\mathbf{A}^{LR}_{10}}{\epsilon_1-\epsilon_0}(\mathbf{F}\cdot\mathbf{A}^{LR}_{01}) - \frac{\mathbf{F}\cdot\mathbf{A}^{LR}_{01}}{\epsilon_1-\epsilon_0}(\mathbf{F}\cdot\mathbf{A}^{LR}_{10})\right)\\ &= -\frac{i}{\hbar}w\left(\epsilon_0 - (\mathbf{F}\cdot\mathbf{A}^{LR}_{00}) - \frac{2(\mathbf{F}\cdot g^{LR}\cdot\mathbf{F})}{\epsilon_1-\epsilon_0}\right)\end{aligned} \tag{C26}$$

where we use the identity of the LR quantum metric from the previous section, we also abbreviated the index in g^{LR} since in a two-band system, the LR quantum metric tensors of the two bands are the same. Eq. (C26) has a general solution of w in the form of

$$w \propto \exp\left[-\frac{i}{\hbar}\int_{t_0}^{t}\left(\epsilon_0 - \mathbf{F}\cdot\left(\mathbf{A}^{LR}_{00} + \frac{2g^{LR}\cdot\mathbf{F}}{\epsilon_1-\epsilon_0}\right)\right)|_{\mathbf{k}=\mathbf{k}_c}dt'\right], \tag{C27}$$

which yields the correction to the phase of the wave packet as

$$\varphi = -\frac{1}{\hbar}\int_{t_0}^{t}\mathrm{Re}\left[\epsilon_0 - \mathbf{F}\cdot\left(\mathbf{A}^{LR}_{00} + \frac{2g^{LR}\cdot\mathbf{F}}{\epsilon_1-\epsilon_0}\right)|_{\mathbf{k}=\mathbf{k}_c}\right]dt'. \tag{C28}$$

Finally, plugging Eq. (C28) into Eq. (C18) and taking the first derivative, we derive the group velocity under first order perturbation as

$$\begin{aligned}(\dot{\mathbf{r}}_c)_i =&\partial_t\left(-\partial_{k_i}\varphi + (A^{RR}_{00})_i + 2\,\mathrm{Re}\left[\frac{(Q^{RR}_0\cdot\mathbf{F})_i}{\epsilon_1-\epsilon_0}\right] - \mathrm{Im}\left[\partial_{k_i}\left(\frac{\mathbf{F}\cdot(\mathbf{A}^{RR}_{00}-\mathbf{A}^{LR}_{00})}{\epsilon_1-\epsilon_0}\right)\right]|_{\mathbf{k}=\mathbf{k}_c}\right)\\ =&\frac{1}{\hbar}\partial_{k_i}\,\mathrm{Re}\left[\epsilon_0 - \sum_j F_j\left((A^{LR}_{00})_j + \frac{2(g^{LR}\cdot\mathbf{F})_j}{\epsilon_1-\epsilon_0}\right)\right]\\ &+\partial_t\left((A^{RR}_{00})_i + 2\,\mathrm{Re}\left[\frac{(Q^{RR}_0\cdot\mathbf{F})_i}{\epsilon_1-\epsilon_0}\right] - \mathrm{Im}\left[\partial_{k_i}\left(\frac{\mathbf{F}\cdot(\mathbf{A}^{RR}_{00}-\mathbf{A}^{LR}_{00})}{\epsilon_1-\epsilon_0}\right)\right]\right)|_{\mathbf{k}=\mathbf{k}_c}\\ =&\frac{1}{\hbar}\partial_{k_i}\,\mathrm{Re}\left[\epsilon_0 - \sum_j F_j\left((A^{LR}_{00})_j + \frac{2(g^{LR}\cdot\mathbf{F})_j}{\epsilon_1-\epsilon_0}\right)\right]\\ &+\frac{1}{\hbar}\sum_j F_j\partial_{k_j}\left((A^{RR}_{00})_i + 2\,\mathrm{Re}\left[\frac{(Q^{RR}_0\cdot\mathbf{F})_i}{\epsilon_1-\epsilon_0}\right] - \mathrm{Im}\left[\partial_{k_i}\left(\frac{\mathbf{F}\cdot(\mathbf{A}^{RR}_{00}-\mathbf{A}^{LR}_{00})}{\epsilon_1-\epsilon_0}\right)\right]\right)|_{\mathbf{k}=\mathbf{k}_c}\end{aligned} \tag{C29}$$

which is the main result presented in the main text.

C.3 Real and Imaginary Parts of Quantum Geometric Tensors

We also note that the real and imaginary parts in the terms in Eq. (C29) can be expanded as

$$\begin{aligned}
\mathrm{Re}\left[\frac{2(Q_0^{RR}\cdot\mathbf{F})}{\Delta\epsilon}\right] =& \frac{\mathrm{Re}[\Delta\epsilon](2g_0^{RR}\cdot\mathbf{F})}{|\Delta\epsilon|^2} - \frac{\mathrm{Im}[\Delta\epsilon](\mathbf{F}\times\boldsymbol{\Omega}_0^{RR})}{|\Delta\epsilon|^2} \\
\mathrm{Im}\left[\frac{\mathbf{F}\cdot(\mathbf{A}_{00}^{RR}-\mathbf{A}_{00}^{LR})}{\Delta\epsilon}\right] =& -\frac{\mathrm{Re}[\Delta\epsilon]\,\mathrm{Im}[\mathbf{F}\cdot\mathbf{A}_{00}^{LR}]}{|\Delta\epsilon|^2} - \frac{\mathrm{Im}[\Delta\epsilon]\,\mathrm{Re}[\mathbf{F}\cdot(\mathbf{A}_{00}^{RR}-\mathbf{A}_{00}^{LR})]}{|\Delta\epsilon|^2} \\
\mathrm{Re}\left[\frac{2(g_0^{LR}\cdot\mathbf{F})}{\Delta\epsilon}\right] =& \frac{\mathrm{Re}[\Delta\epsilon]\Big(2\,\mathrm{Re}[g_0^{LR}]\cdot\mathbf{F}\Big)}{|\Delta\epsilon|^2} + \frac{\mathrm{Im}[\Delta\epsilon]\Big(2\,\mathrm{Im}[g_0^{LR}]\cdot\mathbf{F}\Big)}{|\Delta\epsilon|^2}.
\end{aligned} \tag{C30}$$

where we denote $\Delta\epsilon = \epsilon_1 - \epsilon_0$, and $\mathrm{Im}[\mathbf{A}_{00}^{RR}]$ vanishes since $\mathbf{A}_{00}^{RR}$ is real-valued. This suggest that the RR Berry curvature also plays a role in the correction to the non-Hermitian anomalous Berry connection. Furthermore, it shows that both the real and imaginary parts of the LR QMT are needed to be taken account for in the equation of motion.

To see how each term manifests in the dynamics, we rewrite the equation of motion in the main results using the forms in Eqs. (C30)

$$\begin{aligned}
\hbar\dot{\mathbf{r}}_c =& \nabla_{\mathbf{k}}\,\mathrm{Re}[\epsilon_0 + \mathbf{F}\cdot(\mathbf{A}_{00}^{RR}-\mathbf{A}_{00}^{LR})] \\
&+ \nabla_{\mathbf{k}}\left(\mathbf{F}\cdot\left(\frac{\mathrm{Re}[\Delta\epsilon]\Big(2(g_0^{RR}-\mathrm{Re}[g_0^{LR}])\cdot\mathbf{F}\Big)}{|\Delta\epsilon|^2} - \frac{\mathrm{Im}[\Delta\epsilon]\Big(2\,\mathrm{Im}[g_0^{LR}\cdot\mathbf{F}]\Big)}{|\Delta\epsilon|^2}\right)\right. \\
&\left.+ \mathbf{F}\cdot\nabla_{\mathbf{k}}\left(\frac{\mathrm{Re}[\Delta\epsilon]\,\mathrm{Im}[\mathbf{F}\cdot\mathbf{A}_{00}^{LR}]}{|\Delta\epsilon|^2} + \frac{\mathrm{Im}[\Delta\epsilon]\,\mathrm{Re}[\mathbf{F}\cdot(\mathbf{A}_{00}^{RR}-\mathbf{A}_{00}^{LR})]}{|\Delta\epsilon|^2}\right)\right) \\
&- \mathbf{F}\times\left(\boldsymbol{\Omega}_0^{RR} + \nabla_{\mathbf{k}}\times\frac{\mathrm{Re}[\Delta\epsilon](2g_0^{RR}\cdot\mathbf{F})}{|\Delta\epsilon|^2} + (\mathbf{F}\cdot\nabla_{\mathbf{k}})\frac{\mathrm{Im}[\Delta\epsilon]\boldsymbol{\Omega}_0^{RR}}{|\Delta\epsilon|^2}\right).
\end{aligned} \tag{C31}$$

$$2\left(\frac{\mathrm{Re}[\Delta\epsilon]\left(g_0^{RR}-\mathrm{Re}[g_0^{LR}]\right)}{|\Delta\epsilon|^2} - \frac{\mathrm{Im}[\Delta\epsilon]\left(\mathrm{Im}[g_0^{LR}]\right)}{|\Delta\epsilon|^2}\right)\cdot\mathbf{F}$$

From Eq. (C31), we can see that the real and imaginary parts of the Berry connections together with the LR and the RR quantum metric describe the correction to the Berry conections, while the RR quantum metric and the RR Berry curvature describe the correction to the anomalous Hall drift. Here, we use the identity $\nabla_{\mathbf{k}}\times(-\mathbf{F}\times\boldsymbol{\Omega}_0^{RR}) = \mathbf{F}\cdot\partial_{\mathbf{k}}\boldsymbol{\Omega}_0^{RR}$, which holds in 2D systems when $\boldsymbol{\Omega}_0^{RR} = (0,0,\Omega_0^{z,RR})$.

For the special case presented in the main text, the equation becomes:

$$\begin{aligned}
v_x =& \frac{1}{\hbar}\partial_{k_x}\,\mathrm{Re}\left[F_y\Big(\tilde{A}_{00,y}^{RR}-\tilde{A}_{00,y}^{LR}\Big)\right] - \frac{F_y}{\hbar}\tilde{\Omega}_{0,xy}^{RR} \\
v_y =& \frac{1}{\hbar}\partial_{k_y}\,\mathrm{Re}\left[\epsilon_0 + F_y\Big(\tilde{A}_{00,y}^{RR}-\tilde{A}_{00,y}^{LR}\Big)\right].
\end{aligned} \tag{C32}$$

where

$$\begin{aligned}\tilde{A}^{RR}_{00,y} - \tilde{A}^{LR}_{00,y} =& \frac{\mathrm{Re}[\Delta\epsilon](2(g^{RR}_{0,yy} - \mathrm{Re}[g^{LR}_{0,yy}])F_y) - \mathrm{Im}[\Delta\epsilon](2\,\mathrm{Im}[g^{LR}_{0,yy}]F_y)}{|\Delta\epsilon|^2} \\ &+ \partial_{k_y}\left(\frac{\mathrm{Re}[\Delta\epsilon]\,\mathrm{Im}[A^{LR}_{00,y}]F_y + \mathrm{Im}[\Delta\epsilon]\,\mathrm{Re}[(A^{RR}_{00,y} - A^{LR}_{00,y})]F_y}{|\Delta\epsilon|^2}\right) \\ \tilde{\Omega}^{RR}_{0,xy} =& \Omega^{RR}_{0,xy} + F_y\left(\partial_{k_x}\left(\frac{\mathrm{Re}[\Delta\epsilon]g^{RR}_{0,yy}}{|\Delta\epsilon|^2}\right) - \partial_{k_y}\left(\frac{\mathrm{Re}[\Delta\epsilon]g^{RR}_{0,xy}}{|\Delta\epsilon|^2}\right)\right) + F_y\partial_{k_y}\left(\frac{\mathrm{Im}[\Delta\epsilon]\Omega^{RR}_{0,xy}}{|\Delta\epsilon|^2}\right).\end{aligned} \tag{C33}$$

Both the RR QGT and the LR QMT appears in the equation of motion, despite that the perturbation theory is defined with respects to the "left-right" formalism and that the centre-of-mass position of the wave packet is calculated using the "right-right" formalism.

D Appendix for Non-Hermitian Zitterbewegung Effects in Chapt. 4

D.1 Derivation of the Semi-classical Equation of Motion

To derive the equation of motion in Eq. (4.10), we start with a general non-Hermitian Hamiltonian

$$\begin{aligned}\hat{H}(\mathbf{k}) &= H_0(\mathbf{k})\mathbf{I} + \overrightarrow{\mathbf{H}}(\mathbf{k}) \cdot \overrightarrow{\boldsymbol{\sigma}} \\ \overrightarrow{\mathbf{H}}(\mathbf{k}) &= [H_x(\mathbf{k}), H_y(\mathbf{k}), H_z(\mathbf{k})] \\ \overrightarrow{\boldsymbol{\sigma}} &= [\sigma_x, \sigma_y, \sigma_z]\end{aligned} \tag{D1}$$

where $H_j = G_j + i\Gamma_j$ for $j = 0, x, y, z$ and the Hermitian and the anti-Hermitian parts of the Hamiltonian can be separated into $\hat{H} = \hat{G} + i\hat{\Gamma}$. The dynamics of the centre-of-mass position is described by a generalized Ehrenfest theorem

$$\begin{aligned}\frac{d}{dt}\langle\hat{\mathbf{r}}\rangle &= \frac{i}{\hbar}\langle\hat{H}^\dagger\hat{\mathbf{r}} - \hat{\mathbf{r}}\hat{H}\rangle - \frac{i}{\hbar}\langle\hat{H}^\dagger - \hat{H}\rangle\langle\hat{\mathbf{r}}\rangle \\ &= \frac{i}{\hbar}\langle[\hat{G}, \hat{\mathbf{r}}]\rangle + \frac{1}{\hbar}\langle\{\hat{\Gamma}, \hat{\mathbf{r}}\}\rangle - \frac{2}{\hbar}\langle\hat{\Gamma}\rangle\langle\hat{\mathbf{r}}\rangle\end{aligned} \tag{D2}$$

where $[.,.]$ denotes commutator and $\{.,.\}$ denotes anti-commutator, and $\langle\hat{A}\rangle = \int_{\mathbf{k}}\langle\psi|\hat{A}|\psi\rangle / \int_{\mathbf{k}}\langle\psi|\psi\rangle$ for any operator $\hat{A}$.

We assume the wavepacket to take the form of $|W\rangle = \int_{\mathbf{k}} w_{\mathbf{k}} e^{i\mathbf{k}\cdot\mathbf{r}}|\psi\rangle$ where $w_{\mathbf{k}}$ is a Gaussian and $|\psi\rangle$ is the spinor wavefunction. Each term can then be solved individually. We assume that the Hamiltonian has no spatial dependence, and only dependence on the momentum. The first term in Eq. (D2) can simply be written as

$$\frac{i}{\hbar}\langle[\hat{G},\hat{\mathbf{r}}]\rangle = \frac{1}{\hbar}\langle\partial_{\mathbf{k}}\hat{G}\rangle. \tag{D3}$$

The last term in Eq. (D2), $\langle\hat{\Gamma}\rangle\langle\hat{\mathbf{r}}\rangle$, can be expanded as

$$\begin{aligned}\langle\hat{\Gamma}\rangle\langle\hat{\mathbf{r}}\rangle &= \frac{1}{N^2}\Big(\int_{\mathbf{k}}|w_{\mathbf{k}}|^2\langle\psi|\hat{\Gamma}|\psi\rangle\Big)\Big(\int_{\mathbf{k}}w_{\mathbf{k}}^*\langle\psi|i\partial_{\mathbf{k}}w_{\mathbf{k}}|\psi\rangle\Big)\\ &= \frac{1}{N^2}\Big(\int_{\mathbf{k}}|w_{\mathbf{k}}|^2\langle\psi|\hat{\Gamma}|\psi\rangle\Big)\Big(\int_{\mathbf{k}}|w_{\mathbf{k}}|^2\langle\psi|i\partial_{\mathbf{k}}\psi\rangle+\int_{\mathbf{k}}(w_{\mathbf{k}}^*i\partial_{\mathbf{k}}w_{\mathbf{k}})\langle\psi|\psi\rangle\Big),\end{aligned} \tag{D4}$$

where $N = \int_{\mathbf{k}}|w_{\mathbf{k}}|^2\langle\psi|\psi\rangle$ is the norm, which varies with time due to the growth or loss. We can then separate the amplitude and phase of the Gaussian wavefunction as $w_{\mathbf{k}} = |w_{\mathbf{k}}|e^{i\varphi}$, then the last term can be rewritten as

$$\begin{aligned}\int_{\mathbf{k}}(w_{\mathbf{k}}^*i\partial_{\mathbf{k}}w_{\mathbf{k}})\langle\psi|\psi\rangle &= \int_{\mathbf{k}}|w_{\mathbf{k}}|i\partial_{\mathbf{k}}|w_{\mathbf{k}}|\langle\psi|\psi\rangle - \int_{\mathbf{k}}\partial_{\mathbf{k}}\varphi|w_{\mathbf{k}}|^2\langle\psi|\psi\rangle\\ &= -\frac{i}{2}\int_{\mathbf{k}}|w_{\mathbf{k}}|^2\partial_{\mathbf{k}}(\langle\psi|\psi\rangle) - \int_{\mathbf{k}}\partial_{\mathbf{k}}\varphi|w_{\mathbf{k}}|^2\langle\psi|\psi\rangle\end{aligned} \tag{D5}$$

where we employ integration by parts to obtain the first term on the second line.

After plugging back in $\langle\hat{\Gamma}\rangle\langle\hat{\mathbf{r}}\rangle$, it can be written in the form

$$\langle\hat{\Gamma}\rangle\langle\hat{\mathbf{r}}\rangle = \frac{1}{N^2}\Big(\int_{\mathbf{k}}|w_{\mathbf{k}}|^2\langle\psi|\hat{\Gamma}|\psi\rangle\Big)\Big(\int_{\mathbf{k}}|w_{\mathbf{k}}|^2\langle\psi|i\partial_{\mathbf{k}}\psi\rangle-\frac{i}{2}\int_{\mathbf{k}}|w_{\mathbf{k}}|^2\partial_{\mathbf{k}}(\langle\psi|\psi\rangle) - \int_{\mathbf{k}}\partial_{\mathbf{k}}\varphi|w_{\mathbf{k}}|^2\langle\psi|\psi\rangle\Big). \tag{D6}$$

Assuming that the wavepacket is narrow in momentum space, $|w_{\mathbf{k}}|^2 \to \delta(\mathbf{k}-\mathbf{k}_c)$, the term $\langle\hat{\Gamma}\rangle\langle\hat{\mathbf{r}}\rangle$ can finally be written as

$$\langle\hat{\Gamma}\rangle\langle\hat{\mathbf{r}}\rangle = \frac{\langle\psi|\hat{\Gamma}|\psi\rangle}{\langle\psi|\psi\rangle}\Big(\frac{i}{2}\frac{\langle\psi|\partial_{\mathbf{k}}\psi\rangle}{\langle\psi|\psi\rangle} - \frac{i}{2}\frac{\langle\partial_{\mathbf{k}}\psi|\psi\rangle}{\langle\psi|\psi\rangle} - \partial_{\mathbf{k}}\varphi\Big)\Big|_{\mathbf{k}=\mathbf{k}_c}. \tag{D7}$$

Similarly, the terms $\langle \hat{\mathbf{r}}\hat{\Gamma}\rangle$ and $\langle \hat{\Gamma}\hat{\mathbf{r}}\rangle$ can be simplified as

$$\begin{aligned}
\langle \hat{\mathbf{r}}\hat{\Gamma}\rangle =& \frac{1}{N}\int_{\mathbf{k}} w_{\mathbf{k}}^* \langle\psi|i\partial_{\mathbf{k}}\hat{\Gamma} w_{\mathbf{k}}|\psi\rangle \\
=& \frac{1}{N}\Big(\int_{\mathbf{k}} |w_{\mathbf{k}}|^2 \langle\psi|(i\partial_{\mathbf{k}}\hat{\Gamma})|\psi\rangle + \int_{\mathbf{k}} |w_{\mathbf{k}}|^2 \langle\psi|\hat{\Gamma}|i\partial_{\mathbf{k}}\psi\rangle + \int_{\mathbf{k}} (w_{\mathbf{k}}^* i\partial_{\mathbf{k}} w_{\mathbf{k}})\langle\psi|\hat{\Gamma}|\psi\rangle \Big) \\
=& \frac{1}{N}\int_{\mathbf{k}} |w_{\mathbf{k}}|^2 \Big(\langle\psi|(i\partial_{\mathbf{k}}\hat{\Gamma})|\psi\rangle + \langle\psi|\hat{\Gamma}|i\partial_{\mathbf{k}}\psi\rangle - \partial_{\mathbf{k}}\varphi \langle\psi|\hat{\Gamma}|\psi\rangle - \frac{i}{2}\partial_{\mathbf{k}}(\langle\psi|\hat{\Gamma}|\psi\rangle) \Big) \\
=& \Big(\frac{\langle\psi|(i\partial_{\mathbf{k}}\hat{\Gamma})|\psi\rangle}{\langle\psi|\psi\rangle} + \frac{\langle\psi|\hat{\Gamma}|i\partial_{\mathbf{k}}\psi\rangle}{\langle\psi|\psi\rangle} - \partial_{\mathbf{k}}\varphi \frac{\langle\psi|\hat{\Gamma}|\psi\rangle}{\langle\psi|\psi\rangle} - \frac{i}{2}\frac{\partial_{\mathbf{k}}(\langle\psi|\hat{\Gamma}|\psi\rangle)}{\langle\psi|\psi\rangle} \Big)\Big|_{\mathbf{k}=\mathbf{k}_c} \\
=& \Big(\frac{i}{2}\frac{\langle\psi|(\partial_{\mathbf{k}}\hat{\Gamma})|\psi\rangle}{\langle\psi|\psi\rangle} + \frac{i}{2}\frac{\langle\psi|\hat{\Gamma}|\partial_{\mathbf{k}}\psi\rangle}{\langle\psi|\psi\rangle} - \frac{i}{2}\frac{\langle\partial_{\mathbf{k}}\psi|\hat{\Gamma}|\psi\rangle}{\langle\psi|\psi\rangle} - \partial_{\mathbf{k}}\varphi \frac{\langle\psi|\hat{\Gamma}|\psi\rangle}{\langle\psi|\psi\rangle} \Big)\Big|_{\mathbf{k}=\mathbf{k}_c} \\
\langle \hat{\Gamma}\hat{\mathbf{r}}\rangle =& \frac{1}{N}\int_{\mathbf{k}} w_{\mathbf{k}}^* \langle\psi|\hat{\Gamma} i\partial_{\mathbf{k}} w_{\mathbf{k}}|\psi\rangle \\
=& \frac{1}{N}\Big(\int_{\mathbf{k}} |w_{\mathbf{k}}|^2 \langle\psi|\hat{\Gamma}|i\partial_{\mathbf{k}}\psi\rangle + \int_{\mathbf{k}} (w_{\mathbf{k}}^* i\partial_{\mathbf{k}} w_{\mathbf{k}})\langle\psi|\hat{\Gamma}|\psi\rangle \Big) \\
=& \Big(-\frac{i}{2}\frac{\langle\psi|(\partial_{\mathbf{k}}\hat{\Gamma})|\psi\rangle}{\langle\psi|\psi\rangle} + \frac{i}{2}\frac{\langle\psi|\hat{\Gamma}|\partial_{\mathbf{k}}\psi\rangle}{\langle\psi|\psi\rangle} - \frac{i}{2}\frac{\langle\partial_{\mathbf{k}}\psi|\hat{\Gamma}|\psi\rangle}{\langle\psi|\psi\rangle} - \partial_{\mathbf{k}}\varphi \frac{\langle\psi|\hat{\Gamma}|\psi\rangle}{\langle\psi|\psi\rangle} \Big)\Big|_{\mathbf{k}=\mathbf{k}_c}.
\end{aligned} \tag{D8}$$

By combining these equations, Eq. (D2) can be simplified as

$$\frac{d}{dt}\langle \hat{\mathbf{r}}\rangle = \frac{1}{\hbar}\langle \partial_{\mathbf{k}}\hat{G}\rangle + \frac{i}{\hbar}\Big(\frac{\langle\psi|\hat{\Gamma}|\partial_{\mathbf{k}}\psi\rangle}{\langle\psi|\psi\rangle} - \frac{\langle\partial_{\mathbf{k}}\psi|\hat{\Gamma}|\psi\rangle}{\langle\psi|\psi\rangle} \Big) - \frac{i}{\hbar}\langle\hat{\Gamma}\rangle \Big(\frac{\langle\psi|\partial_{\mathbf{k}}\psi\rangle}{\langle\psi|\psi\rangle} - \frac{\langle\partial_{\mathbf{k}}\psi|\psi\rangle}{\langle\psi|\psi\rangle} \Big)\Big|_{\mathbf{k}=\mathbf{k}_c} \tag{D9}$$

The spinor wavefunction can be written as $|\psi\rangle = e^{-\frac{i\hat{H}t}{\hbar}}|\psi_0\rangle$ where $|\psi_0\rangle$ is the initial state. Assuming that $|\psi_0\rangle$ has no $\mathbf{k}$-dependence, i.e. the pseudospin texture is uniform in the k-space, $\langle\partial_{\mathbf{k}}\psi|$ and $|\partial_{\mathbf{k}}\psi\rangle$ can be rewritten as

$$\begin{aligned}
\langle\partial_{\mathbf{k}}\psi| &= \langle\psi_0|\partial_{\mathbf{k}} e^{\frac{i\hat{H}^\dagger t}{\hbar}} \\
|\partial_{\mathbf{k}}\psi\rangle &= \partial_{\mathbf{k}} e^{-\frac{i\hat{H}t}{\hbar}}|\psi_0\rangle.
\end{aligned} \tag{D10}$$

The first line in Eqs. (D10) can be solved using the identity of the derivative of the exponential map [318, 319]

$$\begin{aligned}
\partial_{\mathbf{k}} e^{\frac{i\hat{H}^\dagger t}{\hbar}} &= e^{\frac{i\hat{H}^\dagger t}{\hbar}} \Bigg(\frac{1-\exp\Big(-\mathrm{ad}_{\frac{i\hat{H}^\dagger t}{\hbar}}\Big)}{\mathrm{ad}_{\frac{i\hat{H}^\dagger t}{\hbar}}} \partial_{\mathbf{k}}\Big(\frac{i\hat{H}^\dagger t}{\hbar}\Big) \Bigg) \\
&= e^{\frac{i\hat{H}^\dagger t}{\hbar}} \sum_{n=0}^{\infty} \frac{(-1)^n}{(n+1)!}\Big(\frac{it}{\hbar}\Big)^{n+1} \mathrm{ad}^n_{\hat{H}^\dagger}\Big(\partial_{\mathbf{k}}\hat{H}^\dagger\Big)
\end{aligned} \tag{D11}$$

where for matrices X, Y ad_X denotes the adjoint representation, $\mathrm{ad}_X Y = [X, Y]$.

Recall that $\hat{H}^\dagger = H_0^*\mathbf{I} + H_x^*\sigma_x + H_y^*\sigma_y + H_z^*\sigma_z$. The zero-th order, the odd and even order terms take the forms of

$$\begin{aligned}
\mathrm{ad}^{0}_{\hat{H}^\dagger}\partial_{\mathbf{k}}\hat{H}^\dagger &= \partial_{\mathbf{k}}H_0^*\mathbf{I} + \partial_{\mathbf{k}}H_x^*\sigma_x + \partial_{\mathbf{k}}H_y^*\sigma_y + \partial_{\mathbf{k}}H_z^*\sigma_z \\
\mathrm{ad}^{2n-1}_{\hat{H}^\dagger}\partial_{\mathbf{k}}\hat{H}^\dagger &= 2^{2n-1}i(H_x^{*2} + H_y^{*2} + H_z^{*2})^{n-1}(A_x^*\sigma_x + A_y^*\sigma_y + A_z^*\sigma_z) \\
\mathrm{ad}^{2n}_{\hat{H}^\dagger}\partial_{\mathbf{k}}\hat{H}^\dagger &= 2^{2n}(H_x^{*2} + H_y^{*2} + H_z^{*2})^{n-1}(B_x^*\sigma_x + B_y^*\sigma_y + B_z^*\sigma_z)
\end{aligned} \tag{D12}$$

for $n = 1, ...\infty$. Where A_i, B_i denote

$$\begin{aligned}
A_x &= H_y\partial_{\mathbf{k}}H_z - H_z\partial_{\mathbf{k}}H_y \\
A_y &= H_z\partial_{\mathbf{k}}H_x - H_x\partial_{\mathbf{k}}H_z \\
A_z &= H_x\partial_{\mathbf{k}}H_y - H_y\partial_{\mathbf{k}}H_x \\
B_x &= \partial_{\mathbf{k}}H_x(H_y^2 + H_z^2) - H_x(H_y\partial_{\mathbf{k}}H_y + H_z\partial_{\mathbf{k}}H_z) \\
B_y &= \partial_{\mathbf{k}}H_y(H_x^2 + H_z^2) - H_y(H_x\partial_{\mathbf{k}}H_x + H_z\partial_{\mathbf{k}}H_z) \\
B_z &= \partial_{\mathbf{k}}H_z(H_x^2 + H_y^2) - H_z(H_x\partial_{\mathbf{k}}H_x + H_y\partial_{\mathbf{k}}H_y)
\end{aligned} \tag{D13}$$

to simplify the expression. Using these identities and noting that the mean-subtracted eigenenergy and its complex conjugate take the forms of $E = \sqrt{H_x^2 + H_y^2 + H_z^2}$, $E^* =$

$\sqrt{H_x^{*2}+H_y^{*2}+H_z^{*2}}$, Eq. (D11) can then be rewritten as

$$
\begin{aligned}
\partial_{\mathbf{k}} e^{\frac{i\hat{H}^\dagger t}{\hbar}} =& e^{\frac{i\hat{H}^\dagger t}{\hbar}} \Bigg(\frac{it}{\hbar}\partial_{\mathbf{k}} H_0^*\mathbf{I} + \frac{it}{\hbar}(\partial_{\mathbf{k}} H_x^*\sigma_x + \partial_{\mathbf{k}} H_y^*\sigma_y + \partial_{\mathbf{k}} H_z^*\sigma_z) \\
&+ \sum_{n=1}^{\infty} \frac{(-1)^{2n-1}}{(2n)!}\Big(\frac{it}{\hbar}\Big)^{2n} 2^{2n-1} i(H_x^{*2}+H_y^{*2}+H_z^{*2})^{n-1}(A_x^*\sigma_x + A_y^*\sigma_y + A_z^*\sigma_z) \\
&+ \sum_{n=1}^{\infty} \frac{(-1)^{2n}}{(2n+1)!}\Big(\frac{it}{\hbar}\Big)^{2n+1} 2^{2n}(H_x^{*2}+H_y^{*2}+H_z^{*2})^{n-1}(B_x^*\sigma_x + B_y^*\sigma_y + B_z^*\sigma_z)\Bigg) \\
=& e^{\frac{i\hat{H}^\dagger t}{\hbar}} \Bigg(\frac{it}{\hbar}\partial_{\mathbf{k}} H_0^*\mathbf{I} + \frac{it}{\hbar}(\partial_{\mathbf{k}} H_x^*\sigma_x + \partial_{\mathbf{k}} H_y^*\sigma_y + \partial_{\mathbf{k}} H_z^*\sigma_z) \\
&- \sum_{n=1}^{\infty} \frac{i^{2n+1}}{(2n)!}\Big(\frac{t}{\hbar}\Big)^{2n} 2^{2n-1} E^{*2n-2}(A_x^*\sigma_x + A_y^*\sigma_y + A_z^*\sigma_z) \\
&+ \sum_{n=1}^{\infty} \frac{i^{2n+1}}{(2n+1)!}\Big(\frac{t}{\hbar}\Big)^{2n+1} 2^{2n} E^{*2n-2}(B_x^*\sigma_x + B_y^*\sigma_y + B_z^*\sigma_z)\Bigg) \\
=& e^{\frac{i\hat{H}^\dagger t}{\hbar}} \Bigg(\frac{it}{\hbar}\partial_{\mathbf{k}} H_0^*\mathbf{I} + \frac{it}{\hbar}(\partial_{\mathbf{k}} H_x^*\sigma_x + \partial_{\mathbf{k}} H_y^*\sigma_y + \partial_{\mathbf{k}} H_z^*\sigma_z) \\
&- \sum_{n=1}^{\infty} \frac{i}{2E^{*2}}\frac{(-1)^n}{(2n)!}\Big(\frac{2E^*t}{\hbar}\Big)^{2n}(A_x^*\sigma_x + A_y^*\sigma_y + A_z^*\sigma_z) \\
&+ \sum_{n=1}^{\infty} \frac{i}{2E^{*3}}\frac{(-1)^n}{(2n+1)!}\Big(\frac{2E^*t}{\hbar}\Big)^{2n+1}(B_x^*\sigma_x + B_y^*\sigma_y + B_z^*\sigma_z)\Bigg) \\
=& e^{\frac{i\hat{H}^\dagger t}{\hbar}} \Bigg(\frac{it}{\hbar}\partial_{\mathbf{k}} H_0^*\mathbf{I} + \frac{it}{\hbar}(\partial_{\mathbf{k}} H_x^*\sigma_x + \partial_{\mathbf{k}} H_y^*\sigma_y + \partial_{\mathbf{k}} H_z^*\sigma_z) \\
&- \frac{i}{2E^{*2}}\Big(\cos\frac{2E^*t}{\hbar} - 1\Big)(A_x^*\sigma_x + A_y^*\sigma_y + A_z^*\sigma_z) \\
&+ \frac{i}{2E^{*3}}\Big(\sin\frac{2E^*t}{\hbar} - \frac{2E^*t}{\hbar}\Big)(B_x^*\sigma_x + B_y^*\sigma_y + B_z^*\sigma_z)\Bigg).
\end{aligned}
\tag{D14}
$$

Similarly, we can solve $\partial_{\mathbf{k}} e^{-\frac{i\hat{\mathbf{H}}t}{\hbar}}$ by taking the Hermitian conjugate of the results in Eq. (D14)

$$
\begin{aligned}
\partial_{\mathbf{k}} e^{-\frac{i\hat{H}t}{\hbar}} =& \Bigg(-\frac{it}{\hbar}\partial_{\mathbf{k}} H_0\mathbf{I} - \frac{it}{\hbar}(\partial_{\mathbf{k}} H_x\sigma_x + \partial_{\mathbf{k}} H_y\sigma_y + \partial_{\mathbf{k}} H_z\sigma_z) \\
&+ \frac{i}{2E^2}\Big(\cos\frac{2Et}{\hbar} - 1\Big)(A_x\sigma_x + A_y\sigma_y + A_z\sigma_z) \\
&- \frac{i}{2E^3}\Big(\sin\frac{2Et}{\hbar} - \frac{2Et}{\hbar}\Big)(B_x\sigma_x + B_y\sigma_y + B_z\sigma_z)\Bigg) e^{-\frac{i\hat{H}t}{\hbar}}.
\end{aligned}
\tag{D15}
$$

We rewrite the expressions in Eqs. (D14,D15) by defining a new operator $\hat{L}$ as

$$\hat{L} = \frac{t}{\hbar}\partial_{\mathbf{k}} H_0 \mathbf{I} + \sum_{j=x,y,z} \left(\frac{t}{\hbar}\partial_{\mathbf{k}} H_j - \frac{\cos\frac{2Et}{\hbar} - 1}{2E^2} A_j + \frac{\sin\frac{2Et}{\hbar} - \frac{2Et}{\hbar}}{2E^3} B_j \right) \sigma_j \tag{D16}$$

and therefore the derivatives of the time evolution operator and its conjugate take the forms of

$$\begin{aligned} \partial_{\mathbf{k}} e^{-\frac{i\hat{H}t}{\hbar}} =& -i\hat{L}e^{-\frac{i\hat{H}t}{\hbar}} \\ \partial_{\mathbf{k}} e^{\frac{i\hat{H}^\dagger t}{\hbar}} =& ie^{\frac{i\hat{H}^\dagger t}{\hbar}}\hat{L}^\dagger, \end{aligned} \tag{D17}$$

and the equation of motion in Eq. (D9) can be rewritten as

$$\frac{d}{dt}\langle \hat{\mathbf{r}} \rangle = \frac{1}{\hbar}\langle \partial_{\mathbf{k}}\hat{G} \rangle + \frac{1}{\hbar}\langle \hat{\Gamma}\hat{L} + \hat{L}^\dagger\hat{\Gamma} \rangle - \frac{1}{\hbar}\langle \hat{\Gamma} \rangle \langle \hat{L} + \hat{L}^\dagger \rangle \bigg|_{\mathbf{k}=\mathbf{k}_c}. \tag{D18}$$

Since the coefficients in $\hat{L}$ can all be complex-valued, we can further simplify the equation by defining two new operators corresponding to the components corresponding to the real and imaginary parts of the coefficients in $\hat{L}$

$$\begin{aligned} \hat{L}^{Re} =& \frac{t}{\hbar}\partial_{\mathbf{k}} G_0 \mathbf{I} + \sum_{j=x,y,z} \left(\frac{t}{\hbar}\partial_{\mathbf{k}} G_j \sigma_j + \mathrm{Re}\left[-\frac{\cos\frac{2Et}{\hbar} - 1}{2E^2} A_j + \frac{\sin\frac{2Et}{\hbar} - \frac{2Et}{\hbar}}{2E^3} B_j \right] \sigma_j \right) \\ \hat{L}^{Im} =& \frac{t}{\hbar}\partial_{\mathbf{k}} \Gamma_0 \mathbf{I} + \sum_{j=x,y,z} \left(\frac{t}{\hbar}\partial_{\mathbf{k}} \Gamma_j \sigma_j + \mathrm{Im}\left[-\frac{\cos\frac{2Et}{\hbar} - 1}{2E^2} A_j + \frac{\sin\frac{2Et}{\hbar} - \frac{2Et}{\hbar}}{2E^3} B_j \right] \sigma_j \right) \end{aligned} \tag{D19}$$

such that $\hat{L} = \hat{L}^{Re} + i\hat{L}^{Im}$ and $\hat{L}^\dagger = \hat{L}^{Re} - i\hat{L}^{Im}$.

The equation of motion in Eq. (D9) can then be further simplified as

$$\frac{d}{dt}\langle \hat{\mathbf{r}} \rangle = \frac{1}{\hbar}\langle \partial_{\mathbf{k}}\hat{G} \rangle + \frac{1}{\hbar}\langle \{\hat{\Gamma}, \hat{L}^{Re}\} \rangle + \frac{i}{\hbar}\langle [\hat{\Gamma}, \hat{L}^{Im}] \rangle - \frac{2}{\hbar}\langle \hat{\Gamma} \rangle \langle \hat{L}^{Re} \rangle|_{\mathbf{k}=\mathbf{k}_c}. \tag{D20}$$

We can then simplify the equation of motion term by term to obtain the main result in Eq. (4.10) in the main text. The first term in Eq. (D20) also appears in the Hermitian case and takes the form of

$$\frac{1}{\hbar}\langle \partial_{\mathbf{k}}\hat{G} \rangle = \frac{1}{\hbar}\Big(\partial_{\mathbf{k}} G_0 + \partial_{\mathbf{k}} G_x S_x + \partial_{\mathbf{k}} G_y S_y + \partial_{\mathbf{k}} G_z S_z \Big) \tag{D21}$$

where $S_j = \langle \sigma_j \rangle$ for $j = x, y, z$. The second term in Eq. (D20) can solved using the anti-commutation relations of the Pauli matrices and the identity matrix $\{\mathbf{I}, \sigma_j\} = 2\sigma_j$,

$\{\sigma_i, \sigma_j\} = 2\delta_{ij}\mathbf{I}$

$$
\begin{aligned}
\frac{1}{\hbar}\langle\{\hat{\Gamma}, \hat{L}^{Re}\}\rangle =& \frac{1}{\hbar}\sum_{i,j=x,y,z}\Bigg(\langle\{\Gamma_0\mathbf{I}, \partial_{\mathbf{k}}G_0\mathbf{I} + \frac{t}{\hbar}\partial_{\mathbf{k}}G_j\sigma_j + \mathrm{Re}\left[-\frac{\cos\frac{2Et}{\hbar}-1}{2E^2}A_j + \frac{\sin\frac{2Et}{\hbar}-\frac{2Et}{\hbar}}{2E^3}B_j\right]\sigma_j\}\rangle \\
&+ \langle\{\Gamma_i\sigma_i, \partial_{\mathbf{k}}G_0\mathbf{I} + \frac{t}{\hbar}\partial_{\mathbf{k}}G_j\sigma_j + \mathrm{Re}\left[-\frac{\cos\frac{2Et}{\hbar}-1}{2E^2}A_j + \frac{\sin\frac{2Et}{\hbar}-\frac{2Et}{\hbar}}{2E^3}B_j\right]\sigma_j\}\rangle\Bigg) \\
=& \frac{2}{\hbar}\sum_{j=x,y,z}\Bigg(\Gamma_0\partial_{\mathbf{k}}G_0 + \frac{t}{\hbar}\Gamma_0\partial_{\mathbf{k}}G_jS_j + \mathrm{Re}\left[-\frac{\cos\frac{2Et}{\hbar}-1}{2E^2}\Gamma_0A_j + \frac{\sin\frac{2Et}{\hbar}-\frac{2Et}{\hbar}}{2E^3}\Gamma_0B_j\right]S_j \\
&+ \Gamma_j\partial_{\mathbf{k}}G_0S_j + \frac{t}{\hbar}\Gamma_j\partial_{\mathbf{k}}G_j + \mathrm{Re}\left[-\frac{\cos\frac{2Et}{\hbar}-1}{2E^2}A_j + \frac{\sin\frac{2Et}{\hbar}-\frac{2Et}{\hbar}}{2E^3}B_j\right]\Gamma_j\Bigg),
\end{aligned}
\tag{D22}
$$

and the third term in Eq. (D20) can be rewritten using the commutation relation $[\sigma_i, \sigma_j] = 2i\epsilon_{ijk}\sigma_k$

$$
\frac{i}{\hbar}\langle[\hat{\Gamma}, \hat{L}^{Im}]\rangle = -\frac{2}{\hbar}\sum_{i,j=x,y,z}\epsilon_{ijk}\left(\frac{t}{\hbar}\Gamma_i\partial_{\mathbf{k}}\Gamma_j + \Gamma_i\,\mathrm{Im}\left[-\frac{\cos\frac{2Et}{\hbar}-1}{2E^2}A_j + \frac{\sin\frac{2Et}{\hbar}-\frac{2Et}{\hbar}}{2E^3}B_j\right]\right)S_k.
\tag{D23}
$$

Finally, the last term in Eq. (D20) is simply

$$
\begin{aligned}
-\frac{2}{\hbar}\langle\hat{\Gamma}\rangle\langle\hat{L}^{Re}\rangle =& -\frac{2}{\hbar}\left(\Gamma_0 + \sum_{i=x,y,z}\Gamma_iS_i\right)\left(\frac{t}{\hbar}\partial_{\mathbf{k}}G_0 + \sum_{j=x,y,z}\left(\frac{t}{\hbar}\partial_{\mathbf{k}}G_jS_j\right.\right. \\
&\left.\left.+ \mathrm{Re}\left[-\frac{\cos\frac{2Et}{\hbar}-1}{2E^2}A_j + \frac{\sin\frac{2Et}{\hbar}-\frac{2Et}{\hbar}}{2E^3}B_j\right]S_j\right)\right) \\
=& -\frac{2}{\hbar}\Gamma_0\left(\frac{t}{\hbar}\partial_{\mathbf{k}}G_0 + \sum_{j=x,y,z}\left(\frac{t}{\hbar}\partial_{\mathbf{k}}G_jS_j + \mathrm{Re}\left[-\frac{\cos\frac{2Et}{\hbar}-1}{2E^2}A_j + \frac{\sin\frac{2Et}{\hbar}-\frac{2Et}{\hbar}}{2E^3}B_j\right]S_j\right)\right) \\
&- \frac{2t}{\hbar^2}\partial_{\mathbf{k}}G_0\left(\Gamma_0 + \sum_{i=x,y,z}\Gamma_iS_i\right) \\
&- \frac{2}{\hbar}\left(\sum_{i=x,y,z}\Gamma_iS_i\right)\left(\sum_{j=x,y,z}\frac{t}{\hbar}\partial_{\mathbf{k}}G_jS_j + \mathrm{Re}\left[-\frac{\cos\frac{2Et}{\hbar}-1}{2E^2}A_j + \frac{\sin\frac{2Et}{\hbar}-\frac{2Et}{\hbar}}{2E^3}B_j\right]S_j\right)
\end{aligned}
\tag{D24}
$$

where we note that the first two lines in the final form of Eq. (D24) will be canceled out with terms in Eq. (D22) and only the terms in the third line, i.e. the $O(S^2)$ terms, will remain.

After summing up and rearranging the terms, Eq. (D20) can be rewritten into

$$
\begin{aligned}
\dot{\mathbf{r}} =& \frac{1}{\hbar}\partial_{\mathbf{k}} G_0 + \frac{1}{\hbar}\sum_i (\partial_{\mathbf{k}} G_i) S_i + \frac{2t}{\hbar^2}\sum_i \Gamma_i \partial_{\mathbf{k}} G_i - \frac{2t}{\hbar^2}\sum_{i,j}\epsilon_{ijk}\Gamma_i(\partial_{\mathbf{k}}\Gamma_j)S_k \\
&- \frac{2t}{\hbar^2}\Big(\sum_i \Gamma_i S_i\Big)\Big(\sum_j (\partial_{\mathbf{k}} G_j) S_j\Big) + \frac{2}{\hbar}\sum_i \mathrm{Re}\Big[-\frac{\cos\frac{2Et}{\hbar}-1}{2E^2}\Gamma_i A_i + \frac{\sin\frac{2Et}{\hbar}-\frac{2Et}{\hbar}}{2E^3}\Gamma_i B_i\Big] \\
&- \frac{2}{\hbar}\sum_{i,j}\epsilon_{ijk}\,\mathrm{Im}\Big[-\frac{\cos\frac{2Et}{\hbar}-1}{2E^2}\Gamma_i A_j S_k + \frac{\sin\frac{2Et}{\hbar}-\frac{2Et}{\hbar}}{2E^3}\Gamma_i B_j S_k\Big] \\
&- \frac{2}{\hbar}\big(\sum_i \Gamma_i S_i\big)\Bigg(\sum_j \mathrm{Re}\Big[-\frac{\cos\frac{2Et}{\hbar}-1}{2E^2}A_j S_j + \frac{\sin\frac{2Et}{\hbar}-\frac{2Et}{\hbar}}{2E^3}B_j S_j\Big]\Bigg).
\end{aligned} \tag{D25}
$$

After re-arranging each term into vector form, this yields my main result in Eq. (4.10) in the main text.

D.2 Quantum Metric Tensor in the Equation of Motion

In the special case with $H_z = 0$, the identities of $\mathrm{ad}^n_{\hat{H}}\hat{H}$ now take the forms

$$
\begin{aligned}
\mathrm{ad}^0_{\hat{H}}\partial_{\mathbf{k}}\hat{H} &= \partial_{\mathbf{k}}H_0\mathbf{I} + \partial_{\mathbf{k}}H_x\sigma_x + \partial_{\mathbf{k}}H_y\sigma_y \\
\mathrm{ad}^{2n-1}_{\hat{H}}\partial_{\mathbf{k}}\hat{H} &= 2^{2n-1}i(H_x^2+H_y^2+H_z^2)^{n-1}(H_x\partial_{\mathbf{k}}H_y - H_y\partial_{\mathbf{k}}H_x)\sigma_z \\
\mathrm{ad}^{2n}_{\hat{H}}\partial_{\mathbf{k}}\hat{H} &= 2^{2n}(H_x^2+H_y^2+H_z^2)^{n-1}(H_x\partial_{\mathbf{k}}H_y - H_y\partial_{\mathbf{k}}H_x)(-H_y\sigma_x + H_x\sigma_y).
\end{aligned} \tag{D26}
$$

We also note the these terms can be identified with components of the left-right quantum metric tensor (LR QMT), $g^{LR}_{n,\mu\nu}$, which are defined as [201, 10, 200, 203]

$$
g^{LR}_{n,\mu\nu} = \frac{1}{2}\Big(\langle\partial_\mu\psi^L_n|\partial_\nu\psi^R_n\rangle + \langle\partial_\nu\psi^L_n|\partial_\mu\psi^R_n\rangle\Big) + \langle\partial_\mu\psi^L_n|\psi^R_n\rangle\langle\psi^L_n|\partial_\nu\psi^R_n\rangle. \tag{D27}
$$

The components of the LR QMT also follow the identity [201, 190, 189]

$$
\begin{aligned}
g^{LR}_{n,\mu\nu} &= \frac{1}{2}\sum_{m\neq n}\Big((\mathbf{A}^{LR}_{nm})_\mu(\mathbf{A}^{LR}_{mn})_\nu + (\mathbf{A}^{LR}_{mn})_\mu(\mathbf{A}^{LR}_{nm})_\nu\Big) \\
&= \frac{1}{2}\sum_{m\neq n}\Bigg(\frac{\langle\psi^L_m|\partial_\mu\hat{H}|\psi^R_n\rangle\langle\psi^L_n|\partial_\nu\hat{H}|\psi^R_m\rangle}{(E_m-E_n)^2} + \frac{\langle\psi^L_n|\partial_\mu\hat{H}|\psi^R_m\rangle\langle\psi^L_m|\partial_\nu\hat{H}|\psi^R_n\rangle}{(E_m-E_n)^2}\Bigg)
\end{aligned} \tag{D28}
$$

where $\mathbf{A}^{LR}_{nm} = \langle\psi^L_n|i\partial_{\mathbf{k}}\psi^R_m\rangle$ denotes the inter-band Berry connection.

In a two-band non-Hermitian system, the LR QMT of the two eigenstates coincide $g^{LR}_{+,\mu\nu} = g^{LR}_{-,\mu\nu} = g^{LR}_{\mu\nu}$ and in the special case with $H_z = 0$, the eigenstates take the forms of

$$\begin{aligned} |\psi^R_\pm\rangle &= \frac{1}{\sqrt{2E^2}} \begin{pmatrix} \pm E \\ H_x + iH_y \end{pmatrix} \\ \langle\psi^L_\pm| &= \frac{1}{\sqrt{2E^2}} \begin{pmatrix} \pm E & H_x - iH_y \end{pmatrix}. \end{aligned} \tag{D29}$$

We note that the diagonal elements of the LR QMT and the inter-band Berry connection take the forms of

$$\begin{aligned} g^{LR}_{\mathbf{kk}} &= \frac{(H_x\partial_{\mathbf{k}}H_y - H_y\partial_{\mathbf{k}}H_x)^2}{4E^4} \\ \mathbf{A}^{LR}_{\pm\mp} = \mathbf{A}^{LR}_{\mp\pm} &= \frac{H_y\partial_{\mathbf{k}}H_x - H_x\partial_{\mathbf{k}}H_y}{2E^2}. \end{aligned} \tag{D30}$$

We therefore identify the term $(H_x\partial_{\mathbf{k}}H_y - H_y\partial_{\mathbf{k}}H_x)/(2E^2)$ with $\sqrt{g^{LR}_{\mathbf{kk}}}$ up to a sign. After this, the equation of motion in Eq. (4.12) in the main text can be derived similarly to the derivation of Eq. (4.10) presented earlier in this section.

Bibliography

[1] Shunyu Yao and Zhong Wang. Edge states and topological invariants of non-Hermitian systems. *Phys. Rev. Lett.*, 121:086803, Aug 2018. doi: 10.1103/PhysRevLett.121.086803. URL `https://link.aps.org/doi/10.1103/PhysRevLett.121.086803`.

[2] Ye Xiong. Why does bulk boundary correspondence fail in some non-Hermitian topological models. *Journal of Physics Communications*, 2(3):035043, mar 2018. doi: 10.1088/2399-6528/aab64a. URL `https://dx.doi.org/10.1088/2399-6528/aab64a`.

[3] Ching Hua Lee and Ronny Thomale. Anatomy of skin modes and topology in non-Hermitian systems. *Phys. Rev. B*, 99:201103, May 2019. doi: 10.1103/PhysRevB.99.201103. URL `https://link.aps.org/doi/10.1103/PhysRevB.99.201103`.

[4] Ananya Ghatak and Tanmoy Das. New topological invariants in non-Hermitian systems. *Journal of Physics: Condensed Matter*, 31(26):263001, apr 2019. doi: 10.1088/1361-648x/ab11b3. URL `https://doi.org/10.1088/1361-648x/ab11b3`.

[5] E. J. Bergholtz, J. C. Budich, and F. K. Kunst. Exceptional topology of non-Hermitian systems. *Rev. Mod. Phys.*, 93:015005, 2021. doi: 10.1103/RevModPhys.93.015005. URL `https://link.aps.org/doi/10.1103/RevModPhys.93.015005`.

[6] Huitao Shen, Bo Zhen, and Liang Fu. Topological band theory for non-Hermitian hamiltonians. *Phys. Rev. Lett.*, 120:146402, Apr 2018. doi: 10.1103/PhysRevLett.120.146402. URL `https://link.aps.org/doi/10.1103/PhysRevLett.120.146402`.

[7] J.P. Provost and G. Vallee. Riemannian structure on manifolds of quantum states. *Commun.Math. Phys.*, 76:289–301, 1980. doi: 10.1007/BF02193559. URL `https://doi.org/10.1007/BF02193559`.

[8] D. D. Solnyshkov, C. Leblanc, L. Bessonart, A. Nalitov, Jiahuan Ren, Qing Liao, Feng Li, and G. Malpuech. Quantum metric and wave packets at exceptional points in non-Hermitian systems. *Phys. Rev. B*, 103:125302, 2021. doi: 10.1103/PhysRevB.103.125302. URL `https://link.aps.org/doi/10.1103/PhysRevB.103.125302`.

[9] Javier Cuerda, Jani M. Taskinen, Nicki Källman, Leo Grabitz, and Päivi Törmä. Pseudospin-orbit coupling and non-Hermitian effects in the quantum geometric tensor of a plasmonic lattice. *Phys. Rev. B*, 109:165439, Apr 2024. doi: 10.1103/

PhysRevB.109.165439. URL `https://link.aps.org/doi/10.1103/PhysRevB.109.165439`.

[10] Yan-Qing Zhu, Wen Zheng, Shi-Liang Zhu, and Giandomenico Palumbo. Band topology of pseudo-Hermitian phases through tensor Berry connections and quantum metric. *Phys. Rev. B*, 104:205103, Nov 2021. doi: 10.1103/PhysRevB.104.205103. URL `https://link.aps.org/doi/10.1103/PhysRevB.104.205103`.

[11] Mengzhen Zhang, William Sweeney, Chia Wei Hsu, Lan Yang, A. D. Stone, and Liang Jiang. Quantum noise theory of exceptional point amplifying sensors. *Phys. Rev. Lett.*, 123:180501, Oct 2019. doi: 10.1103/PhysRevLett.123.180501. URL `https://link.aps.org/doi/10.1103/PhysRevLett.123.180501`.

[12] Iacopo Carusotto and Cristiano Ciuti. Quantum fluids of light. *Rev. Mod. Phys.*, 85:299–366, Feb 2013. doi: 10.1103/RevModPhys.85.299. URL `https://link.aps.org/doi/10.1103/RevModPhys.85.299`.

[13] Hui Deng, Hartmut Haug, and Yoshihisa Yamamoto. Exciton-polariton Bose-Einstein condensation. *Rev. Mod. Phys.*, 82:1489–1537, May 2010. doi: 10.1103/RevModPhys.82.1489. URL `https://link.aps.org/doi/10.1103/RevModPhys.82.1489`.

[14] L. Pickup, H. Sigurdsson, J. Ruostekoski, and P. G. Lagoudakis. Synthetic band-structure engineering in polariton crystals with non-Hermitian topological phases. *Nature Communications*, 11(1):4431, 2020. doi: 10.1038/s41467-020-18213-1. URL `https://doi.org/10.1038/s41467-020-18213-1`.

[15] T. Gao, E. Estrecho, K. Y. Bliokh, T. C. H. Liew, M. D. Fraser, S. Brodbeck, M. Kamp, C. Schneider, S. Höfling, Y. Yamamoto, F. Nori, Y. S. Kivshar, A. G. Truscott, R. G. Dall, and E. A. Ostrovskaya. Observation of non-Hermitian degeneracies in a chaotic exciton-polariton billiard. *Nature*, 526(7574):554–558, 2015. doi: 10.1038/nature15522. URL `https://doi.org/10.1038/nature15522`.

[16] Hengyun Zhou, Chao Peng, Yoseob Yoon, Chia Wei Hsu, Keith A. Nelson, Liang Fu, John D. Joannopoulos, Marin Soljačić, and Bo Zhen. Observation of bulk fermi arc and polarization half charge from paired exceptional points. *Science*, 359(6379): 1009–1012, 2018. doi: 10.1126/science.aap9859. URL `https://www.science.org/doi/abs/10.1126/science.aap9859`.

[17] P. Ehrenfest. Bemerkung über die angenäherte gültigkeit der klassischen mechanik innerhalb der quantenmechanik. *Zeitschrift für Physik*, 45(7):455–457, 1927. doi: 10.1007/BF01329203. URL `https://doi.org/10.1007/BF01329203`.

[18] R.P Feynman and F.L Vernon. The theory of a general quantum system interacting with a linear dissipative system. *Annals of Physics*, 24:118–173, 1963. ISSN 0003-4916. doi: https://doi.org/10.1016/0003-4916(63)90068-X. URL `https://www.sciencedirect.com/science/article/pii/000349166390068X`.

[19] G. Lindblad. On the generators of quantum dynamical semigroups. *Communications in Mathematical Physics*, 48(2):119–130, Jun 1976. ISSN 1432-0916. doi: 10.1007/BF01608499. URL `https://doi.org/10.1007/BF01608499`.

[20] T.L. Gilbert. A phenomenological theory of damping in ferromagnetic materials. *IEEE Transactions on Magnetics*, 40(6):3443–3449, 2004. doi: 10.1109/TMAG.2004.836740.

[21] L. D. Landau and E. M. Lifshitz. “on the theory of the dispersion of magnetic permeability in ferromagnetic bodies. *Phys. Z. Sowjet.*, 8:153–169, 1935.

[22] Ş. K. Özdemir, S. Rotter, F. Nori, and L. Yang. Parity–time symmetry and exceptional points in photonics. *Nature Materials*, 18(8):783–798, 2019. doi: 10.1038/s41563-019-0304-9. URL `https://doi.org/10.1038/s41563-019-0304-9`.

[23] Ramy El-Ganainy, Konstantinos G. Makris, Mercedeh Khajavikhan, Ziad H. Musslimani, Stefan Rotter, and Demetrios N. Christodoulides. Non-Hermitian physics and PT symmetry. *Nature Physics*, 14(1):11–19, 2018. doi: 10.1038/nphys4323. URL `https://doi.org/10.1038/nphys4323`.

[24] G. Gamow. Zur quantentheorie des atomkernes. *Zeitschrift für Physik*, 51(3): 204–212, Mar 1928. ISSN 0044-3328. doi: 10.1007/BF01343196. URL `https://doi.org/10.1007/BF01343196`.

[25] H. Feshbach, C. E. Porter, and V. F. Weisskopf. Model for nuclear reactions with neutrons. *Phys. Rev.*, 96:448–464, Oct 1954. doi: 10.1103/PhysRev.96.448. URL `https://link.aps.org/doi/10.1103/PhysRev.96.448`.

[26] Carl M. Bender and Stefan Boettcher. Real spectra in non-Hermitian Hamiltonians having *PT* symmetry. *Phys. Rev. Lett.*, 80:5243–5246, Jun 1998. doi: 10.1103/PhysRevLett.80.5243. URL `https://link.aps.org/doi/10.1103/PhysRevLett.80.5243`.

[27] Carl M. Bender, Stefan Boettcher, and Peter N. Meisinger. PT-symmetric quantum mechanics. *Journal of Mathematical Physics*, 40:2201–2229, 1998. URL `https://api.semanticscholar.org/CorpusID:119399647`.

[28] Carl M. Bender and Daniel W. Hook. $\mathcal{PT}$-symmetric quantum mechanics. *Rev. Mod. Phys.*, 96:045002, Oct 2024. doi: 10.1103/RevModPhys.96.045002. URL `https://link.aps.org/doi/10.1103/RevModPhys.96.045002`.

[29] Ali Mostafazadeh. Pseudo-Hermiticity versus PT symmetry: The necessary condition for the reality of the spectrum of a non-Hermitian Hamiltonian. *Journal of Mathematical Physics*, 43(1):205–214, 01 2002. ISSN 0022-2488. doi: 10.1063/1.1418246. URL `https://doi.org/10.1063/1.1418246`.

[30] Christian E. Rüter, Konstantinos G. Makris, Ramy El-Ganainy, Demetrios N. Christodoulides, Mordechai Segev, and Detlef Kip. Observation of parity–time

symmetry in optics. *Nature Physics*, 6(3):192–195, Mar 2010. ISSN 1745-2481. doi: 10.1038/nphys1515. URL `https://doi.org/10.1038/nphys1515`.

[31] Joseph Schindler, Ang Li, Mei C. Zheng, F. M. Ellis, and Tsampikos Kottos. Experimental study of active LRC circuits with $\mathcal{PT}$ symmetries. *Phys. Rev. A*, 84: 040101, Oct 2011. doi: 10.1103/PhysRevA.84.040101. URL `https://link.aps.org/doi/10.1103/PhysRevA.84.040101`.

[32] S. Bittner, B. Dietz, U. Günther, H. L. Harney, M. Miski-Oglu, A. Richter, and F. Schäfer. *PT* symmetry and spontaneous symmetry breaking in a microwave billiard. *Phys. Rev. Lett.*, 108:024101, Jan 2012. doi: 10.1103/PhysRevLett.108.024101. URL `https://link.aps.org/doi/10.1103/PhysRevLett.108.024101`.

[33] Daniel Leykam, Konstantin Y. Bliokh, Chunli Huang, Y. D. Chong, and Franco Nori. Edge modes, degeneracies, and topological numbers in non-Hermitian systems. *Phys. Rev. Lett.*, 118:040401, Jan 2017. doi: 10.1103/PhysRevLett.118.040401. URL `https://link.aps.org/doi/10.1103/PhysRevLett.118.040401`.

[34] Flore K. Kunst, Elisabet Edvardsson, Jan Carl Budich, and Emil J. Bergholtz. Biorthogonal bulk-boundary correspondence in non-Hermitian systems. *Phys. Rev. Lett.*, 121:026808, Jul 2018. doi: 10.1103/PhysRevLett.121.026808. URL `https://link.aps.org/doi/10.1103/PhysRevLett.121.026808`.

[35] Dan S. Borgnia, Alex Jura Kruchkov, and Robert-Jan Slager. Non-Hermitian boundary modes and topology. *Phys. Rev. Lett.*, 124:056802, Feb 2020. doi: 10.1103/PhysRevLett.124.056802. URL `https://link.aps.org/doi/10.1103/PhysRevLett.124.056802`.

[36] Ke He, Yayu Wang, and Qi-Kun Xue. Topological materials: Quantum anomalous hall system. *Annual Review of Condensed Matter Physics*, 9(Volume 9, 2018):329–344, 2018. ISSN 1947-5462. doi: https://doi.org/10.1146/annurev-conmatphys-033117-054144. URL `https://www.annualreviews.org/content/journals/10.1146/annurev-conmatphys-033117-054144`.

[37] M. Z. Hasan and C. L. Kane. Colloquium: Topological insulators. *Rev. Mod. Phys.*, 82:3045–3067, Nov 2010. doi: 10.1103/RevModPhys.82.3045. URL `https://link.aps.org/doi/10.1103/RevModPhys.82.3045`.

[38] David S Simon. Topological invariants. In *Topology in Optics (Second Edition)*, 2053-2563, pages 5–1 to 5–15. IOP Publishing, 2021. ISBN 978-0-7503-3471-6. doi: 10.1088/978-0-7503-3471-6ch5. URL `https://doi.org/10.1088/978-0-7503-3471-6ch5`.

[39] T. Senthil. Symmetry-protected topological phases of quantum matter. *Annual Review of Condensed Matter Physics*, 6(Volume 6, 2015):299–324, 2015. ISSN 1947-5462. doi: https://doi.org/10.1146/annurev-conmatphys-031214-014740. URL `https://www.annualreviews.org/content/journals/10.1146/annurev-conmatphys-031214-014740`.

[40] Z. Gong, Y. Ashida, K. Kawabata, K. Takasan, S. Higashikawa, and M. Ueda. Topological phases of non-Hermitian systems. *Phys. Rev. X*, 8:031079, 2018. doi: 10.1103/PhysRevX.8.031079. URL `https://link.aps.org/doi/10.1103/PhysRevX.8.031079`.

[41] Hossein Hodaei, Absar U. Hassan, Steffen Wittek, Hipolito Garcia-Gracia, Ramy El-Ganainy, Demetrios N. Christodoulides, and Mercedeh Khajavikhan. Enhanced sensitivity at higher-order exceptional points. *Nature*, 548(7666):187–191, Aug 2017. doi: 10.1038/nature23280. URL `https://doi.org/10.1038/nature23280`.

[42] Jan Carl Budich and Emil J. Bergholtz. Non-Hermitian topological sensors. *Phys. Rev. Lett.*, 125:180403, Oct 2020. doi: 10.1103/PhysRevLett.125.180403. URL `https://link.aps.org/doi/10.1103/PhysRevLett.125.180403`.

[43] R. Arouca, Jorge Cayao, and Annica M. Black-Schaffer. Topological superconductivity enhanced by exceptional points. *Phys. Rev. B*, 108:L060506, Aug 2023. doi: 10.1103/PhysRevB.108.L060506. URL `https://link.aps.org/doi/10.1103/PhysRevB.108.L060506`.

[44] Kai Zhang, Zhesen Yang, and Chen Fang. Correspondence between winding numbers and skin modes in non-Hermitian systems. *Phys. Rev. Lett.*, 125:126402, Sep 2020. doi: 10.1103/PhysRevLett.125.126402. URL `https://link.aps.org/doi/10.1103/PhysRevLett.125.126402`.

[45] Rijia Lin, Tommy Tai, Linhu Li, and Ching Hua Lee. Topological non-Hermitian skin effect. *Frontiers of Physics*, 18(5):53605, Jul 2023. ISSN 2095-0470. doi: 10.1007/s11467-023-1309-z. URL `https://doi.org/10.1007/s11467-023-1309-z`.

[46] Naomichi Hatano and David R. Nelson. Localization transitions in non-Hermitian quantum mechanics. *Phys. Rev. Lett.*, 77:570–573, Jul 1996. doi: 10.1103/PhysRevLett.77.570. URL `https://link.aps.org/doi/10.1103/PhysRevLett.77.570`.

[47] Naomichi Hatano and David R. Nelson. Vortex pinning and non-Hermitian quantum mechanics. *Phys. Rev. B*, 56:8651–8673, Oct 1997. doi: 10.1103/PhysRevB.56.8651. URL `https://link.aps.org/doi/10.1103/PhysRevB.56.8651`.

[48] Naomichi Hatano and David R. Nelson. Non-Hermitian delocalization and eigenfunctions. *Phys. Rev. B*, 58:8384–8390, Oct 1998. doi: 10.1103/PhysRevB.58.8384. URL `https://link.aps.org/doi/10.1103/PhysRevB.58.8384`.

[49] Kohei Kawabata, Ken Shiozaki, Masahito Ueda, and Masatoshi Sato. Symmetry and topology in non-Hermitian physics. *Phys. Rev. X*, 9:041015, Oct 2019. doi: 10.1103/PhysRevX.9.041015. URL `https://link.aps.org/doi/10.1103/PhysRevX.9.041015`.

[50] Linhu Li, Ching Hua Lee, and Jiangbin Gong. Topological switch for non-Hermitian skin effect in cold-atom systems with loss. *Phys. Rev. Lett.*, 124:250402, Jun

2020. doi: 10.1103/PhysRevLett.124.250402. URL `https://link.aps.org/doi/10.1103/PhysRevLett.124.250402`.

[51] Sibo Guo, Chenxiao Dong, Fuchun Zhang, Jiangping Hu, and Zhesen Yang. Theoretical prediction of a non-Hermitian skin effect in ultracold-atom systems. *Phys. Rev. A*, 106:L061302, Dec 2022. doi: 10.1103/PhysRevA.106.L061302. URL `https://link.aps.org/doi/10.1103/PhysRevA.106.L061302`.

[52] Haowei Li and Wei Yi. Topology and its detection in a dissipative Aharonov-Bohm chain. *Phys. Rev. A*, 106:053311, Nov 2022. doi: 10.1103/PhysRevA.106.053311. URL `https://link.aps.org/doi/10.1103/PhysRevA.106.053311`.

[53] Qian Liang, Dizhou Xie, Zhaoli Dong, Haowei Li, Hang Li, Bryce Gadway, Wei Yi, and Bo Yan. Dynamic signatures of non-Hermitian skin effect and topology in ultracold atoms. *Phys. Rev. Lett.*, 129:070401, Aug 2022. doi: 10.1103/PhysRevLett.129.070401. URL `https://link.aps.org/doi/10.1103/PhysRevLett.129.070401`.

[54] Nobuyuki Okuma, Kohei Kawabata, Ken Shiozaki, and Masatoshi Sato. Topological origin of non-Hermitian skin effects. *Phys. Rev. Lett.*, 124:086801, Feb 2020. doi: 10.1103/PhysRevLett.124.086801. URL `https://link.aps.org/doi/10.1103/PhysRevLett.124.086801`.

[55] Kazuki Yokomizo and Shuichi Murakami. Non-Bloch band theory of non-Hermitian systems. *Phys. Rev. Lett.*, 123:066404, Aug 2019. doi: 10.1103/PhysRevLett.123.066404. URL `https://link.aps.org/doi/10.1103/PhysRevLett.123.066404`.

[56] Kazuki Yokomizo, Taiki Yoda, and Shuichi Murakami. Non-Hermitian waves in a continuous periodic model and application to photonic crystals. *Phys. Rev. Res.*, 4:023089, May 2022. doi: 10.1103/PhysRevResearch.4.023089. URL `https://link.aps.org/doi/10.1103/PhysRevResearch.4.023089`.

[57] Yu-Min Hu, Yin-Quan Huang, Wen-Tan Xue, and Zhong Wang. Non-Bloch band theory for non-Hermitian continuum systems. *Phys. Rev. B*, 110:205429, Nov 2024. doi: 10.1103/PhysRevB.110.205429. URL `https://link.aps.org/doi/10.1103/PhysRevB.110.205429`.

[58] Stefano Longhi. Non-Hermitian skin effect beyond the tight-binding models. *Phys. Rev. B*, 104:125109, Sep 2021. doi: 10.1103/PhysRevB.104.125109. URL `https://link.aps.org/doi/10.1103/PhysRevB.104.125109`.

[59] Pavel Kokhanchik, Dmitry Solnyshkov, and Guillaume Malpuech. Non-Hermitian skin effect induced by Rashba-Dresselhaus spin-orbit coupling. *Phys. Rev. B*, 108:L041403, Jul 2023. doi: 10.1103/PhysRevB.108.L041403. URL `https://link.aps.org/doi/10.1103/PhysRevB.108.L041403`.

[60] C Yuce and H Ramezani. non-Hermitian skin effect in two dimensional continuous systems. *Physica Scripta*, 98(1):015005, dec 2022. doi: 10.1088/1402-4896/aca43b. URL `https://dx.doi.org/10.1088/1402-4896/aca43b`.

[61] Y.-M. Robin Hu, Elena A. Ostrovskaya, and Eliezer Estrecho. Generalized quantum geometric tensor in a non-Hermitian exciton-polariton system [invited]. *Opt. Mater. Express*, 14(3):664–686, Mar 2024. doi: 10.1364/OME.497010. URL `https://opg.optica.org/ome/abstract.cfm?URI=ome-14-3-664`.

[62] Xiujuan Zhang, Yuan Tian, Jian-Hua Jiang, Ming-Hui Lu, and Yan-Feng Chen. Observation of higher-order non-Hermitian skin effect. *Nature Communications*, 12(1):5377, Sep 2021. ISSN 2041-1723. doi: 10.1038/s41467-021-25716-y. URL `https://doi.org/10.1038/s41467-021-25716-y`.

[63] Stefano Longhi. Incoherent non-Hermitian skin effect in photonic quantum walks. *Light: Science & Applications*, 13(1):95, Apr 2024. ISSN 2047-7538. doi: 10.1038/s41377-024-01438-w. URL `https://doi.org/10.1038/s41377-024-01438-w`.

[64] Z. R. Yan, Y. W. Xing, and X. F. Han. Magnonic skin effect and magnon valve effect in an antiferromagnetically coupled heterojunction. *Phys. Rev. B*, 104:L020413, Jul 2021. doi: 10.1103/PhysRevB.104.L020413. URL `https://link.aps.org/doi/10.1103/PhysRevB.104.L020413`.

[65] Subhaskar Mandal, Rimi Banerjee, and Timothy C. H. Liew. From the topological spin-Hall effect to the non-Hermitian skin effect in an elliptical micropillar chain. *ACS Photonics*, 9(2):527–539, Feb 2022. doi: 10.1021/acsphotonics.1c01425. URL `https://doi.org/10.1021/acsphotonics.1c01425`.

[66] Huawen Xu, Kevin Dini, Xingran Xu, Rimi Banerjee, Subhaskar Mandal, and Timothy C. H. Liew. Nonreciprocal exciton-polariton ring lattices. *Phys. Rev. B*, 104:195301, Nov 2021. doi: 10.1103/PhysRevB.104.195301. URL `https://link.aps.org/doi/10.1103/PhysRevB.104.195301`.

[67] Xingran Xu, Ruiqi Bao, and Timothy C. H. Liew. Non-Hermitian topological exciton-polariton corner modes. *Phys. Rev. B*, 106:L201302, Nov 2022. doi: 10.1103/PhysRevB.106.L201302. URL `https://link.aps.org/doi/10.1103/PhysRevB.106.L201302`.

[68] Selma Franca, Viktor Könye, Fabian Hassler, Jeroen van den Brink, and Cosma Fulga. Non-Hermitian physics without gain or loss: The skin effect of reflected waves. *Phys. Rev. Lett.*, 129:086601, Aug 2022. doi: 10.1103/PhysRevLett.129.086601. URL `https://link.aps.org/doi/10.1103/PhysRevLett.129.086601`.

[69] Colin Scheibner, William T. M. Irvine, and Vincenzo Vitelli. Non-Hermitian band topology and skin modes in active elastic media. *Phys. Rev. Lett.*, 125:118001, Sep 2020. doi: 10.1103/PhysRevLett.125.118001. URL `https://link.aps.org/doi/10.1103/PhysRevLett.125.118001`.

[70] Aoxi Wang and Chang Qing Chen. Continuum skin effect in orthotropic elasticity. *Phys. Rev. B*, 110:104105, Sep 2024. doi: 10.1103/PhysRevB.110.104105. URL `https://link.aps.org/doi/10.1103/PhysRevB.110.104105`.

[71] Tobias Hofmann, Tobias Helbig, Frank Schindler, Nora Salgo, Marta Brzezińska, Martin Greiter, Tobias Kiessling, David Wolf, Achim Vollhardt, Anton Kabaši, Ching Hua Lee, Ante Bilušić, Ronny Thomale, and Titus Neupert. Reciprocal skin effect and its realization in a topolectrical circuit. *Phys. Rev. Res.*, 2:023265, Jun 2020. doi: 10.1103/PhysRevResearch.2.023265. URL `https://link.aps.org/doi/10.1103/PhysRevResearch.2.023265`.

[72] Sebastian Weidemann, Mark Kremer, Tobias Helbig, Tobias Hofmann, Alexander Stegmaier, Martin Greiter, Ronny Thomale, and Alexander Szameit. Topological funneling of light. *Science*, 368(6488):311–314, 2020. doi: 10.1126/science.aaz8727. URL `https://www.science.org/doi/abs/10.1126/science.aaz8727`.

[73] Sheng Zhang and Zhi Hong Hang. Photonic realization of non-Hermitian skin effect using topological ring cavities. *Reviews in Physics*, 13:100102, 2025. ISSN 2405-4283. doi: https://doi.org/10.1016/j.revip.2025.100102. URL `https://www.sciencedirect.com/science/article/pii/S2405428325000024`.

[74] Qiuyan Zhou, Jien Wu, Zhenhang Pu, Jiuyang Lu, Xueqin Huang, Weiyin Deng, Manzhu Ke, and Zhengyou Liu. Observation of geometry-dependent skin effect in non-Hermitian phononic crystals with exceptional points. *Nature Communications*, 14(1):4569, Jul 2023. ISSN 2041-1723. doi: 10.1038/s41467-023-40236-7. URL `https://doi.org/10.1038/s41467-023-40236-7`.

[75] Ananya Ghatak, Martin Brandenbourger, Jasper van Wezel, and Corentin Coulais. Observation of non-Hermitian topology and its bulk–edge correspondence in an active mechanical metamaterial. *Proceedings of the National Academy of Sciences*, 117(47):29561–29568, 2020. doi: 10.1073/pnas.2010580117. URL `https://www.pnas.org/doi/abs/10.1073/pnas.2010580117`.

[76] Linhu Li, Ching Hua Lee, Sen Mu, and Jiangbin Gong. Critical non-Hermitian skin effect. *Nature Communications*, 11(1):5491, Oct 2020. ISSN 2041-1723. doi: 10.1038/s41467-020-18917-4. URL `https://doi.org/10.1038/s41467-020-18917-4`.

[77] Alexander McDonald and Aashish A. Clerk. Exponentially-enhanced quantum sensing with non-Hermitian lattice dynamics. *Nature Communications*, 11(1): 5382, Oct 2020. ISSN 2041-1723. doi: 10.1038/s41467-020-19090-4. URL `https://doi.org/10.1038/s41467-020-19090-4`.

[78] Wen-Tan Xue, Yu-Min Hu, Fei Song, and Zhong Wang. Non-Hermitian edge burst. *Phys. Rev. Lett.*, 128:120401, Mar 2022. doi: 10.1103/PhysRevLett.128.120401. URL `https://link.aps.org/doi/10.1103/PhysRevLett.128.120401`.

[79] Xiujuan Zhang, Tian Zhang, Ming-Hui Lu, and Yan-Feng Chen. A review on non-hermitian skin effect. *Advances in Physics: X*, 7(1):2109431, 2022. doi: 10.1080/23746149.2022.2109431. URL `https://doi.org/10.1080/23746149.2022.2109431`.

[80] Arthur P. Ramirez and Brian Skinner. Dawn of the topological age? *Physics Today*, 73(9):30–36, 09 2020. ISSN 0031-9228. doi: 10.1063/PT.3.4567. URL `https://doi.org/10.1063/PT.3.4567`.

[81] K. v. Klitzing, G. Dorda, and M. Pepper. New method for high-accuracy determination of the fine-structure constant based on quantized Hall resistance. *Phys. Rev. Lett.*, 45:494–497, Aug 1980. doi: 10.1103/PhysRevLett.45.494. URL `https://link.aps.org/doi/10.1103/PhysRevLett.45.494`.

[82] D. C. Tsui, H. L. Stormer, and A. C. Gossard. Two-dimensional magnetotransport in the extreme quantum limit. *Phys. Rev. Lett.*, 48:1559–1562, May 1982. doi: 10.1103/PhysRevLett.48.1559. URL `https://link.aps.org/doi/10.1103/PhysRevLett.48.1559`.

[83] Tomoki Ozawa, Hannah M. Price, Alberto Amo, Nathan Goldman, Mohammad Hafezi, Ling Lu, Mikael C. Rechtsman, David Schuster, Jonathan Simon, Oded Zilberberg, and Iacopo Carusotto. Topological photonics. *Rev. Mod. Phys.*, 91: 015006, Mar 2019. doi: 10.1103/RevModPhys.91.015006. URL `https://link.aps.org/doi/10.1103/RevModPhys.91.015006`.

[84] Muhammad Nadeem, Alex R. Hamilton, Michael S. Fuhrer, and Xiaolin Wang. Quantum anomalous Hall effect in magnetic doped topological insulators and ferromagnetic spin-gapless semiconductors—a perspective review. *Small*, 16(42): 1904322, 2020. doi: https://doi.org/10.1002/smll.201904322. URL `https://onlinelibrary.wiley.com/doi/abs/10.1002/smll.201904322`.

[85] Di Xiao, Ming-Che Chang, and Qian Niu. Berry phase effects on electronic properties. *Rev. Mod. Phys.*, 82:1959–2007, Jul 2010. doi: 10.1103/RevModPhys.82.1959. URL `https://link.aps.org/doi/10.1103/RevModPhys.82.1959`.

[86] E. H. Hall. On a new action of the magnet on electric currents. *American Journal of Mathematics*, 2(3):287–292, 1879. ISSN 00029327, 10806377. URL `http://www.jstor.org/stable/2369245`.

[87] Naoto Nagaosa, Jairo Sinova, Shigeki Onoda, A. H. MacDonald, and N. P. Ong. Anomalous hall effect. *Rev. Mod. Phys.*, 82:1539–1592, May 2010. doi: 10.1103/RevModPhys.82.1539. URL `https://link.aps.org/doi/10.1103/RevModPhys.82.1539`.

[88] R. B. Laughlin. Quantized Hall conductivity in two dimensions. *Phys. Rev. B*, 23: 5632–5633, May 1981. doi: 10.1103/PhysRevB.23.5632. URL `https://link.aps.org/doi/10.1103/PhysRevB.23.5632`.

[89] Joseph E. Avron, Daniel Osadchy, and Ruedi Seiler. A topological look at the quantum hall effect. *Physics Today*, 56(8):38–42, 08 2003. ISSN 0031-9228. doi: 10.1063/1.1611351. URL `https://doi.org/10.1063/1.1611351`.

[90] D. J. Thouless, M. Kohmoto, M. P. Nightingale, and M. den Nijs. Quantized Hall conductance in a two-dimensional periodic potential. *Phys. Rev. Lett.*, 49:405–408, Aug 1982. doi: 10.1103/PhysRevLett.49.405. URL `https://link.aps.org/doi/10.1103/PhysRevLett.49.405`.

[91] Barry Simon. Holonomy, the quantum adiabatic theorem, and Berry's phase. *Phys. Rev. Lett.*, 51:2167–2170, Dec 1983. doi: 10.1103/PhysRevLett.51.2167. URL `https://link.aps.org/doi/10.1103/PhysRevLett.51.2167`.

[92] J. E. Avron, R. Seiler, and B. Simon. Homotopy and quantization in condensed matter physics. *Phys. Rev. Lett.*, 51:51–53, Jul 1983. doi: 10.1103/PhysRevLett.51.51. URL `https://link.aps.org/doi/10.1103/PhysRevLett.51.51`.

[93] Qian Niu, D. J. Thouless, and Yong-Shi Wu. Quantized Hall conductance as a topological invariant. *Phys. Rev. B*, 31:3372–3377, Mar 1985. doi: 10.1103/PhysRevB.31.3372. URL `https://link.aps.org/doi/10.1103/PhysRevB.31.3372`.

[94] Michael Victor Berry. Quantal phase factors accompanying adiabatic changes. *Proc. R. Soc. Lond. A*, 392:45–57, March 1984. doi: 10.1098/rspa.1984.0023. URL `http://doi.org/10.1098/rspa.1984.0023`.

[95] Ming-Che Chang and Qian Niu. Berry phase, hyperorbits, and the Hofstadter spectrum: Semiclassical dynamics in magnetic Bloch bands. *Phys. Rev. B*, 53:7010–7023, Mar 1996. doi: 10.1103/PhysRevB.53.7010. URL `https://link.aps.org/doi/10.1103/PhysRevB.53.7010`.

[96] E.H. Hall. Xviii. on the "rotational coefficient" in nickel and cobalt. *The London, Edinburgh, and Dublin Philosophical Magazine and Journal of Science*, 12(74):157–172, 1881. doi: 10.1080/14786448108627086. URL `https://doi.org/10.1080/14786448108627086`.

[97] Robert Karplus and J. M. Luttinger. Hall effect in ferromagnetics. *Phys. Rev.*, 95:1154–1160, Sep 1954. doi: 10.1103/PhysRev.95.1154. URL `https://link.aps.org/doi/10.1103/PhysRev.95.1154`.

[98] Felix Bloch. Über die quantenmechanik der elektronen in kristallgittern. *Zeitschrift für Physik*, 52(7):555–600, Jul 1929. ISSN 0044-3328. doi: 10.1007/BF01339455. URL `https://doi.org/10.1007/BF01339455`.

[99] Ming-Che Chang and Qian Niu. Berry phase, hyperorbits, and the Hofstadter spectrum. *Phys. Rev. Lett.*, 75:1348–1351, Aug 1995. doi: 10.1103/PhysRevLett.75.1348. URL `https://link.aps.org/doi/10.1103/PhysRevLett.75.1348`.

[100] Ganesh Sundaram and Qian Niu. Wave-packet dynamics in slowly perturbed crystals: Gradient corrections and Berry-phase effects. *Phys. Rev. B*, 59:14915–14925, Jun 1999. doi: 10.1103/PhysRevB.59.14915. URL `https://link.aps.org/doi/10.1103/PhysRevB.59.14915`.

[101] Dimitrie Culcer, Yugui Yao, and Qian Niu. Coherent wave-packet evolution in coupled bands. *Phys. Rev. B*, 72:085110, Aug 2005. doi: 10.1103/PhysRevB.72.085110. URL `https://link.aps.org/doi/10.1103/PhysRevB.72.085110`.

[102] Ming-Che Chang and Qian Niu. Berry curvature, orbital moment, and effective quantum theory of electrons in electromagnetic fields. *Journal of Physics: Condensed Matter*, 20(19):193202, apr 2008. doi: 10.1088/0953-8984/20/19/193202. URL `https://doi.org/10.1088/0953-8984/20/19/193202`.

[103] R. Jackiw and C. Rebbi. Solitons with fermion number ½. *Phys. Rev. D*, 13:3398–3409, Jun 1976. doi: 10.1103/PhysRevD.13.3398. URL `https://link.aps.org/doi/10.1103/PhysRevD.13.3398`.

[104] W. P. Su, J. R. Schrieffer, and A. J. Heeger. Solitons in polyacetylene. *Phys. Rev. Lett.*, 42:1698–1701, Jun 1979. doi: 10.1103/PhysRevLett.42.1698. URL `https://link.aps.org/doi/10.1103/PhysRevLett.42.1698`.

[105] B. I. Halperin. Quantized Hall conductance, current-carrying edge states, and the existence of extended states in a two-dimensional disordered potential. *Phys. Rev. B*, 25:2185–2190, Feb 1982. doi: 10.1103/PhysRevB.25.2185. URL `https://link.aps.org/doi/10.1103/PhysRevB.25.2185`.

[106] A. H. MacDonald and P. Středa. Quantized Hall effect and edge currents. *Phys. Rev. B*, 29:1616–1619, Feb 1984. doi: 10.1103/PhysRevB.29.1616. URL `https://link.aps.org/doi/10.1103/PhysRevB.29.1616`.

[107] Yasuhiro Hatsugai. Chern number and edge states in the integer quantum Hall effect. *Phys. Rev. Lett.*, 71:3697–3700, Nov 1993. doi: 10.1103/PhysRevLett.71.3697. URL `https://link.aps.org/doi/10.1103/PhysRevLett.71.3697`.

[108] F. D. M. Haldane. Model for a quantum Hall effect without Landau levels: Condensed-matter realization of the "parity anomaly". *Phys. Rev. Lett.*, 61:2015–2018, Oct 1988. doi: 10.1103/PhysRevLett.61.2015. URL `https://link.aps.org/doi/10.1103/PhysRevLett.61.2015`.

[109] Masaru Onoda and Naoto Nagaosa. Quantized anomalous Hall effect in two-dimensional ferromagnets: Quantum Hall effect in metals. *Phys. Rev. Lett.*, 90:206601, May 2003. doi: 10.1103/PhysRevLett.90.206601. URL `https://link.aps.org/doi/10.1103/PhysRevLett.90.206601`.

[110] C. L. Kane and E. J. Mele. Quantum spin Hall effect in graphene. *Phys. Rev. Lett.*, 95:226801, Nov 2005. doi: 10.1103/PhysRevLett.95.226801. URL `https://link.aps.org/doi/10.1103/PhysRevLett.95.226801`.

[111] C. L. Kane and E. J. Mele. Z_2 topological order and the quantum spin hall effect. *Phys. Rev. Lett.*, 95:146802, Sep 2005. doi: 10.1103/PhysRevLett.95.146802. URL `https://link.aps.org/doi/10.1103/PhysRevLett.95.146802`.

[112] D. P. DiVincenzo and E. J. Mele. Self-consistent effective-mass theory for intralayer screening in graphite intercalation compounds. *Phys. Rev. B*, 29:1685–1694, Feb 1984. doi: 10.1103/PhysRevB.29.1685. URL `https://link.aps.org/doi/10.1103/PhysRevB.29.1685`.

[113] Gordon W. Semenoff. Condensed-matter simulation of a three-dimensional anomaly. *Phys. Rev. Lett.*, 53:2449–2452, Dec 1984. doi: 10.1103/PhysRevLett.53.2449. URL `https://link.aps.org/doi/10.1103/PhysRevLett.53.2449`.

[114] Ningning Hao, Ping Zhang, Zhigang Wang, Wei Zhang, and Yupeng Wang. Topological edge states and quantum Hall effect in the Haldane model. *Phys. Rev. B*, 78:075438, Aug 2008. doi: 10.1103/PhysRevB.78.075438. URL `https://link.aps.org/doi/10.1103/PhysRevB.78.075438`.

[115] K. S. Novoselov, A. K. Geim, S. V. Morozov, D. Jiang, Y. Zhang, S. V. Dubonos, I. V. Grigorieva, and A. A. Firsov. Electric field effect in atomically thin carbon films. *Science*, 306(5696):666–669, 2004. doi: 10.1126/science.1102896. URL `https://www.science.org/doi/abs/10.1126/science.1102896`.

[116] K. S. Novoselov, A. K. Geim, S. V. Morozov, D. Jiang, M. I. Katsnelson, I. V. Grigorieva, S. V. Dubonos, and A. A. Firsov. Two-dimensional gas of massless Dirac fermions in graphene. *Nature*, 438(7065):197–200, 2005. doi: 10.1038/nature04233. URL `https://doi.org/10.1038/nature04233`.

[117] Yuanbo Zhang, Yan-Wen Tan, Horst L. Stormer, and Philip Kim. Experimental observation of the quantum hall effect and berry's phase in graphene. *Nature*, 438(7065):201–204, Nov 2005. ISSN 1476-4687. doi: 10.1038/nature04235. URL `https://doi.org/10.1038/nature04235`.

[118] N. P. Armitage, E. J. Mele, and Ashvin Vishwanath. Weyl and Dirac semimetals in three-dimensional solids. *Rev. Mod. Phys.*, 90:015001, Jan 2018. doi: 10.1103/RevModPhys.90.015001. URL `https://link.aps.org/doi/10.1103/RevModPhys.90.015001`.

[119] A. H. Castro Neto, F. Guinea, N. M. R. Peres, K. S. Novoselov, and A. K. Geim. The electronic properties of graphene. *Rev. Mod. Phys.*, 81:109–162, Jan 2009. doi: 10.1103/RevModPhys.81.109. URL `https://link.aps.org/doi/10.1103/RevModPhys.81.109`.

[120] A. K. Geim and K. S. Novoselov. The rise of graphene. *Nature Materials*, 6 (3):183–191, Mar 2007. ISSN 1476-4660. doi: 10.1038/nmat1849. URL `https://doi.org/10.1038/nmat1849`.

[121] Cui-Zu Chang, Chao-Xing Liu, and Allan H. MacDonald. Colloquium: Quantum anomalous Hall effect. *Rev. Mod. Phys.*, 95:011002, Jan 2023. doi: 10.1103/RevModPhys.95.011002. URL `https://link.aps.org/doi/10.1103/RevModPhys.95.011002`.

[122] Paul Adrien Maurice Dirac. The quantum theory of the electron. *Proc. R. Soc. Lond. A*, 117:610–624, 1928. URL `https://cir.nii.ac.jp/crid/1130000796869683968`.

[123] William. R. Hamilton. Third supplement to an essay on systems of rays. *Transactions of the Royal Irish Academy*, 17:1–144, 1837.

[124] Humphrey Lloyd. On the phenomena presented by light in its passage along the axes of biaxial crystals. *Transactions of the Royal Irish Academy*, 17:145–158, 1837.

[125] Hongming Weng, Rui Yu, Xiao Hu, Xi Dai, and Zhong Fang. Quantum anomalous Hall effect and related topological electronic states. *Advances in Physics*, 64(3): 227–282, 2015. doi: 10.1080/00018732.2015.1068524. URL `https://doi.org/10.1080/00018732.2015.1068524`.

[126] Yu A Bychkov and E I Rashba. Oscillatory effects and the magnetic susceptibility of carriers in inversion layers. *Journal of Physics C: Solid State Physics*, 17(33): 6039, nov 1984. doi: 10.1088/0022-3719/17/33/015. URL `https://dx.doi.org/10.1088/0022-3719/17/33/015`.

[127] Liang Fu and C. L. Kane. Time reversal polarization and a Z_2 adiabatic spin pump. *Phys. Rev. B*, 74:195312, Nov 2006. doi: 10.1103/PhysRevB.74.195312. URL `https://link.aps.org/doi/10.1103/PhysRevB.74.195312`.

[128] B. Andrei Bernevig, Taylor L. Hughes, and Shou-Cheng Zhang. Quantum spin hall effect and topological phase transition in hgte quantum wells. *Science*, 314(5806): 1757–1761, 2006. doi: 10.1126/science.1133734. URL `https://www.science.org/doi/abs/10.1126/science.1133734`.

[129] D. N. Sheng, Z. Y. Weng, L. Sheng, and F. D. M. Haldane. Quantum spin-hall effect and topologically invariant chern numbers. *Phys. Rev. Lett.*, 97:036808, Jul 2006. doi: 10.1103/PhysRevLett.97.036808. URL `https://link.aps.org/doi/10.1103/PhysRevLett.97.036808`.

[130] Xiao-Liang Qi, Yong-Shi Wu, and Shou-Cheng Zhang. Topological quantization of the spin hall effect in two-dimensional paramagnetic semiconductors. *Phys. Rev. B*, 74:085308, Aug 2006. doi: 10.1103/PhysRevB.74.085308. URL `https://link.aps.org/doi/10.1103/PhysRevB.74.085308`.

[131] T. H. R. Skyrme and Basil Ferdinand Jamieson Schonland. A non-linear field theory. *Proceedings of the Royal Society of London. Series A. Mathematical and Physical Sciences*, 260(1300):127–138, 1961. doi: 10.1098/rspa.1961.0018. URL `https://royalsocietypublishing.org/doi/abs/10.1098/rspa.1961.0018`.

[132] T.H.R. Skyrme. A unified field theory of mesons and baryons. *Nuclear Physics*, 31:556–569, 1962. ISSN 0029-5582. doi: https://doi.org/10.1016/0029-5582(62)90775-7. URL `https://www.sciencedirect.com/science/article/pii/0029558262907757`.

[133] Yijie Shen, Qiang Zhang, Peng Shi, Luping Du, Xiaocong Yuan, and Anatoly V. Zayats. Optical skyrmions and other topological quasiparticles of light. *Nature Photonics*, 18(1):15–25, Jan 2024.

[134] Cheng Guo, Meng Xiao, Yu Guo, Luqi Yuan, and Shanhui Fan. Meron spin textures in momentum space. *Phys. Rev. Lett.*, 124:106103, Mar 2020. doi: 10.1103/PhysRevLett.124.106103. URL `https://link.aps.org/doi/10.1103/PhysRevLett.124.106103`.

[135] Stefano Donati, Lorenzo Dominici, Galbadrakh Dagvadorj, Dario Ballarini, Milena De Giorgi, Alberto Bramati, Giuseppe Gigli, Yuri G. Rubo, Marzena Hanna Szymańska, and Daniele Sanvitto. Twist of generalized skyrmions and spin vortices in a polariton superfluid. *Proceedings of the National Academy of Sciences*, 113(52):14926–14931, 2016. doi: 10.1073/pnas.1610123114. URL `https://www.pnas.org/doi/abs/10.1073/pnas.1610123114`.

[136] Börge Göbel, Ingrid Mertig, and Oleg A. Tretiakov. Beyond skyrmions: Review and perspectives of alternative magnetic quasiparticles. *Physics Reports*, 895:1–28, 2021. ISSN 0370-1573. doi: https://doi.org/10.1016/j.physrep.2020.10.001. URL `https://www.sciencedirect.com/science/article/pii/S0370157320303525`. Beyond skyrmions: Review and perspectives of alternative magnetic quasiparticles.

[137] K. Everschor-Sitte, J. Masell, R. M. Reeve, and M. Kläui. Perspective: Magnetic skyrmions—overview of recent progress in an active research field. *Journal of Applied Physics*, 124(24):240901, 2018. doi: 10.1063/1.5048972. URL `https://doi.org/10.1063/1.5048972`.

[138] Alexey A. Kovalev and Shane Sandhoefner. Skyrmions and antiskyrmions in quasi-two-dimensional magnets. *Frontiers in Physics*, 6, 2018. ISSN 2296-424X. doi: 10.3389/fphy.2018.00098. URL `https://www.frontiersin.org/articles/10.3389/fphy.2018.00098`.

[139] Naoto Nagaosa and Yoshinori Tokura. Topological properties and dynamics of magnetic skyrmions. *Nature Nanotechnology*, 8(12):899–911, 2013. doi: 10.1038/nnano.2013.243. URL `https://doi.org/10.1038/nnano.2013.243`.

[140] Kristian Arjas, Jani Matti Taskinen, Rebecca Heilmann, Grazia Salerno, and Päivi Törmä. High topological charge lasing in quasicrystals. *Nature Communications*, 15(1):9544, Nov 2024. ISSN 2041-1723. doi: 10.1038/s41467-024-53952-5. URL `https://doi.org/10.1038/s41467-024-53952-5`.

[141] Fengshan Zheng, Hang Li, Shasha Wang, Dongsheng Song, Chiming Jin, Wenshen Wei, András Kovács, Jiadong Zang, Mingliang Tian, Yuheng Zhang, Haifeng Du, and Rafal E. Dunin-Borkowski. Direct imaging of a zero-field target skyrmion and its polarity switch in a chiral magnetic nanodisk. *Phys. Rev. Lett.*, 119:197205, Nov 2017. doi: 10.1103/PhysRevLett.119.197205. URL `https://link.aps.org/doi/10.1103/PhysRevLett.119.197205`.

[142] Bo Zhen, Chia Wei Hsu, Ling Lu, A. Douglas Stone, and Marin Soljačić. Topological nature of optical bound states in the continuum. *Phys. Rev. Lett.*, 113:257401, Dec 2014. doi: 10.1103/PhysRevLett.113.257401. URL `https://link.aps.org/doi/10.1103/PhysRevLett.113.257401`.

[143] Hugo M. Doeleman, Francesco Monticone, Wouter den Hollander, Andrea Alù, and A. Femius Koenderink. Experimental observation of a polarization vortex at an optical bound state in the continuum. *Nature Photonics*, 12(7):397–401, Jul 2018. ISSN 1749-4893. doi: 10.1038/s41566-018-0177-5. URL `https://doi.org/10.1038/s41566-018-0177-5`.

[144] Alexei N Bogdanov and DA Yablonskii. Thermodynamically stable "vortices" in magnetically ordered crystals. the mixed state of magnets. *Zh. Eksp. Teor. Fiz*, 95 (1):178, 1989.

[145] A. Bogdanov and A. Hubert. Thermodynamically stable magnetic vortex states in magnetic crystals. *Journal of Magnetism and Magnetic Materials*, 138(3):255–269, 1994. ISSN 0304-8853. doi: https://doi.org/10.1016/0304-8853(94)90046-9. URL `https://www.sciencedirect.com/science/article/pii/0304885394900469`.

[146] U. K. Rößler, A. N. Bogdanov, and C. Pfleiderer. Spontaneous skyrmion ground states in magnetic metals. *Nature*, 442(7104):797–801, Aug 2006. ISSN 1476-4687. doi: 10.1038/nature05056. URL `https://doi.org/10.1038/nature05056`.

[147] B. Binz, A. Vishwanath, and V. Aji. Theory of the helical spin crystal: A candidate for the partially ordered state of mnsi. *Phys. Rev. Lett.*, 96:207202, May 2006. doi: 10.1103/PhysRevLett.96.207202. URL `https://link.aps.org/doi/10.1103/PhysRevLett.96.207202`.

[148] Sumanta Tewari, D. Belitz, and T. R. Kirkpatrick. Blue quantum fog: Chiral condensation in quantum helimagnets. *Phys. Rev. Lett.*, 96:047207, Feb 2006. doi: 10.1103/PhysRevLett.96.047207. URL `https://link.aps.org/doi/10.1103/PhysRevLett.96.047207`.

[149] Riccardo Hertel and Claus M. Schneider. Exchange explosions: Magnetization dynamics during vortex-antivortex annihilation. *Phys. Rev. Lett.*, 97:177202, Oct 2006. doi: 10.1103/PhysRevLett.97.177202. URL `https://link.aps.org/doi/10.1103/PhysRevLett.97.177202`.

[150] O. A. Tretiakov and O. Tchernyshyov. Vortices in thin ferromagnetic films and the skyrmion number. *Phys. Rev. B*, 75:012408, Jan 2007. doi: 10.1103/PhysRevB.75.012408. URL `https://link.aps.org/doi/10.1103/PhysRevB.75.012408`.

[151] S. Mühlbauer, B. Binz, F. Jonietz, C. Pfleiderer, A. Rosch, A. Neubauer, R. Georgii, and P. Böni. Skyrmion lattice in a chiral magnet. *Science*, 323(5916):915–919, 2009. doi: 10.1126/science.1166767. URL `https://www.science.org/doi/abs/10.1126/science.1166767`.

[152] David C. Wright and N. David Mermin. Crystalline liquids: the blue phases. *Rev. Mod. Phys.*, 61:385–432, Apr 1989. doi: 10.1103/RevModPhys.61.385. URL `https://link.aps.org/doi/10.1103/RevModPhys.61.385`.

[153] I S Aranson. Topological defects in active liquid crystals. *Physics-Uspekhi*, 62(9): 892, sep 2019. doi: 10.3367/UFNe.2018.10.038433. URL `https://dx.doi.org/10.3367/UFNe.2018.10.038433`.

[154] Jun-Ichi Fukuda and Slobodan Žumer. Quasi-two-dimensional skyrmion lattices in a chiral nematic liquid crystal. *Nature Communications*, 2(1), 2011. doi: 10.1038/ncomms1250. URL `https://www.scopus.com/inward/record.uri?eid=2-s2.0-79953120349&doi=10.1038%2fncomms1250&partnerID=40&md5=0bcaa13fed7ea07b7d310e13b0e0fc41`. Cited by: 207; All Open Access, Bronze Open Access.

[155] Sébastien Fumeron, Bertrand Berche, and Fernando Moraes and. Geometric theory of topological defects: methodological developments and new trends. *Liquid Crystals Reviews*, 9(2):85–110, 2021. doi: 10.1080/21680396.2022.2163515. URL `https://doi.org/10.1080/21680396.2022.2163515`.

[156] SÃ©bastien Fumeron and Bertrand Berche. Introduction to topological defects: from liquid crystals to particle physics. *The European Physical Journal Special Topics*, 232(11):1813–1833, Sep 2023. ISSN 1951-6401. doi: 10.1140/epjs/s11734-023-00803-x. URL `https://doi.org/10.1140/epjs/s11734-023-00803-x`.

[157] Min-Jun Gim, Daniel A. Beller, and Dong Ki Yoon. Morphogenesis of liquid crystal topological defects during the nematic-smectic a phase transition. *Nature Communications*, 8(1):15453, May 2017. ISSN 2041-1723. doi: 10.1038/ncomms15453. URL `https://doi.org/10.1038/ncomms15453`.

[158] S. Tsesses, E. Ostrovsky, K. Cohen, B. Gjonaj, N. H. Lindner, and G. Bartal. Optical skyrmion lattice in evanescent electromagnetic fields. *Science*, 361(6406): 993–996, 2018. doi: 10.1126/science.aau0227. URL `https://www.science.org/doi/abs/10.1126/science.aau0227`.

[159] Shai Tsesses, Kobi Cohen, Evgeny Ostrovsky, Bergin Gjonaj, and Guy Bartal. Spin–orbit interaction of light in plasmonic lattices. *Nano Letters*, 19(6):4010–4016, Jun 2019. ISSN 1530-6984. doi: 10.1021/acs.nanolett.9b01343. URL `https://doi.org/10.1021/acs.nanolett.9b01343`.

[160] Luping Du, Aiping Yang, Anatoly V. Zayats, and Xiaocong Yuan. Deep-subwavelength features of photonic skyrmions in a confined electromagnetic field with orbital angular momentum. *Nature Physics*, 15(7):650–654, Jul 2019. ISSN 1745-2481. doi: 10.1038/s41567-019-0487-7. URL `https://doi.org/10.1038/s41567-019-0487-7`.

[161] Timothy J. Davis, David Janoschka, Pascal Dreher, Bettina Frank, Frank-J. Meyer zu Heringdorf, and Harald Giessen. Ultrafast vector imaging of plasmonic skyrmion dynamics with deep subwavelength resolution. *Science*, 368(6489):eaba6415, 2020. doi: 10.1126/science.aba6415. URL `https://www.science.org/doi/abs/10.1126/science.aba6415`.

[162] Chunyan Bai, Jian Chen, Yuxing Zhang, Dawei Zhang, and Qiwen Zhan. Dynamic tailoring of an optical skyrmion lattice in surface plasmon polaritons. *Opt. Express*, 28(7):10320–10328, Mar 2020. doi: 10.1364/OE.384718. URL `https://opg.optica.org/oe/abstract.cfm?URI=oe-28-7-10320`.

[163] X.-G. Wang, L. Chotorlishvili, N. Arnold, V. K. Dugaev, I. Maznichenko, J. Barnaś, P. A. Buczek, S. S. P. Parkin, and A. Ernst. Plasmonic skyrmion lattice based on the magnetoelectric effect. *Phys. Rev. Lett.*, 125:227201, Nov 2020. doi: 10.1103/PhysRevLett.125.227201. URL `https://link.aps.org/doi/10.1103/PhysRevLett.125.227201`.

[164] P. Cilibrizzi, H. Sigurdsson, T. C. H. Liew, H. Ohadi, A. Askitopoulos, S. Brodbeck, C. Schneider, I. A. Shelykh, S. Höfling, J. Ruostekoski, and P. Lagoudakis. Half-skyrmion spin textures in polariton microcavities. *Phys. Rev. B*, 94:045315, Jul 2016. doi: 10.1103/PhysRevB.94.045315. URL `https://link.aps.org/doi/10.1103/PhysRevB.94.045315`.

[165] H. Flayac, D. D. Solnyshkov, I. A. Shelykh, and G. Malpuech. Transmutation of skyrmions to half-solitons driven by the nonlinear optical spin Hall effect. *Phys. Rev. Lett.*, 110:016404, Jan 2013. doi: 10.1103/PhysRevLett.110.016404. URL `https://link.aps.org/doi/10.1103/PhysRevLett.110.016404`.

[166] D. V. Vishnevsky, H. Flayac, A. V. Nalitov, D. D. Solnyshkov, N. A. Gippius, and G. Malpuech. Skyrmion formation and optical spin-Hall effect in an expanding coherent cloud of indirect excitons. *Phys. Rev. Lett.*, 110:246404, Jun 2013. doi: 10.1103/PhysRevLett.110.246404. URL `https://link.aps.org/doi/10.1103/PhysRevLett.110.246404`.

[167] Mateusz Król, Helgi Sigurdsson, Katarzyna Rechcińska, Przemysław Oliwa, Krzystof Tyszka, Witold Bardyszewski, Andrzej Opala, Michał Matuszewski, Przemysław Morawiak, Rafał Mazur, Wiktor Piecek, Przemysław Kula, Pavlos G. Lagoudakis, Barbara Piętka, and Jacek Szczytko. Observation of second-order meron polarization textures in optical microcavities. *Optica*, 8(2):255–261, Feb 2021. doi: 10.1364/OPTICA.414891. URL `http://opg.optica.org/optica/abstract.cfm?URI=optica-8-2-255`.

[168] N. D. Mermin. The topological theory of defects in ordered media. *Rev. Mod. Phys.*, 51:591–648, Jul 1979. doi: 10.1103/RevModPhys.51.591. URL `https://link.aps.org/doi/10.1103/RevModPhys.51.591`.

[169] I. Dzyaloshinsky. A thermodynamic theory of "weak" ferromagnetism of antiferromagnetics. *Journal of Physics and Chemistry of Solids*, 4(4):241–255, 1958. ISSN 0022-3697. doi: https://doi.org/10.1016/0022-3697(58)90076-3. URL `https://www.sciencedirect.com/science/article/pii/0022369758900763`.

[170] Tôru Moriya. Anisotropic superexchange interaction and weak ferromagnetism. *Physical Review*, 120(1):91 – 98, 1960. doi: 10.1103/PhysRev.120.91. URL `https://www.scopus.com/inward/record.uri?eid=2-s2.0-34547566936&doi=10.1103%2fPhysRev.120.91&partnerID=40&md5=4c6f1029ba2671d9f8c3bc1c69efff4e`. Cited by: 6055.

[171] Xichao Zhang, Jing Xia, Yan Zhou, Daowei Wang, Xiaoxi Liu, Weisheng Zhao, and Motohiko Ezawa. Control and manipulation of a magnetic skyrmionium in nanostructures. *Phys. Rev. B*, 94:094420, Sep 2016. doi: 10.1103/PhysRevB.94.094420. URL `https://link.aps.org/doi/10.1103/PhysRevB.94.094420`.

[172] Börge Göbel, Jürgen Henk, and Ingrid Mertig. Forming individual magnetic biskyrmions by merging two skyrmions in a centrosymmetric nanodisk. *Scientific Reports*, 9(1):9521, Jul 2019. ISSN 2045-2322. doi: 10.1038/s41598-019-45965-8. URL `https://doi.org/10.1038/s41598-019-45965-8`.

[173] Haruya Kokubo, Kenichi Kasamatsu, and Hiromitsu Takeuchi. Pattern formation of quantum Kelvin-Helmholtz instability in binary superfluids. *Phys. Rev. A*, 104:023312, Aug 2021. doi: 10.1103/PhysRevA.104.023312. URL `https://link.aps.org/doi/10.1103/PhysRevA.104.023312`.

[174] SeungJung Huh, Wooyoung Yun, Gabin Yun, Samgyu Hwang, Kiryang Kwon, Junhyeok Hur, Seungho Lee, Hiromitsu Takeuchi, Se Kwon Kim, and Jae-yoon Choi. Stable singular fractional skyrmion spin texture from the quantum Kelvin–Helmholtz instability. *Nature Physics*, Aug 2025. ISSN 1745-2481. doi: 10.1038/s41567-025-02982-x. URL `https://doi.org/10.1038/s41567-025-02982-x`.

[175] Kamal Das, Shibalik Lahiri, Rhonald Burgos Atencia, Dimitrie Culcer, and Amit Agarwal. Intrinsic nonlinear conductivities induced by the quantum metric. *Phys. Rev. B*, 108:L201405, Nov 2023. doi: 10.1103/PhysRevB.108.L201405. URL `https://link.aps.org/doi/10.1103/PhysRevB.108.L201405`.

[176] Naizhou Wang, Daniel Kaplan, Zhaowei Zhang, Tobias Holder, Ning Cao, Aifeng Wang, Xiaoyuan Zhou, Feifei Zhou, Zhengzhi Jiang, Chusheng Zhang, Shihao Ru, Hongbing Cai, Kenji Watanabe, Takashi Taniguchi, Binghai Yan, and Weibo Gao. Quantum-metric-induced nonlinear transport in a topological antiferromagnet. *Nature*, 621(7979):487–492, Sep 2023. ISSN 1476-4687. doi: 10.1038/s41586-023-06363-3. URL `https://doi.org/10.1038/s41586-023-06363-3`.

[177] Pankaj Bhalla, Kamal Das, Dimitrie Culcer, and Amit Agarwal. Resonant second-harmonic generation as a probe of quantum geometry. *Phys. Rev. Lett.*, 129:227401, Nov 2022. doi: 10.1103/PhysRevLett.129.227401. URL `https://link.aps.org/doi/10.1103/PhysRevLett.129.227401`.

[178] Yang Gao, Shengyuan A. Yang, and Qian Niu. Field induced positional shift of Bloch electrons and its dynamical implications. *Phys. Rev. Lett.*, 112:166601, Apr 2014. doi: 10.1103/PhysRevLett.112.166601. URL `https://link.aps.org/doi/10.1103/PhysRevLett.112.166601`.

[179] Yang Gao, Shengyuan A. Yang, and Qian Niu. Geometrical effects in orbital magnetic susceptibility. *Phys. Rev. B*, 91:214405, Jun 2015. doi: 10.1103/PhysRevB.91.214405. URL `https://link.aps.org/doi/10.1103/PhysRevB.91.214405`.

[180] O. Bleu, G. Malpuech, Y. Gao, and D. D. Solnyshkov. Effective theory of nonadiabatic quantum evolution based on the quantum geometric tensor. *Phys. Rev. Lett.*, 121:020401, Jul 2018. doi: 10.1103/PhysRevLett.121.020401. URL `https://link.aps.org/doi/10.1103/PhysRevLett.121.020401`.

[181] Sebastiano Peotta and Päivi Törmä. Superfluidity in topologically nontrivial flat bands. *Nature Communications*, 6(1):8944, Nov 2015. doi: 10.1038/ncomms9944. URL `https://doi.org/10.1038/ncomms9944`.

[182] Haidong Tian, Xueshi Gao, Yuxin Zhang, Shi Che, Tianyi Xu, Patrick Cheung, Kenji Watanabe, Takashi Taniguchi, Mohit Randeria, Fan Zhang, Chun Ning Lau, and Marc W. Bockrath. Evidence for Dirac flat band superconductivity enabled by quantum geometry. *Nature*, 614(7948):440–444, Feb 2023. ISSN 1476-4687. doi: 10.1038/s41586-022-05576-2. URL `https://doi.org/10.1038/s41586-022-05576-2`.

[183] Shuai A. Chen and K. T. Law. Ginzburg-Landau theory of flat-band superconductors with quantum metric. *Phys. Rev. Lett.*, 132:026002, Jan 2024. doi: 10.1103/PhysRevLett.132.026002. URL `https://link.aps.org/doi/10.1103/PhysRevLett.132.026002`.

[184] Richard Jozsa. Fidelity for mixed quantum states. *Journal of Modern Optics*, 41(12):2315–2323, 1994. doi: 10.1080/09500349414552171. URL `https://doi.org/10.1080/09500349414552171`.

[185] SHI-JIAN GU. Fidelity approach to quantum phase transitions. *International Journal of Modern Physics B*, 24(23):4371–4458, 2010. doi: 10.1142/S0217979210056335. URL `https://doi.org/10.1142/S0217979210056335`.

[186] Lei Wang, Ye-Hua Liu, Jakub Imriška, Ping Nang Ma, and Matthias Troyer. Fidelity susceptibility made simple: A unified quantum Monte Carlo approach. *Phys. Rev. X*, 5:031007, Jul 2015. doi: 10.1103/PhysRevX.5.031007. URL `https://link.aps.org/doi/10.1103/PhysRevX.5.031007`.

[187] Bo-Bo Wei and Xiao-Chen Lv. Fidelity susceptibility in the quantum Rabi model. *Phys. Rev. A*, 97:013845, Jan 2018. doi: 10.1103/PhysRevA.97.013845. URL `https://link.aps.org/doi/10.1103/PhysRevA.97.013845`.

[188] Niaz Ali Khan. Fidelity susceptibility probes of dynamical quantum criticality. *Chaos, Solitons & Fractals*, 183:114975, 2024. ISSN 0960-0779. doi: https://doi.org/10.1016/j.chaos.2024.114975. URL `https://www.sciencedirect.com/science/article/pii/S0960077924005277`.

[189] O. Bleu, D. D. Solnyshkov, and G. Malpuech. Measuring the quantum geometric tensor in two-dimensional photonic and exciton-polariton systems. *Phys. Rev. B*, 97:195422, 2018. doi: 10.1103/PhysRevB.97.195422. URL `https://link.aps.org/doi/10.1103/PhysRevB.97.195422`.

[190] Frédéric Piéchon, Arnaud Raoux, Jean-Noël Fuchs, and Gilles Montambaux. Geometric orbital susceptibility: Quantum metric without Berry curvature. *Phys. Rev. B*, 94:134423, Oct 2016. doi: 10.1103/PhysRevB.94.134423. URL `https://link.aps.org/doi/10.1103/PhysRevB.94.134423`.

[191] A. Gianfrate, O. Bleu, L. Dominici, V. Ardizzone, M. De Giorgi, D. Ballarini, G. Lerario, K. W. West, L. N. Pfeiffer, D. D. Solnyshkov, D. Sanvitto, and G. Malpuech. Measurement of the quantum geometric tensor and of the anomalous Hall drift. *Nature*, 578(7795):381–385, 2020. doi: 10.1038/s41586-020-1989-2. URL `https://doi.org/10.1038/s41586-020-1989-2`.

[192] Javier Cuerda, Jani M. Taskinen, Nicki Källman, Leo Grabitz, and Päivi Törmä. Observation of quantum metric and non-Hermitian Berry curvature in a plasmonic lattice. *Phys. Rev. Res.*, 6:L022020, Apr 2024. doi: 10.1103/PhysRevResearch.6.L022020. URL `https://link.aps.org/doi/10.1103/PhysRevResearch.6.L022020`.

[193] Sudipto Singha Roy, Soumik Bandyopadhyay, Ricardo Costa de Almeida, and Philipp Hauke. Unveiling eigenstate thermalization for non-Hermitian systems. *Phys. Rev. Lett.*, 134:180405, May 2025. doi: 10.1103/PhysRevLett.134.180405. URL `https://link.aps.org/doi/10.1103/PhysRevLett.134.180405`.

[194] Dorje C Brody. Biorthogonal quantum mechanics. *Journal of Physics A: Mathematical and Theoretical*, 47(3):035305, dec 2013. doi: 10.1088/1751-8113/47/3/035305. URL `https://dx.doi.org/10.1088/1751-8113/47/3/035305`.

[195] Ali Mostafazadeh. Time-dependent pseudo-Hermitian Hamiltonians defining a unitary quantum system and uniqueness of the metric operator. *Physics Letters B*, 650(2):208–212, 2007. ISSN 0370-2693. doi: https://doi.org/10.1016/j.physletb.2007.04.064. URL `https://www.sciencedirect.com/science/article/pii/S0370269307005485`.

[196] Bartłomiej Gardas, Sebastian Deffner, and Avadh Saxena. non-Hermitian quantum thermodynamics. *Scientific Reports*, 6(1):23408, 2016. doi: 10.1038/srep23408. URL `https://doi.org/10.1038/srep23408`.

[197] Chia-Yi Ju, Adam Miranowicz, Guang-Yin Chen, and Franco Nori. Non-Hermitian Hamiltonians and no-go theorems in quantum information. *Phys. Rev. A*, 100: 062118, Dec 2019. doi: 10.1103/PhysRevA.100.062118. URL `https://link.aps.org/doi/10.1103/PhysRevA.100.062118`.

[198] Norifumi Matsumoto, Kohei Kawabata, Yuto Ashida, Shunsuke Furukawa, and Masahito Ueda. Continuous phase transition without gap closing in non-Hermitian quantum many-body systems. *Phys. Rev. Lett.*, 125:260601, Dec 2020. doi: 10.1103/PhysRevLett.125.260601. URL `https://link.aps.org/doi/10.1103/PhysRevLett.125.260601`.

[199] Qing Liao, Charly Leblanc, Jiahuan Ren, Feng Li, Yiming Li, Dmitry Solnyshkov, Guillaume Malpuech, Jiannian Yao, and Hongbing Fu. Experimental measurement of the divergent quantum metric of an exceptional point. *Phys. Rev. Lett.*, 127: 107402, Sep 2021. doi: 10.1103/PhysRevLett.127.107402. URL `https://link.aps.org/doi/10.1103/PhysRevLett.127.107402`.

[200] Dorje C. Brody and Eva-Maria Graefe. Information geometry of complex Hamiltonians and exceptional points. *Entropy*, 15(9):3361–3378, 2013. ISSN 1099-4300. doi: 10.3390/e15093361. URL `https://www.mdpi.com/1099-4300/15/9/3361`.

[201] Da-Jian Zhang, Qing-hai Wang, and Jiangbin Gong. Quantum geometric tensor in PT-symmetric quantum mechanics. *Phys. Rev. A*, 99:042104, Apr 2019. doi: 10.1103/PhysRevA.99.042104. URL `https://link.aps.org/doi/10.1103/PhysRevA.99.042104`.

[202] G. Huang A. Fan and S. Liang. Complex Berry curvature pair and quantum Hall admittance in non-Hermitian systems. *Journal of Physics Communications*, 4(11): 115006, 2020. URL `https://doi.org/10.1088/2399-6528/abcab6`.

[203] Chao Chen Ye, W. L. Vleeshouwers, S. Heatley, V. Gritsev, and C. Morais Smith. Quantum metric of non-Hermitian Su-Schrieffer-Heeger systems. *Phys. Rev. Res.*, 6: 023202, May 2024. doi: 10.1103/PhysRevResearch.6.023202. URL `https://link.aps.org/doi/10.1103/PhysRevResearch.6.023202`.

[204] Yong Xu, Sheng-Tao Wang, and L.-M. Duan. Weyl exceptional rings in a three-dimensional dissipative cold atomic gas. *Phys. Rev. Lett.*, 118:045701, Jan 2017. doi: 10.1103/PhysRevLett.118.045701. URL `https://link.aps.org/doi/10.1103/PhysRevLett.118.045701`.

[205] Navot Silberstein, Jan Behrends, Moshe Goldstein, and Roni Ilan. Berry connection induced anomalous wave-packet dynamics in non-Hermitian systems. *Phys. Rev. B*, 102:245147, Dec 2020. doi: 10.1103/PhysRevB.102.245147. URL `https://link.aps.org/doi/10.1103/PhysRevB.102.245147`.

[206] Jiong-Hao Wang, Yu-Liang Tao, and Yong Xu. Anomalous transport induced by non-Hermitian anomalous Berry connection in non-Hermitian systems. *Chin. Phys.*

Lett., 39:010301, 2022. ISSN 0256-307X. doi: 10.1088/0256-307X/39/1/010301. URL `http://cpl.iphy.ac.cn/article/10.1088/0256-307X/39/1/010301`.

[207] Yu-Chin Tzeng, Chia-Yi Ju, Guang-Yin Chen, and Wen-Min Huang. Hunting for the non-Hermitian exceptional points with fidelity susceptibility. *Phys. Rev. Res.*, 3:013015, Jan 2021. doi: 10.1103/PhysRevResearch.3.013015. URL `https://link.aps.org/doi/10.1103/PhysRevResearch.3.013015`.

[208] Hui Jiang, Chao Yang, and Shu Chen. Topological invariants and phase diagrams for one-dimensional two-band non-Hermitian systems without chiral symmetry. *Phys. Rev. A*, 98:052116, Nov 2018. doi: 10.1103/PhysRevA.98.052116. URL `https://link.aps.org/doi/10.1103/PhysRevA.98.052116`.

[209] Yi-Ting Tu, Iksu Jang, Po-Yao Chang, and Yu-Chin Tzeng. General properties of fidelity in non-Hermitian quantum systems with PT symmetry. *Quantum*, 7:960, Mar 2023. doi: 10.22331/q-2023-03-23-960. URL `https://doi.org/10.22331/q-2023-03-23-960`.

[210] Peng He, Hai-Tao Ding, and Shi-Liang Zhu. Geometry and superfluidity of the flat band in a non-Hermitian optical lattice. *Phys. Rev. A*, 103:043329, Apr 2021. doi: 10.1103/PhysRevA.103.043329. URL `https://link.aps.org/doi/10.1103/PhysRevA.103.043329`.

[211] Hui Deng, Gregor Weihs, Charles Santori, Jacqueline Bloch, and Yoshihisa Yamamoto. Condensation of semiconductor microcavity exciton polaritons. *Science*, 298(5591):199–202, 2002. doi: 10.1126/science.1074464. URL `https://www.science.org/doi/abs/10.1126/science.1074464`.

[212] R. Balili, V. Hartwell, D. Snoke, L. Pfeiffer, and K. West. Bose-einstein condensation of microcavity polaritons in a trap. *Science*, 316(5827):1007–1010, 2007. doi: 10.1126/science.1140990. URL `https://www.science.org/doi/abs/10.1126/science.1140990`.

[213] J. Kasprzak, M. Richard, S. Kundermann, A. Baas, P. Jeambrun, J. M. J. Keeling, F. M. Marchetti, M. H. Szymańska, R. André, J. L. Staehli, V. Savona, P. B. Littlewood, B. Deveaud, and Le Si Dang. Bose–Einstein condensation of exciton polaritons. *Nature*, 443(7110):409–414, 2006. doi: 10.1038/nature05131. URL `https://doi.org/10.1038/nature05131`.

[214] Maxime Richard, Jacek Kasprzak, Robert Romestain, Régis André, and Le Si Dang. Spontaneous coherent phase transition of polaritons in cdte microcavities. *Phys. Rev. Lett.*, 94:187401, May 2005. doi: 10.1103/PhysRevLett.94.187401. URL `https://link.aps.org/doi/10.1103/PhysRevLett.94.187401`.

[215] L. C. Flatten, Z. He, D. M. Coles, A. A. P. Trichet, A. W. Powell, R. A. Taylor, J. H. Warner, and J. M. Smith. Room-temperature exciton-polaritons with two-dimensional ws2. *Scientific Reports*, 6(1):33134, Sep 2016. ISSN 2045-2322. doi: 10.1038/srep33134. URL `https://doi.org/10.1038/srep33134`.

[216] M. Wurdack, E. Estrecho, S. Todd, C. Schneider, A. G. Truscott, and E. A. Ostrovskaya. Enhancing ground-state population and macroscopic coherence of room-temperature ws_2 polaritons through engineered confinement. *Phys. Rev. Lett.*, 129:147402, Sep 2022. doi: 10.1103/PhysRevLett.129.147402. URL `https://link.aps.org/doi/10.1103/PhysRevLett.129.147402`.

[217] Michael S. Spencer, Yongping Fu, Andrew P. Schlaus, Doyk Hwang, Yanan Dai, Matthew D. Smith, Daniel R. Gamelin, and X.-Y. Zhu. Spin-orbit–coupled exciton-polariton condensates in lead halide perovskites. *Science Advances*, 7(49):eabj7667, 2021. doi: 10.1126/sciadv.abj7667. URL `https://www.science.org/doi/abs/10.1126/sciadv.abj7667`.

[218] Rui Su, Eliezer Estrecho, Dąbrówka Biegańska, Yuqing Huang, Matthias Wurdack, Maciej Pieczarka, Andrew G. Truscott, Timothy C. H. Liew, Elena A. Ostrovskaya, and Qihua Xiong. Direct measurement of a non-Hermitian topological invariant in a hybrid light-matter system. *Science Advances*, 7(45):eabj8905, 2021. doi: 10.1126/sciadv.abj8905. URL `https://www.science.org/doi/abs/10.1126/sciadv.abj8905`.

[219] Steffen Richter, Heinrich-Gregor Zirnstein, Jesús Zúñiga Pérez, Evgeny Krüger, Christiane Deparis, Lukas Trefflich, Chris Sturm, Bernd Rosenow, Marius Grundmann, and Rüdiger Schmidt-Grund. Voigt exceptional points in an anisotropic ZnO-based planar microcavity: Square-root topology, polarization vortices, and circularity. *Phys. Rev. Lett.*, 123:227401, Nov 2019. doi: 10.1103/PhysRevLett.123.227401. URL `https://link.aps.org/doi/10.1103/PhysRevLett.123.227401`.

[220] Karolina Łempicka-Mirek, Mateusz Król, Helgi Sigurdsson, Adam Wincukiewicz, Przemysław Morawiak, Rafał Mazur, Marcin Muszyński, Wiktor Piecek, Przemysław Kula, Tomasz Stefaniuk, Maria Kamińska, Luisa De Marco, Pavlos G. Lagoudakis, Dario Ballarini, Daniele Sanvitto, Jacek Szczytko, and Barbara Pietka. Electrically tunable Berry curvature and strong light-matter coupling in liquid crystal microcavities with 2D perovskite. *Science Advances*, 8(40):eabq7533, 2022.

[221] Hui Deng, Glenn S. Solomon, Rudolf Hey, Klaus H. Ploog, and Yoshihisa Yamamoto. Spatial coherence of a polariton condensate. *Phys. Rev. Lett.*, 99:126403, Sep 2007. doi: 10.1103/PhysRevLett.99.126403. URL `https://link.aps.org/doi/10.1103/PhysRevLett.99.126403`.

[222] C. W. Lai, N. Y. Kim, S. Utsunomiya, G. Roumpos, H. Deng, M. D. Fraser, T. Byrnes, P. Recher, N. Kumada, T. Fujisawa, and Y. Yamamoto. Coherent zero-state and π-state in an exciton–polariton condensate array. *Nature*, 450(7169): 529–532, Nov 2007. ISSN 1476-4687. doi: 10.1038/nature06334. URL `https://doi.org/10.1038/nature06334`.

[223] M. H. Szymańska, J. Keeling, and P. B. Littlewood. Nonequilibrium quantum condensation in an incoherently pumped dissipative system. *Phys. Rev. Lett.*, 96:

230602, Jun 2006. doi: 10.1103/PhysRevLett.96.230602. URL `https://link.aps.org/doi/10.1103/PhysRevLett.96.230602`.

[224] Alberto Amo, Jérôme Lefrère, Simon Pigeon, Claire Adrados, Cristiano Ciuti, Iacopo Carusotto, Romuald Houdré, Elisabeth Giacobino, and Alberto Bramati. Superfluidity of polaritons in semiconductor microcavities. *Nature Physics*, 5(11):805–810, 2009. doi: 10.1038/nphys1364. URL `https://doi.org/10.1038/nphys1364`.

[225] A. Amo, S. Pigeon, D. Sanvitto, V. G. Sala, R. Hivet, I. Carusotto, F. Pisanello, G. Leménager, R. Houdré, E Giacobino, C. Ciuti, and A. Bramati. Polariton superfluids reveal quantum hydrodynamic solitons. *Science*, 332(6034):1167–1170, 2011. doi: 10.1126/science.1202307. URL `https://www.science.org/doi/abs/10.1126/science.1202307`.

[226] D. Sanvitto, F. M. Marchetti, M. H. Szymańska, G. Tosi, M. Baudisch, F. P. Laussy, D. N. Krizhanovskii, M. S. Skolnick, L. Marrucci, A. Lemaître, J. Bloch, C. Tejedor, and L. Viña. Persistent currents and quantized vortices in a polariton superfluid. *Nature Physics*, 6(7):527–533, Jul 2010. ISSN 1745-2481. doi: 10.1038/nphys1668. URL `https://doi.org/10.1038/nphys1668`.

[227] G. Grosso, G. Nardin, F. Morier-Genoud, Y. Léger, and B. Deveaud-Plédran. Soliton instabilities and vortex street formation in a polariton quantum fluid. *Phys. Rev. Lett.*, 107:245301, Dec 2011. doi: 10.1103/PhysRevLett.107.245301. URL `https://link.aps.org/doi/10.1103/PhysRevLett.107.245301`.

[228] Gaël Nardin, Gabriele Grosso, Yoan Léger, Barbara Pitka, François Morier-Genoud, and Benoît Deveaud-Plédran. Hydrodynamic nucleation of quantized vortex pairs in a polariton quantum fluid. *Nature Physics*, 7(8):635–641, Aug 2011. ISSN 1745-2481. doi: 10.1038/nphys1959. URL `https://doi.org/10.1038/nphys1959`.

[229] Alexey Kavokin, Guillaume Malpuech, and Mikhail Glazov. Optical spin hall effect. *Phys. Rev. Lett.*, 95:136601, Sep 2005. doi: 10.1103/PhysRevLett.95.136601. URL `https://link.aps.org/doi/10.1103/PhysRevLett.95.136601`.

[230] C. Leyder, M. Romanelli, J. Ph. Karr, E. Giacobino, T. C. H. Liew, M. M. Glazov, A. V. Kavokin, G. Malpuech, and A. Bramati. Observation of the optical spin hall effect. *Nature Physics*, 3(9):628–631, Sep 2007. ISSN 1745-2481. doi: 10.1038/nphys676. URL `https://doi.org/10.1038/nphys676`.

[231] E. Estrecho, T. Gao, S. Brodbeck, M. Kamp, C. Schneider, S. Höfling, A. G. Truscott, and E. A. Ostrovskaya. Visualising Berry phase and diabolical points in a quantum exciton-polariton billiard. *Scientific Reports*, 6:37653, November 2016. doi: 10.1038/srep37653.

[232] S. Klembt, T. H. Harder, O. A. Egorov, K. Winkler, R. Ge, M. A. Bandres, M. Emmerling, L. Worschech, T. C. H. Liew, M. Segev, C. Schneider, and S. Höfling. Exciton-polariton topological insulator. *Nature*, 562(7728):552–556, 2018. doi: 10.1038/s41586-018-0601-5. URL `https://doi.org/10.1038/s41586-018-0601-5`.

[233] Jiahuan Ren, Qing Liao, Feng Li, Yiming Li, Olivier Bleu, Guillaume Malpuech, Jiannian Yao, Hongbing Fu, and Dmitry Solnyshkov. Nontrivial band geometry in an optically active system. *Nature Communications*, 12(1):689, Jan 2021. ISSN 2041-1723. doi: 10.1038/s41467-020-20845-2. URL `https://doi.org/10.1038/s41467-020-20845-2`.

[234] Laura Polimeno, Giovanni Lerario, Milena De Giorgi, Luisa De Marco, Lorenzo Dominici, Francesco Todisco, Annalisa Coriolano, Vincenzo Ardizzone, Marco Pugliese, Carmela T Prontera, Vincenzo Maiorano, Anna Moliterni, Cinzia Giannini, Vincent Olieric, Giuseppe Gigli, Dario Ballarini, Qihua Xiong, Antonio Fieramosca, Dmitry D. Solnyshkov, Guillaume Malpuech, and Daniele Sanvitto. Tuning of the Berry curvature in 2D perovskite polaritons. *Nature nanotechnology*, 16(12):1349–1354, 2021.

[235] E. S. Sedov, Y. G. Rubo, and A. V. Kavokin. *Zitterbewegung* of exciton-polaritons. *Phys. Rev. B*, 97:245312, Jun 2018. doi: 10.1103/PhysRevB.97.245312. URL `https://link.aps.org/doi/10.1103/PhysRevB.97.245312`.

[236] Wen Wen, Jie Liang, Huawen Xu, Feng Jin, Yuri G. Rubo, Timothy C. H. Liew, and Rui Su. Trembling motion of exciton polaritons close to the Rashba-Dresselhaus regime. *Phys. Rev. Lett.*, 133:116903, Sep 2024. doi: 10.1103/PhysRevLett.133.116903. URL `https://link.aps.org/doi/10.1103/PhysRevLett.133.116903`.

[237] Tamsin Cookson, Kirill Kalinin, Helgi Sigurdsson, Julian D. Töpfer, Sergey Alyatkin, Matteo Silva, Wolfgang Langbein, Natalia G. Berloff, and Pavlos G. Lagoudakis. Geometric frustration in polygons of polariton condensates creating vortices of varying topological charge. *Nature Communications*, 12(1):2120, Apr 2021. ISSN 2041-1723. doi: 10.1038/s41467-021-22121-3. URL `https://doi.org/10.1038/s41467-021-22121-3`.

[238] S.L. Harrison, H. Sigurdsson, S. Alyatkin, J.D. Töpfer, and P.G. Lagoudakis. Solving the max-3-cut problem with coherent networks. *Phys. Rev. Appl.*, 17:024063, Feb 2022. doi: 10.1103/PhysRevApplied.17.024063. URL `https://link.aps.org/doi/10.1103/PhysRevApplied.17.024063`.

[239] W. Verstraelen, P. Deuar, M. Matuszewski, and T.C.H. Liew. Analog spin simulators: How to keep the amplitude homogeneous. *Phys. Rev. Appl.*, 21:024057, Feb 2024. doi: 10.1103/PhysRevApplied.21.024057. URL `https://link.aps.org/doi/10.1103/PhysRevApplied.21.024057`.

[240] Huawen Xu, Tanjung Krisnanda, Wouter Verstraelen, Timothy C. H. Liew, and Sanjib Ghosh. Superpolynomial quantum enhancement in polaritonic neuromorphic computing. *Phys. Rev. B*, 103:195302, May 2021. doi: 10.1103/PhysRevB.103.195302. URL `https://link.aps.org/doi/10.1103/PhysRevB.103.195302`.

[241] Rafał Mirek, Andrzej Opala, Paolo Comaron, Magdalena Furman, Mateusz Król, Krzysztof Tyszka, Bartłomiej Seredyński, Dario Ballarini, Daniele Sanvitto, Tim-

othy C. H. Liew, Wojciech Pacuski, Jan Suffczyński, Jacek Szczytko, Michał Matuszewski, and Barbara Piętka. Neuromorphic binarized polariton networks. *Nano Letters*, 21(9):3715–3720, May 2021. ISSN 1530-6984. doi: 10.1021/acs.nanolett.0c04696. URL `https://doi.org/10.1021/acs.nanolett.0c04696`.

[242] Andrzej Opala and Michał Matuszewski. Harnessing exciton-polaritons for digital computing, neuromorphic computing, and optimization. *Optical Materials Express*, 2023. URL `https://api.semanticscholar.org/CorpusID:259137571`.

[243] J. J. Hopfield. Theory of the contribution of excitons to the complex dielectric constant of crystals. *Phys. Rev.*, 112:1555–1567, Dec 1958. doi: 10.1103/PhysRev.112.1555. URL `https://link.aps.org/doi/10.1103/PhysRev.112.1555`.

[244] Michiel Wouters and Iacopo Carusotto. Excitations in a nonequilibrium bose-einstein condensate of exciton polaritons. *Phys. Rev. Lett.*, 99:140402, Oct 2007. doi: 10.1103/PhysRevLett.99.140402. URL `https://link.aps.org/doi/10.1103/PhysRevLett.99.140402`.

[245] E. P. Gross. Structure of a quantized vortex in boson systems. *Il Nuovo Cimento (1955-1965)*, 20(3):454–477, May 1961. ISSN 1827-6121. doi: 10.1007/BF02731494. URL `https://doi.org/10.1007/BF02731494`.

[246] Pitaevskii L. P. Vortex lines in an imperfect bose gas. *Sov. Phys.-JETP*, 13(2):451, 1961. URL `https://cir.nii.ac.jp/crid/1571698599883889664`.

[247] Michiel Wouters, Iacopo Carusotto, and Cristiano Ciuti. Spatial and spectral shape of inhomogeneous nonequilibrium exciton-polariton condensates. *Phys. Rev. B*, 77:115340, Mar 2008. doi: 10.1103/PhysRevB.77.115340. URL `https://link.aps.org/doi/10.1103/PhysRevB.77.115340`.

[248] P. Comaron, E. Estrecho, M. Wurdack, M. Pieczarka, M. Steger, D. W. Snoke, K. West, L. N. Pfeiffer, A. G. Truscott, M. Matuszewski, M. H. Szymańska, and E. A. Ostrovskaya. Coherence of a non-equilibrium polariton condensate across the interaction-mediated phase transition. *Communications Physics*, 8(1):94, Mar 2025. ISSN 2399-3650. doi: 10.1038/s42005-025-01977-7. URL `https://doi.org/10.1038/s42005-025-01977-7`.

[249] Yow-Ming Robin Hu, Mateusz Król, Lev A. Smirnova, Daria A.and Smirnov, Bianca Rae Fabricante, Karol Winkler, Martin Kamp, Christian Schneider, Sven Höfling, Andrew G. Liew, Timothy C.H. Truscott, Elena A. Ostrovskaya, and Eliezer Estrecho. Momentum-space non-Hermitian skin effect in an exciton-polariton systems. arXiv preprint arXiv:2512.10146.

[250] M. Pieczarka, M. Boozarjmehr, E. Estrecho, Y. Yoon, M. Steger, K. West, L. N. Pfeiffer, K. A. Nelson, D. W. Snoke, A. G. Truscott, and E. A. Ostrovskaya. Effect of optically induced potential on the energy of trapped exciton polaritons below the condensation threshold. *Phys. Rev. B*, 100:085301, Aug 2019.

doi: 10.1103/PhysRevB.100.085301. URL `https://link.aps.org/doi/10.1103/PhysRevB.100.085301`.

[251] I A Shelykh, A V Kavokin, Yuri G Rubo, T C H Liew, and G Malpuech. Polariton polarization-sensitive phenomena in planar semiconductor microcavities. *Semiconductor Science and Technology*, 25(1):013001, dec 2009. doi: 10.1088/0268-1242/25/1/013001. URL `https://dx.doi.org/10.1088/0268-1242/25/1/013001`.

[252] J. M. Luttinger. Quantum theory of cyclotron resonance in semiconductors: General theory. *Phys. Rev.*, 102:1030–1041, May 1956. doi: 10.1103/PhysRev.102.1030. URL `https://link.aps.org/doi/10.1103/PhysRev.102.1030`.

[253] Yinan Fang, Pericles Philippopoulos, Dimitrie Culcer, W A Coish, and Stefano Chesi. Recent advances in hole-spin qubits. *Materials for Quantum Technology*, 3 (1):012003, mar 2023. doi: 10.1088/2633-4356/acb87e. URL `https://doi.org/10.1088/2633-4356/acb87e`.

[254] R. J. Elliott. Theory of the effect of spin-orbit coupling on magnetic resonance in some semiconductors. *Phys. Rev.*, 96:266–279, Oct 1954. doi: 10.1103/PhysRev.96.266. URL `https://link.aps.org/doi/10.1103/PhysRev.96.266`.

[255] Y. Yafet. g factors and spin-lattice relaxation of conduction electrons. volume 14 of *Solid State Physics*, pages 1–98. Academic Press, 1963. doi: https://doi.org/10.1016/S0081-1947(08)60259-3. URL `https://www.sciencedirect.com/science/article/pii/S0081194708602593`.

[256] Michel Dyakonov and V.I. Perel. Spin relaxation of conduction electrons in noncentrosymetric semiconductors. *Fiz. Tverd. Tela*, 13:3851, 1971.

[257] G. E. Pikus and G. L. Bir. Exchange interaction in excitons in semiconductors. *Zh. Eksp. Teor. Fiz.*, 60:195–208, 1971.

[258] M. Z. Maialle, E. A. de Andrada e Silva, and L. J. Sham. Exciton spin dynamics in quantum wells. *Phys. Rev. B*, 47:15776–15788, Jun 1993. doi: 10.1103/PhysRevB.47.15776. URL `https://link.aps.org/doi/10.1103/PhysRevB.47.15776`.

[259] K. V. Kavokin, I. A. Shelykh, A. V. Kavokin, G. Malpuech, and P. Bigenwald. Quantum theory of spin dynamics of exciton-polaritons in microcavities. *Phys. Rev. Lett.*, 92:017401, Jan 2004. doi: 10.1103/PhysRevLett.92.017401. URL `https://link.aps.org/doi/10.1103/PhysRevLett.92.017401`.

[260] I. A. Shelykh, A. V. Kavokin, and G. Malpuech. Spin dynamics of exciton polaritons in microcavities. *physica status solidi (b)*, 242(11):2271–2289, 2005. doi: https://doi.org/10.1002/pssb.200560965. URL `https://onlinelibrary.wiley.com/doi/abs/10.1002/pssb.200560965`.

[261] H. Terças, H. Flayac, D. D. Solnyshkov, and G. Malpuech. Non-abelian gauge fields in photonic cavities and photonic superfluids. *Phys. Rev. Lett.*, 112:066402,

Feb 2014. doi: 10.1103/PhysRevLett.112.066402. URL `https://link.aps.org/doi/10.1103/PhysRevLett.112.066402`.

[262] Giovanna Panzarini, Lucio Claudio Andreani, A. Armitage, D. Baxter, M. S. Skolnick, V. N. Astratov, J. S. Roberts, Alexey V. Kavokin, Maria R. Vladimirova, and M. A. Kaliteevski. Exciton-light coupling in single and coupled semiconductor microcavities: Polariton dispersion and polarization splitting. *Phys. Rev. B*, 59: 5082–5089, Feb 1999. doi: 10.1103/PhysRevB.59.5082. URL `https://link.aps.org/doi/10.1103/PhysRevB.59.5082`.

[263] A. Kuther, M. Bayer, T. Gutbrod, A. Forchel, P. A. Knipp, T. L. Reinecke, and R. Werner. Confined optical modes in photonic wires. *Phys. Rev. B*, 58:15744–15748, Dec 1998. doi: 10.1103/PhysRevB.58.15744. URL `https://link.aps.org/doi/10.1103/PhysRevB.58.15744`.

[264] Wenquan Liu, Yang Wu, Chang-Kui Duan, Xing Rong, and Jiangfeng Du. Dynamically encircling an exceptional point in a real quantum system. *Phys. Rev. Lett.*, 126:170506, Apr 2021. doi: 10.1103/PhysRevLett.126.170506. URL `https://link.aps.org/doi/10.1103/PhysRevLett.126.170506`.

[265] M. Król, I. Septembre, P. Oliwa, M. Kędziora, K. Łempicka-Mirek, M. Muszyński, R. Mazur, P. Morawiak, W. Piecek, P. Kula, W. Bardyszewski, P. G. Lagoudakis, D. D. Solnyshkov, G. Malpuech, B. Pietka, and J. Szczytko. Annihilation of exceptional points from different dirac valleys in a 2d photonic system. *Nature Communications*, 13(1):5340, 2022. doi: 10.1038/s41467-022-33001-9. URL `https://doi.org/10.1038/s41467-022-33001-9`.

[266] Xiangang Wan, Ari M. Turner, Ashvin Vishwanath, and Sergey Y. Savrasov. Topological semimetal and Fermi-arc surface states in the electronic structure of pyrochlore iridates. *Phys. Rev. B*, 83:205101, May 2011. doi: 10.1103/PhysRevB.83.205101. URL `https://link.aps.org/doi/10.1103/PhysRevB.83.205101`.

[267] Gaoyong Sun, Jia-Chen Tang, and Su-Peng Kou. Biorthogonal quantum criticality in non-Hermitian many-body systems. *Frontiers of Physics*, 17(3): 33502, 2021. doi: 10.1007/s11467-021-1126-1. URL `https://doi.org/10.1007/s11467-021-1126-1`.

[268] D. Biegańska, M. Pieczarka, E. Estrecho, M. Steger, D. W. Snoke, K. West, L. N. Pfeiffer, M. Syperek, A. G. Truscott, and E. A. Ostrovskaya. Collective excitations of exciton-polariton condensates in a synthetic Gauge field. *Phys. Rev. Lett.*, 127: 185301, Oct 2021. doi: 10.1103/PhysRevLett.127.185301. URL `https://link.aps.org/doi/10.1103/PhysRevLett.127.185301`.

[269] Stefano Longhi. Non-Hermitian skin effect and self-acceleration. *Phys. Rev. B*, 105: 245143, Jun 2022. doi: 10.1103/PhysRevB.105.245143. URL `https://link.aps.org/doi/10.1103/PhysRevB.105.245143`.

[270] Kohei Kawabata, Ken Shiozaki, and Masahito Ueda. Anomalous helical edge states in a non-Hermitian Chern insulator. *Phys. Rev. B*, 98:165148, Oct 2018. doi: 10.1103/PhysRevB.98.165148. URL `https://link.aps.org/doi/10.1103/PhysRevB.98.165148`.

[271] Y.-M. Robin Hu, Elena A. Ostrovskaya, and Eliezer Estrecho. Wave-packet dynamics in a non-Hermitian exciton-polariton system. *Phys. Rev. B*, 108:115404, Sep 2023. doi: 10.1103/PhysRevB.108.115404. URL `https://link.aps.org/doi/10.1103/PhysRevB.108.115404`.

[272] G. Dattoli, A. Torre, and R. Mignani. Non-Hermitian evolution of two-level quantum systems. *Phys. Rev. A*, 42:1467–1475, Aug 1990. doi: 10.1103/PhysRevA.42.1467. URL `https://link.aps.org/doi/10.1103/PhysRevA.42.1467`.

[273] E. M. Graefe, H. J. Korsch, and A. E. Niederle. Mean-field dynamics of a non-Hermitian Bose-Hubbard dimer. *Phys. Rev. Lett.*, 101:150408, Oct 2008. doi: 10.1103/PhysRevLett.101.150408. URL `https://link.aps.org/doi/10.1103/PhysRevLett.101.150408`.

[274] E Estrecho, M Pieczarka, M Wurdack, M Steger, K West, LN Pfeiffer, D. W. Snoke, A. G. Truscott, and E. A. Ostrovskaya. Low-energy collective oscillations and bogoliubov sound in an exciton-polariton condensate. *Physical Review Letters*, 126(7):075301, 2021.

[275] Mark Steger, Chitra Gautham, David W. Snoke, Loren Pfeiffer, and Ken West. Slow reflection and two-photon generation of microcavity exciton–polaritons. *Optica*, 2 (1):1–5, Jan 2015. doi: 10.1364/OPTICA.2.000001. URL `https://opg.optica.org/optica/abstract.cfm?URI=optica-2-1-1`.

[276] Y.-M. Robin Hu, Elena A. Ostrovskaya, and Eliezer Estrecho. Wave-packet dynamics in a non-Hermitian exciton-polariton system. *Phys. Rev. B*, 108:115404, Sep 2023. doi: 10.1103/PhysRevB.108.115404. URL `https://link.aps.org/doi/10.1103/PhysRevB.108.115404`.

[277] C. Yuce and Z. Turker. Self-acceleration in non-Hermitian systems. *Physics Letters A*, 381(28):2235–2238, 2017. ISSN 0375-9601. doi: https://doi.org/10.1016/j.physleta.2017.05.012. URL `https://www.sciencedirect.com/science/article/pii/S0375960117304504`.

[278] J. Andre Weideman and Ben M. Herbst. Split-step methods for the solution of the nonlinear Schrödinger equation. *SIAM Journal on Numerical Analysis*, 23:485–507, 1986. URL `https://api.semanticscholar.org/CorpusID:120843423`.

[279] Thiab R. Taha and Xiangming Xu. Parallel split-step Fourier methods for the coupled nonlinear Schrödinger type equations. *The Journal of Supercomputing*, 32 (1):5–23, 2005. doi: 10.1007/s11227-005-0183-5. URL `https://doi.org/10.1007/s11227-005-0183-5`.

[280] Morton M. Sternheim and James F. Walker. Non-Hermitian Hamiltonians, decaying states, and perturbation theory. *Phys. Rev. C*, 6:114–121, Jul 1972. doi: 10.1103/PhysRevC.6.114. URL `https://link.aps.org/doi/10.1103/PhysRevC.6.114`.

[281] Y.-M. Robin Hu, Elena A. Ostrovskaya, and Eliezer Estrecho. Quantum geometric tensor and wavepacket dynamics in two-dimensional non-Hermitian systems. *Phys. Rev. Res.*, 7:L012067, Mar 2025. doi: 10.1103/PhysRevResearch.7.L012067. URL `https://link.aps.org/doi/10.1103/PhysRevResearch.7.L012067`.

[282] C. Leblanc, G. Malpuech, and D. D. Solnyshkov. Universal semiclassical equations based on the quantum metric for a two-band system. *Phys. Rev. B*, 104:134312, Oct 2021. doi: 10.1103/PhysRevB.104.134312. URL `https://link.aps.org/doi/10.1103/PhysRevB.104.134312`.

[283] Yow-Ming Robin Hu, Elena Ostrovskaya, and Eliezer Estrecho. Data of the wavepacket centre-of-mass positions used in fig. 1 in supplementary material - quantum geometric tensor and wavepacket dynamics in two- dimensional non-Hermitian systems, February 2025. URL `https://doi.org/10.5281/zenodo.14880225`.

[284] Erwin Schrödinger. Über die kräftefreie bewegung in der relativistischen quantenmechanik. *Sitzungber. Preuss. Akad. Wiss. Phys.-Math. Kl.*, 24:418–428, 1930. URL `https://cir.nii.ac.jp/crid/1130000796869683968`.

[285] David Hestenes. The zitterbewegung interpretation of quantum mechanics. *Foundations of Physics*, 20(10):1213–1232, Oct 1990. ISSN 1572-9516. doi: 10.1007/BF01889466. URL `https://doi.org/10.1007/BF01889466`.

[286] Shun-Qing Shen. Spin transverse force on spin current in an electric field, Oct 2005. URL `https://link.aps.org/doi/10.1103/PhysRevLett.95.187203`.

[287] József Cserti and Gyula Dávid. Unified description of zitterbewegung for spintronic, graphene, and superconducting systems. *Phys. Rev. B*, 74:172305, Nov 2006. doi: 10.1103/PhysRevB.74.172305. URL `https://link.aps.org/doi/10.1103/PhysRevB.74.172305`.

[288] John Schliemann, Daniel Loss, and R. M. Westervelt. Zitterbewegung of electronic wave packets in iii-v zinc-blende semiconductor quantum wells. *Phys. Rev. Lett.*, 94:206801, May 2005. doi: 10.1103/PhysRevLett.94.206801. URL `https://link.aps.org/doi/10.1103/PhysRevLett.94.206801`.

[289] John Schliemann, Daniel Loss, and R. M. Westervelt. Zitterbewegung of electrons and holes in iii–v semiconductor quantum wells. *Phys. Rev. B*, 73:085323, Feb 2006. doi: 10.1103/PhysRevB.73.085323. URL `https://link.aps.org/doi/10.1103/PhysRevB.73.085323`.

[290] Tomasz M. Rusin and Wlodek Zawadzki. Transient zitterbewegung of charge carriers in mono- and bilayer graphene, and carbon nanotubes. *Phys. Rev. B*, 76:195439,

Nov 2007. doi: 10.1103/PhysRevB.76.195439. URL `https://link.aps.org/doi/10.1103/PhysRevB.76.195439`.

[291] Tomasz M. Rusin and Wlodek Zawadzki. Theory of electron zitterbewegung in graphene probed by femtosecond laser pulses. *Phys. Rev. B*, 80:045416, Jul 2009. doi: 10.1103/PhysRevB.80.045416. URL `https://link.aps.org/doi/10.1103/PhysRevB.80.045416`.

[292] J. Y. Vaishnav and Charles W. Clark. Observing zitterbewegung with ultracold atoms. *Phys. Rev. Lett.*, 100:153002, Apr 2008. doi: 10.1103/PhysRevLett.100.153002. URL `https://link.aps.org/doi/10.1103/PhysRevLett.100.153002`.

[293] R. Gerritsma, G. Kirchmair, F. ZÃ¤hringer, E. Solano, R. Blatt, and C. F. Roos. Quantum simulation of the Dirac equation. *Nature*, 463(7277):68–71, Jan 2010. ISSN 1476-4687. doi: 10.1038/nature08688. URL `https://doi.org/10.1038/nature08688`.

[294] L. Lamata, J. León, T. Schätz, and E. Solano. Dirac equation and quantum relativistic effects in a single trapped ion. *Phys. Rev. Lett.*, 98:253005, Jun 2007. doi: 10.1103/PhysRevLett.98.253005. URL `https://link.aps.org/doi/10.1103/PhysRevLett.98.253005`.

[295] Xiangdong Zhang. Observing zitterbewegung for photons near the dirac point of a two-dimensional photonic crystal. *Phys. Rev. Lett.*, 100:113903, Mar 2008. doi: 10.1103/PhysRevLett.100.113903. URL `https://link.aps.org/doi/10.1103/PhysRevLett.100.113903`.

[296] S. Longhi. Photonic analog of zitterbewegung in binary waveguide arrays. *Opt. Lett.*, 35(2):235–237, Jan 2010. doi: 10.1364/OL.35.000235. URL `https://opg.optica.org/ol/abstract.cfm?URI=ol-35-2-235`.

[297] Weimin Ye, Yachao Liu, Jianlong Liu, Simon A. R. Horsley, Shuangchun Wen, and Shuang Zhang. Photonic hall effect and helical zitterbewegung in a synthetic weyl system. *Light: Science & Applications*, 8(1):49, May 2019. ISSN 2047-7538. doi: 10.1038/s41377-019-0160-z. URL `https://doi.org/10.1038/s41377-019-0160-z`.

[298] Seth Lovett, Paul M. Walker, Alexey Osipov, Alexey Yulin, Pooja Uday Naik, Charles E. Whittaker, Ivan A. Shelykh, Maurice S. Skolnick, and Dmitry N. Krizhanovskii. Observation of zitterbewegung in photonic microcavities. *Light: Science & Applications*, 12(1):126, May 2023. ISSN 2047-7538. doi: 10.1038/s41377-023-01162-x. URL `https://doi.org/10.1038/s41377-023-01162-x`.

[299] Eva-Maria Graefe, Hans Jürgen Korsch, and Astrid Elisa Niederle. Quantum-classical correspondence for a non-Hermitian Bose-Hubbard dimer. *Phys. Rev. A*, 82:013629, Jul 2010. doi: 10.1103/PhysRevA.82.013629. URL `https://link.aps.org/doi/10.1103/PhysRevA.82.013629`.

[300] Eva-Maria Graefe, Michael Höning, and Hans Jürgen Korsch. Classical limit of non-Hermitian quantum dynamics—a generalized canonical structure. *Journal of Physics A: Mathematical and Theoretical*, 43(7):075306, feb 2010. doi: 10.1088/1751-8113/43/7/075306. URL `https://dx.doi.org/10.1088/1751-8113/43/7/075306`.

[301] Jinghui Pi, Feng Chen, Qi Liu, Li You, and Rong LÃ¼. The dynamics of an open Bose-Hubbard dimer with effective asymmetric coupling. *The European Physical Journal B*, 97(3):26, Mar 2024. ISSN 1434-6036. doi: 10.1140/epjb/s10051-024-00661-z. URL `https://doi.org/10.1140/epjb/s10051-024-00661-z`.

[302] D. Cius, A. Consuelo-Leal, A. G. Araujo-Ferreira, and R. Auccaise. Mixed states driven by non-Hermitian Hamiltonians of a nuclear spin ensemble. *Phys. Rev. A*, 105:022212, Feb 2022. doi: 10.1103/PhysRevA.105.022212. URL `https://link.aps.org/doi/10.1103/PhysRevA.105.022212`.

[303] Gong-Ping Zheng and Guang-Tao Wang. Time evolution of two-states non-Hermitian systems. *International Journal of Theoretical Physics*, 60(3):1053–1062, Mar 2021. ISSN 1572-9575. doi: 10.1007/s10773-021-04726-y. URL `https://doi.org/10.1007/s10773-021-04726-y`.

[304] Yi-Piao Wu, Guo-Qing Zhang, Cai-Xia Zhang, Jian Xu, and Dan-Wei Zhang. Interplay of nonreciprocity and nonlinearity on mean-field energy and dynamics of a Bose-Einstein condensate in a double-well potential. *Frontiers of Physics*, 17 (4):42503, Dec 2021. ISSN 2095-0470. doi: 10.1007/s11467-021-1133-2. URL `https://doi.org/10.1007/s11467-021-1133-2`.

[305] Y.-M. Robin Hu, Elena A. Ostrovskaya, and Eliezer Estrecho. Zitterbewegung effect and quantum geometry in non-Hermitian exciton-polariton systems. *Applied Physics Letters*, 127(25):253101, 12 2025. ISSN 0003-6951. doi: 10.1063/5.0310064. URL `https://doi.org/10.1063/5.0310064`.

[306] Weimin Ye, Jianlong Liu, Yang Gao, and Shuang Zhang. Exotic zitterbewegung-like motion of wave packets near exceptional points. *Phys. Rev. B*, 106:L060303, Aug 2022. doi: 10.1103/PhysRevB.106.L060303. URL `https://link.aps.org/doi/10.1103/PhysRevB.106.L060303`.

[307] A N Kolmogorov. Local structure of turbulence in an incompressible viscous fluid at very high Reynolds numbers. *Soviet Physics Uspekhi*, 10(6):734, jun 1968. doi: 10.1070/PU1968v010n06ABEH003710. URL `https://dx.doi.org/10.1070/PU1968v010n06ABEH003710`.

[308] Matthew T. Reeves, Thomas P. Billam, Brian P. Anderson, and Ashton S. Bradley. Inverse energy cascade in forced two-dimensional quantum turbulence. *Phys. Rev. Lett.*, 110:104501, Mar 2013. doi: 10.1103/PhysRevLett.110.104501. URL `https://link.aps.org/doi/10.1103/PhysRevLett.110.104501`.

[309] Junsik Han and Makoto Tsubota. Onsager vortex formation in two-component Bose–Einstein condensates. *Journal of the Physical Society of Japan*, 87(6):063601, 2018. doi: 10.7566/JPSJ.87.063601. URL `https://doi.org/10.7566/JPSJ.87.063601`.

[310] R. Panico, P. Comaron, M. Matuszewski, A. S. Lanotte, D. Trypogeorgos, G. Gigli, M. De Giorgi, V. Ardizzone, D. Sanvitto, and D. Ballarini. Onset of vortex clustering and inverse energy cascade in dissipative quantum fluids. *Nature Photonics*, 17 (5):451–456, May 2023. ISSN 1749-4893. doi: 10.1038/s41566-023-01174-4. URL `https://doi.org/10.1038/s41566-023-01174-4`.

[311] Narayan Mohanta, Arno P. Kampf, and Thilo Kopp. Emergent momentum-space skyrmion texture on the surface of topological insulators. *Scientific Reports*, 7(1):45664, 2017. doi: 10.1038/srep45664. URL `https://doi.org/10.1038/srep45664`.

[312] Hiromitsu Takeuchi. Spin-current instability at a magnetic domain wall in a ferromagnetic superfluid: A generation mechanism of eccentric fractional skyrmions. *Phys. Rev. A*, 105:013328, Jan 2022. doi: 10.1103/PhysRevA.105.013328. URL `https://link.aps.org/doi/10.1103/PhysRevA.105.013328`.

[313] J. Beierlein, O. A. Egorov, P. Gagel, T. H. Harder, A. Wolf, M. Emmerling, S. Betzold, F. Jabeen, L. Ma, S. Höfling, U. Peschel, and S. Klembt. Topological optical waveguiding of exciton-polariton condensates. *Annalen der Physik*, 536 (11):2400229, 2024. doi: https://doi.org/10.1002/andp.202400229. URL `https://onlinelibrary.wiley.com/doi/abs/10.1002/andp.202400229`.

[314] Karol Winkler, Julian Fischer, Anne Schade, Matthias Amthor, Robert Dall, Jonas Geßler, Monika Emmerling, Elena A Ostrovskaya, Martin Kamp, Christian Schneider, and Sven Höfling. A polariton condensate in a photonic crystal potential landscape. *New Journal of Physics*, 17(2):023001, jan 2015. doi: 10.1088/1367-2630/17/2/023001. URL `https://dx.doi.org/10.1088/1367-2630/17/2/023001`.

[315] Yuan Luo, Yutian Peng, Lingyu Tian, Zhiyuan An, Haiyun Liu, Yuzhong Chen, Sanjib Ghosh, and Qihua Xiong. Revealing ultrafast optical nonlinearity of trapped exciton polaritons in atomically thin semiconductors. *Nano Letters*, 24(50):15981–15988, Dec 2024. ISSN 1530-6984. doi: 10.1021/acs.nanolett.4c04195. URL `https://doi.org/10.1021/acs.nanolett.4c04195`.

[316] E. Estrecho, T. Gao, N. Bobrovska, D. Comber-Todd, M. D. Fraser, M. Steger, K. West, L. N. Pfeiffer, J. Levinsen, M. M. Parish, T. C. H. Liew, M. Matuszewski, D. W. Snoke, A. G. Truscott, and E. A. Ostrovskaya. Direct measurement of polariton-polariton interaction strength in the Thomas-Fermi regime of exciton-polariton condensation. *Phys. Rev. B*, 100:035306, Jul 2019. doi: 10.1103/PhysRevB.100.035306. URL `https://link.aps.org/doi/10.1103/PhysRevB.100.035306`.

[317] L. Lehtovaara, J. Toivanen, and J. Eloranta. Solution of time-independent schrödinger equation by the imaginary time propagation method. *Journal of Computational Physics*, 221(1):148–157, 2007. ISSN 0021-9991. doi: https://doi.org/10.1016/j.jcp.2006.06.006. URL `https://www.sciencedirect.com/science/article/pii/S0021999106002798`.

[318] G. M. Tuynman. The derivation of the exponential map of matrices. *The American Mathematical Monthly*, 102(9):818–820, 1995. ISSN 00029890, 19300972. URL `http://www.jstor.org/stable/2974511`.

[319] Wulf Rossmann. *Lie Groups: An Introduction Through Linear Groups*. Oxford University Press, 01 2002. ISBN 9780198596837. doi: 10.1093/oso/9780198596837.001.0001. URL `https://doi.org/10.1093/oso/9780198596837.001.0001`.